Università degli Studi di Ferrara

DOCTORAL COURSE IN
PHYSICS

CYCLE XXXVIII

COORDINATOR Prof. Lenisa Paolo

Programming magnons through non-uniform magnetization: voltage-modulated sinusoidal textures for reconfigurable 3D Magnonics

Scientific/Disciplinary Sector (SDS) PHYS-04/A

Candidate
Micaletti Pietro

Supervisor
Prof. Montoncello Federico

Years 2022/2025

A chi mantiene la parola data.

"Vita sei bella, morte fai schifo."
Translation: *"Life, you are beautiful. Death, you suck."*

— Epitaph on Claudio Villa's tomb

SUMMARY

This thesis work explores and develops a versatile route to engineer magnon transport in ferromagnetic films by imprinting a controlled, nanoscale undulation of the equilibrium magnetization through vertical coupling (e.g., multiferroic coupling). The investigation is performed with micromagnetic simulations and Fourier analysis combined with analytical models to establish the magnetization undulation amplitude as a new degree of freedom for magnon propagation. The results are crucial to conceive magnonic devices with advanced functionalities.

In Chapters 1 and 2, we discuss how spin-wave dynamics is ruled by the Landau–Lifshitz–Gilbert (LLG) equation, and the competing exchange and dipolar contributions that shape dispersions and mode symmetries [1]. The simulations are carried out with the GPU-accelerated software MuMax3 [2] which solves the LLG equation on a finite-difference grid; its working principles are discussed extensively in Chapter 3. The simulated systems, made of permalloy or YIG depending on the specific investigation, are discretized into micromagnetic cells with length, width and thickness of few nanometers. In order to emulate vertical coupling, user-defined spatially varying fields and anisotropies are employed. The magnetization space maps, resulting from the applied excitations (broadband field pulses or continuous-wave drives), are collected as a function of time. Then spatiotemporal Fourier transform is applied to compute dispersion relations and mode profiles [3]. The ultimate purpose is to provide a quantitative bridge between imposed textures and the spectra.

In Chapter 4, by setting the groundstate as a sinusoidal distribution along one direction, we introduce periodicity and hence we realize a magnonic crystal. We superimpose to a uniform bias field B_0 a spatially periodic sinusoidal bias field B_S that not only can be applied in real experiments but can be seen as the simulation of a vertical coupling in multiferroics. We find that stationary spin wave modes forming at the Brillouin zone boundary because of Bragg diffraction lift their degeneracy due to the different way they experience the resulting periodic Zeeman term. Interestingly, we find a striking outcome when a chiral bias field B_C is applied: due to its distinctive space distribution, B_C breaks the mirror symmetry in the primitive cell. This effect is at the origin of a remarkable localized mode with a flat dispersion (i.e., stationary), absent in uniform films, and, correspondingly, of an enhanced effective gyromagnetic ratio. This suggests opportunities for compact magnetic sensing and dynamic information storage coexisting with propagating spin waves [4].

In Chapter 5, we study the possibility of keeping B_S fixed while varying its fan angle Θ_F, i.e., its angular spread (for B_C, $\Theta_F = 2\pi$) [5]. It represents a further degree of freedom for the control of magnon propagation: in fact, while B_S can be kept small and constant - with evident implications for the mitigation of the Joule effect [6] - varying only Θ_F changes the periodic Zeeman landscape. This enables a

real-time reconfiguration of the magnonic band diagram. In particular, we show that the gap magnitude at the zone boundary can be tuned almost quadratically by Θ_F while the gap center shifts downward in frequency. By shifting the bandgap position and width, a frequency channel can be toggled between pass- and stop-band (tunable filters). Furthermore, the energy carried by magnons can be steered between branches by enabling/disabling propagation in selected paths (frequency-selective routing/demultiplexing).

As a third step, in Chapter 6, we consider a multiferroic system where a ferroelectric overlayer with periodically varying polarization transfers a spatially periodic magnetic anisotropy to the underlying ferromagnet via inverse magnetostriction, producing a continuous sinusoidal magnetization. We simulate the voltage control by introducing an effective anisotropy K_u with similar domain distribution. By tuning K_u, we find that the magnonic bandstructure is reversibly driven from a magnonic metallic regime (gapless, linear dispersion) to a magnonic insulating regime (up to 1 GHz gap, parabolic dispersion). We also show how effective is the tunability of both the group velocity and the effective mass [7]. Under the magnon insulator conditions, the emerging frequency gap is found to increase with increasing K_u, linearly at first, then gradually reaching saturation. Extending Dirac's magnon picture [8, 9] to this continuous periodic medium helps clarify how the hopping rate, thus magnon conductivity, arises from the combined exchange, dipolar and anisotropy interactions [10].

Finally, in Chapter 7 we apply the technique of the tunable sinusoidal magnetization amplitude discussed above to a directional coupler, a device widely used in ordinary electronics and integrated circuits. The possibility to reconfigure it to function as a variety of devices (power divider, connector, multiplexer) is achieved by introducing a periodic variation of the easy axis in the coupling region. The dipole interaction between the two waveguides, placed close together in the coupling region, is responsible for splitting the otherwise single fundamental mode into a symmetric mode and an antisymmetric mode [11]. The induced magnetization undulation modulates the group velocity and symmetric/antisymmetric mode splitting, enabling fine control of the population transfer between waveguides across a broad window of K_u. Simple analytical models capture the functional behavior of the population transfer as K_u varies. As a natural extension, we also present a preliminary study on the implementation of power-transfer schemes based on the Stimulated Raman Adiabatic Passage (STIRAP) protocol [12] in the same device.

As a whole, these results, summarized in Chapter 8, establish the amplitude of a sinusoidal texture as a powerful, low-dissipation means to program magnon bandgaps, velocities, localization and inter-conduit transfer without altering the physical layout. The demonstrated ability to toggle between propagating and stationary modes, to enable magnonic metal–insulator transitions and to reconfigure couplers on demand points to practical applications in on-chip signal filtering, non-volatile dynamic memories and high-sensitivity magnetic sensing in 3D-magnonic architectures [13].

[1] Daniel D. Stancil and Anil Prabhakar. *Spin Waves: Theory and Applications*. Springer, 2009.

[2] A. Vansteenkiste et al. "The design and verification of MuMax3". In: *AIP Advances* 4.10 (2014), p. 107133. DOI: 10.1063/1.4899186. URL: https://doi.org/10.1063/1.4899186.

[3] B. Van de Wiele and F. Montoncello. "A continuous excitation approach to determine time-dependent dispersion diagrams in 2D magnonic crystals". In: *J. Phys. D: Appl. Phys.* 47 (2014). 10.1088/0022-3727/47/31/315002, p. 315002.

[4] P. Micaletti et al. "A sinusoidal magnetization distribution as an original way to generate a versatile magnonic crystal for magnon propagation". In: *Journal of Magnetism and Magnetic Materials* 622 (2025), p. 172959. ISSN: 0304-8853. DOI: https://doi.org/10.1016/j.jmmm.2025.172959. URL: https://www.sciencedirect.com/science/article/pii/S0304885325001908.

[5] Hyeon Woo Park et al. *Magnon thermal conductivity in multiferroics with spin cycloids*. 2025. arXiv: 2503.11135 [cond-mat.mtrl-sci]. URL: https://arxiv.org/abs/2503.11135.

[6] Harald Ibach and Hans Lüth. *Solid-State Physics: An Introduction to Principles of Materials Science*. 4th. Berlin, Heidelberg: Springer, 2009. ISBN: 978-3-540-93803-3.

[7] V. Ariel and A. Natan. "Electron effective mass in graphene". In: *2013 International Conference on Electromagnetics in Advanced Applications (ICEAA)*. IEEE, 2013, pp. 696–698. DOI: 10.1109/ICEAA.2013.6632357.

[8] J. Fransson, A. M. Black-Schaffer, and A. V. Balatsky. "Magnon Dirac materials". In: *Physical Review B* 94 (2016), p. 075401. DOI: 10.1103/PhysRevB.94.075401. URL: https://doi.org/10.1103/PhysRevB.94.075401.

[9] Sergey S. Pershoguba et al. "Dirac Magnons in Honeycomb Ferromagnets". In: *Phys. Rev. X* 8 (1 Jan. 2018), p. 011010. DOI: 10.1103/PhysRevX.8.011010. URL: https://link.aps.org/doi/10.1103/PhysRevX.8.011010.

[10] Pietro Micaletti et al. "Magnonic analog of a metal-to-insulator transition in a multiferroic heterostructure". In: *Journal of Applied Physics* 137 (2025), p. 153906. DOI: 10.1063/5.0250690. URL: https://doi.org/10.1063/5.0250690.

[11] Qi Wang et al. "Reconfigurable nanoscale spin-wave directional coupler". In: *Science Advances* 4.1 (2018), e1701517. DOI: 10.1126/sciadv.1701517. eprint: https://www.science.org/doi/pdf/10.1126/sciadv.1701517. URL: https://www.science.org/doi/abs/10.1126/sciadv.1701517.

[12] K. Bergmann, H. Theuer, and B. W. Shore. "Coherent population transfer among quantum states of atoms and molecules". In: *Rev. Mod. Phys.* 70 (3 July 1998), pp. 1003–1025. DOI: 10.1103/RevModPhys.70.1003. URL: https://link.aps.org/doi/10.1103/RevModPhys.70.1003.

[13] Md Shamim Sarker et al. “Sensitivity enhancement in magnetic sensor using CoFeB/Y3Fe5O12 resonator”. In: *Scientific Reports* 12.1 (June 2022), p. 11105. ISSN: 2045-2322. DOI: 10.1038/s41598-022-15317-0. URL: https://doi.org/10.1038/s41598-022-15317-0.

LIST OF PUBLICATIONS

The following publications have been produced during the course of this Ph.D. work. They are grouped according to their current publication status. All of them are directly related to the research presented in this thesis.

PUBLISHED PAPERS

The following peer-reviewed articles contain results that are fully or partly included in this dissertation:

- P. Micaletti, A. Roxburgh, E. Iacocca, M. Marzolla, F. Montoncello, A sinusoidal magnetization distribution as an original way to generate a versatile magnonic crystal for magnon propagation, *Journal of Magnetism and Magnetic Materials*, Volume 622, 2025, 172959, https://doi.org/10.1016/j.jmmm.2025.172959.
- P. Micaletti, A. Roxburgh, E. Iacocca, M. Marzolla, F. Montoncello, Magnonic analog of a metal-to-insulator transition in a multiferroic heterostructure, *Journal of Applied Physics*, 137:153906, 2025, https://doi.org/10.1063/5.0250690.
- P. Micaletti, F. Montoncello, Dynamic Footprints of the Specific Artificial Spin Ice Microstate on Its Spin Waves, *Magnetochemistry*, 2023, 9, 158. https://doi.org/10.3390/magnetochemistry9060158.
- A. Roxburgh, P. Micaletti, F. Montoncello, E. Iacocca, Generation of spin-wave packets by reconfigurable nanomagnonic heterojunctions *Physical Review Applied*, 24, 1, 014047, 2025, https://link.aps.org/doi/10.1103/bkqp-vjhy.

PAPERS IN PREPARATION OR UNDER REVIEW

The following manuscripts, currently in preparation or under review, also form part of the present thesis and report ongoing developments of the work discussed herein:

- P. Micaletti, F. Montoncello, *Controlling magnon propagation and frequency gap through the fan angle of a sinusoidal bias field*.
- P. Micaletti, F. Montoncello, *Anisotropy-driven population transfer in magnonic directional nanocouplers*.

CONTENTS

LIST OF FIGURES

LIST OF TABLES

1

INTRODUCTION

ABSTRACT

In this Chapter, we build a concise foundation for magnetism in nanoscale solids, starting from the microscopic origin of magnetic moments and the definition of magnetization as a density of magnetic dipole moment dominated by spin. We classify material responses into diamagnetism, paramagnetism, and ferromagnetism, emphasizing Curie and Curie–Weiss behavior, and extend the discussion to antiferromagnets and ferrimagnets. We then introduce Brown's micromagnetic framework, in which equilibrium textures arise from the competition among exchange, demagnetizing, magnetocrystalline anisotropy and Zeeman energies. Within the framework of the single-domain (macrospin) approximation, we focus on artificial spin ice as a model platform where geometry, dipolar coupling, and anisotropy conspire to produce microstate-dependent spectra and reconfigurable mode profiles. Finally, we develop the essentials of magnetization dynamics, i.e., torque-driven precession with Gilbert damping governed by the Landau–Lifshitz–Gilbert equation, and conclude with ferromagnetic resonance, focusing on the uniform (Kittel) mode and the Kittel relation that links resonance frequency to applied field, demagnetizing factors and anisotropy.

1.1 MAGNETISM IN NANOSTRUCTURES

The most relevant physical quantity used to describe magnetic systems is the magnetization, also known as density of magnetic moment since it involves the volume V of the material [1]. It reads as:

$$\mathbf{M} = \frac{\sum \boldsymbol{\mu}}{V}, \tag{1.1}$$

where $\boldsymbol{\mu}$ is the magnetic moment. Its contributions are the orbital magnetic dipole moment $\boldsymbol{\mu_L}$ and the intrinsinc dipole moment $\boldsymbol{\mu_s}$ (given by the spin); the former depends on the rotation of the electron around the nucleus while the latter is related to the rotation of the electron around its axis. More specifically, we have:

$$\boldsymbol{\mu_L} = -\frac{e}{2m}\mathbf{L}, \tag{1.2}$$

$$\boldsymbol{\mu_S} = -g\frac{e}{2m}\mathbf{S}, \tag{1.3}$$

where e is the electron charge ($e \approx -1.6 \cdot 10^{-19}C$), m is the electron mass ($m \approx 9.1 \cdot 10^{-31}$kg), g the Landé factor ($g \approx 2$ for the electron), crucial in magnetic phenomena such as Zeeman splitting, and $\mathbf{L}$ and $\mathbf{S}$ are the orbital and spin angular momentum, respectively. The total angular momentum of a particle can be expressed as $\boldsymbol{J} = \boldsymbol{L} + \boldsymbol{S}$. Typically, $\boldsymbol{\mu_L}$ is negligible compared to $\boldsymbol{\mu_S}$: for instance, for electrons in lower energy states (s-orbitals) we have $\boldsymbol{L} = 0$ [2]. Even for p-orbitals, in which $\boldsymbol{L} \neq 0$, its contribution to $\boldsymbol{\mu}$ is often small. On the contrary, $\boldsymbol{S}$, and hence $\boldsymbol{\mu_S}$, is a fixed quantity for each particle. In the case of the electron, we have $\boldsymbol{S} = \frac{\hbar}{2}$ and this contribution is particularly significant whenever $\boldsymbol{L}$, and hence $\boldsymbol{\mu_L}$, is limited. Consider, for instance, the valence electrons of metal: ferromagnetic and paramagnetic behaviour, as we will discuss, arise from the predominance of the spin contribution to $\boldsymbol{\mu}$ [3]. A similar situation occurs in low-temperature systems such as Bose-Einstein condensates [4]: while the collective behavior of spins lead to ordered magnetic states, the orbital contribution is negligible.

1.2 DIAMAGNETISM, PARAMAGNETISM AND FERROMAGNETISM

Here the three fundamental classes of magnetic materials are briefly discussed. Since a magnetic field $\boldsymbol{H}$, measured in A/m, interacts with electrons, the magnetization $\boldsymbol{M}$ induced in a material shows a strong dependence on the electronic configuration and hence on the orientation of the spins [5]. The relation that holds between $\boldsymbol{M}$ and $\boldsymbol{H}$ is [6]:

$$\boldsymbol{M} = \chi \boldsymbol{H}, \tag{1.4}$$

where χ is the dimensionless magnetic susceptibility.

In the majority of materials, electrons are paired within orbitals, causing their spin angular momenta to cancel each other out. When an external magnetic field is applied, it induces an opposing magnetization due to the electromotive force created by the orbital motion

of the electrons, as described by Lenz's law [7]. The resulting repulsive interaction between the material and the external magnetic field can be observed experimentally by placing such materials in a non-uniform magnetic field; they are expected to move toward regions of lower magnetic field amplitude. Materials that exhibit this behavior are called diamagnetic and are characterized by a negative magnetic susceptibility, i.e., $\chi < 0$. All materials exhibit diamagnetic behavior to a certain extent, making diamagnetism an universal phenomenon. Typical examples include graphite, copper and bismuth. In all these cases, the corresponding magnetic susceptibility χ_d (the subscript $_d$ stands for *diamagnetic*) is rather small and on the order of 10^{-5}/ - 10^{-6}. On the contrary, a perfect diamagnetic behavior, evidenced by a diamagnetic susceptibility $\chi_d = -1$ is found in superconductors in their Meissner state below their critical temperature. The Meissner effect consists in the complete removal of magnetic fields from the interior of superconductors [2]. In general, however, the response of diamagnetic materials to an external magnetic field can be very often considered so weak as to be negligible. By contrast, if in a certain material uncompensated moments in the electron shells are present, net magnetic moments even without an applied magnetic field are observed. Instead, when a magnetic field is introduced, the magnetic moments are forced to align with it, making the magnetic susceptibility positive, i.e., $\chi_p > 0$. The subscript $_p$ stands for *paramagnetic*, which is the class of materials in question [3]. Anyway, the intensity of the aforementioned alignment is dependent on the strength of the applied magnetic field and on temperature. Curie's law quantifies this behavior in the following way:

$$\chi_p = \frac{C}{T}, \tag{1.5}$$

where C is the Curie constant, a value which is characteristic of the material (it depends on the number of magnetic dipoles and their magnetic moments) and T is the absolute temperature [8]. From Eq. 1.5 it is evident that thermal agitation is responsible for randomizing the magnetic moments, thus reducing the net magnetization. Rare-earth elements (such as gadolinium and dysprosium) and transition metals (e.g., platinum) represent good examples of paramagnetism; more generally, this behavior is found in materials which contain atoms or ions with unpaired electrons. Once the external magnetic field is removed, paramagnets do not retain magnetization. Temporary magnetization underlies some of the most compelling technological applications, notably in certain classes of magnetic-resonance-imaging (MRI) contrast agents and in the electromagnets essential to the operation of motors and generators [3].

If in a paramagnet the interaction between neighbouring electron spins can be considered weak, and this leads to their random directionality across the material if the external magnetic field is removed, in a *ferromagnet*, which is the class of materials that we will consider extensively in this work, the situation is the opposite: the interaction between atoms is strong and all spins, even in the absence of the external magnetic field, are parallel aligned. As a consequence, there is a non-zero net moment. Obviously, the ferromagnetic susceptibility χ_F is positive and exhibits a saturation at a specific strength of

the magnetic field. The phenomenon of spontaneous magnetization within ferromagnets disappears at the Curie temperature T_C, beyond which the material assumes paramagnetic behavior, with variable susceptibility according to the Curie-Weiss law:

$$\chi_F(T) = \frac{C}{T - T_C}. \tag{1.6}$$

Good examples of ferromagnetic materials are cobalt, iron and nichel which are transition metal elements.

1.3 OTHER MAGNETIC ORDERINGS: ANTIFERROMAGNETISM AND FERRIMAGNETISM

In addition to the primary classes discussed in Sec. 1.2, two peculiar magnetic orderings, i.e., *antiferromagnetism* and *ferrimagnetism*, are presented here. The former is characterized by an antiparallel alignment of neighbouring electron spins, which results in a net zero magnetization in the absence of an external magnetic field. The antiparallel spin arrangement is energetically favourable if the system is at a temperature below the so-called Néel temperature T_N. Above this value, we assist at the predominance of thermal fluctuations that result in a paramagnetic behavior from the material. The antiferromagnetic susceptibility χ_A is ruled by a peculiar form of the Curie-Weiss law:

$$\chi_A(T) = \frac{C}{T + \theta}, \tag{1.7}$$

where θ is the Weiss constant and is negative for this class of materials. A precise detection of antiferromagnetic ordering consists in neutron diffraction since it allows for the observation of the periodic arrangement of spins. Representative examples are some oxides - manganese, nickel (particularly used in spintronic devices), and iron - and chromium. In general this class of materials is widely used in the fabrication of magnetic sensors because, as mentioned, their sensitivity to external magnetic fields is remarkable.

The antiparallel alignment of spins is also a typical feature of ferrimagnets but in this case the magnitudes of the opposing moments are not equal, resulting in a net magnetization even in the absence of an external magnetic field. However, the net magnetization exhibits temperature dependence which can give rise to the so-called *compensation point*: at this specific temperature, the magnetization of the two sublattices of difference magnitudes into which we imagine dividing the system cancels out. A systematic description of the ferrimagnetic susceptibility is not possible since the coexistence of unequal magnetic moments makes the Curie-Weiss law definitely not suitable (for instance, there is a peak at the compensation temperature). Ferrimagnets find interestong applications in magnetic recording media and permanent magnets due to their non-zero magnetization; also thermomagnetic applications are possible because of the characteristic temperature-dependent behavior. Good examples of ferrimagnetic materials are magnetite, nickel and cobalt ferrite, and yttrium iron garnet, which is highly used in microwave and communication technologies due to its low damping.

Fig. 1.1 summarizes the discussed magnetic orders.

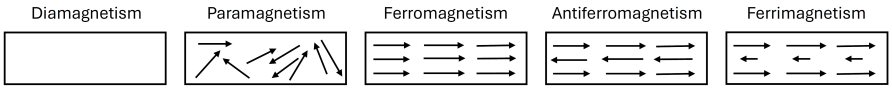

Figure 1.1: Sketch of the different types of magnetic order observed in matter depending on the arrangement of the magnetic dipoles. From left to right: diamagnetism (no permanent moments, weak field repulsion); paramagnetism (randomly oriented moments aligned only under external field); ferromagnetism (parallel alignment of moments); antiferromagnetism (antiparallel alignment with zero net magnetization); ferrimagnetism (antiparallel alignment with unequal moments, resulting in nonzero net magnetization).

1.4 MICROMAGNETISM

From now on, for the purpose of our investigation, we will focus, as already mentioned, on ferromagnetic materials. Our aim is to understand the static and dynamic properties of these materials. In this regard, the rigorous approach would involve positioning at the atomic level and performing summations on the lattice sites. It is known that this approach leads to unsolvable problems, therefore, in investigating the behavior of ferromagnetic materials when nanoscales are considered, it is customary to resort to the theoretical framework developed by W. F. Brown [9], known as *micromagnetism* and valid for ferromagnetic (and ferrimagnetic) systems.

Within this framework, the local configuration of magnetization, $\boldsymbol{M}(\boldsymbol{r})$ is properly described by the interplay of various energy contributions. This principle involves the replacement of the lattice sites with portions of materials that must have a twofold characteristic: on one hand, they ought to be large enough to allow the substitution of the summations with integrals, but, on the other, sufficiently small to consider microscopic anistropies in the distributions of magnetic moments of the material. $\boldsymbol{M}(\boldsymbol{r})$ is typically a non-uniform continuous function of $\boldsymbol{r}$, and each energy term reflects either its local orientation or its spatial variations (such as gradients or divergences). For this reason, the division of the material into magnetic domains defined by different energy density terms reads as:

$$\epsilon_{tot} = \epsilon_{ex} + \epsilon_{demag} + \epsilon_{\alpha} + \epsilon_{Z} \tag{1.8}$$

where ϵ_{ex} is the *exchange energy density*, ϵ_{demag} the *demagnetization* (or *dipolar*) *energy density*, ϵ_{α} the *magneto-crystalline anisotropy energy density* and ϵ_{Z} the *Zeeman energy density*. The terms in Eq. (1.8) are expressed in the form of energy density because of the subsequent derivation of the effective field $\boldsymbol{H}_{eff}$. The interplay of these energies results, in a given magnet, in the spontaneous formation of domains, in which the directions of the magnetization are different, therefore the total free energy of the system is minimized (in this context, the term "free" means that thermal fluctuations are not considered). The presence of magnetic domains with varying magnetization directions leads to the cancellation of the net magnetic moment, effectively reducing the magnetization density to zero. Between these domains lie boundary regions, or *domain walls*, which contribute to increase exchange and dipolar energy. For instance, ferromagnetic particles often exhibit a "single-domain" state, characterized by a uniform

alignment of magnetic moments at the core. However, near the edges, magnetic charges at the boundaries cause "demagnetization," leading to a misalignment of magnetic moments. The two common types of domain walls in ferromagnets are Bloch Walls (Fig. 1.2(a)) in which the magnetization rotates in a plane parallel to the domain boundary, typically observed in bulk materials, and Néel Walls (Fig. 1.2(b)), in which the magnetization rotates in a plane perpendicular to the domain boundary (common in thin films).

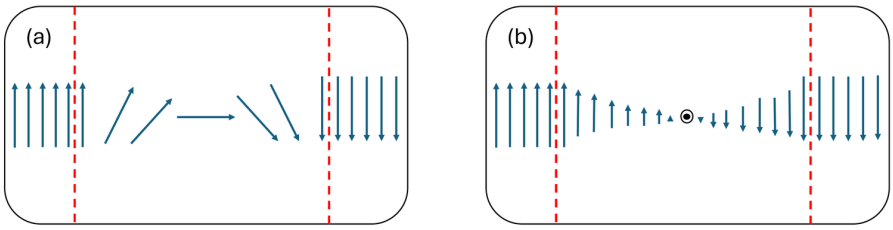

Figure 1.2: Schematic domain structures. (a): Bloch wall; (b): Neel wall.

1.5 MACROSPIN APPROXIMATION AND ARTIFICIAL SPIN ICE

In order to analyze phenomena like precession around the magnetization, *macrospin approximation* is often used. In this model, the exchange energy strongly couples all the spins within a domain, allowing them to behave as a single, unified macrospin. This approximation is valid when the system is small enough to remain in a single-domain state, typically at length scales on the order of the exchange length (it will be introduced in Sec. 1.7), i.e., nanometers. Through such approximations, it becomes possible to study the total free energy of the system and identify the conditions under which it reaches a minimum. In this way an equilibrium state of magnetization is determined.

Based on the macrospin approximation, it is possible to extend the idea from a single-domain particle to entire arrays of nanomagnets. Each elongated ferromagnetic nanoisland, typically fabricated by lithographic techniques [10], is small enough to remain in a single-domain state. As a result, its magnetization can be described by a single macrospin vector. When these nanoislands are arranged in periodic lattices with specific geometries, such as square, Kagome [11], or more complex patterns, the dipolar interactions between neighboring macrospins lead to collective behavior. This is the foundation of artificial spin ice (ASI) systems [12, 13, 10]. ASI structures exhibit geometrical frustration: the arrangement of nanoislands enforces local rules on how spins can orient, such as the "two-in, two-out" ice rule at a vertex in a square lattice. Through the macrospin picture, the study of ASI becomes more tractable. Instead of modeling each atomic spin, the system can be understood as a network of interacting macrospins governed by dipolar energies, anisotropy and external fields.

In this regard, in one of our works [14], we investigated SW dynamics at remanence (zero applied field) in a periodic square ASI, aiming to correlate the spectra with the microstate (macrospin orientations at the vertices) and with the associated vertex magnetic charge. Four different microstates (i.e., with zero, two or four magnetic charges at the vertex) have been considered (see Fig. 1.3). We found that the

frequency gap between the array fundamental mode and the vertex-localized mode increases with the absolute vertex charge, reflecting stronger local demagnetizing fields and enhanced confinement. Geometry provides additional control: reducing the spacing between neighbouring islands softens the vertex mode when the vertex is charged (increased instability) but stabilizes it in charge-neutral vertices, whereas narrowing the islands (lower in-plane aspect ratio) blue-shifts all modes due to stronger lateral confinement. The mode profiles reveal a microstate-dependent displacement of nodal lines toward the edge with the largest magnetization divergence, suggesting a practical spectroscopic read-out of the ASI state for reconfigurable filtering and mode selection.

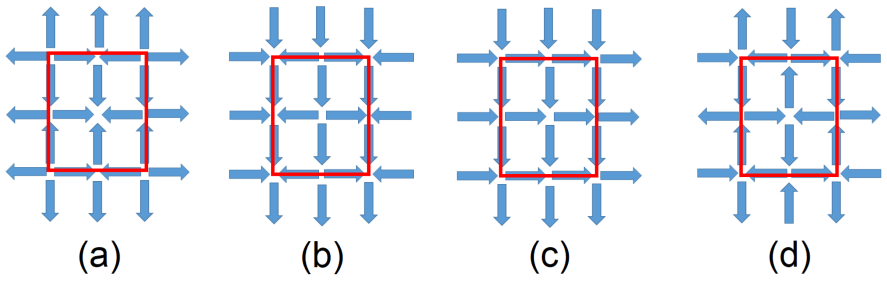

Figure 1.3: The microstates considered in the investigation of the square ASI: (a) four magnetic charges at vertex; (b) three magnetic charges at vertex; (c) zero magnetic charges at vertex; (d) zero magnetic charges at vertex with a closure distribution (vortex). The red square frame encloses the primitive cell.

1.6 EXCHANGE ENERGY

Now we discuss the first term of Eq. 1.8, which is the the exchange energy density ϵ_{ex}: it keeps the neighboring spins aligned and, as a consequence, results in a spontaneous magnetization (if the temperature of the system does not exceed the Curie temperature T_C). ϵ_{ex}, being related to the short-range interactions between neighboring magnetic atoms or molecules, is preminently due to the Pauli exclusion principle modification of Coulomb interaction between neighboring electron spins (Pauli exclusion principle states that two fermions, like electrons, cannot occupy the same quantum state [15]). Therefore, two electrons with spins s_i and s_j exhibit an energy difference that is described by the well-known Heisenberg Hamiltonian [6]:

$$\hat{\boldsymbol{H}} = -\sum_{i \neq j}^{N} J_{ij} \boldsymbol{s}_i \cdot \boldsymbol{s}_j = -2 \sum_{i<j}^{N} J_{ij} \boldsymbol{s}_i \cdot \boldsymbol{s}_j, \tag{1.9}$$

where J_{ij} is the exchange integral between the electrons and it is positive in the case of ferromagnetic materials. If, on one hand, long-range magnetostatic interactions typically display anti-parallel configurations, on the other, ϵ_{ex}, being responsible for pulling neighboring magnetic dipole moments towards the same direction, can be regarded as a short-range interaction: in fact, electron wave functions overlap only for atomic distances; this incidentally justifies the fact that summation is performed exclusively on the first neighbors while the influence of more distant electrons is neglected. ϵ_{ex}, unlike other

energy contributions (e.g., demagnetizing energy) is generally intense and tends to produce uniform magnetization patterns since the energy required to disalign neighboring strongly coupled spins is significant. This fact has consequences also for the dynamics of magnetization. ϵ_{ex} can be computed as:

$$\epsilon_{ex} = A_{ex} \int_V (\nabla \boldsymbol{m}_i)^2 dV, \qquad i = x, y, z, \tag{1.10}$$

where $\boldsymbol{m}_i = M_i / M_S$ is the magnetization along each direction normalized for the saturation magnetization M_S, A_{ex} is the exchange coefficient that is linked to T_C by the dependence relation $A_{ex} \simeq J k_B T_C / 2a_0$ (k_B is the Boltzmann constant, while a_0 is the lattice parameter) and dV is the volume element. The exchange constant can be also expressed in terms of the number of atoms for unitary cell Z_C as $A_{ex} \simeq J S^2 Z_C / a_0$ with S the quantum angular momentum of spin for each atom (or site). Since one wants to determine the total exchange energy of the system, Eq. 1.10 is based on the substitution of the summation with the volume integral and on the replacement of the spins with the magnetization as described in [1].

1.7 DEMAGNETIZING ENERGY

The demagnetizing energy density ϵ_{demag} is originated from interactions between dipoles caused by magnetic charges on the surface of the material. In fact, the magnetization M produces charges that, while acting like a dipole, generate a demagnetizing field $\boldsymbol{H}_{demag}$ in opposite direction to $\boldsymbol{M}$, as can be seen in the sketch in Fig. 1.4.

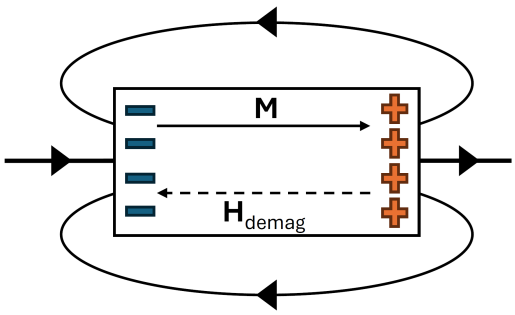

Figure 1.4: Uniform magnetization in a ferromagnetic object. The curved lines outside the object represent external fields while the positive and negative charges indicate surface magnetic charges, which generate the demagnetizing field $\boldsymbol{H}_{demag}$.

As a consequence, the demagnetizing energy tends to minimize the global magnetization of a system. In other words, ϵ_{demag} can be regarded as the energy density of the magnetic moments in their self-induced magnetic field. ϵ_{demag} can be calculated as [6]:

$$\epsilon_{demag} = -\frac{\mu_0}{2} \int_V \boldsymbol{M} \cdot \boldsymbol{H}_{demag} dV, \tag{1.11}$$

where μ_0 is the magnetic permeability of vacuum ($\mu_0 = 4\pi \cdot 10^{-7}$ H/m) and V is the volume of the system. One can express $\boldsymbol{H}_{demag}$ in terms of the scalar potential ϕ_m: in this way, the energy integral can

be determined by means of the superficial and volume distributions $\sigma_M = \boldsymbol{M} \cdot \hat{n}$ and $\rho_M = -\nabla \cdot \boldsymbol{M}$. Following Gauss's law, we have:

$$\boldsymbol{H}_{demag}(\boldsymbol{r}) = \frac{1}{4\pi}\left[-\int_V \frac{(\nabla \cdot \boldsymbol{M})(\boldsymbol{r}-\boldsymbol{r'})}{(\boldsymbol{r}-\boldsymbol{r'})^3} d\boldsymbol{r'} + \int_S \frac{\boldsymbol{M} \cdot \hat{\boldsymbol{n}}(\boldsymbol{r}-\boldsymbol{r'})}{(\boldsymbol{r}-\boldsymbol{r'})^3} d\boldsymbol{r'} \right]. \tag{1.12}$$

If we consider an uniformly magnetized ellipsoid, the volume integral in Eq. (1.12) is zero, while the contribution of the surface integral is given by $-1/2\mu_0 N M_S^2$. The relation between $\boldsymbol{M}$ and $\boldsymbol{H}_{demag}$ is:

$$\boldsymbol{H}_{demag} = -N\boldsymbol{M}, \tag{1.13}$$

where N is the demagnetizing tensor that is represented by a 3 x 3 symmetric matrix. The energetic contribution related to the surface integral is also determined by the shape of the material (especially if the dimensions are smaller than the microscale): it can favour the proximity of the superficial magnetic charges and, therefore, the ease with which the magnetization can align with a certain axis. More generally, the *easy axis* is defined as the direction in which a magnetic moment (or spin) in a ferromagnetic, antiferromagnetic or any anisotropic magnetic material prefers to align under the influence of an external magnetic field. This is the direction of lowest magnetic anisotropy energy. Conversely, the *hard axis* identifies the most difficult direction for the moment to align with an external magnetic field. In the case of an ellipsoid, the long axis is the easy one (Fig. 1.5 (a)), while the short axis is clearly the hard one (Fig. 1.5 (b)). We refer to this situation as shape anisotropy, which is a pure magnetostatic effect provided by the demagnetizing tensor N.

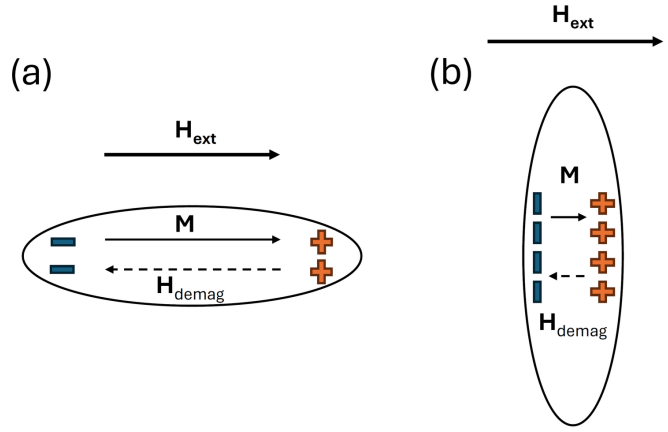

Figure 1.5: Easy axis (a) and hard axis (b) for an ellipsoid.

We now introduce the so-called *exchange length* λ_{ex}, which reflects the competition between the exchange energy and the demagnetizing energy :

$$\lambda_{ex} = \sqrt{\frac{2A_{ex}}{\mu_0 M_S^2}}. \tag{1.14}$$

Typically of the order of nanometers, it is the distance below which the spins tend to spontaneously align, hence, it is a key factor in understanding the formation of magnetic domain structures.

1.8 MAGNETO-CRYSTALLINE ANISOTROPY ENERGY

The spin-orbit coupling [16] is responsible for the creation of certain preferred directions onto the magnetization in a crystal structure. This phenomenon, known as anisotropy, is clearly detectable at the experimental level: reasoning in terms of Cartesian axes, there is one of them along which the magnetization tends to align more easily than others, i.e., the easy axis. The alignment of the magnetization along the hard axes is instead possible by means of external factors, e.g.. the application of a magnetic field. We remark that anisotropy is a measurable effect only in monocrystalline materials since in polycristalline structures - materials constituted by several small crystals randomly oriented - the different easy axes elide each other.

Magneto-crystalline anisotropy allows the occurrence of a privileged magnetization direction even in geometries with perfect symmetric distributions, like a sphere (Fig. 1.6).

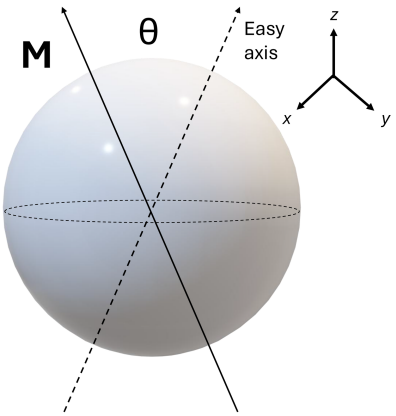

Figure 1.6: Spherical distribution. The straight line represents the magnetization axis, the dashed one the easy axis. Θ is the angle between them.

In this case, the anisotropy energy density ϵ_α represents the tendency of the magnetization to align along the easy axis and can be written as:

$$\epsilon_\alpha = K_1 sin^2\theta, \tag{1.15}$$

where K_1 is the anisotropy constant and its dimensions are J/m^3, θ is the angle between the magnetization and the easy axis. It can be shown that, after some calculations and neglecting higher order terms, the anisotropy field turns out to be:

$$\boldsymbol{H}_\alpha = \frac{2K_1}{M_S} cos\theta. \tag{1.16}$$

1.9 ZEEMAN ENERGY

The application of an external magnetic field $\boldsymbol{H}_{ext}$ makes the magnetization $\boldsymbol{M}$ subject to a torque. This tends to align $\boldsymbol{M}$ parallel to $\boldsymbol{H}_{ext}$ direction. Named after Pieter Zeeman, who first observed the splitting of spectral lines in the presence of a magnetic field [17], the Zeeman energy density ϵ_Z, dependent on the reciprocal orientation between $\boldsymbol{M}$ and $\boldsymbol{H}_{ext}$ and, hence, describing their interaction, is given by [6]:

$$\epsilon_Z = -\mu_0 \boldsymbol{M} \cdot \boldsymbol{H}_{ext}. \tag{1.17}$$

The Zeeman energy E_Z can be expressed as the integral of ϵ_Z over the volume of the magnetic structure as follows:

$$E_Z = -\mu_0 \int_V \boldsymbol{M} \cdot \boldsymbol{H}_{ext} dV = -\int_V \epsilon_Z dV. \tag{1.18}$$

In general, if $\boldsymbol{H}_{ext}$ is weak, the anisotropy term dominates, and $\boldsymbol{M}$ aligns along the easy axis defined by the material. Conversely, when $\boldsymbol{H}_{ext}$ is sufficiently strong, the Zeeman energy surpasses the anisotropy energy, forcing $\boldsymbol{M}$ to align with $\boldsymbol{H}_{ext}$, regardless of the easy axis direction. Fig. 1.7 illustrates the Zeeman effect and its consequences on the atomic energy levels.

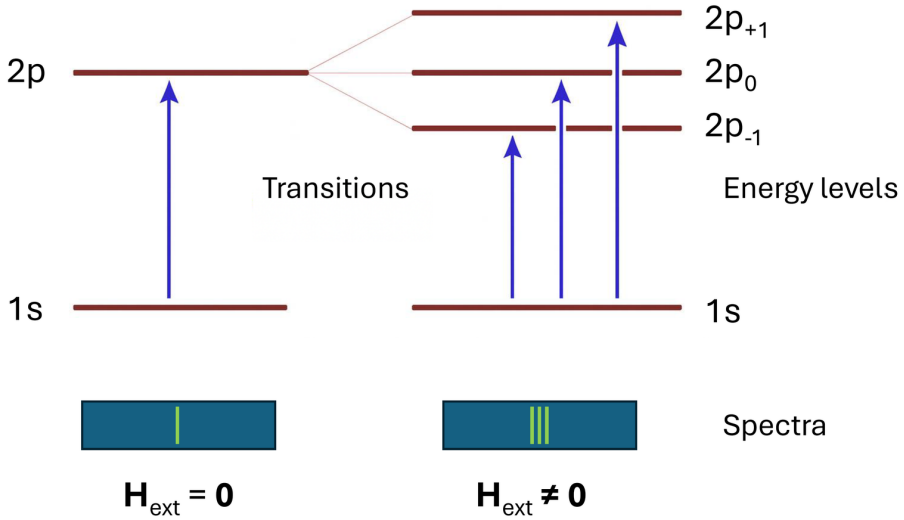

Figure 1.7: Schematic illustration of the Zeeman effect. In the absence of an external magnetic field (left), the atomic $2p$ energy level remains degenerate, resulting in a single spectral line for the $1s \rightarrow 2p$ transition. When a magnetic field is applied (right), the $2p$ level splits into multiple sublevels according to the magnetic quantum number, giving rise to several allowed transitions and the corresponding multiplet structure in the spectrum.

1.10 MAGNETIZATION DYNAMICS. LLG EQUATION

We now turn to the derivation the derivation of the temporal evolution of the magnetization. As will be explained, the magnetization does not align instantaneously with an applied field but undergoes a gyroscopic-like precession. It then relaxes towards equilibrium through dissipative processes. This process is at the heart of many technological applications, from magnetic resonance [18] to spintronic devices [19]. In performing the related calculations, we follow the classic approach described in [20]. It is known that an electron in an atom orbits the nucleus, hence it creates a circular movement of charge: for this reason, an atom can be regarded as an atomic coil. According to the definition of the magnetic (dipole) moment of a coil with an arbitrary shape, we have:

$$\boldsymbol{\mu}_L = iS\hat{\boldsymbol{n}}, \tag{1.19}$$

where i is the current generated by the electron motion and S the coil surface. The electron current can be written as $i = e/T$, with T period of rotation. This is also expressed in terms of the orbital radius r as $T = 2\pi r/v$ (v is the orbital velocity). We are assuming that the electron trajectory is circular, therefore the coil surface can be computed as $S = \pi r^2$. As a consequence, we obtain:

$$\boldsymbol{\mu}_L = \frac{evr}{2}\hat{\boldsymbol{n}}. \tag{1.20}$$

Since the angular momentum is $\boldsymbol{L} \equiv \boldsymbol{r} \times m\boldsymbol{v}$, the magnetic moment $\boldsymbol{\mu}$ becomes:

$$\boldsymbol{\mu}_L = -\frac{e}{2m}\boldsymbol{L}. \tag{1.21}$$

The generalization of Eq. 1.21 with the introduction of the Landé factor [21] and the Bohr magneton $\mu_B = \frac{e\hbar}{2m}$ leads to:

$$\boldsymbol{\mu}_L = -\frac{g_L\mu_B}{\hbar}\boldsymbol{L}. \tag{1.22}$$

The magnetic moment $\boldsymbol{\mu}_L$ in presence of an external magnetic field $\mu_0\boldsymbol{H}_{ext}$, experiences a torque $\boldsymbol{\tau} = \boldsymbol{\mu}_L \times \mu_0\boldsymbol{H}_{ext}$. After recalling the second cardinal equation, $\frac{d\boldsymbol{L}}{dt} = \boldsymbol{\tau}$, we can write:

$$\frac{d\boldsymbol{L}}{dt} = \boldsymbol{\tau} = \boldsymbol{\mu}_L \times \mu_0\boldsymbol{H}_{ext}. \tag{1.23}$$

We now introduce the gyromagnetic ratio $\gamma = -\frac{eg_L}{2m_e} = -\frac{g\mu_B}{\hbar}$, which is a crucial quantity for understanding magnetic dynamics in materials and nanostructures, as its accurate determination directly affects the response to time-varying fields, the design of resonance experiments, and the development of spintronic devices [22]. Now Eq. (1.22) can be written as $\boldsymbol{\mu}_L = \gamma\boldsymbol{L}$, therefore, recalling Eq. (1.23), we obtain:

$$\frac{d\boldsymbol{\mu}_L}{dt} = \gamma\boldsymbol{\tau} = \gamma\mu_0[\boldsymbol{\mu}_L \times \boldsymbol{H}_{ext}]. \tag{1.24}$$

The spin contribution to the total magnetic momentum $\boldsymbol{\mu}_{tot}$ is represented, as discussed previously, by:

$$\boldsymbol{\mu}_S = -\frac{g_S\mu_B}{\hbar}\boldsymbol{S}. \tag{1.25}$$

The total magnetic momentum $\boldsymbol{\mu}_{tot}$ involves the orbital and the spin momentum but, since the former is approximately 3 orders of magnitude smaller than the latter, we can reasonably assume that $\boldsymbol{\mu}_{tot} = \boldsymbol{\mu} = \gamma\boldsymbol{S}$. The macrospin approximation, introduced in Sec. 1.5, allows the study of a sample in terms of the sum of the magnetic moments per unit volume, i.e., $\boldsymbol{M} = \frac{\sum\boldsymbol{\mu}}{V}$. Therefore, in light of the previous reasonings, we can express the time evolution of the magnetization as follows:

$$\frac{d\boldsymbol{M}}{dt} = -\gamma\mu_0[\boldsymbol{\mu} \times \boldsymbol{H}_{ext}]. \tag{1.26}$$

This is the *Landau-Lifshitz* (LL) *equation*, developed by Lev Davidovič Landau and Evgeny Lifshitz in 1935 [23]. It is the cornerstone of magnetism since it predicts the dynamic behavior of magnetization at the nanoscale.

The precessional motion of the magnetization vector $\boldsymbol{M}$ around the effective field is originated from the torque exerted by $\boldsymbol{H}_{ext}$ on $\boldsymbol{M}$, making it rotate without changing its magnitude. However, the precessional motion usually involves dissipative effects that oppose the motion of the magnetization and are described by a damping torque $\boldsymbol{\tau_D}$. This torque causes $\boldsymbol{M}$ to align with $\boldsymbol{H}_{ext}$ over time and can be written as:

$$\boldsymbol{\tau_D} = \frac{\alpha_G}{M_S}\left[\boldsymbol{M} \times \frac{d\boldsymbol{M}}{dt}\right] \tag{1.27}$$

where α_G, known as *Gilbert damping* (and introduced by Thomas Gilbert in the mid-20th century [24]), is a purely phenomenological dimensionless factor that can be determined experimentally, for instance by means of ferromagnetic resonance (FMR) [22], Brillouin light scattering (BLS) [25] or time-resolved magneto-optical Kerr effect (TR-MOKE) [26]. Gilbert damping has a crucial role in governing the temporal evolution of magnetic systems and their relaxation toward equilibrium. Clearly, higher α_G values correspond to faster relaxation, and vice versa. We also notice that the damping torque is weak when the saturation magnetization M_S has a large value. The physical origin of the damping lies in the interaction of the magnetization with its surrounding environment that involves conduction electrons, phonons and lattice vibrations. These interactions transfer the angular momentum of the magnetization into the lattice, thus leading to relaxation. In magnetic thin films, Gilbert damping is often increased by surface effects and spin-orbit coupling.

In the case of a real material, both the contributions given by the torque term and the damping torque term must be contemplated. This is the assumption behind the general equation, called, for obvious reasons, *Landau-Lifshitz-Gilbert* (LLG) *equation*:

$$\frac{d\boldsymbol{M}}{dt} = -\gamma\mu_0[\boldsymbol{\mu} \times \boldsymbol{H}_{ext}] + \frac{\alpha_G}{M_S}\left[\boldsymbol{M} \times \frac{d\boldsymbol{M}}{dt}\right] \tag{1.28}$$

The damping torque term couples the magnetization dynamics to itself through its time derivative. This feedback-like structure, making the equation inherently implicit, reflects the physical coupling between the precession of the magnetization - driven by $\boldsymbol{H}_{ext}$ - and its damping dynamics - which drive the system toward equilibrium. The implicit nature of the LLG equation represents a challenge for direct analytical solutions, therefore numerical approaches are often required. For this purpose, LLG equation can be recast in an explicit form [6], since its resolution, though still complicated, is more manageable:

$$\frac{d\boldsymbol{M}}{dt} = -\gamma_L[\boldsymbol{\mu} \times \boldsymbol{H}_{ext}] + \frac{\alpha_L}{M_S}\boldsymbol{M} \times [\boldsymbol{M} \times \boldsymbol{H}_{ext}], \tag{1.29}$$

where:

$$\gamma_L = \frac{\gamma\mu_0}{1+\alpha_G^2}, \tag{1.30}$$

and:

$$\alpha_L = \frac{\alpha_G\gamma\mu_0}{1+\alpha_G^2}. \tag{1.31}$$

Sophisticated numerical solvers, such as Runge-Kutta methods [27] or implicit solvers designed for stiff equations are particularly suitable when applied to Eq. (1.29). An analytical solution is impracticable in closed form - as a function of time - because of the complexity of the system that depends on, e.g., spatial dependencies, variable time or complex fields. Here we anticipate that, in the framework of micromagnetic simulations, in order to study the time evolution of the magnetization in a sample, it is necessary to solve a set of LLG equations corresponding to each element into which the sample volume is divided.

For the sake of completeness, we add to the discussion an extended form of the traditional LLG equation, known as *iLLG equation* [28]. This includes an inertia term (hence the letter "i") to describe the dynamics of magnetization on ultra-fast timescales, especially in the presence of impulsive magnetic fields or inertial phenomena:

$$\frac{d\boldsymbol{M}}{dt} = -\gamma\mu_0[\boldsymbol{\mu} \times \boldsymbol{H}_{ext}] + \frac{\alpha_G}{M_S}\left[\boldsymbol{M} \times \frac{d\boldsymbol{M}}{dt}\right] + \xi\frac{\mathrm{d}^2\boldsymbol{M}}{\mathrm{d}t^2} \tag{1.32}$$

In Eq. (1.32), ξ measures the strength of inertial effects in magnetization dynamics. The second-order time derivative of $\boldsymbol{M}$ makes Eq. (1.32) analogous to Newton's equations of motion (conversely, the classical LLG equation involves a first-order time derivative only; as a consequence, changes in magnetization are directly proportional to the applied torque). This extension allows the iLLG equation to capture richer dynamics that are inaccessible to the standard LLG framework, even if the inertial term is meaningful only under the very specific conditions discussed. Therefore, in this thesis work, we will always consider the standard LLG equation and the corresponding dynamics.

Typically, the generic field $\boldsymbol{H}_{ext}$ is usually replaced by the effective magnetic field $\boldsymbol{H}_{eff}$ that is expressed by means of the total energy density ϵ_{tot}, as anticipated in Sec. 1.4:

$$\boldsymbol{H}_{eff} = -\frac{1}{M_s}\frac{\delta\epsilon_{tot}}{\delta\boldsymbol{m}}. \tag{1.33}$$

where $\boldsymbol{m}$ represents the unitary vector of the average magnetization. Therefore, LLG equation (1.29) becomes:

$$\frac{d\boldsymbol{M}}{dt} = -\gamma_L[\boldsymbol{\mu} \times \boldsymbol{H}_{eff}] + \frac{\alpha_L}{M_S}\boldsymbol{M} \times [\boldsymbol{M} \times \boldsymbol{H}_{eff}] \tag{1.34}$$

The effective magnetic field $\boldsymbol{H}_{eff}$ is the field that is effectively experienced by the magnetic moments in the material, therefore it depends not only on the external field but also on the internal field, which varies according to the changes in the external one. $\boldsymbol{H}_{eff}$ arises from the total energy contributions within the magnetic domains, with the dominant terms coming from the dipolar interactions among all magnetic moments and from the exchange interactions acting over the exchange length. From. Eq. (1.34), we notice that the magnetization vector $\boldsymbol{M}$ follows a spiral trajectory due to the combined effect of the torque and the damping torque, as can be seen in Fig. 1.8.

It is crucial to stress that $\boldsymbol{H}_{eff}$ is a variational construction arising from the functional derivative of ϵ_{tot} (Eq. (1.33)). $\boldsymbol{H}_{eff}$ is not a physical field in the Maxwellian sense; rather, it collects all energetic

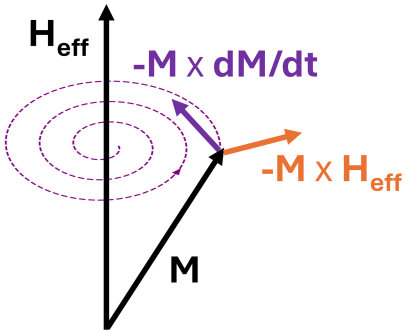

Figure 1.8: Effect of the damping torque that tends to align $\boldsymbol{M}$ toward $\boldsymbol{H}_{eff}$ creating a spiral.

contributions relevant to the Landau-Lifshitz-Gilbert dynamics. It therefore includes both physical fields (such as the externally applied and demagnetizing fields) and non-Maxwellian terms, notably the exchange and anisotropy fields. As such, $\boldsymbol{H}_{eff}$ should be interpreted as the generalized force driving precession and damping. In contrast, the magnetic field $\boldsymbol{H}$ appearing in Maxwell's equations, which will be discussed in Chapter 2, is a physical macroscopic field determined by electric currents, magnetization and boundary conditions. It is a single field obeying the magnetostatic and electrodynamic Maxwell relations, without any decomposition into external, demagnetizing, or internal components. Its role is fundamentally different from that of $\boldsymbol{H}_{eff}$ used in micromagnetic dynamics.

1.11 PRECESSION FREQUENCY. KITTEL FORMULA

As already discussed in Sec. 1.10, the natural response of the magnetization $\boldsymbol{M}$ to $\boldsymbol{H}_{eff}$ is a precession around $\boldsymbol{H}_{eff}$. The corresponding precession frequency (*Larmor frequency*) is proportional to the magnitude of the effective field [22]:

$$\omega = \gamma \mu_0 H_{eff}, \tag{1.35}$$

where $H_{eff} = |\boldsymbol{H}_{eff}|$. In real ferromagnets, however, anisotropy and demagnetizing fields alter the effective field, so that the resonance condition of Eq. (1.35) is more generally described by the *Kittel formula* [29], which relates the precession frequency ω to the applied field, the anisotropy contributions and the effective magnetization of the sample. We now present the derivation of the Kittel formula, following the approach originally developed by Charles Kittel in the 1940s. We anticipate that ferromagnetic resonance corresponds to the fundamental spin-wave excitation at zero wavevector ($k = 0$). At this frequency, all spins precess coherently in phase around $\boldsymbol{H}_{eff}$, leading to a uniform precession of the entire system. This collective mode is commonly referred to as the Kittel mode.

As a first step of the derivation, let us consider an ellipsoid since the corresponding demagnetizing tensor has the simplest form, i.e., it is diagonal:

$$\hat{\boldsymbol{N}} = \boldsymbol{N} = \begin{pmatrix} N_x & 0 & 0 \\ 0 & N_y & 0 \\ 0 & 0 & N_z \end{pmatrix}. \tag{1.36}$$

Furthermore, in an ellipsoid, magnetic field lines are perpendicular to the surface in any point.

The effective field $\boldsymbol{H}_{eff}$ experienced by the ellipsoid is the sum of the external field $\boldsymbol{H}_{ext}$ and the demagnetizing field $\boldsymbol{H}_{demag}$, while exchange interactions can be neglected without loss of generality. $\boldsymbol{H}_{ext}$is aligned to the easy axis (z direction in this case) of the ellipsoid (the two magnetic poles are far apart from each other). All spins are parallel to each other, therefore we have the maximum magnetic moment density (saturation magnetization M_S). From now on, for notational simplicity, the subscript $_{ext}$ denoting the external field will be omitted in the calculations and in Fig. 1.9, which illustrates the ellipsoid, the reference system and the physical quantities involved.

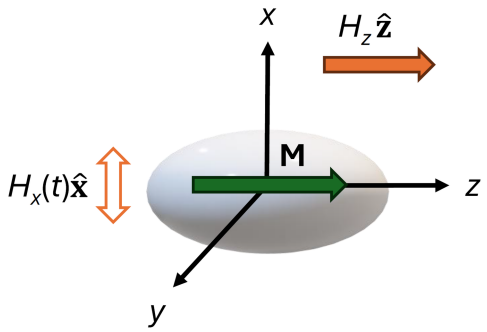

Figure 1.9: A thin-film sample (approximated as an oblate ellipsoid) is subjected to a static field $H_z\hat{\mathbf{z}}$ and a transverse radiofrequency (RF) drive $H_x(t)\hat{\mathbf{x}}$, which excite the uniform ($k = 0$) precession of the magnetization $\boldsymbol{M}$ about the $\hat{\mathbf{z}}$ axis (Kittel mode). The Cartesian axes are indicated for reference.

Neglecting the dissipative contribution, our aim is to write explicitely the three components of the LL equation (1.26), so the cross product must be developed:

$$\frac{d\boldsymbol{M}}{dt} = \gamma \begin{vmatrix} \hat{\boldsymbol{x}} & \hat{\boldsymbol{y}} & \hat{\boldsymbol{z}} \\ M_x & M_y & M_z \\ H^x_{eff} & H^y_{eff} & H^z_{eff} \end{vmatrix}. \tag{1.37}$$

Therefore, we have the following set of equations:

$$\begin{aligned} \frac{dM_x}{dt} &= \gamma\mu_0 \left[M_y H^z_{\text{eff}} - M_z H^y_{\text{eff}}\right] \\ &= \gamma\mu_0 M_y \left[H_z + M_z \left(N_y - N_z\right)\right], \\ \frac{dM_y}{dt} &= -\gamma\mu_0 \left[M_z H^x_{\text{eff}} - M_x H^z_{\text{eff}}\right] \\ &= \gamma\mu_0 \left[M_z H_z - M_z M_x \left(N_x - N_z\right) - M_x H_z\right], \\ \frac{dM_z}{dt} &= \gamma\mu_0 \left[M_x H^y_{\text{eff}} - M_y H^x_{\text{eff}}\right] \\ &= \gamma\mu_0 \left[-M_x N_y M_y - M_y \left(H_x - N_x M_x\right)\right]. \end{aligned} \tag{1.38}$$

Due to the ellipsoidal form considered, the third equation, which involves the time derivative of the magnetization along the z direction, is equal to zero. In fact, for such an ellipsoid $N_x \to N_y$. Furthermore, we also assumed that there is no magnetic field along x direction, hence $H_x \to 0$ and this justifies the previous passage.

A small, temporary excitation along the x direction, $\boldsymbol{H}_{exc}(t) = H_x(t)\,\hat{\mathbf{x}}$, is applied to trigger spin precession; once the spins are set in motion, the excitation is switched off. The excitation is a plane wave along x, which drives the magnetic moments into a precessional motion that traces a cone with base in the xy-plane. Consequently, the magnetization has no z-component and only M_x and M_y oscillate, consistent with $\dot{M}_z = 0$.

Since $H_x(t) = H_{x0}e^{i\omega t}$, the magnetization becomes:

$$\boldsymbol{M}(t) = \begin{pmatrix} M_x(t) = M_{x0}e^{i\omega t} \\ M_y(t) = M_{y0}e^{i\omega t} \\ M_z = M_S \end{pmatrix}. \tag{1.39}$$

where M_{x0} and M_{y0} are the static components of the magnetization. Combining Eqs. (1.38) and (1.39), we have:

$$\begin{cases} M_{x0}(i\omega)e^{i\omega t} = \gamma\mu_0 M_{y0}e^{i\omega t}[H_z + M_S(N_y - N_z), \\ M_{y0}(i\omega)e^{i\omega t} = \gamma\mu_0[M_S H_{x0}e^{i\omega t} - M_S M_{x0}e^{i\omega t}(N_x - N_z) - M_{x0}e^{i\omega t}H_z], \\ 0 = 0. \end{cases} \tag{1.40}$$

After some calculations and arrangements, we are left with:

$$\begin{cases} M_{x0} = \frac{1}{(i\omega)}\gamma\mu_0 M_{y0}[H_z + M_S(N_y - N_z), \\ M_{y0} = \frac{1}{(i\omega)}\gamma\mu_0[M_S H_{x0} - M_S M_{x0}(N_x - N_z) - M_{x0}H_z]. \end{cases} \tag{1.41}$$

The substitution of the second equation into the first one leads to:

$$M_{x0} = \frac{1}{(i\omega)}\gamma\mu_0\left(\frac{1}{i\omega}\gamma\mu_0\left[M_s H_{x0} - M_s M_{x0}(N_x - N_z) - M_{x0}H_z\right]\right) \cdot \left[H_z + M_s(N_y - N_z)\right]. \tag{1.42}$$

Solving for ω, we get:

$$\omega^2 = \gamma^2\mu_0^2\left[H_z - \frac{M_S}{M_{x0}}H_{x0} + M_S(N_x - N_z)\right][H_z + M_S(N_y - N_z)]. \tag{1.43}$$

Since the applied excitation field is small, we can assume $H_{x0} \to 0$, therefore, after taking the square root, we have:

$$\omega = \gamma\mu_0\sqrt{\left[H_z + M_s\left(N_x - N_z\right)\right]\left[H_z + M_s\left(N_y - N_z\right)\right]}. \tag{1.44}$$

Here N_x, N_y, and N_z are the demagnetizing factors, which satisfy $\mathrm{tr}(\hat{\boldsymbol{N}}) \equiv N_x + N_y + N_z = 1$. Because the trace is fixed, an increase of N_z necessarily reduces N_x and N_y. Geometrically, this corresponds to an ellipsoid that is more confined along z (e.g., a film patterned with holes), which enhances the demagnetizing field, lowers the internal effective field, and therefore decreases ω. Within the dipolar regime, Eq. (1.44) is independent of the absolute value of the spin-wave wavevector $\boldsymbol{k}$, although it depends on the direction of $\boldsymbol{k}$, as will be discussed in Chapter 2.

Restoring indices for the external field and moving to the most general configuration, it is immediate to notice that the Kittel expression

can be written in terms of demagnetizing factors along (and transverse to) the field direction as:

$$\omega = \gamma\mu_0\sqrt{\left[H_{\text{ext}} + M_s(N_z - N_H)\right]\left[H_{\text{ext}} + M_s(N_{H,\perp} - N_H)\right]}. \quad (1.45)$$

In Eq. (1.45), H_{ext} denotes the magnitude of the applied field, N_z is the demagnetizing factor along the z axis, N_H is the demagnetizing factor along the direction of $\boldsymbol{H}_{ext}$, and $N_{H,\perp}$ is the demagnetizing factor along an axis perpendicular to $\boldsymbol{H}_{ext}$.

Eq. (1.45) is routinely fitted - either to ferromagnetic resonance data or to Kittel-mode frequencies from micromagnetic simulations - to extract quantitative estimates of the gyromagnetic ratio γ and the saturation magnetization M_s. A direct inspection shows a Zeeman-like linear dependence of ω at large H_{ext}, while at zero applied field a finite frequency remains due to shape anisotropy. In the following, especially in Chapter 5, we will make extensive use of the Kittel formula and its framework.

BIBLIOGRAPHY

[1] S. Blundell. *Magnetism in Condensed Matter*. Oxford Master Series in Condensed Matter Physics 4. OUP Oxford, 2001. ISBN: 9780198505921. URL: https://books.google.it/books?id=yr%5C_-yAEACAAJ.

[2] C. Kittel. *Introduction to Solid State Physics*. Wiley, 2004. ISBN: 97804714152 68. URL: https://books.google.it/books?id=kym4QgAACAAJ.

[3] J.M.D. Coey. *Magnetism and Magnetic Materials*. Magnetism and Magnetic Materials. Cambridge University Press, 2010. ISBN: 9780521816144. URL: https://books.google.it/books?id=Ie72CFd-eSEC.

[4] K. B. Davis et al. "Bose-Einstein Condensation in a Gas of Sodium Atoms". In: *Phys. Rev. Lett.* 75 (22 Nov. 1995), pp. 3969–3973. DOI: 10.1103/PhysRevLett.75.3969. URL: https://link.aps.org/doi/10.1103/PhysRevLett.75.3969.

[5] A.H. Morrish. *The Physical Principles of Magnetism*. Wiley Series on the Science and Technology of Materials. Wiley, 1965. ISBN: 9780471615903. URL: https://books.google.it/books?id=vMzvAAAAMAAJ.

[6] Alberto Guimarães. *Principles of Nanomagnetism*. Jan. 2017. ISBN: 978-3-319-59408-8. DOI: 10.1007/978-3-319-59409-5.

[7] J.D. Jackson. *Classical Electrodynamics*. Wiley, 1998. ISBN: 9780471309321. URL: https://books.google.it/books?id=FOBBEAAAQBAJ.

[8] R.C. O'Handley. *Modern Magnetic Materials: Principles and Applications*. Wiley, 1999. ISBN: 9780471155669. URL: https://books.google.it/books?id=RKV1QgAACAAJ.

[9] W. F. Brown Jr. *Micromagnetics*. New York: Interscience Publishers, John Wiley & Sons, 1963.

[10] R. F. Wang et al. "Artificial 'spin ice' in a geometrically frustrated lattice of nanoscale ferromagnetic islands". In: *Nature* 439.7074 (2006), pp. 303–306. DOI: 10.1038/nature04447.

[11] Itiro Syôzi. "Statistics of Kagomé Lattice". In: *Progress of Theoretical Physics* 6.3 (June 1951), pp. 306–308. ISSN: 0033-068X. DOI: 10.1143/ptp/6.3.306. eprint: https://academic.oup.com/ptp/article-pdf/6/3/306/5239621/6-3-306.pdf. URL: https://doi.org/10.1143/ptp/6.3.306.

[12] Steven T Bramwell and Mark J Harris. "The history of spin ice". In: *Journal of Physics: Condensed Matter* 32.37 (June 2020), p. 374010. DOI: 10.1088/1361-648X/ab8423. URL: https://doi.org/10.1088/1361-648X/ab8423.

[13] D. J. P. Morris et al. "Dirac Strings and Magnetic Monopoles in the Spin Ice $Dy_2Ti_2O_7$". In: *Science* 326.5951 (2009), pp. 411–414. DOI: 10.1126/science.1178868.

[14] Pietro Micaletti and Federico Montoncello. "Dynamic Footprints of the Specific Artificial Spin Ice Microstate on Its Spin Waves". In: *Magnetochemistry* 9.6 (2023). ISSN: 2312-7481. DOI: 10.3390/magnetochemistry9060158. URL: https://www.mdpi.com/2312-7481/9/6/158.

[15] W. Pauli. "Über den Zusammenhang des Abschlusses der Elektronengruppen im Atom mit der Komplexstruktur der Spektren". In: *Zeitschrift für Physik* 31.1 (1925), pp. 765–783. DOI: 10.1007/BF02980631. URL: https://doi.org/10.1007/BF02980631.

[16] R. J. Elliott. "Theory of the Effect of Spin-Orbit Coupling on Magnetic Resonance in Some Semiconductors". In: *Phys. Rev.* 96 (2 Oct. 1954), pp. 266–279. DOI: 10.1103/PhysRev.96.266. URL: https://link.aps.org/doi/10.1103/PhysRev.96.266.

[17] Herbert M. Reese. "The Zeeman Effect". In: *Science* 12.295 (1900), pp. 293–297. ISSN: 00368075, 10959203. URL: http://www.jstor.org/stable/1628310 (visited on 10/18/2025).

[18] C.P. Slichter. *Principles of Magnetic Resonance*. Springer Series in Solid-State Sciences. Springer Berlin Heidelberg, 1996. ISBN: 9783540501572. URL: https://books.google.it/books?id=zgnrRkaIhFoC.

[19] K. Wang, M. Yang, and J. Luo. *Spintronics: Materials, Devices, and Applications*. Wiley Series in Materials for Electronic & Optoelectronic Applications. Wiley, 2022. ISBN: 9781119698975. URL: https://books.google.it/books?id=W296EAAAQBAJ.

[20] Robert Martin Eisberg and Robert Resnick. *Quantum physics of atoms, molecules, solids, nuclei and particles*. New York, NY: Wiley, 1985. URL: https://cds.cern.ch/record/105889.

[21] Klaus Hentschel. "Landés g-factor and g-formula". In: *Compendium of Quantum Physics*. Ed. by Daniel Greenberger, Klaus Hentschel, and Friedel Weinert. Berlin, Heidelberg: Springer Berlin Heidelberg, 2009, pp. 336–337. ISBN: 978-3-540-70626-7. DOI: 10.1007/978-3-540-70626-7_105. URL: https://doi.org/10.1007/978-3-540-70626-7_105.

[22] C. Kittel, P. McEuen, and John Wiley & Sons. *Introduction to Solid State Physics*. John Wiley & Sons, 2015. ISBN: 9788126535187. URL: https://books.google.it/books?id=rAMujwEACAAJ.

[23] Lev Davidovich Landau and E. Lifstatz. "On the Theory of the Dispersion of Magnetic Permeability in Ferromagnetic Bodies". In: *Phys. Z. Sowjetunion* 8 (1935). Ed. by D. ter Haar. DOI: 10.1016/b978-0-08-010586-4.50023-7.

[24] T.L. Gilbert. "A phenomenological theory of damping in ferromagnetic materials". In: *IEEE Transactions on Magnetics* 40.6 (2004), pp. 3443–3449. DOI: 10.1109/TMAG.2004.836740.

[25] Thomas Sebastian et al. "Micro-focused Brillouin light scattering: imaging spin waves at the nanoscale". In: *Frontiers in Physics* Volume 3 - 2015 (2015). ISSN: 2296-424X. DOI: 10.3389/fphy.2015.00035. URL: https://www.frontiersin.org/journals/physics/articles/10.3389/fphy.2015.00035.

[26] Paul S. Keatley et al. "A platform for time-resolved scanning Kerr microscopy in the near-field". In: *Review of Scientific Instruments* 88.12 (Dec. 2017), p. 123708. ISSN: 0034-6748. DOI: 10.1063/1.4998016. eprint: https://pubs.aip.org/aip/rsi/article-pdf/doi/10.1063/1.4998016/13478336/123708_1_online.pdf. URL: https://doi.org/10.1063/1.4998016.

[27] J.C. Butcher. *Numerical Methods for Ordinary Differential Equations*. Wiley, 2008. ISBN: 9780470753750. URL: https://books.google.it/books?id=opd2NkBmMxsC.

[28] E. Olive et al. "Deviation from the Landau-Lifshitz-Gilbert equation in the inertial regime of the magnetization". In: *Journal of Applied Physics* 117.21 (June 2015), p. 213904. ISSN: 0021-8979. DOI: 10.1063/1.4921908. eprint: https://pubs.aip.org/aip/jap/article-pdf/doi/10.1063/1.4921908/15162431/213904_1_online.pdf. URL: https://doi.org/10.1063/1.4921908.

[29] C. Kittel. "On the Theory of Ferromagnetic Resonance Absorption". In: *Physical Review* 73 (1948), p. 155. DOI: 10.1103/PhysRev.73.155.

2

SPIN WAVES

ABSTRACT

In this Chapter, a rigorous framework for magnon propagation in ferromagnetic films - from the microscopic spin-wave model introduced by Bloch to continuum electrodynamics in the magnetostatic approximation - is developed. Starting from Maxwell's equations coupled with the Landau–Lifshitz dynamics, we include both dipolar and exchange interactions to derive the Kalinikos–Slavin dispersion relation, which provides a unified description of spin-wave modes in thin films and confined geometries. Thickness/width quantization and geometric form factors embed dipolar and exchange contributions on equal footing. This framework naturally yields the characteristic behaviors of backward volume, Damon–Eshbach, and forward volume waves, revealing how the interplay between field orientation and propagation direction governs their localization, dispersion and group-velocity trends.

2.1 INTRODUCTION

The concept of *spin wave* or *magnon* was introduced by Felix Bloch in 1930 in order to explain the reduction of spontaneous magnetization in a ferrromagnetic material when its temperature is much lower than the Curie temperature, i.e., $T \ll T_C$ [1]. At that time, this effect could not be explained by Stoner model [2] because of the great energy needed to change the spin direction. It therefore became clear that a previously neglected thermal excitation was responsible for this behavior. Later on, in the 1950s, subsequent developments by Holstein, Primakoff [3] and Dyson [4, 5] provided a quantum mechanical framework for spin wave quantization, giving rise to the concept of magnons as quanta of spin wave excitations.

The starting point in the procedure introduced by Bloch is the Heisenberg model - Eq.(1.9) - that involves the exchange integral in order to separate states with different spin. According to this model, at low temperatures all spins aling in parallel resulting in saturation for magnetization, as shown in Fig. 2.1 (a) and (b). When the temperature is increased, thermal excitation is responsible for reducing the spontaneuous magnetization since now the spins are randomically deflected (internal energy is instead increased). The change in spin orientation propagates like a wave in the material (Fig. 2.1 (c) and (d)) by means of a perturbation, which can be of various kinds, e.g., external magnetic fields or optical excitation with laser pulse. In real magnetic systems, the magnetization precession around the effective magnetic field is not spatially homogeneous, hence the change in the direction of magnetization is both a function of space and time. This set of excited spins above the fundamental level can be described, as already anticipated, in terms of wave propagation with energies typically of only ~ 1μeV. These periodic oscillations in time of magnetization at finite temperatures are named spin waves (SWs) and their quanta magnons. As a consequence, magnons can be regarded as quasi-particles, specifically bosons which obey Bose-Einstein statistics, with energy $\hbar\omega$, momentum $\hbar k$ and angular momentum $\hbar$.

Spin waves in ferromagnetic films are usually classified according to two complementary criteria. First, depending on the dominant interaction, one distinguishes between *magnetostatic* (or *dipolar*) *spin waves* and *exchange spin waves*. A detailed discussion of this interaction-based classification, starting from robust theoretical foundations, is provided in Secs. 2.2 - 2.5. Second, spin waves can also be classified according to their propagation geometry, namely the orientation of the wave vector with respect to the static magnetization and to the film plane. In this framework one distinguishes between *backward volume magnetostatic waves*, *Damon-Eshbach surface waves* and *forward volume magnetostatic waves*. This geometry-based classification will be addressed in Secs. 2.7 - 2.9.

2.2 MAGNETOSTATIC APPROXIMATION

In general, for any geometric configuration and regardless of the type of the SW, the dispersion relations, which relate the frequency to the wavevector, are obtained by solving together the LL equation (1.26)

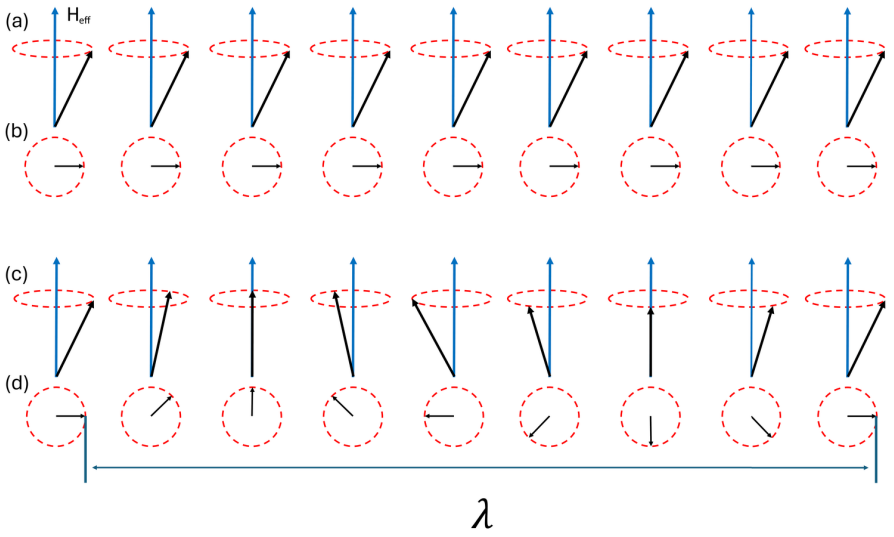

Figure 2.1: (a, b): uniform ($k = 0$) precession of the magnetization $\boldsymbol{M}$ around the effective field $\boldsymbol{H}_{eff}$: side view (a) and top view (b). The dashed red circles indicate the precession cones. (c, d): finite-wavevector spin wave: the local precession phase varies periodically along the sample, producing a spin wave of wavelength λ (wavevector $k = 2\pi/\lambda$); side view (c) and top view (d).

with the Maxwell's equations [6] within the framework of the magnetostatic approximation. In the subsequent discussion, we provide a detailed discussion of this topic, following and elaborating on the strategy outlined in [7].

As a first step, the magnetization and the field vectors are typically separated into time-independent static components $\boldsymbol{M}_0$ and $\boldsymbol{H}_0$ and dynamic components $\boldsymbol{m}(t)$ and $\boldsymbol{h}(t)$: this splitting is allowed since the fluctations in $\boldsymbol{M}(t)$ and $\boldsymbol{H}(t)$ associated with SWs are small compared to the static parts. Therefore, the LL and Maxwell's equations are solved exclusively for the dynamic components; in doing so, appropriate boundary conditions for surfaces and interfaces are considered.

Let us start by recalling Maxwell's equations, i.e., the fundamental equations that govern electromagnetic fields:

$$\nabla \times \boldsymbol{H} = \frac{\partial \boldsymbol{D}}{\partial t} + \boldsymbol{J}, \tag{2.1}$$

$$\nabla \times \boldsymbol{E} = -\frac{\partial \boldsymbol{B}}{\partial t}, \tag{2.2}$$

$$\nabla \cdot \boldsymbol{D} = \rho, \tag{2.3}$$

$$\nabla \cdot \boldsymbol{B} = 0, \tag{2.4}$$

where $\boldsymbol{H}$ is the magnetic field intensity (measured in A/m), $\boldsymbol{D}$ the electric flux density (C/m^2), $\boldsymbol{J}$ the electric voume current density (A/m^2), $\boldsymbol{E}$ the electric field intensity (V/m), $\boldsymbol{B}$ the magnetic flux density (T) and ρ the electric volume charge density (C/m^3). We assume that the field quantities depend explicitly on time. Fields that are varying sinusoidally at a single frequency can be written in the form $\boldsymbol{A}(t) = \mathrm{Re}\left\{\boldsymbol{A}(\omega)e^{-i\omega t}\right\}$ where $\boldsymbol{A}(\omega)$ is a complex quantity that

contains the amplitude and phase information of the field. Therefore, Maxwell's equations can be recast in the frequency domain as follows:

$$\nabla \times \boldsymbol{H} = -i\omega \boldsymbol{D} + \boldsymbol{J}, \tag{2.5}$$

$$\nabla \times \boldsymbol{E} = i\omega \boldsymbol{B}, \tag{2.6}$$

$$\nabla \cdot \boldsymbol{D} = \rho, \tag{2.7}$$

$$\nabla \cdot \boldsymbol{B} = 0. \tag{2.8}$$

It is known that the flux densities in free space can be expressed as a linear function of the field intensities:

$$\boldsymbol{D} = \epsilon_0 \boldsymbol{E}, \tag{2.9}$$

$$\boldsymbol{B} = \mu_0 \boldsymbol{H}, \tag{2.10}$$

where ϵ_0 denotes the vacuum permittivity, $\epsilon_0 \approx 8.85 \times 10^{-12}\,\mathrm{F/m}$, which characterizes the ability of free space to sustain electric fields, while μ_0, already introduced in Chapter 1, is the vacuum permeability, $\mu_0 = 4\pi \times 10^{-7}\,\mathrm{H/m}$, which characterizes the response of free space to magnetic fields. The above relations involve further terms when a material medium is considered since it reacts to the presence of the fields. The general expressions are:

$$\boldsymbol{D} = \epsilon_0 \boldsymbol{E} + \boldsymbol{P}, \tag{2.11}$$

$$\boldsymbol{B} = \mu_0 (\boldsymbol{H} + \boldsymbol{M}), \tag{2.12}$$

where $\boldsymbol{P}$ is the electric dipole moment per unit volume ($\mathrm{C/m^2}$). When the response of a *linear* medium (i.e., a medium in which the dependence of $\boldsymbol{P}$ and $\boldsymbol{M}$ on the fields is a first power) to an applied field is instantaneous, we can write:

$$\boldsymbol{P}(t) = \epsilon_0 \bar{\chi}_e \cdot \boldsymbol{E}(t), \tag{2.13}$$

$$\boldsymbol{M}(t) = \bar{\chi}_m \cdot \boldsymbol{H}(t), \tag{2.14}$$

where $\bar{\chi}_e$ and $\bar{\chi}_m$ are, respectively, the electric and magnetic susceptibility tensors. A medium is called *dispersive* when its response to an applied field is not instantaneous: in this case an integration over all past excitations - in fact, the medium exhibits a "memory" - is needed. Reasoning in the frequency domain instead, a steady state determined by the amplitude of the excitation is always reached in response to a sinusoidal field and it is possible to write:

$$\boldsymbol{P}(\omega) = \epsilon_0 \bar{\chi}_e(\omega) \cdot \boldsymbol{E}(\omega), \tag{2.15}$$

$$\boldsymbol{M}(\omega) = \bar{\chi}_m(\omega) \cdot \boldsymbol{H}(\omega). \tag{2.16}$$

The substitution of Eqs. (2.15) and (2.16) into the general expressions (2.11) and (2.12) leads to:

$$\boldsymbol{D} = \bar{\epsilon} \cdot \boldsymbol{E}, \tag{2.17}$$

and:

$$\boldsymbol{B} = \bar{\mu} \cdot \boldsymbol{H}, \tag{2.18}$$

where:

$$\bar{\epsilon} = \epsilon_0(\bar{I} + \bar{\chi}_e), \tag{2.19}$$

and:

$$\bar{\mu} = \mu_0(\bar{I} + \bar{\chi}_m), \tag{2.20}$$

represent, respectively, the permittivity and the permeability tensor ($\bar{I}$ is the unit matrix). Eqs. (2.17), (2.18), (2.19) and (2.20) are known as *constitutive relations* and represent their general forms. The material is defined as electrically or magnetic *isotropic* if either permittivity or permeability tensor reduces to a scalar constant times the unit matrix. When the tensor representation with a 3×3 matrix is necessary the medium is said to be electrically or magnetic *anisotropic*. In general, vector fields have space and time dependence of the form $exp(i\boldsymbol{k} \cdot \boldsymbol{r} - i\omega t)$. The spatial dependence allows us to replace the ∇ operator with a factor $i\boldsymbol{k}$, hence Maxwell's equations (2.5) can be recast as:

$$i\boldsymbol{k} \times \boldsymbol{H} = -i\omega \boldsymbol{D} + \boldsymbol{J}, \tag{2.21}$$

$$i\boldsymbol{k} \times \boldsymbol{E} = \omega \boldsymbol{B}, \tag{2.22}$$

$$i\boldsymbol{k} \cdot \boldsymbol{D} = \rho, \tag{2.23}$$

$$i\boldsymbol{k} \cdot \boldsymbol{B} = 0. \tag{2.24}$$

Eqs. (2.21) and (2.22) can be rewritten in terms of $\boldsymbol{E}$ and $\boldsymbol{H}$ by means of the constitutive relations (2.9) and (2.10) in the case of a source-free non-conducting medium:

$$\boldsymbol{k} \times \boldsymbol{H} = -\omega \bar{\epsilon} \cdot \boldsymbol{E}, \tag{2.25}$$

$$\boldsymbol{k} \times \boldsymbol{E} = \omega \bar{\mu} \cdot \boldsymbol{H}. \tag{2.26}$$

For an arbitrary propagation direction of uniform plane waves in a ferromagnetic medium, we restrict the analysis to the dynamic components of the fields, denoted, as partly anticipated, by $\boldsymbol{e}$, $\boldsymbol{h}$, and $\boldsymbol{m}$ (while the static bias contributions are represented by $\boldsymbol{H}_0$ and $\boldsymbol{M}_0$). Therefore, we can write:

$$\boldsymbol{k} \times \boldsymbol{h} = -\omega \bar{\epsilon} \cdot \boldsymbol{e}, \tag{2.27}$$

$$\boldsymbol{k} \times \boldsymbol{e} = \omega \mu_0 (\boldsymbol{h} + \boldsymbol{m}). \tag{2.28}$$

By taking the cross product of $\boldsymbol{k}$ with both sides of Eq. (2.27), then applying the vector identity $\boldsymbol{a} \times (\boldsymbol{b} \times \boldsymbol{c}) = \boldsymbol{b}(\boldsymbol{a} \cdot \boldsymbol{c}) - \boldsymbol{c}(\boldsymbol{a} \cdot \boldsymbol{b})$, and substituting Eq. (2.28) into Eq. (2.27), we obtain:

$$\boldsymbol{k}\boldsymbol{k} \cdot \boldsymbol{h} - k^2 \boldsymbol{h} = -\omega^2 \mu_0 \epsilon (\boldsymbol{h} + \boldsymbol{m}). \tag{2.29}$$

According to Maxwell's equation (2.4), we have in this case $\boldsymbol{k} \cdot \boldsymbol{b} = \mu_0 \boldsymbol{k} \cdot (\boldsymbol{h} + \boldsymbol{m}) = 0$, therefore $\boldsymbol{k} \cdot \boldsymbol{h} = -\boldsymbol{k} \cdot \boldsymbol{m}$. In light of this reasoning, Eq. (2.29), becomes, after solving for $\boldsymbol{h}$:

$$\boldsymbol{h} = \frac{k_0^2 \boldsymbol{m} - \boldsymbol{k}\boldsymbol{k} \cdot \boldsymbol{m}}{k^2 - k_0^2}, \tag{2.30}$$

where $k_0^2 = \omega^2 \mu_0 \epsilon$. Similarly, one can derive the following equation for $\boldsymbol{e}$:

$$\boldsymbol{e} = \frac{\omega \mu_0 \boldsymbol{k} \times \boldsymbol{m}}{k_0^2 - k^2}. \tag{2.31}$$

Therefore, by virtue of Eq. (2.27), we have:

$$\nabla \times \boldsymbol{h} = -\frac{k_0^2 \boldsymbol{k} \times \boldsymbol{m}}{k_0^2 - k^2}. \tag{2.32}$$

For large $|\boldsymbol{k}|$, we can notice that $\boldsymbol{h}$ remains finite in Eq. (2.30), provided $\boldsymbol{k} \cdot \boldsymbol{m} \neq 0$. Conversely, Eqs. (2.31) for $\boldsymbol{e}$ and (2.32) for $\nabla \times \boldsymbol{h}$ vanish as $1/k$ in the same limit. Therefore, to the lowest order, we can describe the waves by the magnetostatic equations:

$$\nabla \times \boldsymbol{h} = 0, \tag{2.33}$$

$$\nabla \cdot \boldsymbol{b} = 0, \tag{2.34}$$

which, together with Eq. (2.6), i.e., $\nabla \times \boldsymbol{e} = i\omega \boldsymbol{b}$, constitute the so-called *magnetoquasistatic approximation* to Maxwell's equations, which, however, is also valid in the opposit limit, i.e., $|\boldsymbol{k}| \ll |\boldsymbol{k}_0|$. These equations describe the behavior of magnetoquasistatic waves, more commonly known as *magnetostatic waves*. For these waves, the coupling between the spins, dominated by the dipolar fields from the magnetic moments rather than the exchange interaction, occurs when $k_0 \ll k \ll \pi/a$, where a is the spacing between spins.

2.3 WALKER'S EQUATION AND DIPOLAR SPIN WAVES

Magnetostatic modes are the solution of *Walker's equation*, which derives from the magnetostatic Eqs. (2.33) and (2.34). Let us start by writing the permeability tensor (without considering the exchange and anisotropy contributions) as:

$$\bar{\boldsymbol{\mu}} = \mu_0 \begin{bmatrix} 1+\chi & -i\kappa & 0 \\ i\kappa & 1+\chi & 0 \\ 0 & 0 & 1 \end{bmatrix}, \tag{2.35}$$

where $\chi = \frac{\omega_0 \omega_M}{\omega_0^2 - \omega^2}$ and $\kappa = \frac{\omega \omega_M}{\omega_0^2 - \omega^2}$, with $\omega_M \equiv -\gamma \mu_0 M_S$ and $\omega_0 \equiv -\gamma \mu_0 H_0$. These are the building blocks of the Polder susceptibility tensor, defined as:

$$\bar{\chi} = \begin{bmatrix} \chi & -i\kappa \\ i\kappa & \chi \end{bmatrix}. \tag{2.36}$$

Polder susceptibility tensor $\bar{\chi}$ is a specific variant of the magnetic susceptibility tensor $\bar{\chi}_m$, already introduced in the constitutive relation

(2.16). In fact, $\bar{\chi}$ describes the dynamic response of a uniformly magnetized ferromagnet biased by a static field along the z direction. By virtue of Eq. (2.33), we can introduce a magnetostatic scalar potential, i.e.:

$$\boldsymbol{h} = -\nabla\Psi, \tag{2.37}$$

where the choice of the minus sign, in any case arbitrary, is made in analogy with the electrostatic equation $\boldsymbol{E} = -\nabla V$, with V electrical potential. The combination of Eqs. (2.34) and (2.37), together with the constitutive relation (2.18) leads to:

$$\nabla \cdot (\bar{\boldsymbol{\mu}} \cdot \nabla\Psi) = 0, \tag{2.38}$$

which can be expanded, using Eqs. (2.20) and (2.35), as:

$$(1+\chi)\left[\frac{\partial^2\psi}{\partial x^2} + \frac{\partial^2\psi}{\partial y^2}\right] + \frac{\partial^2\psi}{\partial z^2} = 0, \tag{2.39}$$

which is the aforementioned Walker's equation.

Starting from (2.39), in the case of an uniform plane wave propagation in an infinite medium we have, assuming $\Psi \sim exp(i\boldsymbol{k}\cdot\boldsymbol{r})$:

$$(1+\chi)(k_x^2 + k_y^2) + k_z^2 = 0. \tag{2.40}$$

If the propagation angle with respect to z direction - as well as the direction of the bias field - is θ, we get $k_x^2 + k_y^2 = k^2 sin^2\theta$ and $k_z^2 = k^2 cos^2\theta$, which, substituted in (2.40), lead to, after simplification:

$$\chi sin^2\theta = -1. \tag{2.41}$$

We have already shown that $\boldsymbol{k}\cdot\boldsymbol{h} = -\boldsymbol{k}\cdot\boldsymbol{m}$, which can be recast as:

$$\boldsymbol{h} = -\frac{\boldsymbol{k}\boldsymbol{k}\cdot\boldsymbol{m}}{k^2}. \tag{2.42}$$

The substitution of the constitutive relation $\boldsymbol{m} = \bar{\chi}\boldsymbol{h}$ (i.e., the specific version of Eq. (2.16) in this case) into Eq. (2.42) leads to:

$$\boldsymbol{h} = -\frac{\boldsymbol{k}(\boldsymbol{k}\cdot\bar{\chi}\cdot\boldsymbol{h})}{k^2}, \tag{2.43}$$

that can be rewritten as follows:

$$(k^2\bar{\boldsymbol{I}} + \boldsymbol{k}\boldsymbol{k}\cdot\bar{\chi}\cdot)\boldsymbol{h} = 0. \tag{2.44}$$

Now we can assume $\boldsymbol{k} = k(\hat{y}sin\theta + \hat{z}cos\theta)$ without loss of generality. Therefore:

$$\mathbf{kk} = k^2\begin{bmatrix} 0 & \sin\theta & 0 \\ \sin\theta & \sin^2\theta & \cos\theta\sin\theta \\ 0 & \cos\theta\sin\theta & \cos^2\theta \end{bmatrix}, \tag{2.45}$$

which allows us to compute:

$$\mathbf{kk}\cdot\bar{\chi} = k^2\begin{bmatrix} 0 & \chi\sin\theta & 0 \\ \chi\sin\theta & \chi\sin^2\theta & \chi\cos\theta\sin\theta \\ 0 & \chi\cos\theta\sin\theta & \chi\cos^2\theta \end{bmatrix}. \tag{2.46}$$

Finally, we can write Eq. (2.44) in the following matrix form:

$$k^2\mathbb{I} + \mathbf{kk}\cdot\bar{\chi} = k^2\begin{bmatrix} 1 & \chi\sin\theta & 0 \\ \chi\sin\theta & 1+\chi\sin^2\theta & \chi\cos\theta\sin\theta \\ 0 & \chi\cos\theta\sin\theta & 1+\chi\cos^2\theta \end{bmatrix}. \tag{2.47}$$

For a nontrivial solution for $\boldsymbol{h}$ to exist, the determinant of the matrix must be set equal to zero, i.e., $det(k^2\bar{\boldsymbol{I}} + \boldsymbol{kk}\cdot\bar{\boldsymbol{\chi}}) = 0$. Solving for ω and performing the square root, we get:

$$\omega = \sqrt{\omega_0(\omega_0 + \omega_M sin^2\theta)}. \tag{2.48}$$

Since θ is the angle between the direction of the magnetization and the given propagation direction, Eq. (2.48) shows that the Kittel formula (1.44), introduced in Chapter 1 is dependent on k direction and not on its absolute value, as already claimed.

2.4 EXCHANGE SPIN WAVES

Up to this point, exchange interactions have been neglected; once they are included, however, the situation changes significantly. At reduced dimensionalities - typically below 1 μm - exchange becomes dominant and the previous reasoning no longer applies. We therefore derive the expression that replaces Eq. (2.48) when exchange is considered. We anticipate that the contribution given to magnetocristalline anistropy is not included in the following derivation but the reasoning can be easily extended. As done previously, we assume that the fields can be divided into static and time-varying parts, i.e., $\boldsymbol{M} = \boldsymbol{M}_0 + \boldsymbol{m}(t)$, $\boldsymbol{H} = \boldsymbol{H}_0 + \boldsymbol{h}(t)$ and $\boldsymbol{H}_{ex} = \boldsymbol{H}_{0ex} + \boldsymbol{h}_{ex}(t)$. Therefore, LL equation (1.26) can be rewritten as:

$$\begin{aligned}\frac{1}{\gamma\mu_0}\frac{d\boldsymbol{m}}{dt} &= \boldsymbol{M}_0 \times [\boldsymbol{H}_0 + \boldsymbol{H}_{0ex}] + \boldsymbol{M}_0 \times [\boldsymbol{h} + \boldsymbol{h}_{ex}] \\ &+ \boldsymbol{m} \times [\boldsymbol{H}_0 + \boldsymbol{H}_{0ex}] + \boldsymbol{m} \times [\boldsymbol{h}_0 + \boldsymbol{h}_{ex}].\end{aligned} \tag{2.49}$$

Being interested in single-domain materials, we consider configurations in which $\boldsymbol{M}_0$ is spatially uniform and $\boldsymbol{H}_{0ex}$ vanishes according to the exchange field density expression (1.10). We also notice that the remaining part of the first term on the r.h.s vanishes since the equilibrium configuration implies $\boldsymbol{M}_0 \times \boldsymbol{H}_0 = 0$. It is convenient to assume $\boldsymbol{M}_0 || \boldsymbol{H}_0$, which is true only for directions of high-crystal symmetry. Under these assumptions, it is possible to write (after assuming harmonic time dependence, neglecting terms of second-order in small quantities and choosing the coordinate system so that the equilibrium magnetization points along the z direction) Eq. (2.49) in the following linearized form:

$$i\frac{\omega}{\omega_M}\boldsymbol{m} = \hat{\boldsymbol{z}} \times \left[\boldsymbol{h} + \lambda_{ex}\nabla^2\boldsymbol{m} - \frac{H_0}{M_S}\boldsymbol{m}\right]. \tag{2.50}$$

which yields, after solving for $\boldsymbol{m}$:

$$\boldsymbol{h} = \overline{\boldsymbol{A}}_{\text{op}} \cdot \boldsymbol{m}, \tag{2.51}$$

where:

$$\overline{\boldsymbol{A}}_{\text{op}} = \frac{1}{\omega_M}\begin{bmatrix} \omega_0 - \omega_M\lambda_{ex}\nabla^2 & i\omega \\ -i\omega & \omega_0 - \omega_M\lambda_{ex}\nabla^2 \end{bmatrix}. \tag{2.52}$$

Since in the case of uniform plane wave propagation the spatial dependence of $\boldsymbol{m}$ and $\boldsymbol{h}$ is of the form $exp(i\boldsymbol{k}\cdot\boldsymbol{r})$, the Laplacian operator ∇^2 is replaced by the factor -k^2. Therefore, it is possible to write:

$$\boldsymbol{h} = \overline{\boldsymbol{A}}_{\text{op}}\cdot\boldsymbol{m} = \frac{1}{\omega_M}\begin{bmatrix} \omega_0 + \omega_M\lambda_{ex}k^2 & i\omega \\ -i\omega & \omega_0 + \omega_M\lambda_{ex}k^2 \end{bmatrix}\begin{bmatrix} m_x \\ m_y \end{bmatrix}. \tag{2.53}$$

It can be noted that the occurrence of $\omega_M\lambda_{ex}k^2$, i.e., the exchange term, is always accompanied by ω_0; as a consequence, in the presence of the exchange interaction, the previous dispersion relation (2.48) can be recast as:

$$\omega = \sqrt{\left[\left(\omega_0 + \omega_M\lambda_{ex}k^2\right)\left(\omega_0 + \omega_M\left(\lambda_{ex}k^2 + \sin^2\theta\right)\right)\right]}, \tag{2.54}$$

since ω_0 is substituted by $\omega_0 + \omega_M\lambda_{ex}k^2$ in the plane wave analysis. Eq. (2.54) is the Kittel formula including exchange interactions and, unlike Eq. (2.48), it establishes a one-to-one correspondence between the frequency ω and the wavenumber k. When the exchange term dominates, i.e., when $\omega_M\lambda_{ex}k^2 \gg \omega_0$, the resulting excitations are termed *exchange spin waves*. In this limit, the dispersion relation reduces to $\lim_{k\to\infty}\omega \approx \omega_M\lambda_{ex}k^2$. Conversely, when exchange is negligible, the excitations correspond to *dipolar spin waves*, discussed in Sec. 2.3. For small wavevectors, the dispersion approaches $\lim_{k\to 0}\omega \approx \sqrt{\omega_0\left(\omega_0 + \omega_M\sin^2\theta\right)}$, which is precisely Eq. (2.48). These two limiting forms make it clear that only in the dipolar regime does the frequency depend on the magnetization orientation (through the angle θ); anisotropy in this context therefore originates from the dipolar interaction.

2.5 KALINIKOS-SLAVIN RELATION

Summarizing the main results derived in Secs. 2.3 and 2.4, if an unbound system is considered with both exchange and dipolar interactions, at low k the dispersion curve is rather independent of k (prevalence of dipolar interaction), while at high k the trend is quadratic (prevalence of exchange interaction). However, for practical purposes, the main interest revolves around small magnetic waveguides which were investigated by Kalinikos and Slavin [8]. They developed dispersion relations which consistently incorporate both exchange and dipolar interactions, thereby offering a comprehensive framework for arbitrary wavevectors and propagation angles. An exhaustive derivation of the *Kalinikos–Slavin relation* is provided in Appendix 2.11 at the end of this chapter. Here, the general idea is discussed.

Typically, in real scenarios, spin waves are confined in a 1-dimensional structure, i.e., their propagation direction, while the spin wave beam is confined in length, width and height. In this sense, the confinement takes place in width and height, therefore the wave vector can be

assumed quantized (and not continuous) along these two dimensions. The usual waveguides, such as the ones investigated in this thesis work, have small thickness, hence it is possible to assume that only the zero order thickness mode is present (higher order thickness mode appear at higher frequencies). Under these conditions, the spin-wave amplitude can be assumed uniform across the film thickness. As a result, being the thickness profile effectively constant, the analysis can focus on the mode structure along the width of the waveguide. Although the quantization of the wavevector in the width direction depends on the specific boundary conditions applied at the edges, a widely used approximation becomes valid when the waveguide width is much larger than its thickness. In this case, the lateral wavevector can be expressed as $k_n = \frac{n\pi}{w}$, where n is an integer number, more precisely the transverse mode index. Based on this assumption, the total wavevector magnitude for each quantized mode is given by $k_{\text{tot}} = \sqrt{k^2 + k_n^2}$ where k is the wavevector component along the waveguide length (propagation direction) while k_n represents the quantized component along the width. By applying perturbation theory under specific boundary conditions, i.e., assuming unpinned surfaces (where the surface spins are completely free to precess), one can derive the corresponding dispersion relations for the confined spin wave modes:

$$\omega_n = \sqrt{\left(\omega_0 + \omega_M \lambda_{ex} k_{\text{tot}}^2\right)\left(\omega_0 + \omega_M \lambda_{ex} k_{\text{tot}}^2 + \omega_M F_{nn}\right)}, \qquad (2.55)$$

where F_{nn} is a geometric dipolar factor that encodes how magnetostatic interactions, via film thickness and propagation angle, modify the spin-wave dispersion (for futher details, see Appendix 2.11, Eq. (2.A2)).

Eq. (2.55) is the Kalinikos-Slavin relation and refers to different modes depending on the number n and each mode has its own dispersion as well as a specific waveform given by $m_z^n(x, y, t) \sim \cos(k_n y)\, e^{i(kx - \omega(k)t)}$, with x, y and z representing the longitudinal, the width and the out-of-plane directions, respectively.

We precise that the dispersion relations obtained so far are valid only for uniformly magnetized waveguide. In the case of departure from a non uniform scenario, e.g., for a sinusoidal pattern, which represents the core of this thesis work, an exhaustive theoretical discussion is a great challenge. Therefore, micromagnetic simulations and analytical models, which are the most suitable way to investigate such peculiar systems, are pursued.

2.6 GEOMETRIC CLASSIFICATION OF SPIN WAVES

In thin ferromagnetic films subjected to a static external field $\boldsymbol{H}_{ext}$, the equilibrium magnetization $\boldsymbol{M}$ defines a preferential axis that governs the propagation characteristics of spin waves. As anticipated, a classification of magnetostatic modes can be established according to the relative orientation between the wavevector $\boldsymbol{k}$ and the magnetization $\boldsymbol{M}$. Three fundamental geometries are distinguished (see Fig. 2.2 for a pictorial representation):

1. **Backward Volume Spin Waves (BVSW).** The wavevector is collinear with the magnetization, $\boldsymbol{k} \parallel \boldsymbol{M}$ (parallel or antiparallel,

in-plane, Fig. 2.2(a)). The mode extends throughout the volume of the film, with a nearly uniform amplitude distribution across the thickness. Its hallmark is the backward dispersion: the frequency decreases with increasing k, resulting in opposite signs of phase and group velocities.

2. **Damon-Eshbach (DE) or Surface Spin Waves (SSW).** The wavevector is orthogonal to the in-plane magnetization, $\boldsymbol{k} \perp \boldsymbol{M}$ (Fig. 2.2(b)). The spin-wave amplitude is localized near one surface of the film, decaying exponentially towards the interior. These modes are intrinsically non-reciprocal, as the surface of localization depends on the sign of $\boldsymbol{k}$. Their dispersion relation is typically increasing with k.

3. **Forward Volume Spin Waves (FVSW).** The wavevector is collinear with the magnetization, $\boldsymbol{k} \parallel \boldsymbol{M}$, with $\boldsymbol{M}$ oriented perpendicular to the film plane (out-of-plane magnetization, Fig. 2.2(c)). These are volume modes, uniformly distributed across the thickness, characterized by a forward dispersion, i.e., the frequency increases with increasing k. Unlike the DE case, FV modes are fully reciprocal, exhibiting identical properties for $+\boldsymbol{k}$ and $-\boldsymbol{k}$. This is due to symmetry: when a field is applied normal to the film plane, the propagation characteristics of FVSW are independent of direction in the plane of the film.

This classification, originally developed in the framework of the magnetostatic approximation, constitutes the standard scheme for identifying spin-wave modes in ferromagnetic films and serves as the basis for the analysis of more complex geometries and interaction regimes.

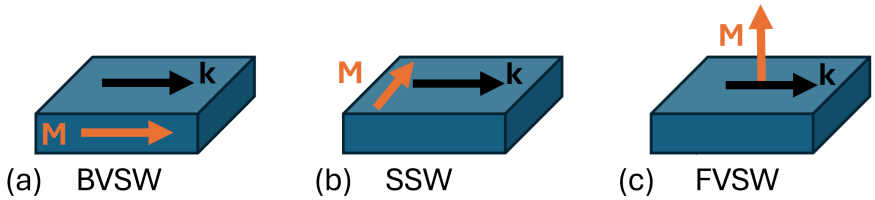

Figure 2.2: Sketch of the three possible configurations of spin waves, according to the relative orientation between $\boldsymbol{k}$ and $\boldsymbol{M}$. (a): $\boldsymbol{k} \parallel \boldsymbol{M}$ (parallel or antiparallel, in-plane). (b): $\boldsymbol{k} \perp \boldsymbol{M}$ (in-plane). (c): $\boldsymbol{k} \parallel \boldsymbol{M}$ (out-of-plane).

2.7 BACKWARD VOLUME WAVES

Let us consider a ferromagnetic film of thickness d, bounded by planes $y = \pm d/2$, with a static bias field $\boldsymbol{H}_{ext}$ applied along $+\hat{\mathbf{z}}$, so that the system is tangentially magnetized (see Fig. 2.3).

We focus on guided magnetostatic waves that propagate along $\pm\hat{\mathbf{z}}$, therefore a harmonic dependence of the type $e^{i\nu k_z z}$ with $\nu = \pm 1$ can be considered (the temporal factor $e^{-i\omega t}$ is common to all fields and is therefore omitted for compactness). Inside the film (Region II), the potential varies across the thickness with a transverse wavenumber k_y. The field inside the film can be built from two counterpropagating

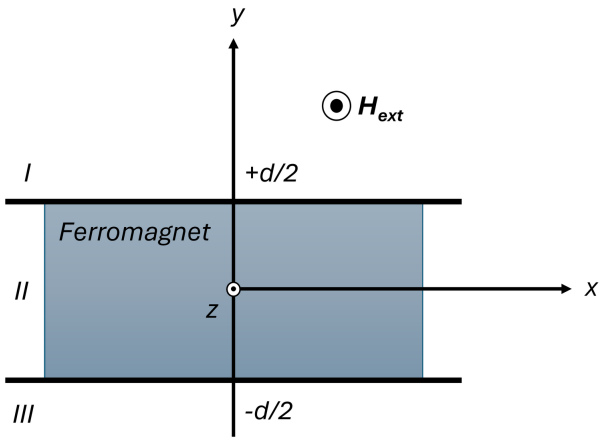

Figure 2.3: System considered for the analysis of spin wave geometry.

plane waves whose normal components have opposite sign but share the same tangential phase constant k_z:

$$\psi_{II}^{(+)}(\mathbf{r}) = A\, e^{i(\nu k_z z + k_y y)}, \qquad \psi_{II}^{(-)}(\mathbf{r}) = B\, e^{i(\nu k_z z - k_y y)}. \tag{2.56}$$

To obtain the odd thickness symmetry (a node at the midplane $y = 0$), we form the antisymmetric combination of the two counter-propagating waves. This choice yields the lowest-order backward volume wave mode. Up to an overall phase/convention:

$$\psi_{II}(\mathbf{r}) = \frac{1}{2i}\left[\psi_{II}^{(+)}(\mathbf{r}) - \psi_{II}^{(-)}(\mathbf{r})\right]. \tag{2.57}$$

Choosing equal magnitudes $A = B = \psi_0$ and absorbing any common phase into ψ_0, Eqs. 2.56 and 2.57 lead to:

$$\psi_{II}(\mathbf{r}) = \frac{\psi_0}{2i}\, e^{i\nu k_z z}\left(e^{ik_y y} - e^{-ik_y y}\right) = \psi_0\, e^{i\nu k_z z}\, \sin(k_y y). \tag{2.58}$$

This is precisely the odd-parity (antisymmetric) thickness profile with a node at $y = 0$. As for the regions outside the film, the medium is nonmagnetic and isotropic to an excellent approximation with $\boldsymbol{B} \simeq \mu_0 \boldsymbol{H}$. In the magnetostatic regime it is possible to write:

$$\nabla \times \boldsymbol{H} = \mathbf{0} \quad \rightarrow \quad \boldsymbol{H} = -\nabla \psi_d, \tag{2.59}$$

$$\nabla \cdot \boldsymbol{B} = 0 \;\rightarrow\; \nabla \cdot \boldsymbol{H} = 0 \;\rightarrow\; \nabla^2 \psi_d = 0, \tag{2.60}$$

where ψ_d is the magnetostatic scalar potential. Since there is no x-variation for the guided waves, i.e., $\partial/\partial x = 0$, Laplace's equation in this case reduces to:

$$\left(\frac{\partial^2}{\partial y^2} + \frac{\partial^2}{\partial z^2}\right) \psi_d(y, z) = 0. \tag{2.61}$$

We seek separated solutions of the form $\psi_d(y, z) = Y(y)\, Z(z)$. Eq. 2.61 yields:

$$\frac{Z''(z)}{Z(z)} = -\frac{Y''(y)}{Y(y)} = -\lambda^2, \tag{2.62}$$

hence:

$$Z'' + \lambda^2 Z = 0 \;\rightarrow\; Z(z) = e^{\pm i\lambda z}, \tag{2.63}$$

$$Y'' - \lambda^2 Y = 0 \;\rightarrow\; Y(y) = A\, e^{+\lambda y} + B\, e^{-\lambda y}. \tag{2.64}$$

Because fields in the film vary as $e^{i\nu k_z z}$, continuity of ψ across $y = \pm d/2$ for all z enforces the same z-phase constant in the outside regions (*tangential phase matching*):

$$\lambda = k_{z,out} = k_z. \tag{2.65}$$

Therefore, the general dielectric solution compatible with the backward z-dependence is:

$$\psi_d(y,z) = \left(A\, e^{+k_z y} + B\, e^{-k_z y}\right) e^{i\nu k_z z}. \tag{2.66}$$

Physical admissibility requires the fields to remain bounded (and in practice to decay) as $|y| \to \infty$ outside the film. Let us examine the two different spatial regions.

- **Region I** (above the film): $y > +d/2$ and $y \to +\infty$. The term $e^{+k_z y}$ diverges, so its coefficient must vanish. Only the decaying branch $e^{-k_z y}$ is physically admissible, therefore:

$$\Psi_I(\mathbf{r}) = Ce^{-k_z y}\, e^{i\nu k_z z}. \tag{2.67}$$

- **Region III** (below the film): $y < -d/2$ and $y \to -\infty$. The term $e^{-k_z y}$ diverges, so its coefficient must vanish. Only the decaying branch $e^{+k_z y}$ is physically admissible, therefore:

$$\Psi_{III}(\mathbf{r}) = D\, e^{+k_z y}\, e^{i\nu k_z z}. \tag{2.68}$$

The constants C and D are complex amplitudes that are determined by boundary matching. Eqs. (2.67), (2.58) and (2.68) represent the trial potential functions in each region of the considered system. In the ferromagnetic film, k_y and k_z are related by Walker's equation (2.39):

$$(1+\chi)k_y^2 + k_z^2 = 0. \tag{2.69}$$

It must be noted that solutions for real k_y and k_z require $(1+\chi) < 0$. Thus, guided modes, which can be separated into plane waves bouncing back and forth in the film, can only occur for frequencies within the volume wave manifold (i.e., the set of frequencies $\omega_0 \leq \omega \leq \sqrt{\omega_0(\omega_0+\omega_M)}$ - bounded below by the Larmor frequency and above by the ferromagnetic-resonance limit - over which multiple magnetostatic plane-wave modes exist and can propagate for nonzero in–plane wave numbers). The following step consists in implementing the boundary conditions at $y = \pm d/2$. First, we require ψ to be continuous. This yields:

$$C\, e^{-k_z d/2} = \psi_0\, \sin(k_y d/2), \tag{2.70}$$

$$D\, e^{-k_z d/2} = -\psi_0\, \sin(k_y d/2). \tag{2.71}$$

From Eqs. (2.70) and (2.71) we see that $C = -D$, as expected for an odd function. The other boundary condition involves the continuity of normal $\boldsymbol{b}$ at $y = \pm d/2$. The normal component of $\boldsymbol{b}$ in this geometry is b_y. From the constitutive relation (2.10), we have:

$$b_y = i\mu_0\kappa h_x + \mu_0(1+\chi)h_y. \tag{2.72}$$

The first term is suppressed because the potential is independent of x. Therefore, the requirement that b_y has to be continuous at $y = \pm d/2$ leads to:

$$-k_z C\, e^{-k_z d/2} = k_y(1+\chi)\, \psi_0 \cos(k_y d/2), \tag{2.73}$$

$$k_z D\, e^{-k_z d/2} = k_y(1+\chi)\, \psi_0 \cos(k_y d/2). \tag{2.74}$$

Since $C = -D$, Eqs. (2.73) and (2.74) are equivalent. Combining them with the previous boundary conditions, i.e., Eqs. (2.70) and (2.71) yields:

$$\tan(k_y d/2) = -(1+\chi)\,\frac{k_y}{k_z}. \tag{2.75}$$

Walker's equation (2.69) allows one to eliminate k_y. Therefore, we can write:

$$\tan\left[\frac{k_z d}{2}\sqrt{-(1+\chi)}\right] = \sqrt{-(1+\chi)}. \tag{2.76}$$

Eq. 2.76 is the dispersion relation for modes with odd potential functions. In the case of an even potential we would have had $-\cot\left[\frac{k_z d}{2}\sqrt{-(1+\chi)}\right] = \sqrt{-(1+\chi)}$). However, by means of the identity $\tan\left(\theta - \frac{\pi}{2}\right) = -\cot\theta$ we can combine even and odd mode solutions. In fact, although we start with the odd ansatz for convenience, the even symmetry is not excluded; it completes the alternating parity ladder of thickness modes and is required to express the dispersion in the unified form:

$$\tan\left[\frac{k_z d}{2}\sqrt{-(1+\chi)} - \frac{(n-1)\pi}{2}\right] = \sqrt{-(1+\chi)}, \quad n = 1, 2, 3, ... \tag{2.77}$$

An approximation of Eq. (2.77) that can be solved for ω was obtained by Kalinikos for the lowest-order mode ($n = 1$) [9]. Here we summarize the key points of his reasoning. First of all, it is convenient to operate the substitution: $\tan\left(\frac{k_z d}{2}\sqrt{-(1+\chi)}\right) = \sqrt{-(1+\chi)} \equiv u$, so that $\frac{k_z d}{2} = \frac{\arctan u}{u}$. Together with the Polder susceptibility (recall the building blocks of Eq. (2.36)), one gets:

$$\omega^2 = \omega_0\left[\omega_0 + \omega_M\,\frac{1}{1+u^2}\right].$$

Now, Fourier-transforming along z ($e^{ik_z z}$) reduces the magnetostatic coupling across the film thickness to a 1D convolution with the Green kernel $G_{k_z}(y-y') \propto e^{-k_z|y-y'|}$. The projection of the dipolar field onto a trial odd-thickness eigenfunction $f(y)$ (first antisymmetric thickness harmonic) yields a dynamic demagnetizing factor:

$$N_{\text{eff}}(k_z d) = \frac{\displaystyle\int_{-d/2}^{d/2}\int_{-d/2}^{d/2} f(y)\, e^{-k_z|y-y'|}\, f(y')\, dy\, dy'}{\displaystyle\int_{-d/2}^{d/2} f^2(y)\, dy}, \tag{2.78}$$

which, evaluated for the fundamental odd profile, gives the analytic form factor $F_{\text{BVSW}}(k_z d) \equiv N_{\text{eff}}(k_z d) = 1 - \frac{e^{-k_z d}}{k_z d}$. Operationally, Kalinikos replaced $\frac{1}{1+u^2}$ with $F_{\text{BVW}}(k_z d)$, which leads to the explicit dispersion:

$$\omega^2 = \omega_0 \left[\omega_0 + \omega_M \left(1 - \frac{e^{-k_z d}}{k_z d} \right) \right]. \tag{2.79}$$

The closed form of Eq. (2.79) captures the thickness-averaged dipolar coupling of the fundamental mode over the engineering-relevant range of $k_z d$, while avoiding the inversion of the tangent in Eq. (2.77).

The solutions of Eq. (2.77) are shown in Fig. 2.4.

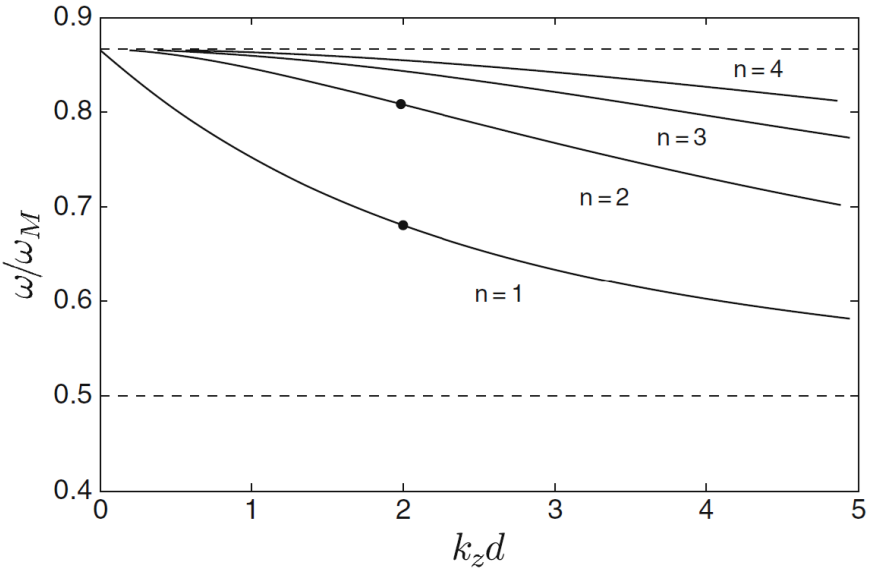

Figure 2.4: Dispersion diagram for backward volume waves with $\omega_0/\omega_M = 0.5$. The $n = 1$ solution is the closed form found by Kalinikos. Image reproduced from [7].

These modes can be decomposed into plane waves bouncing back and forth between the top and bottom surfaces of the film while propagating along the z-direction. When $k_z = 0$, the plane waves are propagating perpendicular to $\boldsymbol{B}_{ext}$. Referring to Eq. (2.54), this corresponds to the limit $\theta = \pi/2$ so that the frequency is that on top of the magnetostatic wave manifold. As k_z increases, the angle of the total $\boldsymbol{k}$ vector of the constituent plane waves decreases. In the limit of large k_z, the plane waves are propagating parallel to $\boldsymbol{B}_{ext}$ ($\theta = 0$) and the frequency approaches a lower manifold edge.

The group velocity is obtained by differentiating the dispersion relation (2.77) with respect to ω. We have:

$$\frac{1}{v_g} = \frac{\chi \kappa}{\omega_M d} \left[\frac{2}{\chi} + \frac{k_z d}{1+\chi} \right]. \tag{2.80}$$

For $n = 1$, $k_z d \ll 1$, the result is:

$$\left. \frac{1}{v_g} \right|_{kd=0} = -\frac{4}{\omega_M d} \frac{\sqrt{\omega_0(\omega_0 + \omega_M)}}{\omega_0}. \tag{2.81}$$

The initial slope of the present dispersion relation depends on the field as well as geometrical and material parameters. In the absence of exchange, all thickness modes in a tangentially magnetized film share the same cutoff frequency; consequently, there exists no frequency interval in which only a single mode propagates. Moreover, the dispersion relation is independent of the direction parameter ν, so

reversing the propagation direction does not alter the modal characteristics (within the validity of the present analysis, which assumes $\boldsymbol{k}$ parallel or antiparallel to $\boldsymbol{H}$). At any point (ω_1, k_{z1}) on the dispersion curves of Fig. 2.4, the phase velocity is $v_p = \omega_1/k_{z1} > 0$, whereas the group velocity, given by the local slope $v_g = \partial\omega/\partial k_z$, is negative. Hence, phase and energy flow in opposite directions, which is the defining signature of a backward wave. The modal amplitude exhibits a sinusoidal distribution across the film thickness. Taken together, these features motivate the terminology *magnetostatic backward volume wave* (or *backward volume spin wave*).

2.8 SURFACE SPIN WAVES (DAMON-ESHBACH)

Let us now consider propagation perpendicular to an in-plane bias field, or along the $\pm x$ direction for the same configuration system (see Fig. 2.3). As anticipated, this configuration is also known as Damon–Eshbach geometry. [10]. We can assume for a trial solution an even potenial without loss of generality, so the wavefunctions read as:

$$\psi_I(\mathbf{r}) = Ce^{-k_x y + i\nu k_x x}, \tag{2.82}$$

$$\psi_{II}(\mathbf{r}) = \psi_0 \cos(k_y y) e^{i\nu k_x x}, \tag{2.83}$$

$$\psi_{III}(\mathbf{r}) = De^{k_x y + i\nu k_x x}. \tag{2.84}$$

In the ferromagnetic film, Walker's equation (2.39) becomes:

$$(1+\chi)(k_x^2 + k_y^2) = 0. \tag{2.85}$$

One possible solution to this equation is $1 + \chi = 0$, however this only occurs for one specific frequency. The alternative is to require $k_y^2 = -k_x^2$. If k_x is required to be real for propagating waves, then k_y is necessarily imaginary; hence, ψ_{II} must consist of growing and decaying exponentials. As a consequence, the potential (2.83) is replaced with:

$$\psi_{II} = \left[\psi_0^+ e^{ky} + \psi_0^- e^{-ky}\right] e^{i\nu kx} \tag{2.86}$$

where the wave number subscripts have been eliminated because $|k_y| = k_x \equiv k$. As done previously, the boundary conditions at $y = \pm d/2$ must be applied. The imposition of the continuity to ψ leads to:

$$Ce^{-kd/2} = \psi_0^+ e^{kd/2} + \psi_0^- e^{-kd/2}, \tag{2.87}$$

$$De^{-kd/2} = \psi_0^+ e^{-kd/2} + \psi_0^- e^{kd/2}. \tag{2.88}$$

It can be noted that Eqs. (2.87) and (2.88) do not imply even or odd mode symmetry. The other boundary condition requires b_y to be continuous. From (2.72) for b_y and the potential functions (2.82), (2.86) and (2.84), we have:

$$Ce^{-kd/2} = \nu\kappa\left[\psi_0^+ e^{kd/2} + \psi_0^- e^{-kd/2}\right] - (1+\chi)\left[\psi_0^+ e^{kd/2} - \psi_0^- e^{-kd/2}\right], \tag{2.89}$$

$$De^{-kd/2} = -\nu\kappa\left[\psi_0^+ e^{-kd/2} + \psi_0^- e^{kd/2}\right] + (1+\chi)\left[\psi_0^+ e^{-kd/2} - \psi_0^- e^{kd/2}\right]. \tag{2.90}$$

At this stage, the boundary conditions (2.87) and (2.88) are substituted for the left sides of (2.89) and (2.90) and the terms collected. This leads to:

$$\begin{bmatrix} (\chi+2-\nu\kappa)e^{kd/2} & -(\chi+\nu\kappa)e^{-kd/2} \\ -(\chi-\nu\kappa)e^{-kd/2} & (\chi+2+\nu\kappa)e^{kd/2} \end{bmatrix} \begin{bmatrix} \psi_0^+ \\ \psi_0^- \end{bmatrix} = 0. \tag{2.91}$$

The determinant of the coefficient matrix (2.91) must be set to zero to obtain the dispersion relation. After simplifications, we have:

$$e^{-2kd} = \frac{(\chi+2)^2-\kappa^2}{\chi^2-\kappa^2}. \tag{2.92}$$

As evident from (2.92), there is no more dependence on ν: this means the dispersion relation is not altered if the direction of propagation is reversed. The substitution for χ and κ (recall the building blocks of the Polder's susceptibility tensor (2.36)) gives, solving for ω:

$$\omega^2 = \omega_0(\omega_0+\omega_M) + \frac{\omega_M^2}{4}\left[1-e^{-2kd}\right]. \tag{2.93}$$

Solving instead for k results in:

$$k = -\frac{1}{2d}\ln\left[1+\frac{4}{\omega_M^2}\left[\,\omega_0(\omega_0+\omega_M)-\omega^2\,\right]\right]. \tag{2.94}$$

It is important to stress that k can only take on positive values in both Eqs. (2.93) and (2.94). The dispersion relation is plotted in Fig. 2.5.

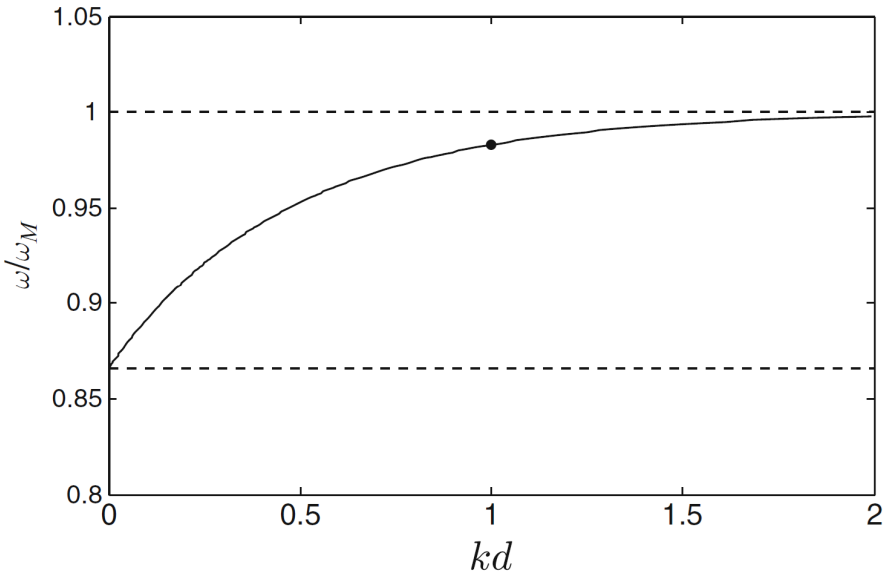

Figure 2.5: Dispersion diagram for surface spin waves with $\omega_0/\omega_M = 0.5$. Image reproduced from [7].

We can obtain the group velocity by differentiating Eq. (2.93)

$$\frac{1}{v_g} = \frac{4\omega}{\omega_M^2 d}e^{2kd}. \tag{2.95}$$

Near $kd = 0$ the group velocity is:

$$\left.\frac{1}{v_g}\right|_{kd=0} = \frac{4}{\omega_M d}\sqrt{\frac{\omega_0(\omega_0+\omega_M)}{\omega_M}}. \tag{2.96}$$

Again the initial group velocity is found to depend on the field as well as on geometrical and material parameters.

In contrast to backward volume waves (but also forward waves, as we will be shown in Sec. 2.9), the tangentially magnetized surface-wave configuration supports only a single propagating mode; there is no ladder of thickness harmonics. While the dispersion curve itself is independent of the direction parameter ν, the field distribution is not: reversing the propagation direction shifts the energy density from one interface to the opposite. This phenomenon is known as *field–displacement nonreciprocity*. The reason the dispersion remains unchanged is the symmetry of the electromagnetic boundary conditions at the two film surfaces; if that symmetry were broken (for example, by placing a conducting plane on only one side), the dispersion would acquire an explicit ν dependence.

2.9 FORWARD VOLUME WAVES

We now consider forward volume waves using the same coordinate system adopted in the backward and surface-wave analyses (Fig. 2.3). The film occupies $|y| \leq d/2$ (film plane x–z, thickness along y), and the bias field is taken normal to the film, i.e., $\boldsymbol{H}_{ext} \parallel \hat{\boldsymbol{y}}$. The in–plane wavevector is $\boldsymbol{k}_t = k_x\hat{\boldsymbol{x}} + k_z\hat{\boldsymbol{z}}$ with magnitude $k_t = \sqrt{k_x^2 + k_z^2}$. We invoke the two results already established in the preceding sections: (i) outside the ferromagnetic film, $\nabla^2\psi = 0$ so that, with no x–z curvature, the normal wavenumber equals the in-plane one, $k_{y,d} = \pm k_{t,d}$; (ii) tangential phase matching enforces $k_{t,d} = k_t$. Choosing decay away from the film leads to the standard evanescent forms:

$$\psi_I = C\, e^{-k_t y}\, e^{i\boldsymbol{k}_t\cdot\boldsymbol{r}_t}, \qquad \psi_{III} = D\, e^{+k_t y}\, e^{i\boldsymbol{k}_t\cdot\boldsymbol{r}_t}, \qquad \boldsymbol{r}_t \equiv (x, 0, z). \tag{2.97}$$

Inside the ferromagnetic film, guided waves are constructed from plane waves bouncing between the interfaces, yielding even/odd thickness profiles in y:

$$\psi_{II}^{(e)} = \psi_0 \cos(k_y y)\, e^{i\boldsymbol{k}_t\cdot\boldsymbol{r}_t}, \qquad \psi_{II}^{(o)} = \psi_0 \sin(k_y y)\, e^{i\boldsymbol{k}_t\cdot\boldsymbol{r}_t}. \tag{2.98}$$

For a normally magnetized film, Walker's equation (2.39) relates k_y and k_t as:

$$k_y^2 + (1+\chi)\, k_t^2 = 0 \quad \rightarrow \quad \frac{k_t}{k_y} = \frac{1}{\sqrt{-(1+\chi)}}, \tag{2.99}$$

with $1+\chi < 0$ in the manifold. Continuity of ψ and of the normal flux density b_y at the two interfaces gives, for the even trial:

$$C\, e^{-k_t d/2} = \psi_0 \cos(k_y d/2), \tag{2.100}$$

$$D\, e^{-k_t d/2} = \psi_0 \cos(k_y d/2), \tag{2.101}$$

$$k_t C\, e^{-k_t d/2} = \psi_0 k_y \sin(k_y d/2), \tag{2.102}$$

$$-k_t D\, e^{-k_t d/2} = -\psi_0 k_y \sin(k_y d/2). \tag{2.103}$$

From the previous relations, we notice immediately $C = D$. Furthermore, the amplitudes can be eliminated so that:

$$\tan\left(\frac{k_y d}{2}\right) = \frac{k_t}{k_y}. \tag{2.104}$$

Using (2.99) this becomes the even dispersion relation:

$$\tan\left[\frac{k_t d}{2}\sqrt{-(1+\chi)}\right] = \frac{1}{\sqrt{-(1+\chi)}}. \tag{2.105}$$

Repeating the steps with the odd trial $\psi_{II}^{(o)}$ yields:

$$-\cot\left[\frac{k_t d}{2}\sqrt{-(1+\chi)}\right] = \frac{1}{\sqrt{-(1+\chi)}}. \tag{2.106}$$

Now we combine (2.105)–(2.106) using $\tan(\theta - \pi/2) = -\cot\theta$ in order to obtain the unified thickness–mode family:

$$\tan\left[\frac{k_t d}{2}\sqrt{-(1+\chi)} - \frac{n\pi}{2}\right] = \frac{1}{\sqrt{-(1+\chi)}}, \qquad n = 0, 1, 2, ... \tag{2.107}$$

Following the same projection argument used previously (now for the fundamental even profile in y) by Kalinikos [9], it is possible to obtain the explicit approximation:

$$\omega^2 = \omega_0\left[\omega_0 + \omega_M\left(1 - \frac{1 - e^{-k_t d}}{k_t d}\right)\right], \tag{2.108}$$

which is the forward–volume analogue of the backward wave closed form, with k_t playing the role of the in–plane wavenumber in the x–z film plane. In Fig. 2.6 the solutions of (2.107) are plotted.

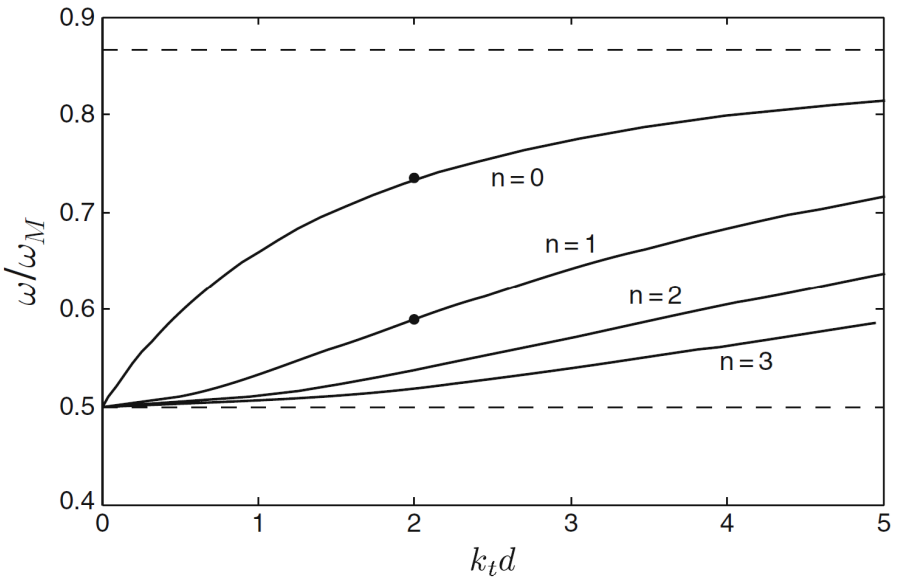

Figure 2.6: Dispersion diagram for forward volume waves with $\omega_0/\omega_M = 0.5$. Image reproduced from [7].

Differentiating (2.107) with respect to ω gives the usual expression for the inverse group velocity:

$$\frac{1}{v_g} = \frac{\chi\kappa}{(1+\chi)\,\omega_M d}\left(\frac{2}{\chi} - k_t d\right), \tag{2.109}$$

$$\left.\frac{1}{v_g}\right|_{k_t d \ll 1, n=0} = \frac{4}{\omega_M d}. \tag{2.110}$$

The complete mode shapes in Regions I/II/III follow directly from the boundary matching: once the interface conditions fix the amplitudes, one inserts the solved coefficients into the piecewise potentials,

yielding $C = D$ for the even family and $C = -D$ for the odd family. In the absence of exchange, all thickness harmonics share a common cutoff frequency; consequently, there is no spectral interval in which only a single mode propagates (this degeneracy is lifted in sufficiently thin films by the exchange interaction). The dispersion depends on the magnitude of the in–plane wavevector, $|\boldsymbol{k}_t|$, but not on its azimuthal angle (propagation is therefore isotropic within the film plane, unless magnetocrystalline anisotropy is present). Although phase and group velocities generally differ in magnitude, they are co–directed, which establishes the forward character of these waves; the field amplitude, moreover, exhibits a sinusoidal variation across the film thickness. For these reasons, and within the magnetostatic approximation under which they are derived, the modes are referred to collectively as *magnetostatic forward volume waves* (or *forward volume spin waves*).

2.10 SUMMARY ON SPIN WAVE DISPERSION RELATIONS

In the previous sections, we have shown how spin waves in a ferromagnetic film of thickness d display different dispersions depending on the propagation direction of the in-plane wavevector $\boldsymbol{k}$ with respect to the magnetization $\boldsymbol{M}$ and on whether the dynamics is dominated by long-range dipolar fields or by short-range exchange. Reasoning in broad terms and within a standard notational framework, the dimensionless parameter kd conveniently separates the regimes: for $kd \lesssim 1$ the spectrum is dipole dominated, whereas for $kd \gg 1$ the exchange term controls the dispersion. A convenient schematic form of the fundamental-mode dispersion is represented by the Kalinikos-Slavin relation (2.55). As shown in Appendix 2.11, the factor F_{nn} is dependent on kd and φ, which is the in-plane angle between $\boldsymbol{k}$ and $\boldsymbol{M}$ (in the case of forward waves, φ is not defined). In the exchange limit $kd \to \infty$ one has $F_{nn} \to 0$, recovering the quadratic law discussed in Sec. 2.4. More precisely, we have:

- **Backward volume waves** ($\boldsymbol{k} \parallel \boldsymbol{M}$): all geometries converge to the common exchange parabola: $f(k) \simeq f_{\mathrm{FMR}} + \frac{\gamma}{2\pi} \lambda_{ex}^2, k^2$, so the group velocity is positive and scales as $v_g \propto k$.
- **Damon-Eshbach surface wave** ($\boldsymbol{k} \perp \boldsymbol{M}$): same quadratic dispersion as above; $v_g > 0$ with $v_g \propto k$.
- **Forward volume waves** ($\boldsymbol{M}$ out of plane): same quadratic dispersion as above; $v_g > 0$ with $v_g \propto k$. Because their monotonic increase is steeper, the forward-volume branch can cross the Damon-Eshbach or backward-volume branches before all geometries converge to the same exchange parabola at large k.

For $kd \ll 1$ instead, the factor F_{nn} is of order unity and encodes the qualitative differences:

- **Backward volume waves** ($\boldsymbol{k} \parallel \boldsymbol{M}$, $\varphi = 0$): F_{nn} leads to a negative initial slope, $v_g < 0$ at small k.
- **Damon-Eshbach surface wave** ($\boldsymbol{k} \perp \boldsymbol{M}_0$, $\varphi = \pi/2$): F_{nn} yields a positive slope, $v_g > 0$, and surface localization with depth

$\sim 1/k$; the amplitude is non-reciprocal for $\pm k$ in asymmetric stacks.

- **Forward volume waves** (***M*** out of plane): F_{nn} gives a forward-like, monotonic increase with k and no surface localization.

Fig. 2.7 provides an overview of the main features of the dispersion relations discussed above.

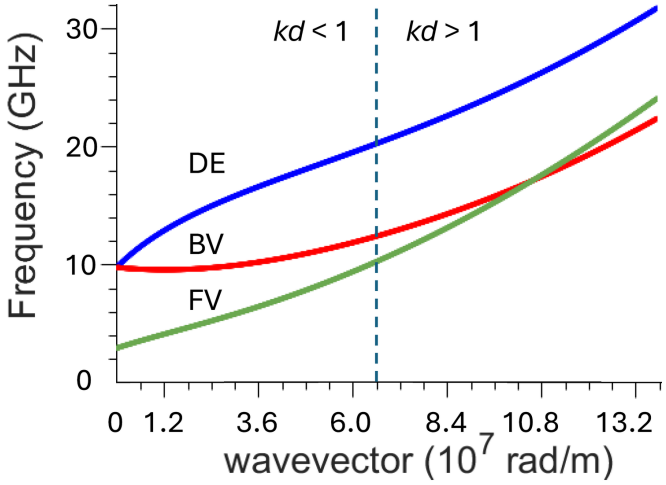

Figure 2.7: Dispersion relations of backward volume spin waves (BV), Damon-Eshbach waves (DE) and forward volume spin waves (FV) in a 15-nm-thick permalloy waveguide. The external magnetic field is $B = 100$ mT. The grey vertical line marks the crossover at $kd = 1$, separating the dipole-dominated and exchange-dominated regimes, whose distinct dispersive behaviors have been discussed above.

For the sake of completeness, we conclude this section with some brief remarks. The rigorous crossover between the dipolar and the exchange regime follows from $\lambda_{ex}k^2 \sim F_{nn}(kd, \varphi)$ and thus depends on both $k\lambda_{ex}$ and kd; the kd rule is quantitatively reliable mainly when $t/\lambda_{ex} = \mathcal{O}(1)$.

In all cases, the $k \to 0$ limit reduces to the uniform precession at f_{FMR}, and at large k the spectra collapse onto the exchange parabola. Effects beyond this picture (e.g. interfacial Dzyaloshinskii-Moriya interaction [11], perpendicular anisotropies [12], or pinning of higher thickness modes [13]) introduce asymmetries or mode splittings but do not alter the basic dipolar/exchange classification presented here.

2.11 APPENDIX

Derivation of the Kalinikos-Slavin relation

Here, the intermediate steps leading to the derivation of the Kalinikos–Slavin relation are presented. We consider a laterally infinite ferromagnetic film of thickness d (surfaces at $x = \pm d/2$, surface normal $\hat{\boldsymbol{x}}$), uniformly magnetized by a static internal field $\boldsymbol{H}_\mathrm{i}$; the in–plane axis $\hat{\boldsymbol{z}}$ is chosen along the in–plane projection of $\boldsymbol{H}_\mathrm{i}$. The equilibrium magnetization is collinear with the field, i.e., $\boldsymbol{M}_0 = M_s\big(\sin\theta\,\hat{\boldsymbol{z}} + \cos\theta\,\hat{\boldsymbol{x}}\big)$, where M_s is the saturation magnetization and θ is the polar tilt of $\boldsymbol{H}_\mathrm{i}$ from the film normal. Small transverse oscillations $\boldsymbol{m}(\boldsymbol{r},t) \perp \boldsymbol{M}_0$ obey the undamped, linearized Landau–Lifshitz equation (appropriate for eigenfrequency problems):

$$\frac{\partial \boldsymbol{m}}{\partial t} = -\,\gamma\,\mu_0\Big(\boldsymbol{M}_0 \times \boldsymbol{h}_\mathrm{eff} + \boldsymbol{m} \times \boldsymbol{H}_\mathrm{i}\Big) \;\rightarrow\; i\omega\,\boldsymbol{m} = \widehat{\mathcal{L}}\boldsymbol{m},$$

where $\widehat{\mathcal{L}}$ is the linear operator that collects the (precession) cross products with the static fields and the dynamic effective field $\boldsymbol{h}_\mathrm{eff}$. The dynamic effective field contains exchange and dipolar (magnetostatic) parts:

$$\boldsymbol{h}_\mathrm{eff} = \lambda_{ex}\nabla^2\boldsymbol{m} - \nabla\int G(\boldsymbol{r}-\boldsymbol{r}')\,\nabla'\cdot\boldsymbol{m}(\boldsymbol{r}')\,\mathrm{d}^3r',$$

where $G(\boldsymbol{r}) = 1/(4\pi|\boldsymbol{r}|)$ is the magnetostatic Green kernel ($-\nabla^2 G = \delta$). We assume plane–wave propagation in the film plane and factorize the thickness profile:

$$\boldsymbol{m}(\boldsymbol{r},t) = \widetilde{\boldsymbol{m}}(x)\,e^{i(\boldsymbol{k}\cdot\boldsymbol{r}-\omega t)}, \qquad \boldsymbol{k} = (0,k_y,k_z),\;\; k = |\boldsymbol{k}|,$$

where the azimuth φ is measured from $\hat{\boldsymbol{z}}$. Mixed pinning models surface anisotropy at $x = \pm d/2$:

$$\left.\frac{\partial m_{x,y}}{\partial x}\right|_{x=\pm d/2} = \pm\,p_{1,2}\;m_{x,y}\big|_{x=\pm d/2},$$

with p_1 and p_2 (m^{-1}) quantifying the degree of pinning at each surface ($p = 0$ free, $p \to \infty$ rigid; symmetric pinning: $p_1 = p_2 = p$). To diagonalize the exchange along x we solve:

$$-\lambda_{ex}\psi_n'' = \lambda_n\psi_n,$$

where $\lambda_n = \lambda_{ex}K_n^2$. We apply the same boundary conditions and obtain:

$$\psi_n(x) = A_n\cos(K_n x) + B_n\sin(K_n x),$$
$$\big(K_n^2 - p_1p_2\big)\tan(K_nL) = K_n(p_1+p_2),$$

and the length normalization $\int_{-d/2}^{d/2}\psi_n^2\mathrm{d}x = d$. We expand the dynamic magnetization on this basis:

$$\boldsymbol{m}(x) = \sum_n\big[a_n\,\psi_n(x)\,\hat{\boldsymbol{e}}_y + b_n\,\psi_n(x)\,\hat{\boldsymbol{e}}_x\big], \qquad k_\mathrm{tot}^2 = k^2 + K_n^2,$$

where a_n, b_n are the complex modal amplitudes and k_tot combines the in–plane and quantized thickness wave numbers. Projecting the linearised equation onto ψ_n yields an infinite matrix system:

$$\sum_{n'}\big[D_{nn'}(\omega) + R_{nn'}\big]\begin{pmatrix} a_{n'} \\ b_{n'}\end{pmatrix} = \boldsymbol{0},$$

where D is block-diagonal in n (Zeeman + exchange + longitudinal dipolar self-energies) and R contains off-diagonal transverse dipolar couplings between different thickness modes. Treating R as a perturbation, the zero-order dispersion of a non–degenerate branch n follows from $\det D_{nn}(\omega) = 0$:

$$\omega_n^2 = \Big(\omega_H + \omega_M \lambda_{ex} k_{\mathrm{tot}}^2\Big)\Big(\omega_H + \omega_M \lambda_{ex} k_{\mathrm{tot}}^2 + \omega_M F_{nn}\Big). \tag{2.A1}$$

All dipolar geometry and angular dependence is contained in the dimensionless factor F_{nn}:

$$F_{nn} = P_{nn} + \sin^2\theta \Big[1 - P_{nn}\big(1 + \cos^2\varphi\big)\Big] + U_{nn}, \tag{2.A2}$$

where $P_{nn} = P_{nn}(k; K_n, p_{1,2}, d) \in [0, 1)$ is the mode–resolved dynamic demagnetizing element (diagonal dipolar self-energy projected on ψ_n) and:

$$U_{nn} = \frac{\omega_M \, P_{nn}\big(1 - P_{nn}\big) \, \sin^2\varphi}{\omega_H + \omega_M \lambda_{ex} k_{\mathrm{tot}}^2},$$

is the ellipticity correction due to noncircular precession.

In the magnetostatic long-wavelength limit $kd \ll 1$ with unpinned surfaces ($p_{1,2} = 0$), one finds:

$$P_{nn} \simeq \begin{cases} \dfrac{kd}{2}, & n = 0, \\ \dfrac{(kd)^2}{n^2\pi^2}, & n \geq 1, \end{cases}$$

which recovers the above limits for $kd \ll 1$ and approaches $P \to 1$ for $kd \gg 1$. Non-degenerate branches acquire only $\mathcal{O}(R^2)$ frequency shifts from off-diagonal dipolar couplings. Near degeneracy of two branches $\{n, n'\}$ requires diagonalizing the 2×2 secular subspace, leading to an avoided crossing set by the effective coupling matrix element and the modal overlaps. Collecting all pieces, the compact dispersion is:

$$\omega_n = \sqrt{\Big(\omega_0 + \omega_M \lambda_{ex} k_{\mathrm{tot}}^2\Big)} \cdot \sqrt{\Big(\omega_0 + \omega_M \lambda_{ex} k_{\mathrm{tot}}^2 + \omega_M \big[P_{nn} + \sin^2\theta\big(1 - P_{nn}(1 + \cos^2\varphi)\big) + U_{nn}\big]\Big)}. \tag{2.A3}$$

In the magnetostatic limit $\lambda_{ex} \to 0$ this reproduces the standard magnetostatic dispersions (e.g. Damon-Eshbach for $\theta = \pi/2$, $\varphi = \pi/2$) upon using the appropriate P_{nn}; in the $kd \ll 1$ limit the above asymptotics recover the known slopes of the fundamental ($n = 0$) and higher ($n \geq 1$) branches.

BIBLIOGRAPHY

[1] Felix Bloch. "Zur Theorie des Ferromagnetismus". In: *Zeitschrift für Physik* 61 (1930), pp. 206–219. URL: https://api.semanticscholar.org/CorpusID:120459635.

[2] Edmund Clifton Stoner. "Collective electron ferromagnetism". In: *Proceedings of the Royal Society of London. Series A. Mathematical and Physical Sciences* 165.922 (1938), pp. 372–414. DOI: 10.1098/rspa.1938.0066. eprint: https://royalsocietypublishing.org/doi/pdf/10.1098/rspa.1938.0066. URL: https://royalsocietypublishing.org/doi/abs/10.1098/rspa.1938.0066.

[3] T. Holstein and H. Primakoff. "Field Dependence of the Intrinsic Domain Magnetization of a Ferromagnet". In: *Phys. Rev.* 58 (12 Dec. 1940), pp. 1098–1113. DOI: 10.1103/PhysRev.58.1098. URL: https://link.aps.org/doi/10.1103/PhysRev.58.1098.

[4] Freeman J. Dyson. "General Theory of Spin-Wave Interactions". In: *Phys. Rev.* 102 (5 June 1956), pp. 1217–1230. DOI: 10.1103/PhysRev.102.1217. URL: https://link.aps.org/doi/10.1103/PhysRev.102.1217.

[5] Freeman J. Dyson. "Thermodynamic Behavior of an Ideal Ferromagnet". In: *Phys. Rev.* 102 (5 June 1956), pp. 1230–1244. DOI: 10.1103/PhysRev.102.1230. URL: https://link.aps.org/doi/10.1103/PhysRev.102.1230.

[6] J.D. Jackson. *Classical Electrodynamics*. Wiley, 1998. ISBN: 9780471309321. URL: https://books.google.it/books?id=FOBBEAAAQBAJ.

[7] Daniel D. Stancil and Anil Prabhakar. *Spin Waves: Theory and Applications*. Springer, 2009.

[8] B A Kalinikos and A N Slavin. "Theory of dipole-exchange spin wave spectrum for ferromagnetic films with mixed exchange boundary conditions". In: *Journal of Physics C: Solid State Physics* 19.35 (Dec. 1986), p. 7013. DOI: 10.1088/0022-3719/19/35/014. URL: https://dx.doi.org/10.1088/0022-3719/19/35/014.

[9] B. A. Kalinikos. "Excitation of propagating spin waves in ferromagnetic films". In: *IEE Proceedings H - Microwaves, Optics and Antennas* 127.1 (1980), pp. 4–10. DOI: 10.1049/ip-h-1.1980.0002.

[10] R.W. Damon and J.R. Eshbach. "Magnetostatic modes of a ferromagnet slab". In: *Journal of Physics and Chemistry of Solids* 19.3 (1961), pp. 308–320. ISSN: 0022-3697. DOI: https://doi.org/10.1016/0022-3697(61)90041-5. URL: https://www.sciencedirect.com/science/article/pii/0022369761900415.

[11] S. Y. Xia et al. "Source and origin of the interfacial Dzyaloshinskii-Moriya interaction in a heavy-metal | magnetic-insulator bilayer". In: *Phys. Rev. B* 105 (18 May 2022), p. 184417. DOI: 10.1103/PhysRevB.105.184417. URL: https://link.aps.org/doi/10.1103/PhysRevB.105.184417.

[12] J. Solano et al. "Spin-wave study of magnetic perpendicular surface anisotropy in single crystalline MgO/Fe/MgO films". In: *Phys. Rev. Mater.* 6 (12 Dec. 2022), p. 124409. DOI: 10.1103/PhysRevMaterials.6.124409. URL: https://link.aps.org/doi/10.1103/PhysRevMaterials.6.124409.

[13] E. Burgos et al. "Surface pinning in ferromagnetic films with perpendicular anisotropy". In: *Phys. Rev. B* 83 (17 May 2011), p. 174417. DOI: 10.1103/PhysRevB.83.174417. URL: https://link.aps.org/doi/10.1103/PhysRevB.83.174417.

3

MICROMAGNETIC SIMULATIONS

ABSTRACT

This Chapter motivates and systematizes the use of micromagnetic simulations as an essential complement to analytics and experiment when realistic, non-ideal magnetic nanostructures are considered. In using the GPU-accelerated software MuMax3 as the core simulation platform, we discuss the discretization process, the exchange-length–based convergence criteria and the simulation protocols adopted for energy minimization, broadband excitation, and frequency-domain analysis. Post-processing yields amplitude/phase maps, FMR/BLS-like spectra, and dispersion relations (through space–time Fourier transforms). The role of boundary conditions in shaping demagnetizing fields, mode profiles, and switching dynamics is highlighted, together with guidelines for parameter sweeps and runtime–accuracy trade-offs. These elements define a robust and efficient simulation methodology used throughout this thesis work.

3.1 THE NECESSITY OF NUMERICAL SIMULATORS IN MODERN RESEARCH

Even the most elegant pen-and-paper derivations fall short as soon as one leaves the realm of textbook simplicity and tries to tackle real-world systems. In fact, the governing equations of physics - whether it is the Navier–Stokes equations of fluid dynamics or, not surprisingly, the Landau–Lifshitz–Gilbert equation (1.34) - are inherently nonlinear partial differential equations whose exact, closed-form solutions exist only for the most idealized geometries and boundary conditions. The investigation of a patterned nanostructure, an irregular device interface or a material with varying properties from one region to another cannot be solved by hand calculations since the problem, due to its complexity, rapidly outstrips our mental resources. Furthermore, to make matters worse, a pen-and-paper-only analysis has to sacrifice either spatial resolution or physical realism, glossing over localized phenomena such as domain-wall pinning at defects or the precise shape of spin-wave modes in three-dimensional networks. On the contrary, practical devices span an enormous range of length scales, from the nanometer-scale exchange length in a magnetic film to millimeter-scale structures in integrated circuits. Despite not covered in this thesis work, the addition of thermal effects represents another challenge for our capabilities: the introduction of stochastic thermal noise converts a deterministic dynamical equation into a stochastic differential equation whose full probability distributions can only be obtained by running thousands, even millions, of Monte Carlo or Langevin trajectories. Such extensive sampling is computationally intensive and cannot realistically be performed without automated numerical methods.

Beyond the mathematical issues mentioned above, modern research usually demands the exploration of several parameter as well as their combinations - varying magnetic field strengths, anisotropy constants, temperature, geometry and material properties - in order to optimize device performance. The automation of these continuous parameter changes on CPUs (Central Processing Units) or GPUs (Graphics Processing Units) makes it possible to handle a combinatorial workload that would be unattainable with old school procedures. At the same time, numerical simulators deliver powerful visualization and post-processing tools: time-resolved three-dimensional magnetization textures, frequency-domain spectra via fast Fourier transforms, animated propagation of waves or switching events. Such massive graphical output is essential both for interpreting physical mechanisms and for presenting results in the best guise; no hand-drawn sketch could ever convey the same level of details to any extent. The iterative loop - design, simulate, compare with experiment, refine, and re-simulate - is now standard practice in device engineering. Whether the development of spin-transfer-torque memories, magnonic crystals or skyrmion-based logic gates, only a numerical simulator can validate theoretical concepts, benchmark against known analytic limits and ensure close agreement with experimental observations, all within a timescale compatible with academic research as well as industrial sector. Computational simulators combine mathematical generality,

computational speed, geometric flexibility [1, 2] and the ability to treat complex, multiscale and stochastic phenomena in a way that pen and paper alone, despite still fascinating, worthy of consideration and often representing the starting point of a thorough investigation, simply cannot match. In this regard, all the investigations within this thesis work have been conducted by using the software MuMax3; its principles of operation will be explained in Sec. 3.2. As for post-processing and data analysis, the software package MATLAB (The MathWorks, Natick, MA, USA) [3] was employed.

3.2 MUMAX3

MuMax3 is an open source program devoted to micromagnetic simulations [4]. It has been developed at Ghent University by the DyNaMat group leaded by Prof. Van Waeyenberge. Unlike the widely-applicable OOMMF (Objected Oriented MicroMagnetic Framework) [5], which is a CPU-based micromagnetic solver, MuMax3 is a GPU-accelerate program based on NVIDIA GPU architecture. It is capable of the speedup of computation compared to OOMMF and suits the demanding numerical evaluation of magnetization dynamics in the present work. MuMax3 makes use of a *finite-difference discretization* approach to solve the magnetization dynamics given by the time evolution of the Landau-Lifshitz-Gilbert equation (1.34) and represents a suitable framework to study ferromagnetic resonance as well as propagating spin waves. When the focus instead is on static problems and, as a consequence, one wants to obtain the magnetization ground state, MuMax3 provides a function to minimize the system energy while disabling the precession term of Landau-Lifshitz-Gilbert equation, thus recovering Landau-Lifshitz equation (1.26).

The finite-difference discretization method, used to compute the spatial and temporal dynamics of the magnetization, consists in dividing the system volume into a set of orthorhombic (or cuboidal) cells whose typical dimensions are on the order of a few nanometers. For completeness, an alternative is the *finite-element discretization*, in which the computational domain is partitioned into a large number of discretization elements forming an arbitrarily shaped volumetric mesh. Although feasible, this method is generally less efficient than the finite-difference approach in terms of computational cost, ease of setup and implementation, and with respect to the typical target applications of MuMax3, which usually rely on cells of uniform size. For these reasons, MuMax3 and its finite-difference-based strategy are generally preferred. The main limitation of this approach lies in the more complicated treatment of curved structures: in fact, due to the discretization procedure, the so-called *staircasing* occurs (see Fig. 3.1). It is an effect resulting in a spurious local anisotropy at the curved sections. In order to mitigate the staircase phenomenon, one may use smaller cell sizes or finite element discretization at the cost of introducing more computational burdens. However, since the effort in terms of memory and time would be almost impracticable in some cases, a reasonable compromise between the complete attenuation of the artifact and the onerous demand for the machine is often sought,

as indeed done systematically in this work, e.g., in Chapter 5 with regard to the discretization of the primitive cell.

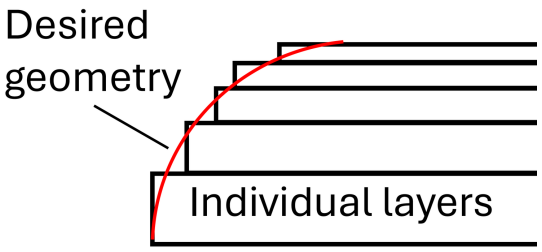

Figure 3.1: Illustration of the staircase effect arising from layer-wise discretization of a curved geometry.

MuMax3 offers a broad suite of tunable parameters. Consequently, the fidelity of any study hinges on understanding how each input choice propagates into the final result. This is especially true when adopting settings that shorten runtimes: if a given strategy produces negligible changes in the outcome, then one can justify more cost-effective simulation design decisions. Such trade-offs become decisive in campaigns that repeat nominally identical runs over wide sweeps of field magnitude and orientation, while maintaining the frequency and spatial resolution required to resolve subtle structure in, e.g., ferromagnetic resonance spectra. Delineating the solver regime of validity is also crucial. For exchange-dominated dynamics, the discretization must be chosen with cell dimensions smaller than the material exchange length; otherwise, short-wavelength physics is under-resolved. Conversely, studies targeting edge-localized states often demand even finer meshing near boundaries to capture geometry faithfully. In short, systematic parameter exploration should proceed hand-in-hand with convergence checks and problem-specific mesh criteria to ensure that speedups do not come at the expense of physical accuracy.

Material parameters are assigned, by means of look up tables, to each cell based on a region number between 0 and 255. This means that the maximum number of distinct regions that can be defined is 256, indexed from 0 to 255. Volumetric quantities (e.g. saturation magnetization, effective field) are stored in a matrix of 256 entries, while coupling parameters (such as the exchange interaction) are organized in a triangular matrix. This design provides an efficient strategy for memory conservation. Such a limitation is not arbitrary but arises from the internal data structure of the code since each simulation cell stores only an 8-bit integer as its region identifier, which allows for $2^8 = 256$ possible values. In practice, this number is generally sufficient, since even complex geometries rarely require more than a few dozen distinct material types (for example, in this thesis work, even if the systems investigated are complex, especially the directional coupler with the implementation of the STIRAP protocol in Chapter 7, we never exceeded 30 regions). For cases involving larger variations, one typically consolidates similar materials within the same region and introduces parameter gradients or spatial masks to reproduce the desired inhomogeneity without exceeding the region limit. In general, in MuMax3, the different types of geometries are realized by means of functions that undergo translations, rotations and Boolean operations in order to form the desired samples. Furthermore, the

user can import image files, also known as *bitmaps*, to set a specific geometry: the advantage is concrete when running multiple simulations, as the geometry calculation needs to be performed only once. An example of this approach is shown in Fig. 3.2. In this case, a complex geometry that would be difficult to define analytically, is generated directly from a bitmap. The imported image is first converted into the corresponding discretized sample in MuMax3, and then the system is relaxed to obtain the ground state configuration of the magnetization.

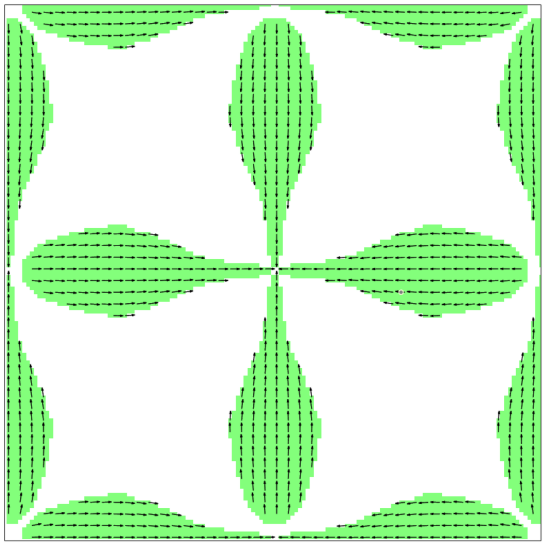

Figure 3.2: Ground state magnetization configuration in MuMax3 for a complex geometry defined via bitmap. The different elements of the structure are entirely specified by the input image. The arrows are averages of the magnetization out of 3 elemental cells, indicating the direction of the local magnetization.

Before delving into the details related to simulations, let us shortly discuss the management of simulation outputs. After performing micromagnetic simulations, data are typically saved in "OVF" data format and are converted to a MATLAB readable format using different codes and scripts depending on the physical quantity under investigation. According to the specific needs, different post-processing strategies can be employed in order to visualize the resulting dynamics. For instance, by evaluating the complex response on a pixel-by-pixel basis at each excitation frequency, one obtains spatial maps of amplitude and phase. These maps reveal the mode profiles [6], i.e., how the oscillations are distributed across the sample at a given frequency. It is also possible to integrate the power density over the entire sample in order to obtain a single spectral value per frequency [7]. This procedure yields resonance spectra that can be directly compared with experimental measurements such as FMR [8] or BLS [9]. Furthermore, if the data are spatiotermporal Fourier-transformed [10], one can also extract dispersion relations $\omega(\boldsymbol{k})$.

Since in this thesis work different systems are investigated, we refer the reader to Chapters 4, 5, 6 and 7 for detailed information on each numerical investigation. Here, the general aspects related to micromagnetic simulations are discussed, which serve as a background for subsequent considerations.

The numerical micromagnetic simulations carried out in this thesis work were performed on high-performance computing (HPC) facilities provided by the University of Ferrara, the Consorzio Interuniversitario del Nord-Est per il Calcolo Automatico, also known as CINECA (at the Bologna technopole) and the University of Colorado | Colorado Springs. See Sec. 3.3 for further information.

3.2.1 *Energy minimization procedure*

As anticipated in 3.2, in order to obtain the ground state of a system, MuMax3 seeks the configuration of minimum energy. This is achieved by suppressing the precessional dynamics in Eq. (1.34) through the choice of a damping parameter equal (or close) to unity, thereby forcing the magnetization to relax directly along the gradient of decreasing energy until convergence at the numerical noise floor. Near equilibrium, the torque magnitude decays monotonically and, since torque provides a less noisy indicator than the energy itself, the minimization routine uses it as the primary convergence criterion. It is worth briefly discussing the possible convergence of the minimization procedure to a saddle point or a flat region of the energy landscape. This is particularly relevant in hysteresis simulations where the `minimize()` command is employed to relax the system into a local minimum, especially if the applied field is aligned with a high-symmetry axis of the geometry. A common strategy to mitigate this issue is to tilt the applied field slightly away from the symmetry axis. In some cases, the algorithm may produce an unphysical antiferromagnetic arrangement, with neighboring cells aligned antiparallel. Although this configuration reduces the overall energy due to vanishing net magnetization, it is clearly spurious in simulations of purely ferromagnetic materials without interlayer antiferromagnetic coupling (e.g. RKKY interactions). Re-running the simulation typically restores a physically consistent ferromagnetic state. Other instances of convergence to spurious local minima or saddle points may be less apparent. These can manifest during angular-dependent hysteresis loops, where the magnetization reversal occurs unexpectedly earlier or later compared to adjacent angles. Such discrepancies often originate from stochastic numerical fluctuations in the energy evaluation. In these situations, repeating the simulation multiple times remains the most reliable method to ensure robust results.

3.2.2 *Excitation*

In our investigation, after the assegnation of geometry and material parameters, the sample is relaxed to a ground state or static magnetization at a specific field or after some applied field protocol in order to simulate FMR. Very often, a varying external field is applied to the system as a temporal sinc pulse in order to excite a broadband range of frequencies. In general, we have:

$$b(t) = b_0 \frac{\sin 2\pi f_{cutoff}(t - t_0)}{2\pi f_{cutoff}(t - t_0)}, \tag{3.1}$$

where each term has a specific physical meaning:

- $b(t)$: it is the instantaneous value (T) of the external magnetic field applied to the system. In MuMax3, it typically enters through the time-dependent vector B_{ext}, for example as $B_{ext} = Vector(0, 0, b(t))$ if the field is applied along the z axis.

- b_0: this parameter sets the amplitude of the excitation. At $t = t_0$, the sinc function satisfies $\lim_{x\to 0} \sin(x)/x = 1$, so that $b(t_0) = b_0$. Therefore b_0 determines the peak strength of the applied field. For linear-response FMR measurements one usually keeps b_0 in the mT range (or smaller) in order to avoid nonlinear effects.

- $\sin(2\pi f_{\text{cutoff}}(t - t_0))$: the sinusoidal numerator provides the oscillatory structure of the sinc pulse. Unlike a monochromatic drive, the sinc function contains multiple oscillations whose envelope decays as $1/|t - t_0|$.

- f_{cutoff}: the cutoff frequency defines the effective bandwidth of the excitation. In the Fourier domain, the transform of the sinc pulse is (up to scaling factors) a rectangular function,

$$\mathcal{F}\{b(t)\}(f) \propto b_0 \,\text{rect}\left(\frac{f}{2f_{\text{cutoff}}}\right),$$

  which is flat for $|f| < f_{\text{cutoff}}$ and zero beyond.

- 2π: this factor converts the frequency f_{cutoff} into an angular frequency $\omega = 2\pi f$, ensuring that the argument of the sine function is dimensionless.

- $(t - t_0)$: this temporal shift centers the main lobe of the pulse at t_0. In practice, choosing t_0 slightly greater than zero ensures that the dominant peak of the excitation occurs after the solver has initialized, thus avoiding artifacts associated with the simulation start.

- $2\pi f_{\text{cutoff}}(t - t_0)$: the denominator normalizes the argument and produces the characteristic $1/(t - t_0)$ decay of the side lobes. It guarantees that the function is finite at $t = t_0$ (where the value is set by the limiting process) and that the total spectral energy of the excitation remains bounded.

It can be noted that Eq. (3.1) vanishes whenever $t = t_0 \pm n/f_{\text{cutoff}}$ with $n \in \mathbb{N}$, marking the boundaries between side lobes in the time domain. In the frequency domain, these correspond exactly to the sharp edges of the rectangular spectrum. From a physical perspective, the sinc pulse represents an ideally broadband, band-limited excitation: it is temporally localized around t_0 while efficiently exciting all modes up to the chosen cutoff frequency. This makes it particularly powerful for micromagnetic simulations: instead of running multiple simulations with single-frequency sinusoidal drives, one can apply a single sinc pulse and subsequently Fourier transform the system response to extract the resonance modes. In MuMax3 this approach is widely used to compute FMR spectra, spin-wave dispersion relations, or to probe localized eigenmodes of nontrivial textures such as skyrmions and domain walls.

3.2.3 *Sampling, Nyquist constraint and the choice of dt and t_{tot}*

In micromagnetic simulations, as well as in time-domain micromagnetic spectroscopy, the magnetization signal is recorded as a discrete time series in order to estimate its frequency content via Fourier transform. Let $s(t)$ denote a scalar observable extracted from the simulation (for instance, the spatial average $\langle m_x(t)\rangle$). MuMax3 produces samples of the type:

$$s[n] \equiv s(n\,dt), \qquad n = 0, 1, \ldots, N-1,$$

at regular intervals dt for a total observation time $t_{\mathrm{tot}} = N\,dt$. The sampling frequency is $f_s = 1/dt$ and the associated Nyquist frequency is $f_{\mathrm{Nyq}} = \frac{f_s}{2} = \frac{1}{2\,dt}$. According to the sampling theorem, first introduced by Nyquist and later rigorously formalized by Shannon [11], if the continuous-time spectrum $S(f)$ of $s(t)$ is strictly limited to $|f| \leq f_{\max}$, then perfect reconstruction from samples is possible provided $f_s > 2f_{\max}$, i.e. $f_{\mathrm{Nyq}} > f_{\max}$. Since, as already explained in Sec. 3.2.2, in the broadband excitation protocol described in Eq. (3.1) the ideal drive has a rectangular spectrum which is flat for $|f| < f_{\mathrm{cutoff}}$ and zero beyond, it is convenient to choose the sampling interval dt so that the Nyquist frequency equals or exceeds the excitation bandwidth, namely:

$$f_{\mathrm{Nyq}} \equiv \frac{1}{2\,dt} \gtrsim f_{\mathrm{cutoff}}. \quad \rightarrow \quad dt \lesssim \frac{1}{2\,f_{\mathrm{cutoff}}}.$$

In this way, at the level of the recorded time series, no spectral content intentionally injected by the source will alias back into the baseband. Instead, any content above the Nyquist frequency $f_{\mathrm{Nyq}} = 1/(2dt)$ will fold back as aliasing. Since a sinc excitation ideally limits the drive to f_{cutoff}, one must enforce $f_{\mathrm{Nyq}} \gtrsim f_{\mathrm{cutoff}}$. In practice, truncation of the sinc in time and weak nonlinear responses introduce small spectral weight beyond f_{cutoff}. It is therefore preferable to adopt a guard factor $\beta > 1$ so that:

$$dt \lesssim \frac{1}{2\beta f_{\mathrm{cutoff}}}, \qquad f_{\mathrm{Nyq}} = \beta f_{\mathrm{cutoff}},$$

thereby reducing aliasing at negligible computational cost.

It is important to distinguish between the internal integration step dt_{int}, controlled by `MaxDt`, and the output sampling step dt set by `TableAutoSave`. The Nyquist criterion applies to the latter, while the former must remain much smaller than the fastest torque timescale $\sim 1/(\gamma\mu_0 H_{\max})$ to guarantee accurate trajectories. In practice, the integration of the Landau-Lifshitz-Gilbert equation (1.29) is carried out by the Dormand-Prince solver [12], an explicit Runge-Kutta method of order 5(4) (meaning that a fifth-order accurate solution is computed together with a fourth-order estimate, the latter being used to assess the local error and adapt the integration step). This high–order integrator provides both a solution estimate and an embedded error estimate at each step. While in adaptive mode the solver can vary its step size according to the local torque amplitude, in the context of spectral analysis one often disables adaptivity and enforces a fixed integration step dt_{int}. This ensures that the recorded time trace is equispaced

without the need for interpolation, which is essential for a mathematically consistent Fourier transform. The choice of a fixed step, however, must satisfy two conditions simultaneously: (i) dt_{int} must be small enough to resolve the fastest precessional motion, and (ii) dt_{int} must be consistent with the Nyquist requirement set by the chosen f_{cutoff}. In this sense, the Dormand-Prince method in fixed-step mode represents a compromise: one sacrifices some of the efficiency of adaptive stepping in exchange for the strict regularity of sampling required for frequency-domain analysis, while still retaining the superior accuracy per step of a high-order Runge-Kutta scheme.

The total observation time $t_{\text{tot}} = N\,dt$ sets the frequency bin width $\Delta f = 1/t_{\text{tot}}$, which determines spectral resolution. To resolve resonances of linewidth Γ, one requires $\Delta f \ll \Gamma$; hence t_{tot} must be several times larger than the inverse linewidth. Windowing reduces spectral leakage introduced by the finite observation interval, while zero-padding merely interpolates the discrete Fourier spectrum, increasing visual smoothness without altering the actual frequency resolution. A concrete guideline is the following:

- choose dt from the bandwidth requirement with $\beta \simeq 1.2$–2;
- set t_{tot} such that Δf is comfortably below the expected linewidth;
- verify that the integrator step dt_{int} chosen for the Dormand–Prince solver is at least one order of magnitude smaller than $1/(2\pi f_{\text{cutoff}})$, ensuring both numerical stability and spectral fidelity.

With this combination, the recorded magnetization time series provides an alias-free, well-resolved basis for Fourier analysis of FMR spectra and spin-wave modes.

Let us conclude this section with an illustrative numerical example: suppose the excitation bandwidth is $f_{\text{cutoff}} = 20$ GHz. The borderline choice $dt = 1/(2f_{\text{cutoff}}) = 25$ ps yields $f_{\text{Nyq}} = 20$ GHz and only two samples per oscillation at the band edge, which is fragile against leakage. A safer choice with $\beta = 1.5$ sets $dt = 1/(2\beta f_{\text{cutoff}}) \approx 16.7$ ps and $f_{\text{Nyq}} = 30$ GHz. If the expected resonance linewidth is $\Gamma \approx 50$ MHz, does it make sense to take, e.g., $t_{\text{tot}} \geq 0.1$ ms? No, that would be excessive. Since $\Delta f = 1/t_{\text{tot}}$, it is reasonable to choose $t_{\text{tot}} = 50$ ns to achieve $\Delta f = 20$ MHz, comfortably smaller than Γ and compatible with typical GPU runtimes. This produces $N = t_{\text{tot}}/dt \approx 3{,}000$ samples, sufficient to obtain a smooth, reliable spectrum when combined with the fixed-step Dormand-Prince integration scheme.

3.2.4 *Cell size*

The spatial discretization of the magnetization field on a regular mesh is a crucial aspect of micromagnetic simulations since all effective fields are ultimately evaluated on cell averages. In particular, phenomena dominated by exchange interactions impose strict requirements on the cell size. The relevant length scale is the exchange length λ_{ex}, already introduced in Chapter 1 and defined as $\lambda_{ex} = \sqrt{\frac{2A_{\text{ex}}}{\mu_0 M_s^2}}$. It sets the natural length over which magnetization textures vary smoothly. In order for the numerical discretization to provide an

accurate representation of the continuum theory, the linear cell size Δr must remain smaller than the characteristic exchange length λ_{ex}: in fact, if $\Delta r > \lambda_{ex}$, the discretized exchange field may fail to connect smoothly across adjacent cells, producing artificial discontinuities or suppressing short-wavelength modes. Hence, the conservative criterion is: $\Delta x, \Delta y, \Delta z \lesssim \lambda_{ex}$, so that the mesh can resolve the intrinsic exchange-driven curvature of $\boldsymbol{M}(\boldsymbol{r})$ (an even stricter criterion, i.e., $\Delta r \leq \frac{1}{2}\lambda_{ex}$, is sometimes adopted when simulating strongly inhomogeneous structures such as domain walls and skyrmions, ensuring that these textures span at least several cells). These considerations apply in particular for exchange-dominated phenomena, such as short-wavelength spin waves, vortex core dynamics, or domain-wall internal structure. The failure to resolve λ_{ex} in such cases would suppress key modes and distort the energy balance. However, not all excitations require the same spatial resolution. Magnetostatic spin waves and FMR are largely governed by dipole–dipole interactions, which act on micrometer scales. In such dipolar-dominated regimes, it is acceptable to use cell sizes somewhat larger than λ_{ex}, thus alleviating computational cost, without significant loss of accuracy, because the critical features of the magnetization vary slowly. As can be inferred from the definition, λ_{ex} is material dependent because it involves the exchange stiffness A_{ex} and the saturation magnetization M_S. For instance, this work focuses on two widely used soft magnetic materials, i.e., permalloy ($Ni_{80}Fe_{20}$), abbreviated as Py, and yttrium iron garnet ($Y_3F_5\ O_{12}$), abbreviated as YIG; the corresponding exchange lenghts are $\lambda_{ex}^{\mathrm{Py}} \approx 5.7\,\mathrm{nm}$ and $\lambda_{ex}^{\mathrm{YIG}} \approx 12\,\mathrm{nm}$. These values imply that, for accurate simulations, the cell size must be chosen accordingly. For example, simulating Py nanostructures with $\Delta r = 10\,\mathrm{nm}$ would be inadequate for exchange-dominated dynamics, while the same discretization is acceptable for YIG due to its larger exchange length, and this is exactly what has been done in the investigation regarding the directional coupler in Chapter 7.

Clearly, the choice of discretization cannot be separated from the assessment of computational feasibility. The number of cells scales as $N = N_x N_y N_z$ and the cost per integration step scales approximately as $\mathcal{O}(N \log N)$ because the demagnetizing field is computed via Fast Fourier Transforms (FFTs). Reducing the cell size by a factor of two in all dimensions increases the number of cells by a factor of $2^3 = 8$, quickly inflating memory and runtime requirements. For large samples or long-time dynamics, it is compulsory to balance accuracy against tractability. Before submitting large-scale jobs to HPC clusters, it is essential to estimate runtimes and memory footprints, possibly via smaller test runs, to ensure resources are used efficiently.

3.2.5 *Periodic boundary conditions*

Periodic boundary conditions (PBC) replace a finite sample by an infinite tiling of identical simulation boxes along one, two, or three directions, restoring translational invariance and suppressing edge effects in those directions. In other words, they treat the magnetization as continuous across opposite boundaries In MuMax3. This is implemented by accounting for the dipolar fields generated by a finite set of

replicated cells beyond the simulation domain. PBC are requested via `SetPBC(nx,ny,nz)`, where the integers `(nx,ny,nz)` control the number of periodic repetitions accounted for in the demagnetostatic lattice sum. If `SetPBC(0,0,0)` is set, the system is left open with no periodic copies, which is appropriate for finite devices where edges and shape anisotropy are essential.

The demagnetizing field is computed as the convolution of the magnetization $\boldsymbol{M}(\boldsymbol{r})$ with a demagnetizing tensor kernel $\mathsf{N}(\mathbf{r})$. On a uniform mesh this becomes a discrete convolution that is evaluated efficiently in Fourier space using FFTs. In systems without PBC, i.e., with open boundaries, N is the free-space demagnetizing kernel of a single, isolated computational box. Under PBC, N is replaced by a lattice-summed kernel that accounts for the magnetostatic field created by all periodic replicas of the simulation box. Operationally, MuMax3 precomputes the appropriate $\widehat{\mathsf{N}}(\boldsymbol{k})$ for the chosen periodicity and then uses it in the usual $\boldsymbol{k}$-space multiplication.

The integers `(nx,ny,nz)` specify how many periodic image boxes are included in this lattice sum along each direction. They do not change the physical periodicity, they only control the convergence of the demagnetizing field toward the infinite lattice limit. Convergence must always be checked by increasing `(nx,ny,nz)` until relevant observables (e.g., energy density, equilibrium state, resonance frequencies) stop changing within the desired tolerance. If the simulation box is too small under PBC, artificial self-interaction between a texture and its own periodic images can occur.

Short-range micromagnetic fields such as exchange are treated differently. With PBC, spatial derivatives are evaluated using wrap-around finite differences: a neighbor across a periodic boundary is taken from the corresponding cell in the replicated box. With open boundaries, the finite-difference stencil is truncated at the sample edge, so derivatives do not probe beyond the physical domain. In this way free boundary conditions are imposed. Therefore, "open" and "periodic" boundaries are not merely numerical choices: they represent distinct physical situations (isolated finite element vs. infinite repetition of a unit cell).

In practice, PBC are typically used to model extended media and bulk-like physics (e.g., an effectively infinite film, an infinitely long strip or wire, a skyrmion crystal without edge pinning), while open boundaries are essential to capture device edges, end charges and nucleation at physical terminations. Some recurring situations are presented below.

- **Magnetostatics.** For an isolated (open) body, surface and edge magnetic charges generate stray fields that favor flux closure and give rise to shape anisotropy. For instance, a long and narrow strip with open ends tends to align $\boldsymbol{M}$ along its axis to avoid creating magnetic poles at the two ends; its effective demagnetizing tensor is strongly geometry dependent. Under PBC along the strip direction (x), those end charges are removed by construction, and the system mimics an infinitely long waveguide with translational symmetry along x. Similarly, applying PBC in x and y emulates an extended film; in the ultrathin limit the demagnetizing factors approach $(N_x, N_y, N_z) \to (0, 0, 1)$, i.e. in-

plane components are weakly penalized while the out-of-plane component is strongly opposed. In that case, edge-induced flux-closure domains are suppressed because there are no physical edges in-plane.

- **Equilibrium states and magnetic textures.** Open boundaries allow for closure patterns at the sample edges, curling at corners, and the chiral boundary canting imposed by interfacial DMI through its natural boundary conditions. PBC remove these edge-specific features: a domain wall does not terminate at a free surface but instead repeats periodically, skyrmions do not "feel" a literal device edge, and DMI-induced edge twists are suppressed. As a consequence, PBC are well suited to study bulk textures such as Bloch or Néel walls in the middle of a track, helices, and skyrmion lattices, as well as intrinsic domain periods unperturbed by edges. Conversely, open boundaries are mandatory to capture nucleation at real notches or corners, depinning at device edges, and other edge-localized phenomena.

- **Spin waves and spectroscopy.** With PBC along a direction of length L_α, translational invariance enforces discrete wavevectors $k_\alpha = 2\pi n_\alpha / L_\alpha$ with $n_\alpha \in \mathbb{Z}$. This enables a clean extraction of dispersion relations after performing space-time FFTs; the system behaves as an infinite waveguide or film along that periodic direction. In contrast, an open system supports standing-wave modes and edge modes. Its spectrum reflects reflections at the boundaries and the free-boundary quantization of the dynamic magnetization. Practically, the FMR spectrum of a PBC film resembles the familiar Kittel-like uniform mode plus bulk Damon-Eshbach / backward-volume branches, whereas an open platelet exhibits additional edge-localized resonances and inhomogeneous broadening due to nonuniform demagnetizing fields.

- **Coercivity and switching.** PBC eliminate end charges and remove obvious nucleation sites. As a result, switching fields computed under PBC probe intrinsic barriers such as coherent rotation or the propagation of a domain wall along an infinitely long track. Open boundaries generally lower the switching barrier, because reversal can start at an edge via curling or wall nucleation and then propagate inward; this better represents patterned devices with finite length, notches, or corners. Thus, PBC may overestimate coercivity and underestimate depinning from lithographic defects, while purely open simulations may underestimate the mobility of walls in truly extended media (due to reflections from the finite ends).

To sum up, the boundary condition must mirror the experimental geometry and the magnetic phenomenon of interest. PBC in-plane are appropriate when modeling extended films for FMR or spin-wave dispersion, infinite waveguides for guided magnonics, or periodic textures such as helices and skyrmion lattices. Open boundaries are essential whenever device edges, corners, and terminations play a direct role, e.g., in switching by edge nucleation, depinning at

notches, or edge-localized chiral twists (interfacial DMI), as well as when modeling magnetostatic coupling to nearby structures with non-periodic spacing.

A common practical compromise in strip/waveguide geometries is to impose mixed boundary conditions, e.g., `SetPBC(1,0,0)`: the system is periodic along the nominal propagation direction (avoiding artificial end reflections and enforcing a well-defined k_x), but open across the confined width, so that the lateral quantization and demagnetizing pinning at the physical edges are retained. This reproduces the correct width-dependent mode profiles without introducing spurious standing waves at the waveguide ends.

3.3 ACKNOWLEDGEMENT OF COMPUTATIONAL RESOURCES

The author gratefully acknowledges the availability of advanced high-performance computing facilities that have been essential for the development, testing, and optimization of the numerical simulations and algorithms discussed in this thesis work.

- In particular, the Computing On Kepler Architectures (COKA) cluster, funded by the University of Ferrara with the support of Istituto Nazionale di Fisica Nucleare (INFN), has provided fundamental computational support. COKA consists of four computing nodes, each equipped with dual 8-core Intel Xeon processors and eight NVIDIA K80 accelerator cards, with two GPUs per card. The nodes are tightly interconnected through two high-bandwidth interfaces to an InfiniBand switched network, enabling efficient low-latency communication. The theoretical peak performance of the system is on the order of 100 Tflops. The cluster is primarily devoted to supporting research activities in computational physics, large-scale numerical simulations, and the design and optimization of parallel algorithms, and has been a critical resource for the work carried out by the research groups of the University of Ferrara and INFN.

- Additional computational resources have been provided by the LEONARDO supercomputer, a pre-exascale Tier-0 EuroHPC system hosted by Cineca at the Bologna Technopole. LEONARDO is ranked seventh among the most powerful supercomputers worldwide according to the Top500 list. Supplied by ATOS, the system is organized into two main partitions: the *Booster Module* and the *Data-centric Module*. The Booster Module is based on BullSequana XH2135 nodes, each equipped with four NVIDIA Tensor Core GPUs and a single Intel CPU, while the Data-centric Module is built on BullSequana X2140 three-node CPU blades, each featuring two Intel Sapphire Rapids CPUs with 56 cores per processor. The overall architecture employs NVIDIA Mellanox HDR 200 Gb/s InfiniBand connectivity, enhanced with smart in-network computing acceleration engines. This infrastructure ensures extremely low latency and high throughput, thereby delivering outstanding performance and scalability for both high-performance computing and artificial intelligence workloads.

- Finally, complementary simulations have been carried out on Prof. Ezio Iacocca's local high-performance computing cluster at the University of Colorado | Colorado Springs. This system is based on a set of compute nodes each hosting an NVIDIA RTX 3090 Ti GPU with 24 GB of GDDR6X memory, paired with high-frequency multi-core CPUs and 128 GB of system RAM. The nodes are interconnected via a high-speed Ethernet fabric, ensuring efficient data transfer for medium-scale workloads. This cluster has been particularly valuable for code debugging, preliminary testing, and parameter sweeps, thereby serving as an essential complement to large-scale production runs on COKA and LEONARDO.

BIBLIOGRAPHY

[1] M. Dvornik, Y. Au, and Volodymyr Kruglyak. "Micromagnetic Simulations in Magnonics". In: vol. 125. Jan. 2013, pp. 101–115. ISBN: 978-3-642-30246-6. DOI: 10.1007/978-3-642-30247-3_8.

[2] Claas Abert. "Micromagnetics and spintronics: models and numerical methods". In: *The European Physical Journal B* 92.6 (2019), p. 120. ISSN: 1434-6036. DOI: 10.1140/epjb/e2019-90599-6. URL: https://doi.org/10.1140/epjb/e2019-90599-6.

[3] Cleve Moler. *Introduction to MATLAB*. Tech. rep. Accessed: 2025-10-25. University of New Mexico and The MathWorks, Inc., 2004. URL: https://www.mathworks.com/content/dam/mathworks/mathworks-dot-com/moler/intro.pdf.

[4] Arne Vansteenkiste et al. "The design and verification of MuMax3". In: *AIP Advances* 4.10 (2014), p. 107133. DOI: 10.1063/1.4899186.

[5] M. J. Donahue and D. G. Porter. *OOMMF User's Guide, Version 1.0*. Tech. rep. NISTIR 6376. Gaithersburg, MD: National Institute of Standards and Technology, Sept. 1999. URL: http://math.nist.gov/oommf.

[6] Pietro Micaletti and Federico Montoncello. "Dynamic Footprints of the Specific Artificial Spin Ice Microstate on Its Spin Waves". In: *Magnetochemistry* 9.6 (2023). ISSN: 2312-7481. DOI: 10.3390/magnetochemistry9060158. URL: https://www.mdpi.com/2312-7481/9/6/158.

[7] G. Gubbiotti et al. "Spin dynamics in thin nanometric elliptical Permalloy dots: A Brillouin light scattering investigation as a function of dot eccentricity". In: *Physical Review B* 72.18 (2005), p. 184419. DOI: 10.1103/PhysRevB.72.184419.

[8] M. B. Jungfleisch et al. "Dynamic response of an artificial square spin ice". In: *Physical Review B* 93.10 (2016), p. 100401. DOI: 10.1103/PhysRevB.93.100401.

[9] Thomas Sebastian et al. "Micro-focused Brillouin light scattering: imaging spin waves at the nanoscale". In: *Frontiers in Physics* Volume 3 - 2015 (2015). ISSN: 2296-424X. DOI: 10.3389/fphy.2015.00035. URL: https://www.frontiersin.org/journals/physics/articles/10.3389/fphy.2015.00035.

[10] B. Van de Wiele and F. Montoncello. "A continuous excitation approach to determine time-dependent dispersion diagrams in 2D magnonic crystals". In: *J. Phys. D: Appl. Phys.* 47 (2014). 10.1088/0022-3727/47/31/315002, p. 315002.

[11] Claude E. Shannon. "Communication in the Presence of Noise". In: *Proceedings of the IRE* 37.1 (1949), pp. 10–21. DOI: 10.1109/JRPROC.1949.232969.

[12] John R. Dormand and Peter J. Prince. "A Family of Embedded Runge–Kutta Formulae". In: *Journal of Computational and Applied Mathematics* 6.1 (1980), pp. 19–26. DOI: 10.1016/0771-050X(80)90013-3.

4

SINUSOIDAL MAGNETIZATION DISTRIBUTION FOR EFFICIENT MAGNON PROPAGATION

ABSTRACT

Manipulating the magnetization of a thin film at the nanoscale is among the most effective routes to real-time control of spin-wave propagation. Within 3D Magnonics, vertical or interfacial coupling to patterned layers can drive the film magnetization away from uniformity; in general, this introduces additional spin-wave modes and thus extra degrees of freedom for signal manipulation. In this work, we propose a sinusoidal magnetization distribution as an original and effective means to create a magnonic crystal and steer its magnon dynamics. Together with a uniform bias field, we apply a sinusoidal bias field within the film layer to emulate vertical/interfacial interactions with adjacent layers; after relaxation, the film attains a sinusoidal equilibrium magnetization. Using micromagnetic simulations followed by Fourier analysis, we demonstrate control of the magnon dynamics by tuning the amplitude and symmetry of the magnetization undulation. We compute magnon dispersion relations and spatial profiles, reveal the emergence of new degrees of freedom for signal processing, and observe localized and stationary magnon modes. We elucidate the physical mechanisms governing the onset and evolution of the zone-boundary frequency gap. Finally, we outline a practical implementation of a sinusoidal field (and the resulting magnetization) when the vertical coupling is provided by the inverse magnetoelastic interaction between ferroelectric and ferromagnetic films. Our results introduce a new mechanism for controlling magnon propagation, notable for its wide range of tunable effects on magnon dynamics, with particular relevance to engineered signal filtering, information storage and delivery, and sensing.

4.1 STATE OF THE ART. OVERVIEW

The study of spin-wave dynamics in periodically modulated ferromagnetic systems, known as *magnonic crystals*, can definitely be considered a central topic of interest in contemporary condensed matter physics and spintronics [1, 2]. The analogy with photonic crystals, where spatially periodic variations in refractive index lead to frequency gaps and tailored propagation of electromagnetic waves, has inspired several strategies to impose similar periodicity on magnonic systems [3]. Early work in this field investigated geometric patterning of thin films, typically through lithographic techniques, in order to realize periodic arrays of magnetic wires, thickness-modulated strips and antidot lattices [4]. The study of these systems revealed the existence of magnonic band gaps, mode folding at the Brillouin zone boundaries as well as the possibility of tailoring spin-wave propagation by structural design [5]. However, in this preliminary stage, there was an intrinsic lack of reconfigurability since, once patterned, the magnetic microstructure was frozen and the band structure essentially immutable.

Later, a different line of research has explored the possibility of inducing periodicity in alternative ways: the sample geometry was no longer changed, but instead external fields or interfacial interactions were superimposed on the system [6]. In other words, in such "field/texture-imprinted" magnonic crystals, the underlying magnetic medium remains physically continuous and unpatterned, while the equilibrium magnetization adopts a periodically modulated configuration under the action of some external or interfacial agent. In this regard, some examples include the use of standing magnetic fields generated by current lines, periodic strain fields coupled through magnetoelastic interactions and shape-induced magnetic anisotropy to stabilize remanent states [7]. These approaches are extremely flexible because the periodic modulation can in principle be switched, tuned, or reoriented dynamically, thereby enabling reconfigurable magnonic devices.

Within this general context, our recent proposal of employing a *sinusoidal magnetization distribution* as the equilibrium state of a ferromagnetic film represents a conceptually significant step forward. Rather than patterning the magnetic layer into a physically periodic structure, the magnetization itself is allowed to relax into a smoothly varying, nearly sinusoidal profile along one spatial direction. This texture can be stabilized by applying a weak but spatially periodic bias field, for instance arising from interfacial interactions with an adjacent layer [8]. The crucial point is that such a sinusoidal configuration naturally produces a periodic modulation of the internal effective field experienced by magnons. As a result, propagating spin waves undergo Bragg scattering at reciprocal lattice vectors of the modulation, which in turn opens band gaps at the Brillouin-zone edges. In other words, the sinusoidal state defines a magnonic crystal in which the undulated magnetization plays the role of the periodic background. Crucially, we identify the *amplitude* of the undulated magnetization as an independent, continuously tunable parameter that functions as a new degree of freedom for magnon manipulation. The amplitude

control is achieved by adjusting the strength and phase of the stabilizing sinusoidal field which engineer the magnonic response. This continuous parameter space makes it possible to reshape the magnonic band structure in a smooth and predictable manner: band gaps can be widened or closed, mode hybridization enhanced or suppressed and propagation directed - all within what is nominally still a uniform ferromagnetic film. The engineered magnetization texture thus acts as an effective potential for magnons, influencing their dispersion, scattering channels and transmission properties.

From a theoretical standpoint, the sinusoidal state provides a particularly clean and analytically tractable background. The sinusoidal character of the modulation also limits the complexity of inter-mode coupling, thereby offering a controlled playground for fundamental studies. In addition, it furnishes an ideal reference limit against which more complex or distorted periodic textures can be compared. Once this reference is understood, one can systematically incorporate further features - such as interfacial Dzyaloshinskii–Moriya interaction, non-collinear anisotropies, or weak field gradients - and directly assess how they deform the underlying magnonic band structure.

Building on this idea, this thesis work investigates, proposes, and validates a versatile strategy to tailor and control magnon transport in ferromagnetic thin films by imprinting a spatially periodic, nanoscale *undulation* of the equilibrium magnetization. One may view the periodic bias field used to stabilize the sinusoidal state as the first practical route to create such a modulated ground state. This aspect is addressed in this Chapter, which revisits and presents the results reported in [9], and in Chapter 5. Then, in Chapters 6 and 7, we extend that philosophy by exploring vertical coupling mechanisms - in particular, *multiferroic coupling* - as a means to impose the same type of sinusoidal (or more generally periodic) magnetization landscape directly on an otherwise uniform ferromagnet. The ultimate purpose is to conceive magnonic devices with advanced functionalities, such as adaptive waveguides, tunable filters, and programmable spin-wave logic elements, operating entirely through engineered magnetization landscapes.

For completeness, we briefly summarize an alternative approach for controlling magnon transport, in particular through frequency-gap manipulation, that we have recently introduced, in which a magnonic system is engineered by a nanoscale sinusoidal modulation of the *exchange stiffness* [10]. The exchange modulation opens a magnonic band gap whose center frequency is shifted by an external magnetic field. A uniform field displaces the gap approximately linearly, whereas a localized offset applied to a central section realizes a reconfigurable "magnonic heterojunction" that selectively attenuates or transmits spin waves at a fixed carrier. Making the localized offset time dependent turns the heterojunction into a dynamic barrier that generates spin-wave packets and, in the nonlinear regime, a magnonic frequency comb.

4.2 INTRODUCTION

A key challenge in contemporary research is conceiving portable, multifunctional, and environmentally friendly devices [11, 12]. While miniaturization remains pivotal, over the past two decades it has become evident that below a certain scale the gains are offset by nanoscale chip overheating (due to electron scattering), which undermines efficiency and portability [13]. This, in particular, helps explain why current processor clock rates are nearly the same as twenty years ago [12]. Moreover, mounting concerns about the carbon footprint of everyday devices underscore the urgency of alternatives to conventional electronics [14].

One promising route is to achieve data transfer and manipulation via SWs, which do not entail charge motion and therefore generate minimal waste heat [15, 16, 17]. In the GHz regime, SWs possess nanometric wavelengths and are thus well suited to miniaturized architectures. In practice, SW propagation can be tailored through Bragg diffraction by designing appropriate geometries in the ferromagnetic medium confining the waves [18, 19, 20, 21, 22, 23, 24, 25, 26, 27, 28]. More recently, thanks to improved fabrication methods, the study of SW physics has expanded to 3D platforms - periodic arrangements or stacks of layers with different geometries [29, 30, 31, 32] - revealing new possibilities such as reconfigurable SW microstate fingerprinting [33, 34, 35] and interlayer dynamic coupling [36, 37, 38, 39], both especially promising for controlling magnons at the nanoscale. The Dzyaloshinskii-Moriya interaction, which forms at interfaces with metal layers, can likewise be regarded as a vertical (interfacial) interaction [19, 40, 41]. This interfacial mechanism is particularly appealing because it can furnish a magnonic frequency comb for signal multiplexing [42] and can induce non-reciprocal dispersions and magnonic mode localization [43]. Furthermore, its dependence on electric fields enables a strain-mediated magnetoelectric coupling between layers [44], which is promising for voltage-driven SW dynamics. Of particular interest, in recent years several works have demonstrated the creation of a temperature-activated magnonic crystal in the film layer of a ferromagnet/superconductor hybrid metamaterial (e.g., an Nb/Permalloy/Nb trilayer), owing to stray fields (vertical coupling) generated by periodic superconducting structures upon entering the Meissner (diamagnetic) state at temperature $T < T_c \equiv 9\,\mathrm{K}$. The induced periodicity has been confirmed experimentally through the observation of band gaps at the zone boundary [45, 46, 47, 48].

In summary, within a 3D magnonic structure the top layer can act as a gate to control the periodicity, group velocity and phase of SWs. Among the various 3D configurations, a particularly attractive class consists of a ferromagnetic waveguide capped with a different layer that imprints and modifies SW properties via vertical coupling [43, 49]. In this context, computing the SW dispersion in a film with a *non-uniform magnetization* - arising from *vertical interaction* - is crucial: depending on the group velocity at a given wavevector and on the widths of allowed and forbidden bands, one can design devices with enhanced functionalities.

Our work addresses precisely this objective: we introduce a *sinusoidal magnetization distribution* as an original way to generate a magnonic crystal, and we show how its *symmetry* and *amplitude* govern key features of magnon dynamics - such as dispersion slope and curvature, the widths of allowed and forbidden bands, and the emergence of localized and stationary modes. We consider a film with a sinusoidal magnetization (Fig. 4.1) determined by an equally *sinusoidal bias field* [50], which we view as a simulation of a vertical (or interfacial) interaction resulting from the film being part of a 3D system with suitable geometry.

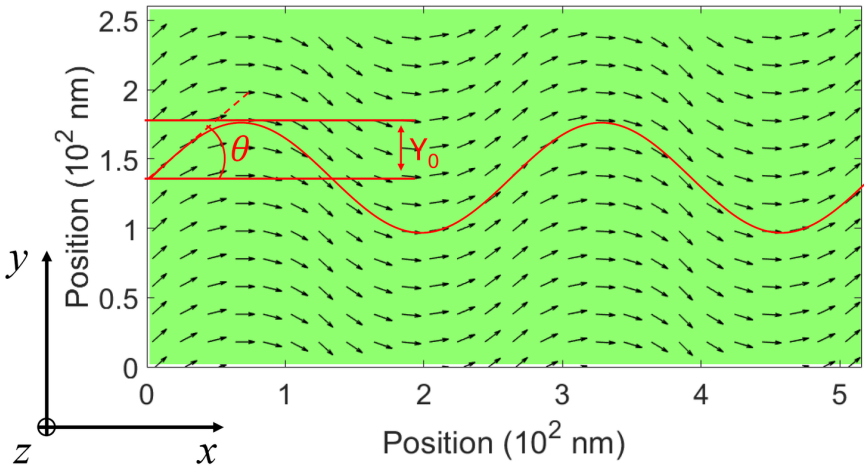

Figure 4.1: Generic ground state with a sinusoidal magnetization and the reference system. The angle $\theta \equiv \Theta_F/2$ is the slope of the magnetization at $x = 0$, while Y_0 is the spatial amplitude of the undulation, namely the maximum deflection from the ideal straight magnetization direction of an isolated film.

We present simulated dispersion relations $f(k)$ (i.e., frequency vs. wavevector) as a function of the sinusoidal field magnitude B_S and discuss the appearance of frequency gaps and stationary solutions as the magnetization undulation amplitude increases. Note that, in the sinusoidal field B_S of Fig. 4.2(a), the *fan angle* (i.e., the angular spread of the vector field) is fixed to $\Theta_F = \pi/2$. In Chapter 5, the fan angle will be examined in detail as a controllable degree of freedom for magnon manipulation and propagation. The corresponding relaxed magnetization (Fig. 4.2(b)) instead exhibits a reduced fan angle, due to the constant presence of the uniform bias field B_0 in addition to B_S. We also examine magnetization distributions obtained after relaxation to a *chiral field*, namely a vector field with a fan angle $\Theta_F = 2\pi$, covering the full angle along a period (Fig. 4.2(c)). This modifies the symmetry of the relaxed magnetization but not the sign of its x-component; hence the resulting state remains sinusoidal, albeit asymmetric (Fig. 4.2(d)). We will show that this case yields a richer dispersion diagram with localized, stationary modes that are highly sensitive - in both number and frequency - to variations in the sinusoidal field magnitude. The simultaneous presence of localized and propagating modes separated by only a few MHz, and with similar profile symmetry, is especially attractive for signal processing in magnonics and spin-wave computing [15, 16, 51].

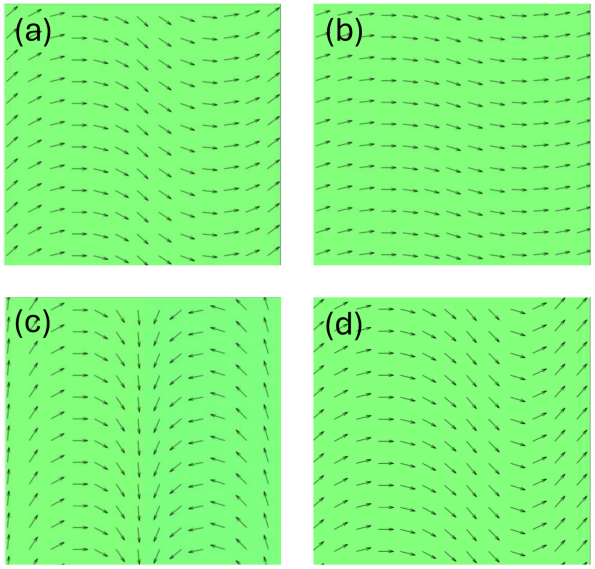

Figure 4.2: Sketches of the vector field distributions subject of the investigation (the color marks the background, the arrows are only illustrative of the undulation). Panel (a): sine field which, combined with the uniform one, results, after relaxation, in the magnetization shown in panel (b). Panel (c): chiral field which, combined with the uniform one, results, after relaxation, in the magnetization shown in panel (d). In (d) the magnetization curvature is more pronounced in the second half of the primitive cell.

A sinusoidal distribution of static magnetization in thin films was first observed by electron microscopy in 1960 by Fuller and Hale [52]. Many subsequent efforts sought a theoretical description of this natural effect and proposed various physical origins - e.g., surface roughness and magnetic anisotropy due to inverse magnetostriction [53, 54, 55]. In our study, we not only consider shorter undulation wavelengths (approaching the exchange-dominated limit), but we also focus on the induced effects on spin-wave dynamics. In particular, we make a conceptual leap: we propose deliberately creating the magnetization undulation with a tunable amplitude to control magnons at the nanoscale. This is clearly a new concept that brings along new physics.

Achieving a sinusoidal magnetization in a film has practical implications, especially in the realm of 3D Magnonics [30, 56, 57]. In stacks of layers with different geometries or material properties, an appropriate distribution of macrospins or ferroelectric domains could generate a periodic, non-uniform interaction field that imprints in the film layer a corresponding sinusoidal, non-uniform magnetization. Control of the sinusoidal field amplitude by manipulating macrospin orientation in the ASI layer sets the magnetization amplitude, which in turn reshapes the magnonic band diagrams and the spin dynamics. Our results shed light on the complexity of dynamics in 3D magnonic architectures and directly support the engineering of signal filtering, information storage and delivery, and sensing. The ultimate purpose of our work is to highlight the potential of magnon dynamics emerging from the undulation itself, providing motivation for both the practical realization of such a magnetic configuration and its experimental/applicative investigation.

4.3 METHODOLOGY AND GROUND STATES

Micromagnetic simulations are performed using the GPU-accelerated software MuMax3 [58]. We adopt permalloy parameters, namely the saturation magnetization $M_s = 800$ kA/m, the exchange constant $A_{ex} = 10$ pJ/m and the gyromagnetic ratio $\gamma = 185$ rad GHz/T. We consider a 5 nm-thick film with a periodic magnetization, lattice constant (period) $a = 256$ nm, and primitive cell volume $256 \times 256 \times 5$ nm^3. The geometric Brillouin zone (BZ) width is therefore $\Delta k = 2\pi/a = 0.0245$ rad/nm, and in the following we will also address a wider BZ, $\Delta k = 0.0490$ rad/nm, due to an additional magnetization symmetry. Since our goal is to compute dispersion curves by Fourier analysis, we replicate the volume 200 times along the x direction so that the supercell is $51200 \times 256 \times 5$ nm^3. The latter is discretized into $4 \times 4 \times 5$ nm^3 micromagnetic cells. Consequently, each primitive cell contains $64 \times 64 \times 1$ cells. With the above parameters, the exchange length below which spins align spontaneously is $\lambda_{ex} = 4.99$ nm, which justifies our choice of a 4 nm elemental cell. We employ quasi-periodic boundary conditions [59], namely 800 copies of the primitive cell along the x and y coordinates to mimic an extended, realistic thin film.

In our study, we account for both in-plane and out-of-plane undulations, as well as dispersions with k parallel and perpendicular to the average magnetization (assumed along the x-axis), corresponding to backward-volume (BV or BA) and Damon-Eshbach (DE) surface spin waves, respectively [60]. With reference to Fig. 4.1, to quantify the undulation amplitude Y_0 we consider the *relative amplitude* of the magnetization components $A = m_y^0/m_x^0$ taken at $x = 0$. Hence Y_0 can be viewed as the spatial deflection from the uniform case ($A = 0$). Using the metric relation:

$$y(x) = Y_0 \sin\left(\frac{2\pi}{a}\, x\right), \tag{4.1}$$

and the slope $\theta = \arctan(A)$, which is half the fan angle ($\Theta_F = 2\theta$), we obtain

$$Y_0 = \frac{A\, a}{2\pi}.$$

Although in what follows we will refer only to A, it is useful for practical applications to correlate the ratio of magnetization components with the actual spatial deflection along y (i.e., Y_0). For example, in our geometry $A = 0.5$ implies $Y_0 \approx 20.4$ nm. This information is valuable not only during fabrication, to design the geometry and cover the desired amplitudes (e.g., if stripes, and not just films, are involved), but also during characterization, when magnetic-force microscopy or space-resolved Kerr magnetometry are used to analyze real samples.

The plan of the investigation is as follows. First, we isolate the effects on SW dynamics arising solely from a sinusoidal periodicity of the film magnetization (Fig. 4.1) with a period equal to the primitive cell length. We consider different amplitudes ($A = m_y^0/m_x^0 = 0, 0.1, 0.2, 0.3\ldots$). Such states, however, are not at equilibrium, particularly when a uniform bias field $B_0 = 0.1$ T is applied. Therefore, we perform conservative simulations (eliminating damping), which is unrealistic but artificially preserves the undulated magnetization in a (fictitious) stable state. This allows comparison with the dynamics of a uniformly

magnetized film. We remark that, by keeping zero damping, our simulations indirectly assume the existence of a "physical cause" for such a non-uniform distribution, which we take, at this stage, to have no (or too little) influence on the spin-wave modes. For instance, an interaction (say, inverse magnetostriction) could be strong enough to create a slight magnetization undulation and thus induce periodicity, yet not strong enough to lift the degeneracy of stationary modes forming at the zone boundary beyond measurement resolution. As we will see, this step is necessary to understand that magnonic frequency gaps originate from the interaction of SW modes with the "physical cause" of the magnetization curvature.

In a second and more realistic approach, we generate the sinusoidal magnetization by relaxing an initially uniform state under a sinusoidal bias field $B_S(x, y)$ (Fig. 4.2, panel (a)), added to the uniform field $B_0 = 0.1$ T. This method is particularly interesting because the sine-field keeps the undulated magnetization at equilibrium in the presence of non-vanishing damping. Moreover, the sine-field realistically mimics a possible vertical (or interfacial) interaction with another layer which, due to its geometry or material, can be responsible for such a non-uniform distribution. Here, we expect to observe the effects of the dynamic interaction with the physical cause of the non-uniform magnetization. After relaxation, the magnetization reaches a sinusoidal equilibrium distribution (Fig. 4.2, panel (b)). We will refer to this case as a magnetization undulation polarized in the xy-plane. Note that B_S can be seen as a *non-chiral vector field*, in the sense that the rotation of the field vector is incomplete (i.e., smaller than 2π, Fig. 4.2(a)) [61]. Based on this observation, we consider in a third step a chiral vector field B_C, namely a field whose flux completes a 2π rotation along the x-axis (Fig. 4.2, panel (c)). The resulting relaxed magnetization (Fig. 4.2, panel (d)) remains sinusoidal (i.e., not chiral); however, the left–right symmetry of the primitive cell is broken, since magnetization and B_C point locally either in the same (panels (c-d), left half) or opposite (panels (c-d), right half) directions. Hence, the magnetization undulation in the two halves of the primitive cell is no longer equivalent. Finally, we investigate the effects of an undulation polarized in the xz plane (i.e., an out-of-plane undulation).

We observe that even when applying a chiral vector field, the resulting magnetization is not chiral (see, for example, Fig. 4.2(d)), nor is any of the involved interaction; careful inspection of the dispersion relations across $k = 0$ shows that the results are reciprocal, regardless of the undulation polarization or wavevector direction [62].

To calculate, by Fourier analysis, the dispersion curves and SW space profiles [63], we apply a sinc microwave field for a total time of 100 ns, defining the frequency resolution $\delta f = 0.01$ GHz. We record time-resolved spatial maps at intervals $\delta t = 25$ ps, giving the Nyquist-limited frequency $f_{\max} = 1/(2\delta t) = 20$ GHz. The simulations are performed on a supercell of 200 replicas of the primitive cell, defining the wavevector resolution $\delta k = \frac{2\pi}{200\,a} = 0.123 \times 10^7$ rad/m $\equiv$ 0.0123 rad/nm. The plots we show are limited to slightly more than a BZ, sufficient to identify, through their dispersion curves, either propagating or stationary modes.

For the spatial dependence, we adopt a wavevector $k_x = 0.0490\,\mathrm{rad/nm}$, i.e., twice the BZ. For the temporal dependence, we use:

$$b(t) = \frac{b_0 \sin\left(2\pi f_{cutoff}(t - t_0)\right)}{2\pi f_{cutoff}(t - t_0)}, \tag{4.2}$$

with $b_0 = 1$ mT, cutoff frequency $f_{cutoff} = 40$ GHz, and delay time $t_0 = 50$ ns. Eq. (4.2) is precisely the type of excitation discussed in Chapter 3, Sec. 3.2.2. Once the time-resolved 2D magnetization maps are recorded, we apply the Fast Fourier Transform (FFT) to obtain the SW dispersion relations [64]. We also determine SW spatial profiles by performing simulations on a single primitive cell (rather than a 200-cell supercell), retaining the previous periodic boundary conditions to mimic a realistic film. This technique limits the results to $k = 0$; hence, we obtain the profiles as the real part of the FFT coefficients of each micromagnetic cell in the primitive cell. Such profiles must be understood within the Bloch picture, whereby the spin wavefunction (i.e., the magnetization fluctuation) in periodic magnetic systems is expressed as [65]:

$$\delta m_k(\boldsymbol{r}) = \delta \tilde{m}_k(\boldsymbol{r}) e^{i\boldsymbol{k}\cdot\boldsymbol{r}}, \tag{4.3}$$

where $\delta \tilde{m}_k(\boldsymbol{r})$ is the SW cell function (which extends over the primitive cell and has the periodicity of the system), $\boldsymbol{k}$ is the wavevector and $\boldsymbol{r}$ is the position across the lattice. Hence, the profiles we show are the real part of the z-component of the SW cell function (always relevant to experiments) [66, 67, 68, 69].

4.4 RESULTS AND DISCUSSION

We now present micromagnetic simulation results that track how the BV and DE dispersions evolve as the film magnetization changes from a uniform to an undulated state. Recall that the undulation is aligned with the applied field (magnetic moments in a head-to-tail arrangement), namely along the x-axis. After identifying the physical mechanism responsible for opening *frequency gaps* at the zone boundary, we examine the spin-wave dynamics of undulated magnetization distributions generated by either a sine or a chiral bias field. In all simulations, we include an additional uniform field fixed at 0.1 T. Because the magnetization undulation propagates along a fixed direction (x-axis, Fig. 4.1), we expect a band structure only along this axis, i.e., for the BV configuration ($\boldsymbol{k} \parallel \boldsymbol{M}$), while no periodicity is expected along the other in-plane direction (y-axis, corresponding to the DE configuration with $\boldsymbol{k} \perp \boldsymbol{M}$). Nevertheless, we will show that the mere presence of periodicity in one direction influences the dynamics in the orthogonal direction, introducing new solutions. For completeness, we note that the alternative case, with magnetic moments perpendicular to the undulation direction and therefore parallel to each other in any in-plane direction, would correspond to a uniformly magnetized film.

4.4.1 *Spin wave dispersions under an in-plane sinusoidal magnetization distribution: "non-interacting" case*

Following the plan of the investigation outlined in Sec. 4.3, we prepared an in-plane sine magnetization with period a, with undulation at different relative amplitudes A, and subject to a uniform bias field B_0. However, no relaxation was allowed, nor was any external periodic field introduced; we may refer to this as the "non-interacting" case. As previously mentioned, in the simulation we set this distribution as an artificial equilibrium point (ground state) by fixing the damping parameter to zero ($\alpha_G = 0$). The application of an excitation to this artificial ground state produces small fluctuations around it, arising solely from spin waves.

In Fig. 4.3 we show the dispersion relations for the cases (a) $A = 0$, (b) $A = 0.2$ and (c) $A = 0.5$. We recall that the direction of the magnetization undulation is parallel to the direction of the wavevector, so the dispersions correspond to the BV mode [60, 70]. In thicker films at low k, this volume mode is usually characterized by a negative slope in its dispersion relation, resulting in a negative group velocity. In our case, due to the very small thickness (5 nm), exchange interaction dominates and only a positive slope is observed at low k.

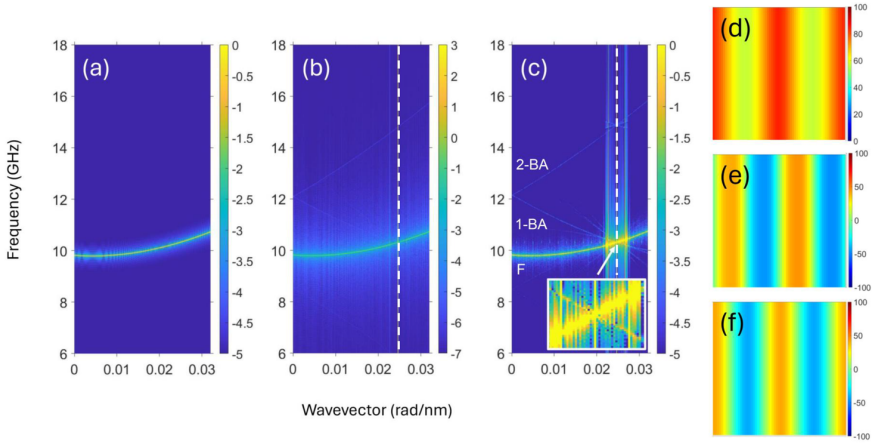

Figure 4.3: Magnonic dispersion relations for BA waves in the non-interacting case of a film with in-plane sinusoidal magnetization prepared at different relative amplitude $A = m_y^0/m_x^0$: (a) $A = 0$, i.e., the reference, uniformly magnetized film; (b) $A = 0.2$; (c) $A = 0.5$. Note in (b) and (c) the occurrence of the mirroring to the first BZ due to periodicity, and the remarkable absence of any frequency gap at the BZB, i.e., $k = 0.0245$ rad/nm, as demonstrated in the inset by the crossing of the curves (in the inset the image is magnified and saturated). The color-bar is in arbitrary units, chosen to highlight the tiny lines mirroring in the reduced BZ to prove periodicity. Panels on the right: cell function profiles (real part of the z-component of the dynamic magnetization) of (d) the fundamental (F) mode, (e) the 1-BV mode, crossing the F mode curve at the BZB, and (f) the 2-BV mode. The magnetization undulation underlying these mode profiles qualitatively corresponds to the one shown in Fig. 4.2(b).

Despite being unrealistic due to the vanishing damping, the resulting SW dispersion relations reveal two interesting features. First, the Brillouin zone boundary (BZB) occurs at $k_{\mathrm{BZB}} = 0.0245$ rad/nm,

twice the expected value of 0.01225 rad/nm. This implies that the *actual lattice constant* d is half of the geometric one a, and thus that the SW dynamics is invariant under a *mirror operation* σ_h in the magnetization (across the horizontal axis, namely a change of sign of the m_y component) [71]. As a consequence, the BZB wavevector is $k_{\mathrm{BZB}} = \pi/d \equiv 2\pi/a = 0.0245$ rad/nm. Second, no gap emerges at the zone boundary, independent of the relative amplitude A. This is illustrated in the inset of Fig. 4.3(c), where the dispersion of the fundamental mode F is crossed by its reflection, 1-BV, with opposite group velocity. Because the bias field is uniform, the modes responsible for the dispersion curves at the BZB are invariant under translations of half a period ($d/2$) [70]. The cell function ($k = 0$) of these SW modes is shown in Fig. 4.3. In panel (d) we display the fundamental mode (F), occurring at 9.81 GHz; in panel (e) the backward mode with one nodal line in the cell function (1-BV), at 12.2 GHz; and in panel (f) the 2-BV mode, almost degenerate in frequency with 1-BV. According to Eq. (2), at the BZB the F and 1-BV modes are indistinguishable and therefore degenerate in frequency, since the medium is continuous and homogeneous and only a uniform field is applied. Of course, in the case of dot or antidot lattices, or even multi-material systems [72], the two modes cannot remain degenerate and a gap opens. In fact, in Sec. 4.4.2 we will illustrate in detail how the band gap arises as a consequence of *translational symmetry breaking*, achieved by introducing a sinusoidal bias field with period a ("interacting case"). We emphasize here that periodicity is a necessary, but not sufficient, condition for the opening of a gap [73]. It is also worth noting that the crossing of the F and 1-BA dispersions at the BZB is linear, reminiscent of the behavior of topological Dirac magnons with gapless metallic character [74, 75, 76], which will be the focus of Chapter 6.

4.4.2 *"Interacting" case: Relaxation to in-plane periodic bias fields*

As mentioned in the investigation plan (Sec. 4.3), a more realistic way to obtain a sinusoidal magnetization is to relax an initially uniform magnetization under the action of a periodic bias field B_P, in addition to the uniform field $B_0 = 0.1$ T, with $B_P/B_0 \leq 1$. We apply first a sine oscillation ($B_P \equiv B_S$) and then a chiral oscillation ($B_P \equiv B_C$) (Fig. 4.2(a, c)). It is worth recalling that the fan angle is partial in the former, $\Theta_F = \pi/2$, while it is complete in the latter, $\Theta_F = 2\pi$. In both cases, we consider an in-plane field oscillation, namely $B_P = B_P(x, y)$, which affects the resulting magnetization distribution and can be interpreted as a simulation of the vertical interaction with another layer in the context of 3D Magnonics. The application of B_P with a given magnitude and symmetry determines the relative amplitude of the equilibrium magnetization distribution and, hence, the fan angle of $M(x, y)$. Since B_P is a bounded function, the total vector sum $\boldsymbol{B}_{tot} = \boldsymbol{B}_P + \boldsymbol{B}_0$ has a fan angle that is always smaller than that of $\boldsymbol{B}_P$ alone. For this reason, the apparent amplitude of the resulting magnetization oscillation (Fig. 4.2(b, d)) appears less pronounced compared with the corresponding sine or chiral fields (Fig. 4.2(a, c)).

In this case, we compute a relaxed equilibrium magnetization before applying the excitation. Thus, a non-vanishing damping parameter

α_G had to be used. However, in order to both reach equilibrium and obtain well-defined dispersion curves within reasonable times, we use only 1% of the real damping (i.e., $\alpha_G = 0.0001$), allowing long-lasting precession and consequently larger Fourier coefficients. We emphasize that in the linear (low-power) regime, the damping parameter does not influence the relation between frequency and wavevector; it only attenuates and possibly broadens the intensity of the corresponding curve at high k [72, 77, 78].

4.4.3 *Sine field*

First we investigate the effects on the SWs of a periodic sinusoidal field, $B_P \equiv B_S$. As shown previously, after relaxation the magnetization varies along the x-direction as a sine function with amplitude $Y_0 \propto A$. The relative amplitude A of the magnetization undulation as a function of the magnitude of B_S is plotted in Fig. 4.4, so that it is possible to establish a correspondence with the cases of Sec. 4.4.1, where only A was given.

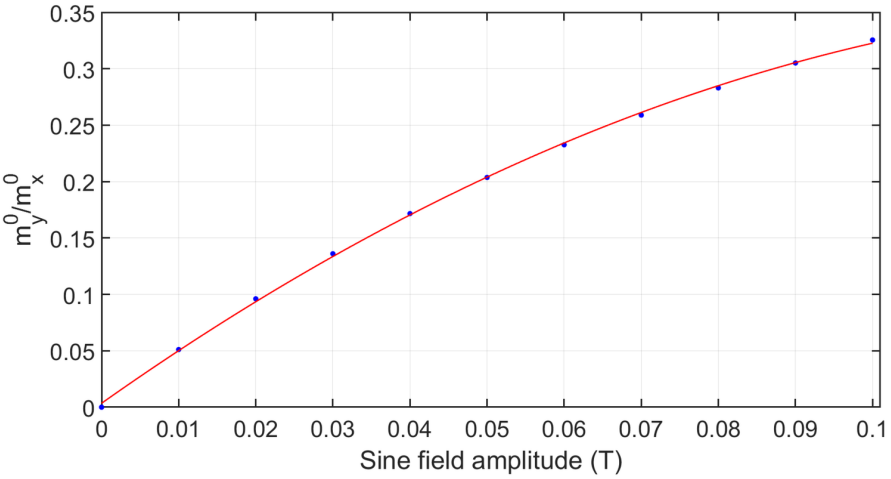

Figure 4.4: Relative amplitude $A = m_y^0/m_x^0$ between the y and x components of the magnetization at $x = 0$ as a function of the B_S magnitude (in tesla). The red line is a guide for the eye. For a correspondence with Fig. 4.3, we obtain $A = 0.2$ for $B_S = 0.0227$ T and $A = 0.5$ for $B_S = 0.06$ T.

The resulting SW dispersion curves, as a function of the magnitude of B_S, are shown in Fig. 4.5.

In general, we observe that the frequency increases with the magnitude of B_S, namely as the undulation amplitude of the magnetization increases. Indeed, by increasing B_S, the overall bias field (superposition of $B_S(x, y)$ and B_0) also increases, thus the Zeeman potential energy increases, making the magnetization stiffer against deflections from equilibrium; consequently, the frequency (at a given k) rises as well. This effect is general and independent of the propagation direction of the wave. Accordingly, it is also observed for DE waves, as shown in Fig. 4.6. As in the previous case without a sine-field, the dynamics is invariant under the change of sign of the m_y component, and the primitive unit cell corresponds to half the

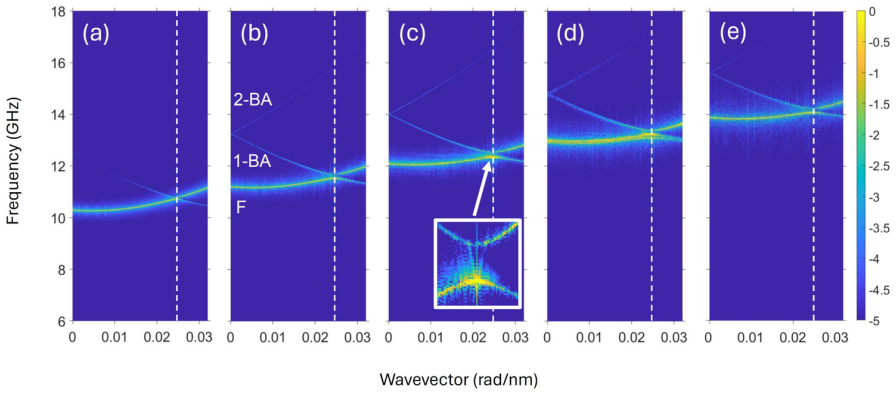

Figure 4.5: Magnonic dispersion curves for BV waves (intensity in arbitrary units) at different values of the sine field magnitude B_S (polarization in the xy plane). Panel (a): 0.01 T. Panel (b): 0.03 T. Panel (c): 0.05 T. Panel (d): 0.07 T. Panel (e): 0.09 T. In (c) the inset highlights by magnification the opening of a gap at the BZB.

geometric one, with lattice constant $d = a/2$. Hence, the BZB occurs at $k_{\mathrm{BZB}} = \pi/d \equiv 2\pi/a = 0.0245$ rad/nm (Fig. 4.5).

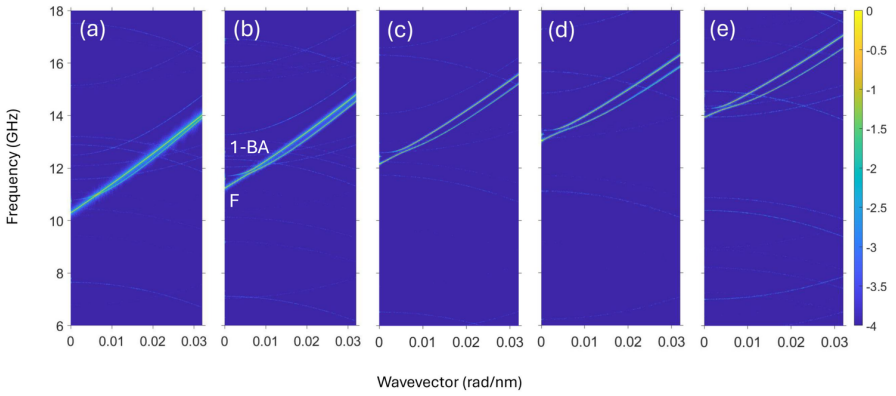

Figure 4.6: Magnonic dispersion curves for DE waves (intensity in arbitrary units) at different values of B_S (polarization in the xy plane). Panel (a): 0.01 T. Panel (b): 0.03 T. Panel (c): 0.05 T. Panel (d): 0.07 T. Panel (e): 0.09 T.

In contrast to the previous non-interacting case, here a frequency gap arises at the BZB for sufficiently large B_S. The two spin-wavefunctions F and 1-BV (Fig. 4.7 (b, c)) are no longer degenerate in frequency (energy) because of the sinusoidal bias field B_S with period a. Consequently, the frequency gap originates from the dynamic interaction with the vector field $B_S(x, y)$ that drives the undulation.

The mechanism behind the origin of frequency gap is the following. Due to Bragg diffraction, two stationary wavefunctions form at the zone boundary: one with nodes coinciding with the nodes of the sine field (i.e., at $d = a/2$), and the other with nodes coinciding with its maxima (i.e., at $d/2 \equiv a/4$). This is illustrated in Fig. 4.8.

The two waves interact differently with B_S: the former acquires the *lowest frequency* (top of the lower band), while the latter attains the *highest frequency* (bottom of the upper band), thereby producing a visible frequency gap (inset of Fig. 4.5(c)). By contrast, in Fig. 4.3 no gap exists at the zone boundary (degeneracy). In that case, the absence of the non-uniform sine field B_S restores translational sym-

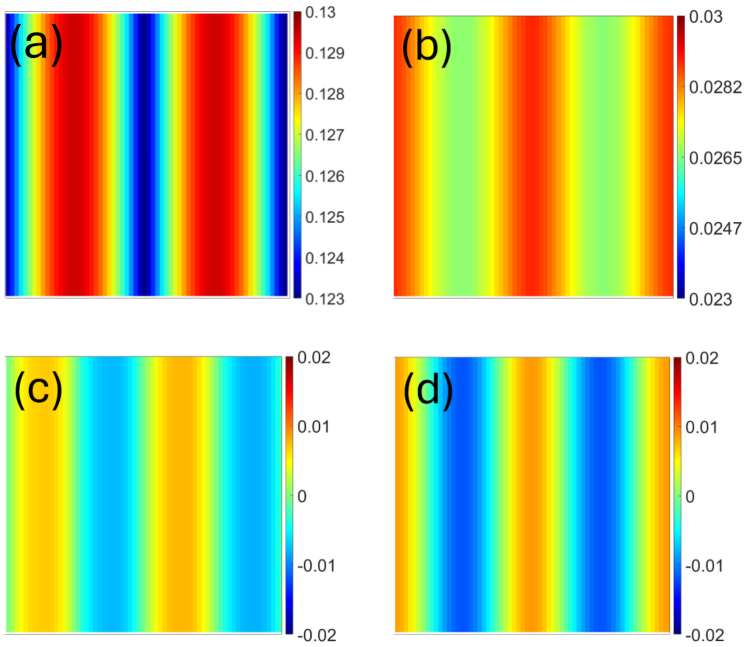

Figure 4.7: (a) Effective field B_{eff} profile for in-plane polarized magnetization at $B_S = 0.03$ T (color bar in tesla). (b-d) Real part of the out-of-plane (z) component of the dynamic magnetization at $k = 0$ at the frequencies giving non-vanishing signal in the dispersions at $B_S = 0.03$ T: (b) F-mode (11.13 GHz); (c) 1-BV mode (13.14 GHz); (d) 2-BV mode (13.14 GHz). Intensity in arbitrary units. The magnetization undulation underlying these mode profiles qualitatively corresponds to the one shown in Fig. 4.2(b).

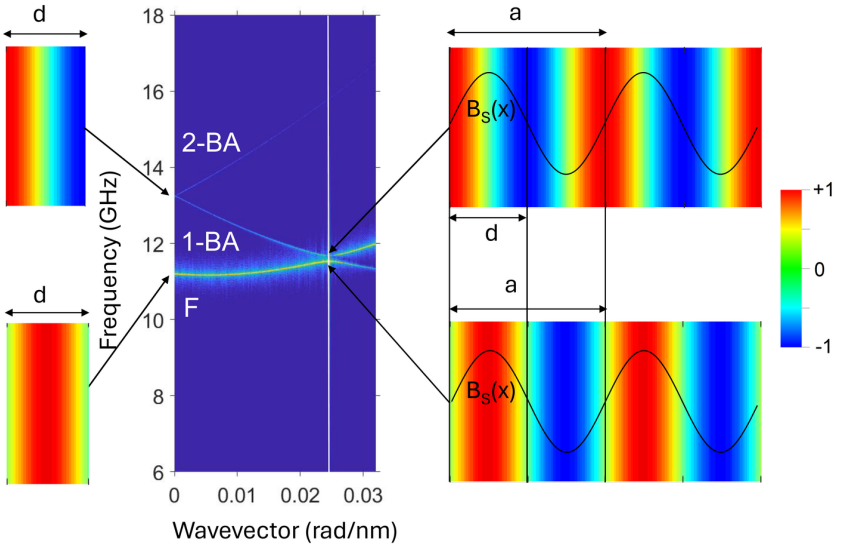

Figure 4.8: Illustration of the origin of the frequency gap at the BZB: at the center, the (indicative) dispersion diagram taken from panel (c) of Fig. 4.5. On the left, the mode profiles F and 1-BV at $k = 0$, referred to the actual primitive cell which is demonstrated to be $d = a/2$. On the right, the two reconstructed profiles (colors in arbitrary units) as must appear at the BZB following Eq. (4.3), superimposed to the sine-field $B_S(x)$ (black curves) which has a period a. at the BZB the two wavefunctions F and 1-BV differ only for the translation of $a/4 \equiv d/2$ and lead to the emergence of the frequency gap because of the different phase relationship with $B_S(x)$.

metry and invariance under translations of $d/2$, making it impossible to distinguish between the F and 1-BA wavefunctions (Fig. 4.3(d, e)). As the undulation amplitude increases, the deviation between the local magnetization direction and the overall bias field $\boldsymbol{B}_S + \boldsymbol{B}_0$ grows, particularly at the center and ends of the primitive cell. Consequently, the energy difference between F and 1-BV increases, i.e., the frequency gap widens (Fig. 4.9).

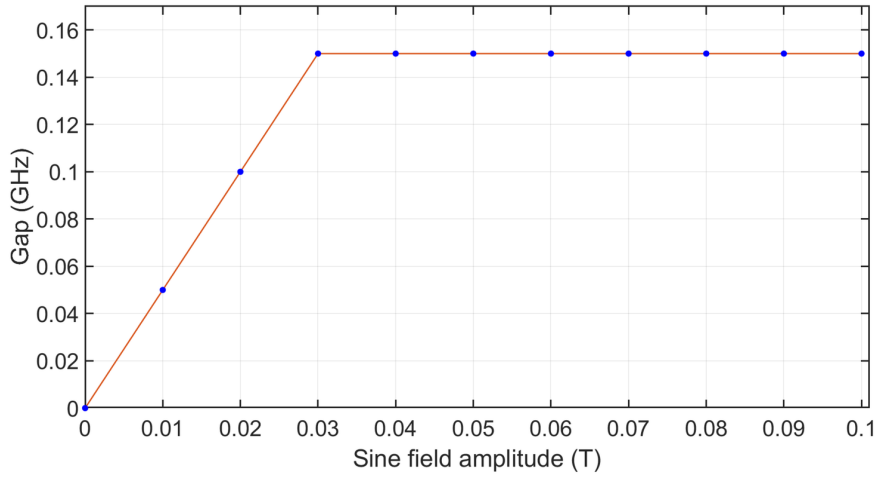

Figure 4.9: Evolution of the frequency gap as the amplitude of the sine field (in tesla) is varied (magnetization in xy plane). Blue dot: data. Red line: linear fit ($y = 5x$ in the range $[0, 0.03$ T], then $y = const = 0.15$).

More precisely, starting from $B_S = 0$, and with increasing B_S, the y component of the magnetization progressively increases at the nodes of B_S (i.e., at $x = 0, a/2, a$), while remaining nearly zero at the crests (where the derivative vanishes, $x = a/4, 3a/4$). In other words, the average angle θ_k between the local magnetization and the propagation direction (x) becomes increasingly larger in the first regions, where 1-BV has maxima, but remains nearly constant in the second regions, where F has maxima. This divergence causes the corresponding frequencies to separate further (as can be understood, for example, using the Herring-Kittel formula [79] or its thin-film counterpart[80]). Thus, as B_S grows, the transverse magnetization component m_y follows, driving the gap increase. This increase is found to be linear up to $B_S = 0.03$ T, after which it saturates. Apparently, once m_y reaches a critical value, the energy difference between the two regions no longer increases. By linear interpolation we estimate the growth rate (up to $B_S = 0.03$ T) as approximately 5.00 rad GHz/T.

The Bloch wave profiles underlying the dispersion of Fig. 4.5(b), with $B_S = 0.03$ T, are shown in Fig. 4.7: panel (a) corresponds to the lowest-frequency curve (fundamental mode), panel (b) to the 1-BV mode, responsible for a negative dispersion curve that terminates in a gap at the BZB, and panel (c) to the 2-BV mode, nearly degenerate with 1-BV at $k_x = 0$ but displaying a positive slope. These curves are very similar to the non-interacting case ($B_S = 0$) shown in Fig. 4.3.

Furthermore, we assess how periodicity in one direction (x) affects the dynamics in the perpendicular direction (y). This is a direct consequence of Bloch's theorem: due to periodicity, the dispersion along k_x folds into the reduced BZ, intersecting the $k_x = 0$ axis at many

points. Hence, while a uniform film has a single solution at $k_x = 0$, a periodic system has many (higher-order modes, labeled as F or 0-BV, 1-BV, 2-BV, 3-BV, etc.). Each of these new solutions corresponds to a distinct cell function for a new Bloch wave (Eq. (4.3)) traveling also along the y-axis, and showing a single-valued dispersion curve analogous to magnetostatic waves in uniformly magnetized films. Along the y-axis no periodicity exists, explaining why only single-valued curves are found. This is also valid for the xz polarization (Sec. 4.4.5). Thus, periodicity along x introduces additional spin-wave degrees of freedom also along y, visible as multiple dispersion curves.

4.4.4 *Chiral field*

The application of a chiral field $B_C(x, y)$ (Fig. 4.2(c)) to a film with saturated magnetization breaks the mirror symmetry observed in the previous case, so that the physical primitive cell now coincides with the geometric one (i.e., the lattice constant is a). The change of sign of the B_C^x component, occurring at $a/2$, divides the primitive cell into two nonequivalent regions. Since the x-component of B_C is always smaller or equal to that of B_0, its sign change cannot alter the corresponding m_x component. Thus, it cannot induce a chiral magnetization but it effectively enhances the demagnetizing field in the second half of the primitive cell due to its antiparallel orientation. This effect, combined with the persistent negative m_y component across the turning point, allows the magnetization flux to complete its sinusoidal profile, though with stronger curvature in the second half. As we will see, this asymmetry transfers to the effective internal field and, consequently, to the SW dynamics (mode profile and frequency).

In Fig. 4.10 the ratio $A = m_y^0/m_x^0$ of the magnetization components, taken at $x = 0$, is plotted as a function of B_C for direct comparison with the analogous Fig. 4.4. In the first half of the primitive cell, both the average chiral field and the magnetization vectors point in the same direction, making the comparison straightforward. Because of the larger fan angle inherent to the chiral field, the magnetization relative amplitude A is larger than in the sine-field case (B_S).

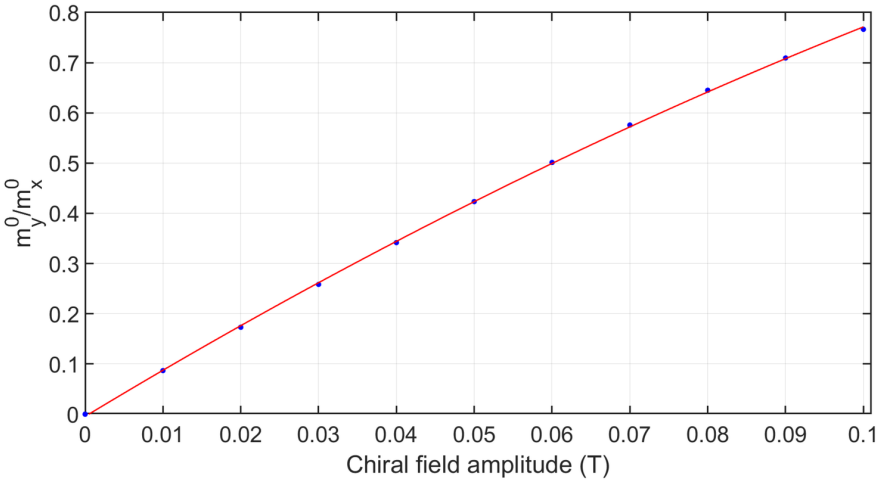

Figure 4.10: Relative amplitude $A = m_y^0/m_x^0$ between the y and x components at $x = 0$ as a function of the B_C magnitude (in tesla). The red line is a guide for the eye.

In Fig. 4.11 we show the evolution of the dispersion curves as the chiral field magnitude B_C increases. More than one BZ is included in the figure to identify both stationary and propagating modes.

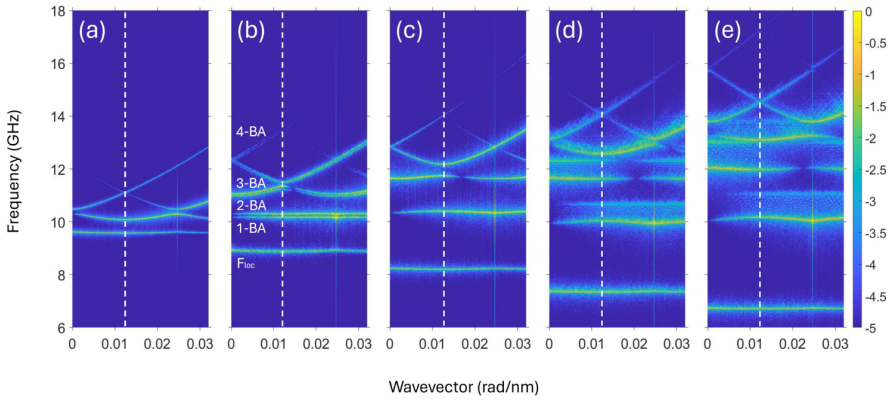

Figure 4.11: Magnonic dispersion curves for BV waves (intensity in arbitrary units) at different values of the chiral field B_C. Panel (a): 0.01 T. Panel (b): 0.03 T. Panel (c): 0.05 T. Panel (d): 0.07 T. Panel (e): 0.09 T. Note that, due to a reduced magnetization symmetry, when a chiral field is applied the BZB occurs at $k_x = 0.01225$ rad/nm.

The first observation is that the BZ boundary now occurs at $k_{\mathrm{BZB}} = \pi/a \equiv 0.01225$ rad/nm, consistent with the fact that the physical primitive cell coincides with the geometric one. Similar to the B_S case, increasing B_C shifts the dispersion structures toward higher frequencies. Ultimately, B_C acts as an additional bias field, just as B_S does, and its increase enhances the overall Zeeman interaction, thereby raising the frequencies [15]. However, the frequency increase is smaller under a chiral field than under a sine field. This is because dipolar (demagnetizing) fields are on average stronger in the chiral case, and these fields oppose the Zeeman interaction, limiting the frequency rise [81, 80, 82].

Unlike the sine-field case, here we observe the emergence of flat dispersions (stationary modes) even at low B_C, with the first one appearing around 9.5 GHz for $B_C = 0.01$ T (Fig. 4.11(a)). Not only does its frequency decrease as B_C grows, but also the number of flat dispersions increases with B_C. These features, distinctive of the chiral field, can be explained by examining B_{eff} (Fig. 4.12(a)).

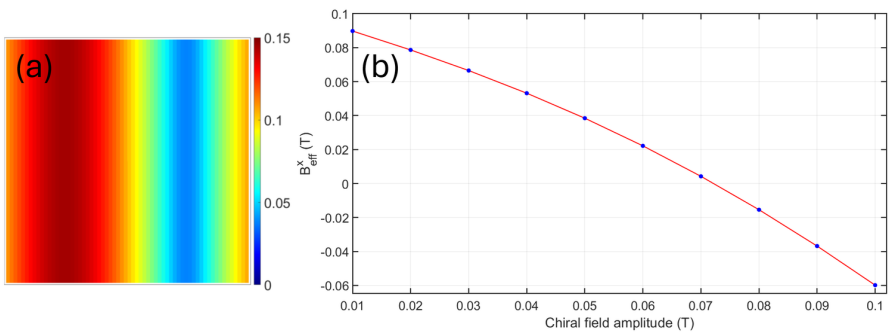

Figure 4.12: (a) B_{eff} along the x direction (color bar in tesla) when $B_C = 0.05$ T, and (b) its behavior as a function of the chiral field amplitude (magnetization undulation polarized in the xz plane, BV configuration). The red line is a guide for the eye.

In contrast with the previous case, the application of a chiral field breaks the mirror symmetry σ_v [71], and on the right side of the primitive cell B_{eff} reaches a deep absolute minimum, acting as a well for SWs. Thus, even at low B_C, the lowest-frequency mode localizes in this well, with its spin-wavefunction rapidly decaying outside (Fig. 4.13(a)).

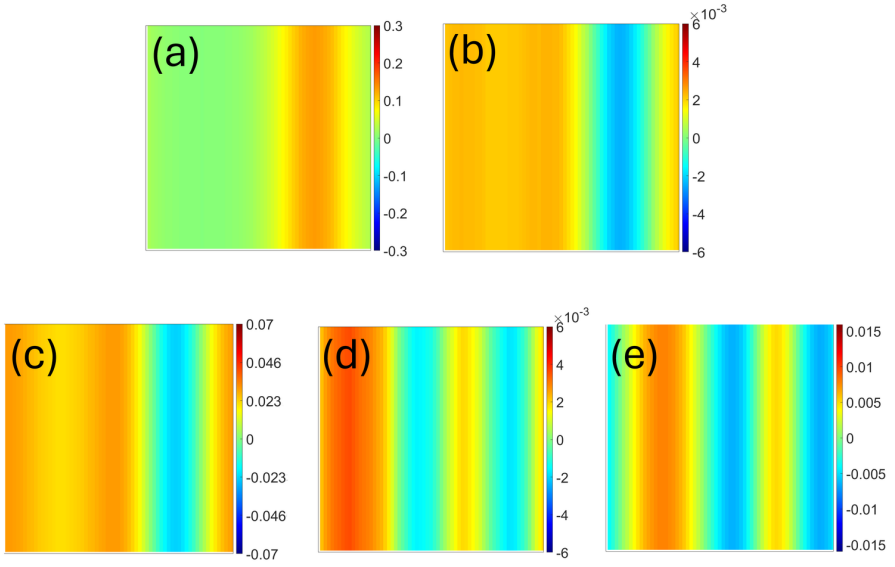

Figure 4.13: Real part of the out-of-plane (z) component of the dynamic magnetization at $k_x = 0$ at the frequencies giving non-vanishing signal in the dispersions (intensity in arbitrary units). For $B_C = 0.05$ T: (a) localized F-mode F_{loc}, 8.23 GHz; (b): 1-BV mode, 10.34 GHz; (c): 2-BV mode, 11.58 GHz; (d) 3-BV mode, 13.17 GHz; (e) 4-BV mode, 13.17 GHz. The magnetization undulation underlying these mode profiles qualitatively corresponds to the one shown in Fig. 4.2(d).

The localization of the lowest-frequency mode in the minimum of B_{eff} (Fig. 4.12(a)) is a well-known phenomenon [23, 83, 84, 85, 86, 87, 88]. Because of the strong localization (limited spatial extension), its dynamic stray fields are too weak to produce a significant bandwidth, so the mode becomes stationary (zero group velocity $v_g = \partial\omega/\partial k$) [87]. Moreover, as B_C increases, B_{eff} becomes progressively deeper (Fig. 4.12(b)) on the right side of the primitive cell, where the magnetization is antiparallel to the chiral field. On the one hand, this allows the well to host additional localized modes, yielding more flat dispersions. On the other, it explains the progressive frequency decrease of these localized modes with increasing B_C, as seen in the dispersions.

The dependence of this localized mode on B_C is shown in Fig. 4.14: by linear interpolation, we obtain a slope $df/dB = -35.2$ GHz/T, corresponding to an *effective gyromagnetic ratio* [24]:

$$\gamma_{\text{eff}} = 2\pi\, df/dB = -221 \text{ rad GHz/T}, \tag{4.4}$$

significantly larger in magnitude than that of permalloy (185 rad GHz/T). The negative sign indicates the increasing instability of the magnetization on the right side of the primitive cell, where the chiral field and the magnetization are antiparallel.

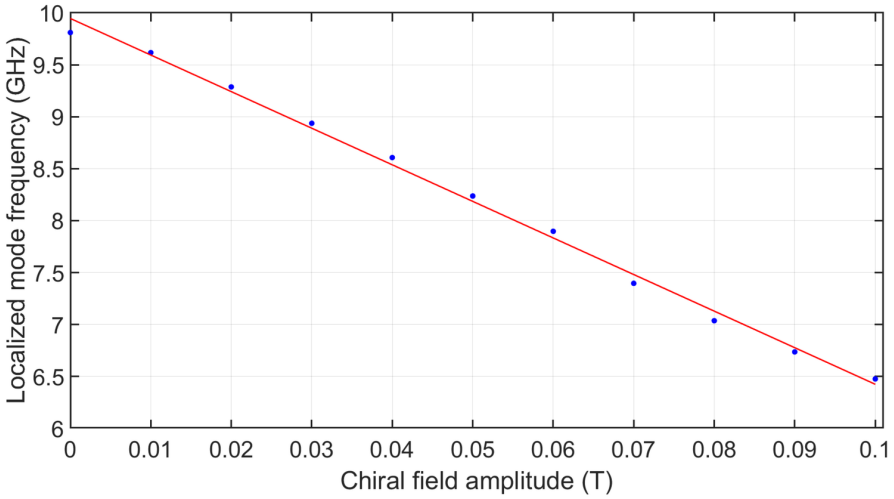

Figure 4.14: Evolution of the frequency of the localized mode as the amplitude of the chiral field is varied (magnetization undulation polarized in xy plane). Blue dot: data. Red line: linear fit ($y = -35.2x + 9.9$)

Remarkably, the periodicity of the magnetization endows the film with effective properties, such as γ_{eff}, that the base material does not possess. This is a hallmark of *metamaterials*, which exhibit enhanced properties arising from structural design [89]. The possibility of tailoring γ_{eff} by engineering the magnetization distribution is particularly appealing for realizing indirect measurements of magnetic field variations in next-generation sensing devices [90, 91, 92].

We highlight the importance of having, in a single system, multiple solutions within a few hundred MHz that display opposite dynamic behavior (stationary vs. propagating), yet possess compatible cell-function symmetries (Fig. 4.13(b, c)). Under such conditions, the same antenna can excite one or the other simply by applying a small frequency shift. As a result, information can be stored or transmitted on the same physical device in real time. Our results clearly demonstrate that applying a chiral field provides a ferromagnetic film with this capability.

4.4.5 *Out-of-plane magnetization oscillation*

We apply the relaxation approach to compute the dispersions in a film with an out-of-plane oscillation of the magnetization (i.e., polarized in the xz-plane), extending along the x-axis. Such an undulation is obtained after applying a sine field B_S with the same polarization and modulation, to which the magnetization relaxes. We again consider both BV and DE waves, whose dispersions are shown in Figs. 4.15 and 4.16, respectively.

Clearly, the periodic structure is noticeable only for BV waves, while DE waves behave as if they were propagating in a homogeneous medium. Nevertheless, the folding of the BV dispersion to the reduced BZ introduces new solutions even for the DE waves, in particular the DE wave with a 1-BV cell function, visible in the dispersions as an additional sister curve crossing the $k = 0$ axis at higher frequency. In principle, any DE wave with an n-BV ($n > 1$) cell-function profile

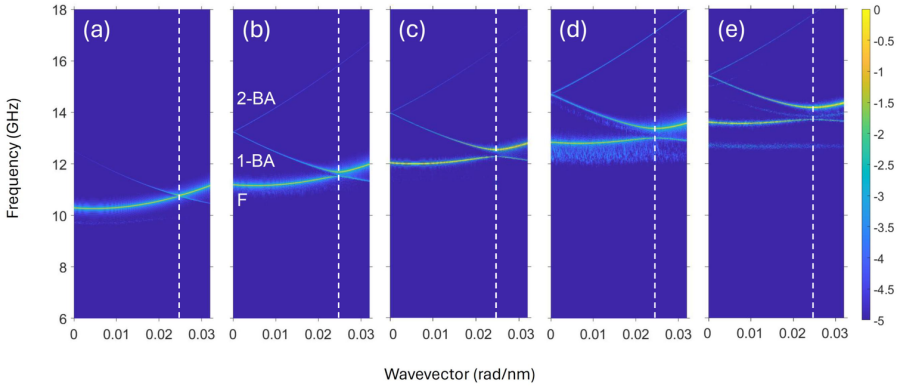

Figure 4.15: Magnonic dispersion curves for BV waves (intensity in arbitrary units) at different values of the sine field B_S polarized in the xz plane. Panel (a): $B_S = 0.01$ T. Panel (b): $B_S = 0.03$ T. Panel (c): $B_S = 0.05$ T. Panel (d): $B_S = 0.07$ T. Panel (e): $B_S = 0.09$ T.

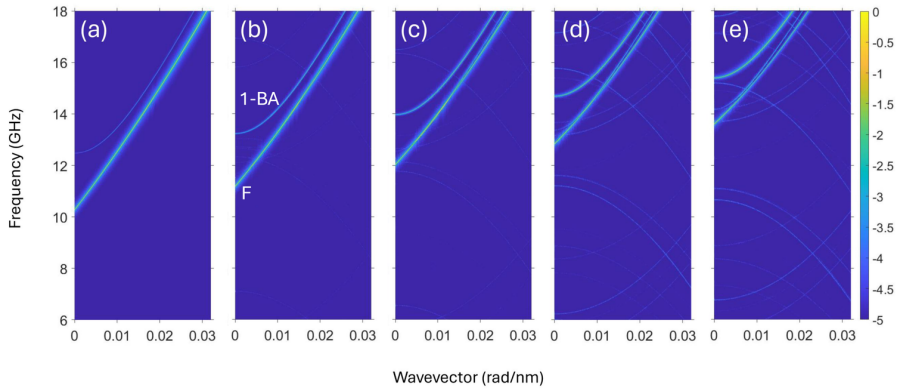

Figure 4.16: Magnonic dispersion curves for DE waves (intensity in arbitrary units) at different values of the sine field B_S polarized in xz plane. Panel (a): $B_S = 0.01$ T. Panel (b): $B_S = 0.03$ T. Panel (c): $B_S = 0.05$ T. Panel (d): $B_S = 0.07$ T. Panel (e): $B_S = 0.09$ T.

generates its own dispersion, although its intensity decreases rapidly with increasing n. We also observe that the slope of the DE dispersion is much steeper for an out-of-plane undulation (Fig. 4.16) than for the in-plane case (Fig. 4.6). This can be ascribed to the different orientation of the magnon wavevector with respect to the polarization plane of the magnetization undulation, even though $\boldsymbol{k}$ is always directed along the y-axis. In the in-plane case, $\boldsymbol{k}$ lies within the polarization plane of the magnetization and therefore truly corresponds to the DE configuration. In contrast, in the out-of-plane case, $\boldsymbol{k}$ is perpendicular to the polarization plane of the magnetization, corresponding more appropriately to *forward volume spin wave modes* (FVSW), discussed in Chapter 2, Sec. 2.9. In uniformly magnetized films, FVSW dispersions generally exhibit a steeper slope than DE dispersions, owing to the different roles of the demagnetizing field [93]. The mode profiles responsible for the out-of-plane dispersion curves are displayed in Fig. 4.17 and resemble those found in the in-plane case of Sec. 4.4.3.

The fundamental (F) mode is characterized by an in-phase amplitude (no phase changes) throughout the primitive cell, with stronger values at the nodes of the sine field $B_S(x)$, following the behavior of B_{eff} (Fig. 17(a)). The F mode produces the most intense curve, with positive slope, in both BV and DE configurations. The 1-BV and

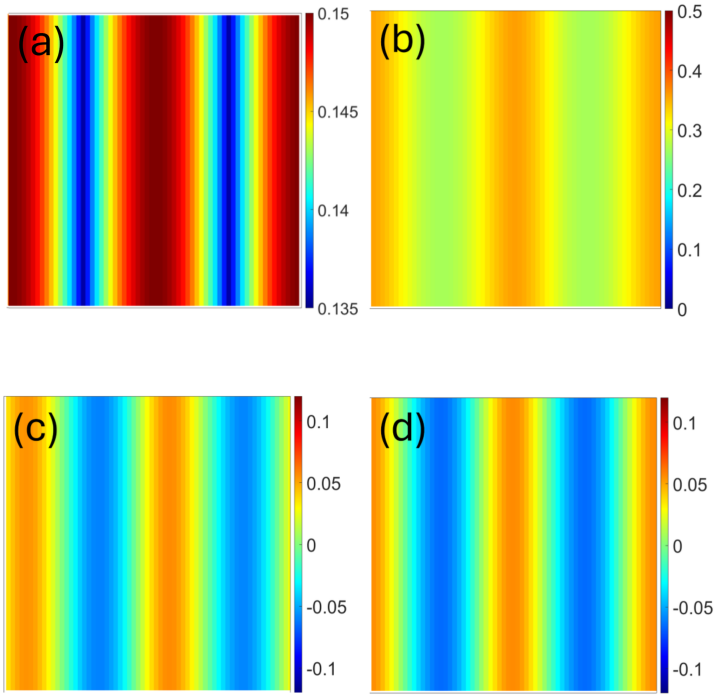

Figure 4.17: (a) Space profile of the x-component of B_{eff} when $B_S = 0.05$ T, where the color bar units are in tesla; (b-d) Spatial profiles, in arbitrary units, of the modes giving the dispersions of Fig. 4.15(c) with $B_S = 0.05$ T (magnetization undulation polarized in xz plane, BA configuration): (b): FM (12.03 GHz); (c): 1-BV mode forming a gap at the BZB with the FM (13.97 GHz); (d): 2-BV mode (13.97 GHz).

2-BV modes are responsible for the folding of the dispersion into the reduced BZ along the x direction. As noted above, the 1-BV mode also produces the second most intense curve in the DE configuration, where $\boldsymbol{k} \perp \hat{\boldsymbol{x}}$ (Fig. 4.16).

Similar to the in-plane case, a frequency gap appears at the BZB as B_S is increased. The dependence of this gap on the applied sine field $B_S(x, z)$ is shown in Fig. 4.18.

Interestingly, unlike the in-plane case, the curve does not saturate but maintains its linear growth independently of B_S. This behavior can be attributed to the limited increase of the transverse magnetization component m_z in the out-of-plane case, compared with m_y in the in-plane case, thereby constraining the energy difference between the complementary regions of the primitive cell where F and 1-BV modes have their maxima (see Sec. 4.4.3). The strong demagnetizing fields in the thin film significantly restrict the growth of the out-of-plane magnetization component m_z for any given B_S. This is confirmed by comparing Fig. 4.4 with Fig. 4.19: at a fixed B_S, the relative amplitude in the out-of-plane case is about one order of magnitude smaller than in the in-plane case. Thus, the critical value of the transverse component is barely reached when this component is oriented along the film thickness, due to strong dipolar fields, and consequently the curve does not saturate. From linear interpolation, we determined the average growth rate to be about 5.30 rad GHz/T, which is close to the rate found in the in-plane case (limited to the interval $[0, 0.03]$ T

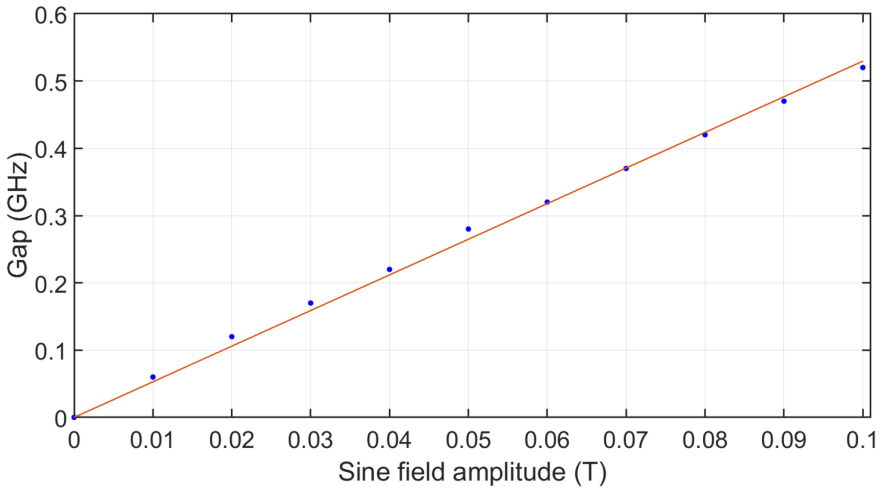

Figure 4.18: Evolution of the gap as the amplitude of the sine field is varied (polarization in xz plane). Blue dot: data. Red line: linear fit ($y = 5.3x$)

before saturation) and thus provides strong validation of the proposed theory. Once again, the linear sensitivity of the gap to fine variations of the applied B_S is highly promising for sensing applications [91, 92].

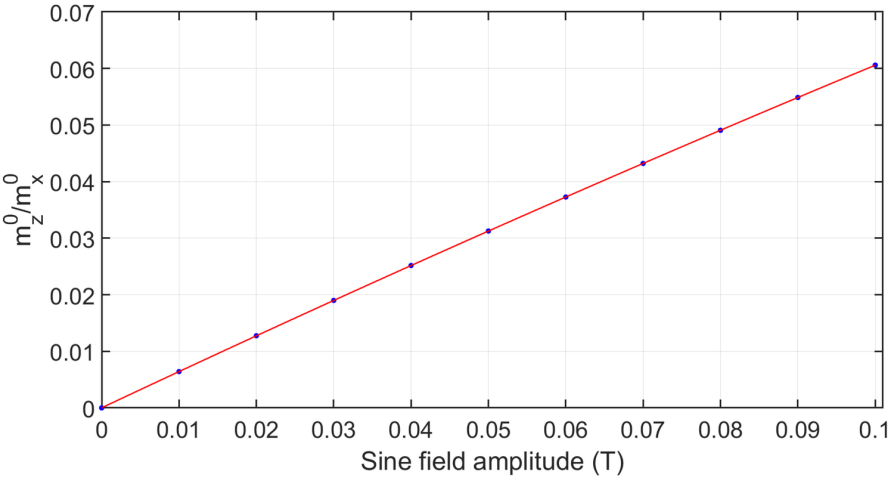

Figure 4.19: Relative amplitude $A = m_z^0/m_x^0$ between the z and x components of the magnetization at $x = 0$ as a function of the out-of-plane B_S magnitude (in tesla). Here B_S is polarized in the xz plane. The red line is a guide for the eye.

In summary, in a system with undulated magnetization, progressively increasing B_S, whether in in-plane or out-of-plane geometry, results in a general rise of both the dispersion curves and the frequency gap at the BZ boundary. The increase of the gap is directly linked to the enhancement of the transverse magnetization component through its relative amplitude A. In contrast with the chiral case, however, no evidence of localized modes was found in either the in-plane or out-of-plane configurations.

4.4.6 *Conclusions*

We devised an original method to control SW propagation along a ferromagnetic film by manipulating the spatial undulation (both amplitude and symmetry) of its magnetization. First, we identified the frequency gaps, emerging after the introduction of periodicity, as the result of the interaction between the SW modes and the magnetic field responsible for the non-uniform magnetization. This interaction can be interpreted as a vertical or interfacial coupling in a multilayer system, where the sinusoidal distribution is conveyed by an overlayer with appropriate symmetry (e.g., macrospin chains, artificial spin ice, Dzyaloshinskii-Moriya interaction or ferroelectric domains in multiferroics). To implement this dynamic interaction, we introduced a sinusoidal magnetic bias field B_S, in addition to the uniform field B_0, leading the magnetization to relax into a sinusoidal distribution. The amplitude of this distribution can be finely tuned by adjusting the magnitude of the sinusoidal field. The interaction of the SW modes with B_S produces frequency gaps whose magnitude and frequency range can be controlled by properly tuning B_S. From a dynamic perspective, the physical primitive cell corresponds to half of the geometric one, since the orientation of the magnetization crests is ineffective and only the absolute value matters. We also considered the magnetization distribution obtained after relaxation under a chiral field. In this case, the primitive cell divides into two inequivalent halves: one where the magnetization and chiral field are on average parallel, and the other almost antiparallel. In the latter, the demagnetizing interaction is stronger, due to the greater divergence of the magnetization, which creates a deeper effective field well where low-frequency SWs become localized. This asymmetry is reflected in every magnon space profile. In particular, even at small B_C, an additional solution arises at low frequencies: it is uniform but localized within the second half of the primitive cell. Interestingly, its frequency decreases as B_C increases, but its dispersion remains flat, meaning this mode is localized and stationary regardless of B_C. Localized modes are absent in uniformly magnetized films and do not appear under a sinusoidal field. They arise only under a chiral field, and being simultaneous with propagating modes of similar symmetry and separated by only a few MHz, they provide an additional channel to store and sort dynamic information. This implies that a waveguide can be switched into a dynamic memory without altering the physical ferromagnetic system. Moreover, we found that the effective gyromagnetic ratio of this localized mode exceeds that of FMR in permalloy, which is promising for next-generation magnetic sensor design.

In conclusion, we conceived and characterized a system where spin-wave propagation properties can be modified on demand by tuning the amplitude of the sinusoidal spatial distribution of magnetization. This result is particularly relevant in 3D magnonics, where suitable macrospin distributions, magnetic domains, or ferroelectric domain orientations in a layer can, via vertical interaction, induce such a sinusoidal distribution in the magnetization of the underlying ferromagnetic film. The ultimate goal is not only to provide insights into the complexity of dynamics in 3D magnonic architectures but also

to offer and characterize new degrees of freedom for signal filtering, manipulation, information storage, and delivery. Furthermore, the enhanced properties arising from the sinusoidal distribution (e.g., the effective gyromagnetic ratio) make our system a strong candidate for metamaterial-based sensing. For these reasons, we hope to stimulate interest in this subject and encourage its practical realization through dedicated experimental investigations.

BIBLIOGRAPHY

[1] Andrii Chumak et al. "Magnon Spintronics". In: *Nature Physics* 11 (June 2015), pp. 453–461. DOI: 10.1038/nphys3347.

[2] B. Lenk et al. "The building blocks of magnonics". In: *Physics Reports* 507.4 (2011), pp. 107–136. ISSN: 0370-1573. DOI: https://doi.org/10.1016/j.physrep.2011.06.003. URL: https://www.sciencedirect.com/science/article/pii/S0370157311001694.

[3] J. Rychły et al. "Magnonic crystals—Prospective structures for shaping spin waves in nanoscale". In: *Low Temperature Physics* 41.10 (Oct. 2015), pp. 745–759. ISSN: 1063-777X. DOI: 10.1063/1.4932348. eprint: https://pubs.aip.org/aip/ltp/article-pdf/41/10/745/15603136/745_1_online.pdf. URL: https://doi.org/10.1063/1.4932348.

[4] S. Neusser et al. "Magnonic minibands in antidot lattices with large spin-wave propagation velocities". In: *Phys. Rev. B* 84 (9 Sept. 2011), p. 094454. DOI: 10.1103/PhysRevB.84.094454. URL: https://link.aps.org/doi/10.1103/PhysRevB.84.094454.

[5] M Krawczyk and D Grundler. "Review and prospects of magnonic crystals and devices with reprogrammable band structure". In: *Journal of physics. Condensed matter : an Institute of Physics journal* 26.12 (Mar. 2014), p. 123202. ISSN: 0953-8984. DOI: 10.1088/0953-8984/26/12/123202. URL: https://doi.org/10.1088/0953-8984/26/12/123202.

[6] Krzysztof Szulc et al. "Reconfigurable Magnonic Crystals Based on Imprinted Magnetization Textures in Hard and Soft Dipolar-Coupled Bilayers". In: *ACS Nano* 16.9 (2022). PMID: 36043881, pp. 14168–14177. DOI: 10.1021/acsnano.2c04256. eprint: https://doi.org/10.1021/acsnano.2c04256. URL: https://doi.org/10.1021/acsnano.2c04256.

[7] Arabinda Haldar and Adekunle Olusola Adeyeye. "Reconfigurable and self-biased magnonic metamaterials". In: *Journal of Applied Physics* 128.24 (Dec. 2020), p. 240902. ISSN: 0021-8979. DOI: 10.1063/5.0033254. eprint: https://pubs.aip.org/aip/jap/article-pdf/doi/10.1063/5.0033254/20019716/240902_1_5.0033254.pdf. URL: https://doi.org/10.1063/5.0033254.

[8] P. Micaletti et al. "A sinusoidal magnetization distribution as an original way to generate a versatile magnonic crystal for magnon propagation". In: *Journal of Magnetism and Magnetic Materials* 622 (2025), p. 172959. DOI: 10.1016/j.jmmm.2025.172959. URL: https://doi.org/10.1016/j.jmmm.2025.172959.

[9] P. Micaletti et al. "A sinusoidal magnetization distribution as an original way to generate a versatile magnonic crystal for magnon propagation". In: *Journal of Magnetism and Magnetic Materials* 622 (2025), p. 172959. ISSN: 0304-8853. DOI: https://doi.org/10.1016/j.jmmm.2025.172959. URL: https://www.sciencedirect.com/science/article/pii/S0304885325001908.

[10] A. Roxburgh et al. "Generation of spin-wave packets by reconfigurable nanomagnonic heterojunctions". In: *Phys. Rev. Appl.* 24 (1 July 2025), p. 014047. DOI: 10.1103/bkqp-vjhy. URL: https://link.aps.org/doi/10.1103/bkqp-vjhy.

[11] Hamed Rahmani et al. "Next-Generation IoT Devices: Sustainable Eco-Friendly Manufacturing, Energy Harvesting, and Wireless Connectivity". In: *IEEE Journal of Microwaves* 3 (Jan. 2023), pp. 237–255. DOI: 10.1109/JMW.2022.3228683.

[12] Karl Rupp. *50 Years of Microprocessor Trend Data*. Accessed: 2022. 2022. URL: https://github.com/karlrupp/microprocessor-trend-data.

[13] M. Mitchell Waldrop. "More than Moore". In: *Nature* 530 (2016), pp. 144–147. DOI: 10.1038/530144a. URL: https://doi.org/10.1038/530144a.

[14] Loïc Lannelongue et al. "GREENER principles for environmentally sustainable computational science". In: *Nature Computational Science* 3.6 (June 2023), pp. 514–521. ISSN: 2662-8457. DOI: 10.1038/s43588-023-00461-y. URL: https://doi.org/10.1038/s43588-023-00461-y.

[15] Abdulqader Mahmoud et al. "Introduction to spin wave computing". In: *Journal of Applied Physics* 128 (Oct. 2020), p. 161101. DOI: doi.org/10.1063/5.0019328. URL: http://doi.org/10.1063/5.0019328.

[16] György Csaba, Ádám Papp, and Wolfgang Porod. "Perspectives of using spin waves for computing and signal processing". In: *Physics Letters A* 381 (17 Mar. 2017), p. 1471. DOI: 10.1016/j.physleta.2017.02.042. URL: https://doi.org/10.1016/j.physleta.2017.02.042.

[17] Mojtaba Taghipour Kaffash, SergiLendinez, and M. Benjamin-Jungfleisch. "Nanomagnonics with artificial spin ice". In: *Physics Letters A* 402 (Apr. 2021), p. 127364. DOI: 10.1016/j.physleta.2021.127364. URL: https://doi.org/10.1016/j.physleta.2021.127364.

[18] Anjan Barman et al. "The 2021 Magnonics Roadmap". In: *Journal of Physics: Condensed Matter* 33.41 (Aug. 2021), p. 413001. DOI: 10.1088/1361-648X/abec1a. URL: https://dx.doi.org/10.1088/1361-648X/abec1a.

[19] Ezio Iacocca and Olle Heinonen. "Topologically Nontrivial Magnon Bands in Artificial Square Spin Ices with Dzyaloshinskii-Moriya Interaction". In: *Phys. Rev. Applied* 8 (3 Sept. 2017), p. 034015. DOI: 10.1103/PhysRevApplied.8.034015. URL: https://link.aps.org/doi/10.1103/PhysRevApplied.8.034015.

[20] G. Gubbiotti et al. "Collective spin waves in arrays of permalloy nanowires with single-side periodically modulated width". In: *Applied Physics Letters* 111.19 (Nov. 2017), p. 192403. ISSN: 0003-6951. DOI: 10.1063/1.5006294. eprint: https://pubs.aip.org/aip/apl/article-pdf/doi/10.1063/1.5006294/14100898/192403_1_online.pdf. URL: https://doi.org/10.1063/1.5006294.

[21] Huajun Qin et al. "Low-loss YIG-based magnonic crystals with large tunable bandgaps". In: *Nature Communications* 9 (Dec. 2018). DOI: 10.1038/s41467-018-07893-5.

[22] D. Kumar et al. "Magnonic band structure, complete bandgap, and collective spin wave excitation in nanoscale two-dimensional magnonic crystals". In: *Journal of Applied Physics* 115.4 (Jan. 2014), p. 043917. ISSN: 0021-8979. DOI: 10.1063/1.4862911. eprint: https://pubs.aip.org/aip/jap/article-pdf/doi/10.1063/1.4862911/15132756/043917_1_online.pdf. URL: https://doi.org/10.1063/1.4862911.

[23] Ali Frotanpour et al. "Magnetization dynamics of a Fibonacci-distorted kagome artificial spin ice". In: *Physical Review B* 102 (2020), p. 224435. DOI: 10.1103/PhysRevB.102.224435.

[24] Wonbae Bang et al. "Influence of the Vertex Region on Spin Dynamics in Artificial Kagome Spin Ice". In: *Phys. Rev. Appl.* 14 (1 July 2020), p. 014079. DOI: 10.1103/PhysRevApplied.14.014079. URL: https://link.aps.org/doi/10.1103/PhysRevApplied.14.014079.

[25] Sergi Lendinez et al. "Nonlinear multi-magnon scattering in artificial spin ice". In: *Nature Communications* 14 (2023), p. 3419. URL: https://www.nature.com/articles/s41467-023-38992-7.

[26] Kanta Mori et al. "Orientation-dependent two-dimensional magnonic crystal modes in an ultralow-damping ferrimagnetic waveguide containing repositioned hexagonal lattices of Cu disks". In: *Phys. Rev. Appl.* 21 (1 Jan. 2024), p. 014061. DOI: 10.1103/PhysRevApplied.21.014061. URL: https://link.aps.org/doi/10.1103/PhysRevApplied.21.014061.

[27] Alison Roxburgh and Ezio Iacocca. "Nano-Magnonic Crystals by Periodic Modulation of Magnetic Parameters". In: *Magnetochemistry* 10.3 (2024). ISSN: 2312-7481. DOI: 10.3390/magnetochemistry10030014. URL: https://www.mdpi.com/2312-7481/10/3/14.

[28] Pietro Micaletti and Federico Montoncello. "Dynamic footprints of the specific artificial spin ice microstate on its spin waves". In: *Magnetochemistry* 9.6 (2023), p. 158. DOI: 10.3390/magnetochemistry9060158. URL: https://www.mdpi.com/2312-7481/9/6/158.

[29] Jean-Claude Serge Levy. *Magnetic Structures of 2D and 3D Nanoparticles: Properties and Applications*. Jenny Stanford Publishing, 2016. ISBN: 9789814613675.

[30] G. Gubbiotti. *Three-Dimensional Magnonics: Layered, Micro- and Nanostructures*. Singapore: Jenny Stanford Publishing, 2019.

[31] Sourav Sahoo et al. "Observation of Coherent Spin Waves in a Three-Dimensional Artificial Spin Ice Structure". In: *Nano Lett.* 21 (2021), p. 4629. DOI: 10.1021/acs.nanolett.1c00650. URL: https://doi.org/10.1021/acs.nanolett.1c00650.

[32] S. Ladak, A. Fernández-Pacheco, and P. Fischer. "Science and technology of 3D magnetic nanostructures". In: *APL Materials* 10.1 (Science and Technology of 3D Magnetic Nanostructures 2022), p. 5. DOI: /10.1063/5.0136801. URL: https://doi.org/10.1063/5.0136801.

[33] Jack C. Gartside et al. "Reconfigurable training and reservoir computing in an artificial spin-vortex ice via spin-wave fingerprinting". In: *Nature Nanotechnology* 17.5 (May 2022), pp. 460–469. ISSN: 1748-3395. DOI: 10.1038/s41565-022-01091-7. URL: https://doi.org/10.1038/s41565-022-01091-7.

[34] Jack C. Gartside et al. "Reconfigurable magnonic mode-hybridisation and spectral control in a bicomponent artificial spin ice". In: *Nature Communications* 12 (2021), p. 2488. DOI: 10.1038/s41467-021-22723-x. URL: https://doi.org/10.1038/s41467-021-22723-x.

[35] Ezio Iacocca, Sebastian Gliga, and Olle G. Heinonen. "Tailoring Spin-Wave Channels in a Reconfigurable Artificial Spin Ice". In: *Phys. Rev. Applied* 13 (4 Apr. 2020), p. 044047. DOI: 10.1103/PhysRevApplied.13.044047. URL: https://link.aps.org/doi/10.1103/PhysRevApplied.13.044047.

[36] Troy Dion et al. "Ultrastrong magnon-magnon coupling and chiral spin-texture control in a dipolar 3D multilayered artificial spin-vortex ice". In: *Nature Communications* 15.1 (May 2024), p. 4077. ISSN: 2041-1723. DOI: 10.1038/s41467-024-48080-z. URL: https://doi.org/10.1038/s41467-024-48080-z.

[37] R. Negrello et al. "Dynamic coupling and spin-wave dispersions in a magnetic hybrid system made of an artificial spin-ice structure and an extended NiFe underlayer". In: *APL Materials* 10 (2022), p. 091115. DOI: 10.1063/5.0102571. URL: https://doi.org/10.1063/5.0102571.

[38] F. Montoncello et al. "A Brillouin light scattering study of the spin-wave magnetic field dependence in a magnetic hybrid system made of an artificial spin-ice structure and a film underlayer". In: *Journal of Applied Physics* 133 (Recent Advances in Magnonics Feb. 2023), p. 083901. DOI: 10.1063/5.0140866. URL: http://dx.doi.org/10.1063/5.0140866.

[39] Davide Girardi et al. "Three-dimensional spin-wave dynamics, localization and interference in a synthetic antiferromagnet". In: *Nature Communications* 15.1 (Apr. 2024), p. 3057. ISSN: 2041-1723. DOI: 10.1038/s41467-024-47339-9. URL: https://doi.org/10.1038/s41467-024-47339-9.

[40] Yong-Keun Park et al. "Experimental observation of the correlation between the interfacial Dzyaloshinskii–Moriya interaction and work function in metallic magnetic trilayers". In: *NPG Asia Materials* 10.10 (Oct. 2018), pp. 995–1001. ISSN: 1884-4057. DOI: 10.1038/s41427-018-0090-x. URL: https://doi.org/10.1038/s41427-018-0090-x.

[41] A. Sud et al. "Tailoring interfacial effect in multilayers with Dzyaloshinskii–Moriya interaction by helium ion irradiation". In: *Scientific Reports* 11.1 (Dec. 2021), p. 23626. ISSN: 2045-2322. DOI: 10.1038/s41598-021-02902-y. URL: https://doi.org/10.1038/s41598-021-02902-y.

[42] Zhenyu Wang et al. "Magnonic Frequency Comb through Nonlinear Magnon-Skyrmion Scattering". In: *Phys. Rev. Lett.* 127 (3 July 2021), p. 037202. DOI: 10.1103/PhysRevLett.127.037202. URL: https://link.aps.org/doi/10.1103/PhysRevLett.127.037202.

[43] J. Flores-Farías et al. "Selective nonreciprocal localization of flat magnonic modes induced by a periodic Dzyaloshinskii-Moriya interaction". In: *Phys. Rev. B* 109 (5 Feb. 2024), p. 054423. DOI: 10.1103/PhysRevB.109.054423. URL: https://link.aps.org/doi/10.1103/PhysRevB.109.054423.

[44] N. S. Gusev et al. "Manipulation of the Dzyaloshinskii–Moriya Interaction in Co/Pt Multilayers with Strain". In: *Phys. Rev. Lett.* 124 (15 Apr. 2020), p. 157202. DOI: 10.1103/PhysRevLett.124.157202. URL: https://link.aps.org/doi/10.1103/PhysRevLett.124.157202.

[45] Julia Kharlan et al. *Tunable magnonic crystal in a hybrid superconductor–ferrimagnet nanostructure*. 2024. arXiv: 2408.01240 [cond-mat.mes-hall]. URL: https://arxiv.org/abs/2408.01240.

[46] Igor A. Golovchanskiy et al. "Ferromagnet/Superconductor Hybrid Magnonic Metamaterials". In: *Advanced Science* 6.16 (2019), p. 1900435. DOI: https://doi.org/10.1002/advs.201900435. eprint: https://onlinelibrary.wiley.com/doi/pdf/10.1002/advs.201900435. URL: https://onlinelibrary.wiley.com/doi/abs/10.1002/advs.201900435.

[47] I.A. Golovchanskiy et al. "Magnetization Dynamics in Proximity-Coupled Superconductor-Ferromagnet-Superconductor Multilayers". In: *Phys. Rev. Appl.* 14 (2 Aug. 2020), p. 024086. DOI: 10.1103/PhysRevApplied.14.024086. URL: https://link.aps.org/doi/10.1103/PhysRevApplied.14.024086.

[48] I. A. Golovchanskiy et al. "Nonlinear spin waves in ferromagnetic/superconductor hybrids". In: *Journal of Applied Physics* 127.9 (Mar. 2020), p. 093903. ISSN: 0021-8979. DOI: 10.1063/1.5141793. eprint: https://pubs.aip.org/aip/jap/article-pdf/doi/10.1063/1.5141793/13371075/093903_1_online.pdf. URL: https://doi.org/10.1063/1.5141793.

[49] Krzysztof Szulc, Mateusz Zelent, and Maciej Krawczyk. *Reconfigurable spin-wave platform based on interplay between nanodots and waveguide in hybrid magnonic crystal*. 2024. arXiv: 2404.10493 [cond-mat.mes-hall].

[50] Even though outside the field of 3D-Magnonics, interestingly in Ref. [94] a sinusoidal field was implemented by electric current flowing through a meander-type geometry.

[51] A. V. Chumak et al. "Advances in Magnetics Roadmap on Spin-Wave Computing". In: *IEEE Transactions on Magnetics* 58.6 (2022), pp. 1–72. DOI: 10.1109/TMAG.2022.3149664.

[52] Harrison W. Fuller and Murray E. Hale. "Determination of Magnetization Distribution in Thin Films Using Electron Microscopy". In: *Journal of Applied Physics* 31.2 (Feb. 1960), pp. 238–248. ISSN: 0021-8979. DOI: 10.1063/1.1735552. eprint: https:

//pubs.aip.org/aip/jap/article-pdf/31/2/238/18320948/238_1_online.pdf. URL: https://doi.org/10.1063/1.1735552.

[53] K. J. Harte. "Theory of Magnetization Ripple in Ferromagnetic Films". In: *Journal of Applied Physics* 39.3 (Feb. 1968), pp. 1503–1524. ISSN: 0021-8979. DOI: 10.1063/1.1656388. eprint: https://pubs.aip.org/aip/jap/article-pdf/39/3/1503/18345605/1503_1_online.pdf. URL: https://doi.org/10.1063/1.1656388.

[54] H. Hoffmann. "Theory of magnetization ripple". In: *IEEE Transactions on Magnetics* 4.1 (1968), pp. 32–38. DOI: 10.1109/TMAG.1968.1066186.

[55] H. Riedel. "Micromagnetic Theory of Large-Angle Ripples and Stripe Domains in Thin Ferromagnetic Films". In: *physica status solidi (a)* 24.2 (1974), pp. 449–460. DOI: https://doi.org/10.1002/pssa.2210240209. eprint: https://onlinelibrary.wiley.com/doi/pdf/10.1002/pssa.2210240209. URL: https://onlinelibrary.wiley.com/doi/abs/10.1002/pssa.2210240209.

[56] 3D Magnonics is a relatively recent research field where the magnon excitation and propagation properties are studied and designed as emerging from the interactions occurring along all the three Cartesian directions. As a consequence, magnon control at the nanoscale is attained by the design of the geometric and magnetic structure along the three directions. It must be considered distinct from the concept of 3D magnonic crystal (a ferromagnetic diffraction grating where periodicity is along all the three directions), which is rather a subset field of 3D Magnonics. In particular, 3D stacks of layers are considered a subject of 3D Magnonics, even when periodicity (and magnon propagation) is along two or even one direction only, as in our case.

[57] Amalio Fernández-Pacheco et al. "Three-dimensional nanomagnetism". In: *Nature Communications* 8.1 (June 2017), p. 15756. ISSN: 2041-1723. DOI: 10.1038/ncomms15756. URL: https://doi.org/10.1038/ncomms15756.

[58] Arne Vansteenkiste et al. "The design and verification of MuMax3". In: *AIP Advances* 4.10 (2014), p. 107133. DOI: 10.1063/1.4899186.

[59] Hans Fangohr et al. "A new approach to (quasi) periodic boundary conditions in micromagnetics: The macrogeometry". In: *Journal of Applied Physics* 105 (2009), p. 07D529. DOI: 10.1063/1.3068637. eprint: https://doi.org/10.1063/1.3068637. URL: https://doi.org/10.1063/1.3068637.

[60] R.W. Damon and J.R. Eshbach. "Magnetostatic modes of a ferromagnet slab". In: *Journal of Physics and Chemistry of Solids* 19.3 (1961), pp. 308–320. ISSN: 0022-3697. DOI: https://doi.org/10.1016/0022-3697(61)90041-5. URL: https://www.sciencedirect.com/science/article/pii/0022369761900415.

[61] Hans-Benjamin Braun. "Topological effects in nanomagnetism: from superparamagnetism to chiral quantum solitons". In: *Advances in Physics* 61.1 (2012), pp. 1–116. DOI: 10.1080/00018732.2012.663070. eprint: https://doi.org/10.1080/00018732.2012.663070. URL: https://doi.org/10.1080/00018732.2012.663070.

[62] F. Brevis et al. "The toroidal moments in confined nanomagnets and its impact on magnonics". In: *arXiv preprint* (2024). arXiv: 2412.13309 [cond-mat.mes-hall]. URL: https://arxiv.org/abs/2412.13309.

[63] B. Van de Wiele and F. Montoncello. "A continuous excitation approach to determine time-dependent dispersion diagrams in 2D magnonic crystals". In: *J. Phys. D: Appl. Phys.* 47 (2014). 10.1088/0022-3727/47/31/315002, p. 315002.

[64] G. Venkat et al. "Proposal for a standard micromagnetic problem: spin wave dispersion in a magnonic waveguide". In: *IEEE Trans. Magn.* 49 (2013), p. 524. URL: https://ieeexplore.ieee.org/document/6228538.

[65] C. Kittel, P. McEuen, and John Wiley & Sons. *Introduction to Solid State Physics*. John Wiley & Sons, 2015. ISBN: 9788126535187. URL: https://books.google.it/books?id=rAMujwEACAAJ.

[66] R. D. McMichael and B. B. Maranville. "Edge saturation fields and dynamic edge modes in ideal and nonideal magnetic film edges". In: *Phys. Rev. B* 74 (2 July 2006), p. 024424. DOI: 10.1103/PhysRevB.74.024424. URL: https://link.aps.org/doi/10.1103/PhysRevB.74.024424.

[67] Justin M. Shaw et al. "Spin dynamics and mode structure in nanomagnet arrays: Effects of size and thickness on linewidth and damping". In: *Phys. Rev. B* 79 (18 May 2009), p. 184404. DOI: 10.1103/PhysRevB.79.184404. URL: https://link.aps.org/doi/10.1103/PhysRevB.79.184404.

[68] G. Gubbiotti et al. "Spin dynamics in thin nanometric elliptical Permalloy dots: A Brillouin light scattering investigation as a function of dot eccentricity". In: *Phys. Rev. B* 72 (18 Nov. 2005), p. 184419. DOI: 10.1103/PhysRevB.72.184419. URL: https://link.aps.org/doi/10.1103/PhysRevB.72.184419.

[69] R. Zivieri et al. "Collective spin modes in chains of dipolarly interacting rectangular magnetic dots". In: *Phys. Rev. B* 83 (5 Feb. 2011), p. 054431. DOI: 10.1103/PhysRevB.83.054431. URL: https://link.aps.org/doi/10.1103/PhysRevB.83.054431.

[70] F. Montoncello and G. Gubbiotti. "Controlling the three dimensional propagation of spin waves in continuous ferromagnetic films with an increasing out of plane undulation". In: *Scientific Reports* 11 (Nov. 2021), p. 21344. DOI: 10.1038/s41598-021-00479-0. URL: https://doi.org/10.1038/s41598-021-00479-0.

[71] Michael Tinkham. *Group Theory and Quantum Mechanics*. Dover Publications, 2003. ISBN: 9780486432472,0486432475.

[72] S. Mamica et al. "Large magnonic band gaps and spectra evolution in three-dimensional magnonic crystals based on magnetoferritin nanoparticles". In: *Phys. Rev. B* 86 (14 Oct. 2012), p. 144402. DOI: 10.1103/PhysRevB.86.144402. URL: https://link.aps.org/doi/10.1103/PhysRevB.86.144402.

[73] Karl W. Böer and Udo W. Pohl. "The Origin of Band Structure". In: *Semiconductor Physics*. Cham: Springer International Publishing, 2017, pp. 1–20. ISBN: 978-3-319-06540-3. DOI: 10.1007/978-3-319-06540-3_6-1. URL: https://doi.org/10.1007/978-3-319-06540-3_6-1.

[74] Hao Sun et al. "Interacting topological Dirac magnons". In: *Phys. Rev. B* 107 (13 Apr. 2023), p. 134426. DOI: 10.1103/PhysRevB.107.134426. URL: https://link.aps.org/doi/10.1103/PhysRevB.107.134426.

[75] L. Giovannini. "Dirac magnons in honeycomb nanostructures". In: *Phys. Rev. B* 107 (10 Mar. 2023), p. 104418. DOI: 10.1103/PhysRevB.107.104418. URL: https://link.aps.org/doi/10.1103/PhysRevB.107.104418.

[76] Sergey S. Pershoguba et al. "Dirac Magnons in Honeycomb Ferromagnets". In: *Phys. Rev. X* 8 (1 Jan. 2018), p. 011010. DOI: 10.1103/PhysRevX.8.011010. URL: https://link.aps.org/doi/10.1103/PhysRevX.8.011010.

[77] S. Mamica and M. Krawczyk. "Reversible tuning of omnidirectional band gaps in two-dimensional magnonic crystals by magnetic field and in-plane squeezing". In: *Physical Review B* 100 (2019), p. 214410. DOI: 10.1103/PhysRevB.100.214410. URL: https://link.aps.org/doi/10.1103/PhysRevB.100.214410.

[78] R A Gallardo et al. "Spin-wave non-reciprocity in magnetization-graded ferromagnetic films". In: *New Journal of Physics* 21.3 (Mar. 2019), p. 033026. DOI: 10.1088/1367-2630/ab0449. URL: https://dx.doi.org/10.1088/1367-2630/ab0449.

[79] Conyers Herring and Charles Kittel. "On the Theory of Spin Waves in Ferromagnetic Media". In: *Phys. Rev.* 81 (5 Mar. 1951), pp. 869–880. DOI: 10.1103/PhysRev.81.869. URL: https://link.aps.org/doi/10.1103/PhysRev.81.869.

[80] B A Kalinikos and A N Slavin. "Theory of dipole-exchange spin wave spectrum for ferromagnetic films with mixed exchange boundary conditions". In: *Journal of Physics C: Solid State Physics* 19.35 (Dec. 1986), p. 7013. DOI: 10.1088/0022-3719/19/35/014. URL: https://dx.doi.org/10.1088/0022-3719/19/35/014.

[81] S. Mamica. "The influence of the demagnetizing field on the concentration of spin wave energy in two-dimensional magnonic crystals". In: *Journal of Magnetism and Magnetic Materials* 588 (2023), p. 171395. ISSN: 0304-8853. DOI: https://doi.org/10.1016/j.jmmm.2023.171395. URL: https://www.sciencedirect.com/science/article/pii/S0304885323010454.

[82] C. Kittel. "On the Theory of Ferromagnetic Resonance Absorption". In: *Physical Review* 73 (1948), p. 155. DOI: 10.1103/PhysRev.73.155.

[83] M. Bailleul, R. Höllinger, and C. Fermon. "Microwave spectrum of square Permalloy dots: Quasisaturated state". In: *Phys. Rev. B* 73 (10 Mar. 2006), p. 104424. DOI: 10.1103/PhysRevB.73.104424. URL: https://link.aps.org/doi/10.1103/PhysRevB.73.104424.

[84] J. Jorzick et al. "Spin Wave Wells in Nonellipsoidal Micrometer Size Magnetic Elements". In: *Physical Review Letters* 88 (4 Jan. 2002), p. 047204. DOI: 10.1103/PhysRevLett.88.047204. URL: https://link.aps.org/doi/10.1103/PhysRevLett.88.047204.

[85] J. P. Park et al. "Spatially Resolved Dynamics of Localized Spin-Wave Modes in Ferromagnetic Wires". In: *Phys. Rev. Lett.* 89 (27 Dec. 2002), p. 277201. DOI: 10.1103/PhysRevLett.89.277201. URL: https://link.aps.org/doi/10.1103/PhysRevLett.89.277201.

[86] K. Y. Guslienko, R. W. Chantrell, and A. N. Slavin. "Dipolar localization of quantized spin-wave modes in thin rectangular magnetic elements". In: *Phys. Rev. B* 68 (2 July 2003), p. 024422. DOI: 10.1103/PhysRevB.68.024422. URL: https://link.aps.org/doi/10.1103/PhysRevB.68.024422.

[87] G. Gubbiotti et al. "Spin wave dispersion and intensity correlation in width-modulated nanowire arrays: A Brillouin light scattering study". In: *Journal of Applied Physics* 124 (Aug. 2018), p. 083903. DOI: doi.org/10.1063/1.5047393. URL: http://doi.org/10.1063/1.5047393.

[88] D. Kuźma et al. "Spin wave propagation properties across configurational antiferro/ferro-magnetic transitions". In: *Journal of Applied Physics* 124.22 (Dec. 2018), p. 223902. ISSN: 0021-8979. DOI: 10.1063/1.5057419. eprint: https://pubs.aip.org/aip/jap/article-pdf/doi/10.1063/1.5057419/13708421/223902_1_online.pdf. URL: https://doi.org/10.1063/1.5057419.

[89] V.V. Kruglyak et al. "Magnonic Metamaterials". In: *Metamaterial*. Ed. by Xun-Ya Jiang. Rijeka: IntechOpen, 2012. Chap. 14. DOI: 10.5772/37454. URL: https://doi.org/10.5772/37454.

[90] O. Haas, B. Dufay, and S. Saez. "Development of a Magnonic-Based Magnetic Sensor: Comparison of Two Different Implementations With YIG Material". In: *IEEE Transactions on Magnetics* 59.2 (2023), pp. 1–6. DOI: 10.1109/TMAG.2022.3215274.

[91] Md Shamim Sarker et al. "Sensitivity enhancement in magnetic sensor using CoFeB/Y3Fe5O12 resonator". In: *Scientific Reports* 12.1 (June 2022), p. 11105. ISSN: 2045-2322. DOI: 10.1038/s41598-022-15317-0. URL: https://doi.org/10.1038/s41598-022-15317-0.

[92] C. L. Degen, F. Reinhard, and P. Cappellaro. "Quantum sensing". In: *Rev. Mod. Phys.* 89 (3 July 2017), p. 035002. DOI: 10.1103/RevModPhys.89.035002. URL: https://link.aps.org/doi/10.1103/RevModPhys.89.035002.

[93] Sergej O. Demokritov and Andrei N. Slavin. "Spin Waves". In: *Handbook of Magnetism and Magnetic Materials*. Ed. by J. M. D. Coey and Stuart S.P. Parkin. Cham: Springer International Publishing, 2021, pp. 281–346. ISBN: 978-3-030-63210-6. DOI: 10.1007/978-3-030-63210-6_6. URL: https://doi.org/10.1007/978-3-030-63210-6_6.

[94] A. V. Chumak et al. "A current-controlled, dynamic magnonic crystal". In: *Journal of Physics D: Applied Physics* 42.20 (2009), p. 205005. DOI: 10.1088/0022-3727/42/20/205005. URL: http://dx.doi.org/10.1088/0022-3727/42/20/205005.

5

CONTROLLING MAGNON PROPAGATION AND FREQUENCY GAP THROUGH THE FAN ANGLE OF A SINUSOIDAL BIAS FIELD

ABSTRACT

Continuing the investigation of the system discussed in the Chapter 4, we investigate, by means of micromagnetic simulations, the spin dynamics of a ferromagnetic film to which a sinusoidal magnetic field is applied with magnitude B_S and a variable fan angle Θ_F. Such a field configuration can be realized through a meander-type geometry or, in multiferroic bilayers, by means of the vertical coupling to a periodically polarized ferroelectric layer, thereby generating a relaxed sinusoidal magnetization distribution depending on B_S and Θ_F. We illustrate in detail how the dispersion curves and the frequency gap at the zone boundary vary with Θ_F, highlighting the sensitivity of the system to the modulation parameters. In particular, we demonstrate an almost parabolic functional behavior of the frequency gap with Θ_F, which provides valuable insight into the tunability of spin-wave spectra in engineered magnetic structures. Therefore, alongside with B_S magnitude, Θ_F represents a further degree of freedom for the control of magnon propagation.

5.1 INTRODUCTION

3D Magnonics [1] explores the manipulation and propagation of spin waves in 3D nanostructures, enabling an advanced control of the information transfer at the nanoscale, for applications in magnon-spintronic devices [2] and next-generation computing technologies [3, 4, 5]. A magnetic film layer generally maintains a uniform magnetic distribution unless it is physically corrugated [6, 7, 8, 9, 10] or coupled with a patterned overlayer. Such a pattern might be irregular though produced by a deterministic rules, like Fibonacci or Penrose tiling structures [11, 12, 13, 14], or regular and periodic, like artificial spin ice systems [15, 16, 17, 18, 19], periodic ferroelectric domain polarization in multiferroics [20, 21], and even periodic superconducting structures [22, 23, 24]. The presence of a non-uniform magnetization in a ferromagnetic film produces confinement effects typical of patterned structures, in particular numerous spin wave modes, which provide additional degrees of freedom, with respect to the single one of the uniform film, extremely useful for signal manipulation. In the investigation carried out in Chapter 4, we studied the evolution of magnonic band structures in a ferromagnetic film when a sinusoidal field is applied with variable amplitude [25]. In the experiments, this field can be directly applied to the system through a meander-type geometry, through which a current flows: the geometry of the meander determines the period and amplitude of the sinusoidal field [26, 27]. In the context of a multilayer geometry, the sinusoidal field can be produced by the vertical coupling with an overlayer with a periodic pattern (ferromagnetic, ferroelectric, superconducting and so on [20]). Hence, the sinusoidal field we used is ultimately the simulation of any of the above periodic mechanisms. In the same study we focused on the effect on the magnonic band structure of an increasing magnitude of such a sinusoidal field. In the present Chapter, instead, we study the influence of its fan angle (i.e., its angular spread) at a fixed magnitude. It is not trivial to devise a good degree of freedom to manipulate the spin wave dynamics (group velocity, frequency gap, effective mass etc.) without the help of any magnetic field or electric current variations. We demonstrate that varying the fan angle (hence, geometry) at a fixed (and possibly small) magnetic field magnitude can produce the same results that strong field magnitude variations would have produced, with interesting consequences in the mitigation of the *Joule effect* [28]. The experimental realization of this geometric variation might be challenging, nevertheless we will suggest a few possibilities, keeping in mind that our very purpose is to present a potential scenario, indicating a path for further experimental investigations. We observe that our approach, based on the implementation of a sinusoidal spin pattern, could be easily extended to the case of a fan angle equal to 2π, namely to spin cycloid structures [29, 30]: these special spin textures could be also obtained through appropriate ferroelectric domain distributions and can give origin to non-reciprocal effects which are outside the scope of the present investigation.

5.2 METHODOLOGY

By means of the GPU-accelerated software MuMax3 [31] we perform micromagnetic simulations . The system studied is the same as in Chapter 4. However, for convenience, we summarize the parameter values again below. In order to simulate an extended, realistic square system, quasi-periodic boundary conditions [32] are applied, with 800 copies of the primitive cell along each coordinate axis. Unless otherwise specified, in general we apply a uniform bias field $B_0 = 0.1$ T, along the x direction, to obtain at $k = 0$ a frequency around 10 GHz, but, under some circumstances that will be explained later on, we consider different values for B_0, from 0.03 to 0.15 T. Furthermore, we add a sine-like magnetic field $\boldsymbol{B_S}$, and consider either a magnitude (B_S) or fan angle (Θ_F) variation. B_S varies from 0 to 0.1 T with steps of 0.01 T, Θ_F varies from 0 to π with steps of $\pi/6$. We consider a 5-nm-thick magnetic film layer made of permalloy, with the following magnetic parameters: saturation magnetization $M_S = 800$ kA/m, exchange stiffness $A_{ex} = 10$ pJ/m, and gyromagnetic ratio $\gamma = 185$ rad GHz/T. The primitive cell of the system (Fig. 5.1, panel (a)) is a square with side $a = 256$ nm (lattice constant) and thickness 5 nm. The system is discretized into micromagnetic cells with dimension $4 \times 4 \times 5$ nm^3. Being x the oscillation direction, we consider two polarization planes for B_S: xy (in-plane polarization) and xz (out-of-plane polarization): after the application of B_S, the film magnetization relaxes at equilibrium to a sinusoidal distribution, the amplitude of which depends on both B_S and Θ_F. As an example, in Fig. 5.3 we show the equilibrium magnetization when $\Theta_F = \pi/2$ (panel (a)), and when $\Theta_F = \pi$ (panel (b)), and visibly in the second case the undulation amplitude of the magnetization is larger.

In order to calculate the dispersion curves by means of Fourier analysis, we replicate the primitive cell 200 times along the x-axis, creating a supercell of dimensions $51200 \times 256 \times 5$ nm^3. This allows a wavevector resolution of $0.122 \cdot 10^{-3}$ rad/nm.

To the relaxed magnetization (a stable equilibrium configuration), we apply a non-uniform sinc microwave field for 100 ns and save the time resolved magnetization maps at intervals of $dt = 25$ ps. This allows a frequency resolution of 0.01 GHz and a maximum frequency of 20 GHz. On those magnetization maps, we perform a space-time Fast Fourier Transform to get the dispersion relations. Additional details regarding the sinc and the simulations can be found in Chapter 4, Sec. 4.3.

Furthermore, since we are interested in the comparison of the film with a sinusoidal magnetization to an effective film with a uniform magnetization, we focus on the *equivalence* between the relaxed magnetization under $\boldsymbol{B} \equiv \boldsymbol{B_S} + \boldsymbol{B_0}$ and the relaxed magnetization under a uniform field applied to the system. In particular, we aim to determine the value B^* of the uniform field that, applied alone to an uniformly magnetized film, would give the *same* energy density of the simulated system with a sinusoidal magnetization subject to the magnetic field B (equivalence).

Therefore, we make use of the *Kittel formula* for a thin film [33]:

$$\omega = \gamma \sqrt{B^*(B^* + \mu_0 M_S)}, \tag{5.1}$$

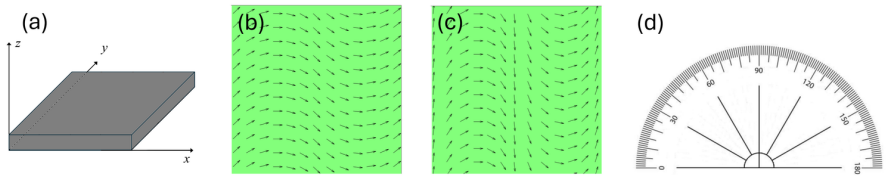

Figure 5.1: Panel (a): scheme of the primitive unit cell and corresponding reference system. Panels (b) and (c): sketches of the vector field distributions subject of the investigation (the color marks the background, the arrows are only illustrative of the undulation). B_S with $\Theta_F = \pi/2$ and B_S with $\Theta_F = \pi$, respectively. In the second case the correspondent undulation amplitude is larger. Panel (d): fan angles considered throughout the investigation.

where γ is the gyromagnetic ratio, B^* is the uniform field applied to the system, μ_0 the magnetic permeability of the vacuum, and M_S the saturation magnetization. Eq. (5.1) is the particular form of the general Kittel formula (1.45) introduced in Chapter 1.

The *magnetic energy density* is given by:

$$u = -\sum_i (M_x^i B_x^i + M_y^i B_y^i + M_z^i B_z^i), \tag{5.2}$$

where the summation index goes over all the micromagnetic cells in the primitive cell, the magnetization components M_x, M_y, M_z are obtained after the relaxation process and the magnetic field components B_x, B_y, B_z represent the contributions of B_S and B_0. Clearly, the better the discretization of the micromagnetic cell, the more accurate the computed energy density: this aspect will be addressed in Sec. 5.3 and represents an important validation of the simulations. The energy density can also be expressed in terms of the saturation magnetization M_S as follows:

$$u = -M_s B^*. \tag{5.3}$$

In this approach, B^* reproduces in the uniform film what B does in the sinusoidally magnetized one to provide the same energy density, within a certain accuracy. By requiring the equivalence between the energy densities of Eqs. (5.2) and (5.3), we obtain the *fictitious field* B^*, which should enter the Kittel formula 5.1 to determine the exact resonance frequency found by the micromagnetic simulations, for each value of B_S or Θ_F.

5.3 RESULTS

The application of $\boldsymbol{B}_S$ makes the film magnetization relax into a likewise sinusoidal distribution, with a spatial amplitude correlated to the magnitude B_S and the fan angle Θ_F. Being in our case the oscillation only along a single direction (x-axis), the induced periodicity turns the film into a one-dimensional (1-D) magnonic crystal, as already explained. Therefore, along that direction, magnons undergo Bragg diffraction and their dispersion curve shows the distinctive marks: *periodic folding* to the reduced Brillouin zone and *frequency gaps* at the Brillouin zone boundary. In Chapter 4, we observed that in undulated systems the actual (physical) lattice constant d governing the spin-wave dynamics is a half of the geometric one, i.e., $d = a/2$. Hence,

the actual Brillouin zone boundary occurs at $k = 0.0245$ rad/nm, i.e., twice the geometric one (0.01225 rad/nm). The underlying reason is that the spin-wave spectrum is invariant under a horizontal mirror operation σ_y on the magnetization, and that corresponds to a sign inversion of its y component. This additional symmetry is responsible for the doubling of the actual Brillouin zone boundary. The application of a bias field that is periodic along a direction (x-axis) influences the dynamics also in the transverse direction (y-axis), since new modes arise as Bloch waves, additional to the film spin-wave. In our case, since the magnetization vector flux is oriented parallel to the x-direction, the backward volume (BV) mode dispersion shows the typical band structure, and the folding to the reduced Brillouin zone determines new modes at $k = 0$ which were not present in the uniformly magnetized film. These modes have a cell function with a progressively increasing number n of backward nodes, i.e., nodal lines perpendicular to the propagation direction: n-BV. Hence, these new modes, generated by the folding of the BV dispersion, are also the cell function of new Bloch waves (propagating along y), and produce their individual dispersion. In Fig. 5.2 we show the band structure for sinusoidal magnetized films with $B_S = 0.03$ T ($\Theta_F = \pi$) in the two undulation polarizations xy (left panel) and xz (right panel). The right half of each panel shows the band structure of BV modes (characterized by periodicity), while the left half shows the DE dispersions of the first two modes, specifically the fundamental one, also named o-BV, and the 1-BV. In fact, the higher order modes are not perceptible in the plots. Hence, even if periodicity is not present along this direction, the dynamics is influenced as well.

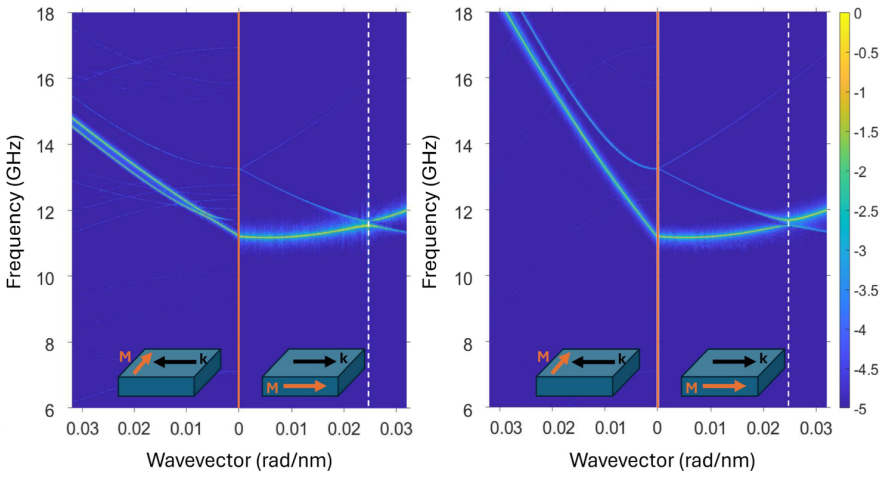

Figure 5.2: Band structure for a sinusoidal magnetization in-plane (left panel) and out-of-plane (right panel) polarized, when $B_S = 0.03$ T. On the left half of each panel the DE dispersions are plotted, while on the right half of each panel the BV dispersions are plotted waves for $B_S = 0.03$ T. The dashed white line marks the zone boundary ($k = 0.0245$ rad/nm), where a frequency gap opens. The color bar on the right represents intensity in arbitrary units.

5.3.1 *Influence of fan angle*

Now we investigate the role of Θ_F in controlling the equilibrium magnetization and hence both the magnon band structure and frequency gap. As observed in Sec. 5.1, a sinusoidal magnetization can be induced in a film in many ways. Hence, in real experiments, Θ_F can be changed depending on the specific used method. For example, Θ_F can be varied by varying the polarization direction of each ferroelectric domain, if a ferroelectric/ferromagnetic heterojunction is concerned [34, 35], or by varying the meander-type geometry, if a current flow is used [26] and so on.

In the next simulations, we fix $B_S = 0.07$ T and vary Θ_F. In Fig.5.3 we show the equilibrium magnetization obtained after the relaxation to a sinusoidal field with $\Theta_F = \pi/2$ (panel (a)) and $\Theta_F = \pi$ (panel (b)). Notice that in panel (b) the undulation of the magnetization has a larger amplitude, as a consequence of the larger fan angle of B_S (favoring m_y at the expense of m_x).

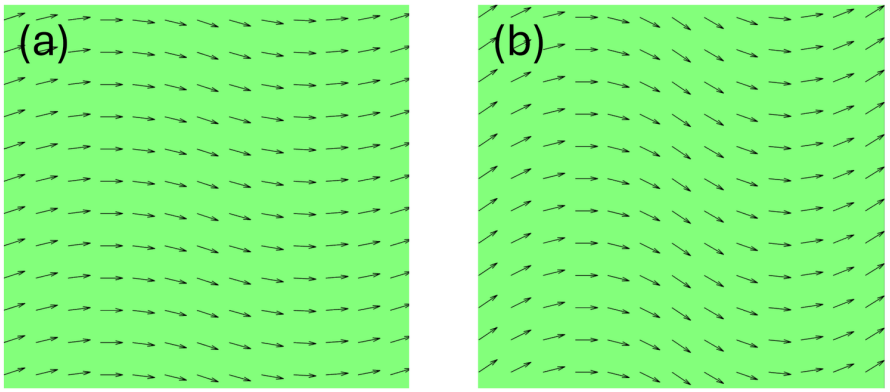

Figure 5.3: Magnetization distribution after relaxation to sinusoidal fields with $B_S = 0.1$ T and $\Theta_F = \pi/2$ (a) or $\Theta_F = \pi$ (b) (the sinusoidal fields are shown in Fig. 5.1 in panels (a) and (b)). Higher fan angles result in a larger undulation amplitude. The presence of the additional uniform field $B_0 = 0.1$ T justifies the mismatch between B_S and magnetization profiles.

Clearly, both Θ_F and B_S magnitude concur to produce similar effects on the magnetization undulation: in particular, different combinations of B_S and Θ_F can produce precisely the same magnetization undulation. This is an interesting result, particularly useful when aiming to reduce the applied field magnitude, e.g., to contain power dissipation: playing with the fan angle only is effective to the purpose.

In Fig. 5.4 we plot the BV dispersion curves at four different values of Θ_F. A first effect is that increasing Θ_F (while B_S is fixed) determined a general frequency downshift. The explanation of this behavior is twofold: from one side, the progressively increasing magnetization amplitude makes the angle between the total bias field $\boldsymbol{B}_S(x,y) + \boldsymbol{B_0}$ and the magnetization $\boldsymbol{M}(x,y)$ larger at any given point (x,y). This reduces the Zeeman potential energy (which depends on the scalar product) and hence the mode frequency. From the other, the progressive increase of the undulation amplitude makes the internal dipolar fields larger, which follows in a general decrease of the internal effective field and hence of the mode frequency [36].

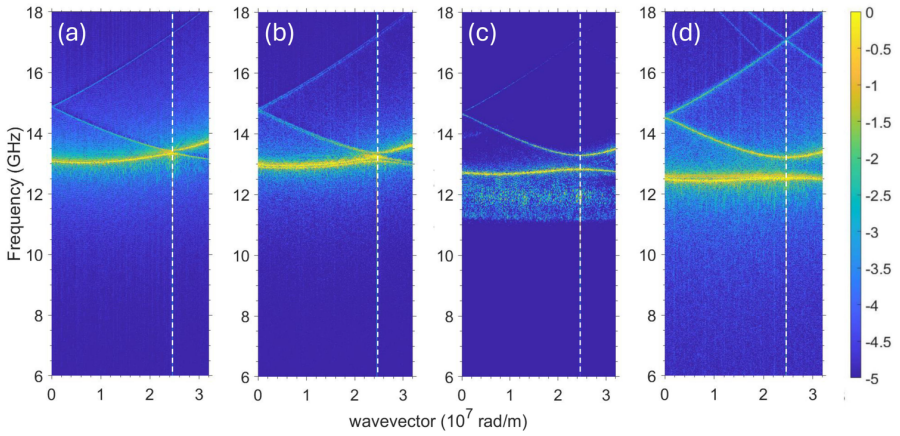

Figure 5.4: Magnonic band structures for BV waves ($B_S = 0.07$ T, polarization in the xy plane) and different Θ_F. Panel (a): $\Theta_F = \pi/3$. Panel (b): $\Theta_F = \pi/2$. Panel (c): $\Theta_F = 5\pi/6$. Panel (d): $\Theta_F = \pi$. Zone boundary occurs at $k = 0.0245$ rad/nm, marked by the dashed white line. The color bar on the right represents intensity in arbitrary units.

The second remarkable effect is that the frequency gap at zone boundary increases for increasing Θ_F. In Chapter 4 we explained the presence of such a gap in terms of the interaction between B_S and the magnon profiles. More precisely, the spin-wavefunctions of the fundamental mode (FM, also called 0-BV) and 1-BV, which at zone boundary are indistinguishable after a translation of half a primitive cell, and hence degenerate, are no longer invariant in frequency because of their different phase relationship with B_S oscillation. Then, the two waves do experience B_S in different ways: the former achieving the lowest frequency (the top of the lower band), the latter the highest frequency (the bottom of the upper band), hence producing a visible frequency gap. Since we already established that increasing Θ_F at a fixed B_S produces an increased undulation amplitude in the magnetization, the effect is equivalent of increasing B_S at a fixed Θ_F: hence, by increasing Θ_F the frequency difference (gap) between the two modes increases.

This is shown in Fig. 5.5, Panel (a), where the frequency gap values (red dots) are plotted together with the calculated specific trend (blue line). In particular, to a first approximation, the best fit turns out to be quadratic: the system exhibits an equilibrium configuration where the potential energy as a function of the fan angle, $u(\Theta_F)$, assumes a *parabolic* expression (Fig. 5.5, Panel (b), blue line). This trend shifts to the magnon frequencies, and in turn to the gap. Considering Eq. 5.1, a parabolic energy density is produced by a likewise parabolic magnitude of the applied field (Fig. 5.5, Panel (b), red line), which, substituted in the Kittel formula, determines a parabolic behavior in frequency (Fig. 5.6).

We find that the previous considerations with respect to magnonic band diagrams, resonance frequencies and frequency gaps apply whenever $B_0 > B_S$. In fact, after fixing B_S (in our case to 0.07 T), if we consider a smaller value of B_0 we assist at a general shift towards lower frequencies as well as a parabolic behaviour in resonance frequencies and in the frequency gap, as Θ_F is increased, only until a *critical* Θ_F^{crit} (in this case $\Theta_F^{crit} \approx 2\pi/3$). If $\Theta_F > \Theta_F^{crit}$, the groundstate has a signif-

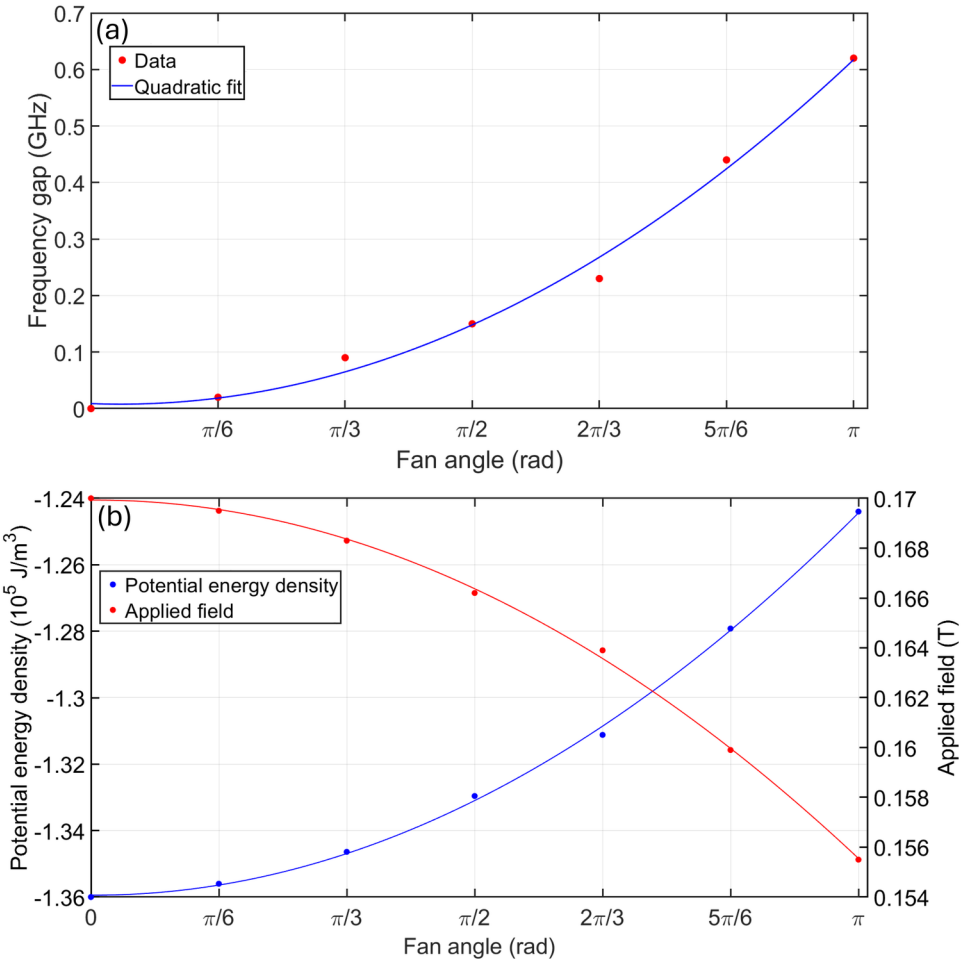

Figure 5.5: Panel (a): frequency gap as a function of Θ_F for $B_S = 0.07$ T (magnetization in xy plane). Red dots: micromagnetic simulations. Blue line: best fit, which is quadratic to a first approximation. Panel (b): potential energy density u (blue dots) with the corresponding quadratic fit (blue line) and applied field $\boldsymbol{B}$ (red dots) with the corresponding quadratic fit (red line).

icant undulation amplitude Y_0 since now B_0, being weaker than B_S, cannot effectively stabilize the magnetization along the x direction, i.e., the propagation one. Strong sinusoidal modulations, being now not suppressed anymore, lead to a series of consequences involving the energy contributions that have been discussed in Chapter 1. First of all, since the exchange energy increases with the divergence of the magnetization $\nabla \boldsymbol{M}$, the cost in exchange energy rises significantly. The demagnetizing energy is also affected, since strong undulations generate surface and volume magnetic charges that produce large demagnetizing fields, thereby penalizing the stability of the configuration. Finally, if the material possesses a preferred magnetization direction like in the present case, any large deviation from this axis results in an additional increase of the anisotropy energy. Accordingly, we observe in simulations, for $\Theta_F > \Theta_F^{crit}$, a general raise in the dispersions and in the resonance frequencies which also imply a reduction in the frequency gap at zone boundary and, therefore, a departure from the quadratic functional behavior of Θ_F.

In conclusion, by operating on Θ_F at a fixed B_S it is possible to tune the width of the frequency gap and the frequency region where it is

located. Hence the gap can be easily varied even if B_S is kept constant and possibly low, to minimize the waste heat.

5.3.2 *Resonance frequencies*

Our purpose is to compare two systems: from one side, the film with undulated magnetization subject to both a uniform bias field B_0 (now fixed to 0.1 T) and a sinusoidal bias field B_S, the results of which were found through micromagnetic simulations. From the other, a fictitious uniformly magnetized film, to which we apply the same field magnitude of the previous system, i.e., the same magnitude of $\boldsymbol{B} = \boldsymbol{B}_0 + \boldsymbol{B}_S$ (the vector summation takes into account the local orientation of $\boldsymbol{B}_S$). We wonder under what conditions the two systems give the same resonance frequencies at zero wavevector.

As a first step to that purpose, for each fan angle Θ_F we compare the resonance frequencies found in the simulations, i.e., for a sinusoidal magnetization under $\boldsymbol{B} = \boldsymbol{B}_0 + \boldsymbol{B}_S$, with the resonance frequencies of an effective uniformly magnetized film, calculated with the Kittel formula using a uniform field determined with two different approaches: in one case we utilize the same $\boldsymbol{B}$ of the simulation forcing it to be uniform by means of the following equation:

$$|\boldsymbol{B}| = \frac{\sum_i^N \sqrt{(B_x^i)^2 + (B_y^i)^2}}{N} \tag{5.4}$$

where the value of $\boldsymbol{B}$ is computed as the average over the entire primitive cell. In the other case, we use an effective field, which gives the same potential energy density u of the simulations.

This comparison is plotted in Fig. 5.6: as Θ_F is increased, the resonance frequencies decrease, for the reasons explained in Sec. 5.3.1.

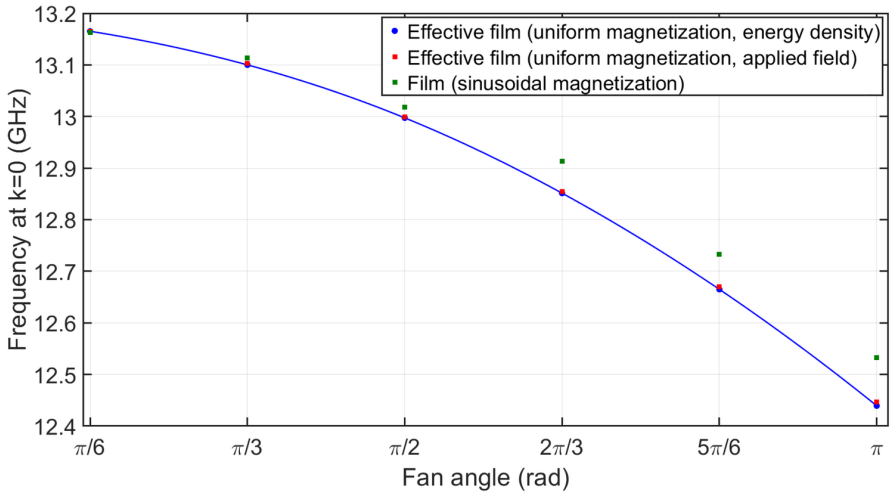

Figure 5.6: Frequency calculated at $k = 0$ as a function of Θ_F (magnetization in xy plane) for $B_S = 0.07$ T. Green dots: film with a sinusoidal magnetization (simulations). Red dots: effective film with a uniform magnetization subject to exactly the same $\boldsymbol{B}$ used in the simulations. Blue dots: effective film with a uniform magnetization subject to a B^* which gives the potential energy density of the simulation (the line is a guide for the eye).

Furthermore, it can be noted that the frequencies of the effective film - calculated, by means of the two methods outlined, with the

Kittel formula - are systematically lower than those found with simulations and related to the undulated film. This is due to the forced introduction, in the effective uniform film, of a magnetic field with an undulated pattern which, acting with the local direction of the magnetization, makes the system unstable with an energy decrease. Clearly, the mismatch between the frequencies of the effective uniform film and those of the undulated film which become larger for increasing Θ_F is explained in terms of the progressive departure from an uniform scenario, the only one accurately described by the Kittel formula.

In Tab. 5.1 the magnetic fields as a function of Θ_F to which the two films are subjected are shown. The fields used in simulating an undulated magnetization and a uniformly magnetized film are compared at the same resonance frequency.

	Θ_F (rad)					
	$\pi/6$	$\pi/3$	$\pi/2$	$2\pi/3$	$5\pi/6$	π
$\boldsymbol{B}$ | B^* uniform (T)	0.1695	0.1681	0.1658	0.1625	0.1584	0.1534
B^* sinusoidal (T)	0.1695	0.1683	0.1662	0.1639	0.1599	0.1555

Table 5.1: Comparison of $\boldsymbol{B}$, determined according to Eq. 5.4 and B^* calculated with the Kittel formula (for an effective uniform film), and B^* calculated with micromagnetic simulations (film with sinusoidal magnetization) for $B_0 = 0.1$ T and $B_S = 0.07$ T (polarization along the xy plane).

5.3.3 *Equivalence of energy densities*

The second step is to compare the frequencies of the two systems after imposing the equivalence of the energy density while either the fan angle or the magnitude of B_S is increased.

To this purpose, as explained in Section 5.2, we first calculate the virtual uniform field B^* which would give the same energy density of the sinusoidal one, and insert it on the Kittel formula to obtain the corresponding ferromagnetic resonance frequency. In Fig. 5.7 we compare the resonance frequencies obtained with this method with the results of the simulations on the sinusoidal magnetization.

The agreement is very good, which confirms the leading role of the energy density in determining the ultimate magnon frequencies. The slight mismatch at $B_S \geq 0.08$ T is due again to the micromagnetic discretization resolution.

To confirm that the discrepancy is only due to the micromagnetic discretization, we use smaller micromagnetic cells in a couple of dedicated simulations. We consider a half of the previous micromagnetic cell size, i.e., $2 \times 2 \times 5$ nm^3 and then a quarter, i.e., $1 \times 1 \times 5$ nm^3, while the physical system is left unchanged. We find that the corresponding frequencies get closer to the ones calculated with the Kittel formula: as an example, for an applied $B_S = 0.09$ T, the frequency found in the simulations is 13.95 GHz for a $4 \times 4 \times 5$ nm^3 micromagnetic cell, 13.88 GHz for a $2 \times 2 \times 5$ nm^3 micromagnetic cell, and 13.85 GHz for a $1 \times 1 \times 5$ nm^3 micromagnetic cell. The last value coincides with the one derived with the Kittel formula (13.85 GHz, Fig. 5.7), showing that a very refined discretization improves the agreement. However,

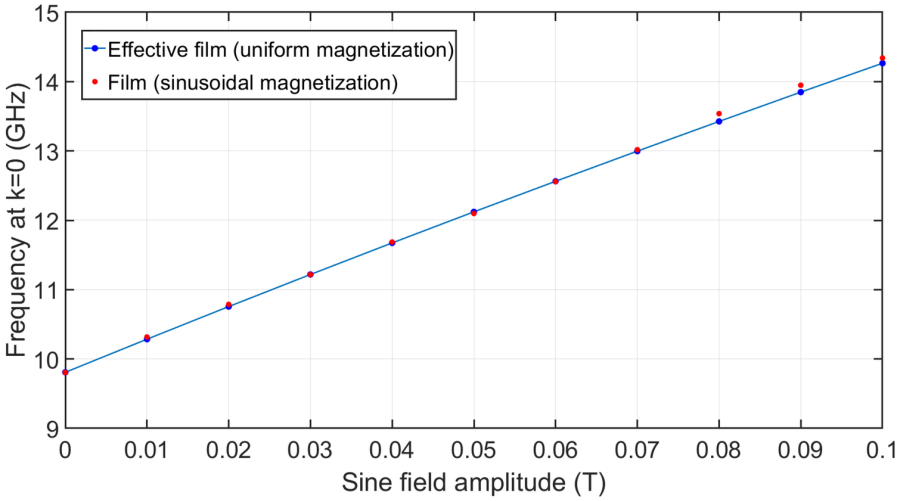

Figure 5.7: Resonance frequencies as a function of B_S after imposing the equivalence of the energy density (magnetization undulation in xy plane). Red dots: simulations on a film with sinusoidal magnetization. Blue dots: uniformly magnetized film. The slight discrepancy at high amplitudes is due to the micromagnetic grid resolution.

the corresponding computational effort in terms of memory and time would be almost impracticable.

The agreement of this approach (equivalence of the energy density) and the simulations is very good also when the magnetization is in the xz plane (see Fig. 5.8).

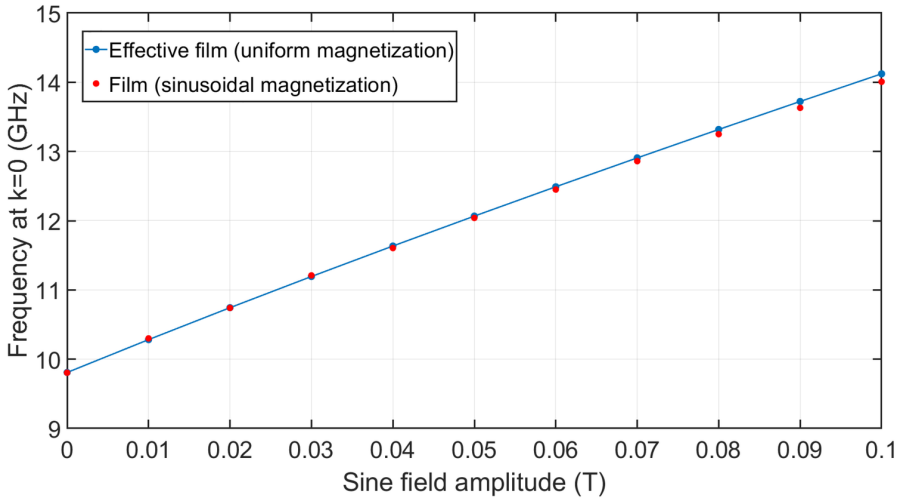

Figure 5.8: Resonance frequencies as a function of B_S (magnetization in xz plane). Blue dots: frequencies of the uniformly magnetized film after imposing the equivalence of the energy density (the line is a guide for the eye). Red dots: simulations on the sinusoidal magnetization.

A little mismatch occurs only for $B_S \geq 0.08\ T$, where the analytical approach provides frequencies slightly larger than those found in the corresponding simulations: again, this is due to computational artifacts. In fact, since the magnetization lies in the xz plane and only a single micromagnetic layer is present (film thickness equal to the micromagnetic cell thickness), in this case the dipolar fields are always antiparallel to the magnetic moments, favoring a (slight) frequency

decrease (computational artifact). This is in contrast to the previous case, where the magnetization lied in the xy plane: with reference to a given magnetic moment, there were also neighboring magnetic moments almost parallel, a condition which favors a frequency increase. In conclusion, even in the xz-plane configuration we recognize the energy density as the ruling ultimate parameter for the spin dynamics.

5.4 CONCLUSIONS

In this Chapter we investigated the behavior of a ferromagnetic film under the influence of a sinusoidal magnetic field with variable fan angle Θ_F. We demonstrated that it is possible to control the magnon dynamics in a ferromagnetic film by varying only the fan angle of an applied sinusoidal field, while its magnitude is left unchanged (and possibly very small, to limit the waste heat).

In particular, we found that, when the uniform bias field B_0 is greater than the magnitude B_S of the sinusoidal one, the frequency gap increases for increasing Θ_F in an almost quadratic behavior, while its position in frequency decreases (when $B_0 < B_S$ instead, the same considerations are valid only if $\Theta_F < \Theta_F^{crit}$). These effects were credited to the periodic Zeeman interaction and the internal dipolar field variations, respectively. This knowledge allows to consider magnonic crystals to which no or very small current generated magnetic fields are applied, and the dynamics is ruled by Θ_F only. In this regard, a practical implementation can be operating through electric fields on the polarization direction in the ferroelectric domains if a ferroelectric/ferromagnetic bilayer is considered, or changing the geometry of a meander if a current flow is considered.

BIBLIOGRAPHY

[1] G. Gubbiotti. *Three-Dimensional Magnonics: Layered, Micro- and Nanostructures*. Singapore: Jenny Stanford Publishing, 2019.

[2] Alexy D. Karenowska et al. "Magnon Spintronics". In: *Handbook of Spintronics*. Ed. by Yongbing Xu, David D. Awschalom, and Junsaku Nitta. Dordrecht: Springer Netherlands, 2014, pp. 1–38. ISBN: 978-94-007-7604-3. DOI: 10.1007/978-94-007-7604-3_53-1. URL: https://doi.org/10.1007/978-94-007-7604-3_53-1.

[3] Qi Wang et al. "Nanoscale magnonic networks". In: *Phys. Rev. Appl.* 21 (4 Apr. 2024), p. 040503. DOI: 10.1103/PhysRevApplied.21.040503. URL: https://link.aps.org/doi/10.1103/PhysRevApplied.21.040503.

[4] Makoto Kohda et al. "Perspective on spin-based wave-parallel computing". In: *Applied Physics Letters* 123.19 (Nov. 2023), p. 190502. ISSN: 0003-6951. DOI: 10.1063/5.0168083. eprint: https://pubs.aip.org/aip/apl/article-pdf/doi/10.1063/5.0168083/19981004/190502_1_5.0168083.pdf. URL: https://doi.org/10.1063/5.0168083.

[5] Abdulqader Mahmoud et al. "Introduction to spin wave computing". In: *Journal of Applied Physics* 128 (Oct. 2020), p. 161101. DOI: doi.org/10.1063/5.0019328. URL: http://doi.org/10.1063/5.0019328.

[6] P.A. Kolodin and B. Hillebrands. "Spin-wave propagation across periodically corrugated thin metallic ferromagnetic films". In: *Journal of Magnetism and Magnetic Materials* 161 (1996), pp. 199–202. ISSN: 0304-8853. DOI: https://doi.org/10.1016/S0304-8853(96)00019-4. URL: https://www.sciencedirect.com/science/article/pii/S0304885396000194.

[7] Harrison W Fuller and Murray E Hale. "Determination of magnetization distribution in thin films using electron microscopy". en. In: *J. Appl. Phys.* 31.2 (Feb. 1960), pp. 238–248.

[8] K J Harte. "Theory of magnetization ripple in ferromagnetic films". en. In: *J. Appl. Phys.* 39.3 (Feb. 1968), pp. 1503–1524.

[9] F. Montoncello and G. Gubbiotti. "Controlling the three dimensional propagation of spin waves in continuous ferromagnetic films with an increasing out of plane undulation". In: *Scientific Reports* 11 (Nov. 2021), p. 21344. DOI: 10.1038/s41598-021-00479-0. URL: https://doi.org/10.1038/s41598-021-00479-0.

[10] L. Giovannini. "Theory of dipole-exchange spin-wave propagation in periodically corrugated films". In: *Phys. Rev. B* 105 (21 June 2022), p. 214426. DOI: 10.1103/PhysRevB.105.214426. URL: https://link.aps.org/doi/10.1103/PhysRevB.105.214426.

[11] Ali Frotanpour et al. "Magnetization dynamics of a Fibonacci-distorted kagome artificial spin ice". In: *Physical Review B* 102 (2020), p. 224435. DOI: 10.1103/PhysRevB.102.224435.

[12] F. Montoncello et al. "Dynamic origin of segment magnetization reversal in thin-film Penrose tilings". In: *Journal of Magnetism and Magnetic Materials* 423 (2017). 10.1016/j.jmmm.2016.09.090, pp. 158–163.

[13] V. S. Bhat et al. "Controlled Magnetic Reversal in Permalloy Films Patterned into Artificial Quasicrystals". In: *Phys. Rev. Lett.* 111 (2013). 10.1103/PhysRevLett.111.077201, p. 077201.

[14] B. Farmer et al. "Magnetic response of aperiodic wire networks based on Fibonacci distortions of square antidot lattices". In: *J. Appl. Phys.* 117 (2015). 10.1063/1.4913820, 17B714.

[15] Pietro Micaletti and Federico Montoncello. "Dynamic Footprints of the Specific Artificial Spin Ice Microstate on Its Spin Waves". In: *Magnetochemistry* 9.6 (2023). ISSN: 2312-7481. DOI: 10.3390/magnetochemistry9060158. URL: https://www.mdpi.com/2312-7481/9/6/158.

[16] R. Negrello et al. "Dynamic coupling and spin-wave dispersions in a magnetic hybrid system made of an artificial spin-ice structure and an extended NiFe underlayer". In: *APL Materials* 10 (2022), p. 091115. DOI: 10.1063/5.0102571. URL: https://doi.org/10.1063/5.0102571.

[17] S. Ladak, A. Fernández-Pacheco, and P. Fischer. "Science and technology of 3D magnetic nanostructures". In: *APL Materials* 10.1 (Science and Technology of 3D Magnetic Nanostructures 2022), p. 5. DOI: /10.1063/5.0136801. URL: https://doi.org/10.1063/5.0136801.

[18] F. Montoncello et al. "A Brillouin light scattering study of the spin-wave magnetic field dependence in a magnetic hybrid system made of an artificial spin-ice structure and a film underlayer". In: *Journal of Applied Physics* 133 (Recent Advances in Magnonics Feb. 2023), p. 083901. DOI: 10.1063/5.0140866. URL: http://dx.doi.org/10.1063/5.0140866.

[19] Troy Dion et al. "Ultrastrong magnon-magnon coupling and chiral spin-texture control in a dipolar 3D multilayered artificial spin-vortex ice". In: *Nature Communications* 15.1 (May 2024), p. 4077. ISSN: 2041-1723. DOI: 10.1038/s41467-024-48080-z. URL: https://doi.org/10.1038/s41467-024-48080-z.

[20] Pietro Micaletti et al. "Magnonic analog of a metal-to-insulator transition in a multiferroic heterostructure". In: *Journal of Applied Physics* 137 (2025), p. 153906. DOI: 10.1063/5.0250690. URL: https://doi.org/10.1063/5.0250690.

[21] Huajun Qin et al. "Electric-Field Control of Propagating Spin Waves by Ferroelectric Domain-Wall Motion in a Multiferroic Heterostructure". In: *Advanced Materials* 33.27 (2021), p. 2100646. DOI: https://doi.org/10.1002/adma.202100646. eprint: https://onlinelibrary.wiley.com/doi/pdf/10.1002/adma.202100646. URL: https://onlinelibrary.wiley.com/doi/abs/10.1002/adma.202100646.

[22] Julia Kharlan et al. *Tunable magnonic crystal in a hybrid superconductor–ferrimagnet nanostructure*. 2024. arXiv: 2408.01240 [cond-mat.mes-hall]. URL: https://arxiv.org/abs/2408.01240.

[23] I.A. Golovchanskiy et al. "Magnetization Dynamics in Proximity-Coupled Superconductor-Ferromagnet-Superconductor Multilayers". In: *Phys. Rev. Appl.* 14 (2 Aug. 2020), p. 024086. DOI: 10.1103/PhysRevApplied.14.024086. URL: https://link.aps.org/doi/10.1103/PhysRevApplied.14.024086.

[24] I. A. Golovchanskiy et al. "Nonlinear spin waves in ferromagnetic/superconductor hybrids". In: *Journal of Applied Physics* 127.9 (Mar. 2020), p. 093903. ISSN: 0021-8979. DOI: 10.1063/1.5141793. eprint: https://pubs.aip.org/aip/jap/article-pdf/doi/10.1063/1.5141793/13371075/093903_1_online.pdf. URL: https://doi.org/10.1063/1.5141793.

[25] P. Micaletti et al. "A sinusoidal magnetization distribution as an original way to generate a versatile magnonic crystal for magnon propagation". In: *Journal of Magnetism and Magnetic Materials* 622 (2025), p. 172959. ISSN: 0304-8853. DOI: https://doi.org/10.1016/j.jmmm.2025.172959. URL: https://www.sciencedirect.com/science/article/pii/S0304885325001908.

[26] A V Chumak et al. "A current-controlled, dynamic magnonic crystal". In: *Journal of Physics D: Applied Physics* 42.20 (Sept. 2009), p. 205005. DOI: 10.1088/0022-3727/42/20/205005. URL: https://dx.doi.org/10.1088/0022-3727/42/20/205005.

[27] A. V. Chumak et al. "Advances in Magnetics Roadmap on Spin-Wave Computing". In: *IEEE Transactions on Magnetics* 58.6 (2022), pp. 1–72. DOI: 10.1109/TMAG.2022.3149664.

[28] Harald Ibach and Hans Lüth. *Solid-State Physics: An Introduction to Principles of Materials Science*. 4th. Berlin, Heidelberg: Springer, 2009. ISBN: 978-3-540-93803-3.

[29] Hyeon Woo Park et al. *Magnon thermal conductivity in multiferroics with spin cycloids*. 2025. arXiv: 2503.11135 [cond-mat.mtrl-sci]. URL: https://arxiv.org/abs/2503.11135.

[30] Isaac A. Harris et al. "Symmetry-Based Phenomenological Model for Magnon Transport in a Multiferroic". In: *Phys. Rev. Lett.* 134 (1 Jan. 2025), p. 016703. DOI: 10.1103/PhysRevLett.134.016703. URL: https://link.aps.org/doi/10.1103/PhysRevLett.134.016703.

[31] Arne Vansteenkiste et al. "The design and verification of MuMax3". In: *AIP Advances* 4.10 (2014), p. 107133. DOI: 10.1063/1.4899186.

[32] Hans Fangohr et al. "A new approach to (quasi) periodic boundary conditions in micromagnetics: The macrogeometry". In: *Journal of Applied Physics* 105 (2009), p. 07D529. DOI: 10.1063/1.3068637. eprint: https://doi.org/10.1063/1.3068637. URL: https://doi.org/10.1063/1.3068637.

[33] C. Kittel. "On the Theory of Ferromagnetic Resonance Absorption". In: *Physical Review* 73 (1948), p. 155. DOI: 10.1103/PhysRev.73.155.

[34] Tuomas H. E. Lahtinen, Kévin J. A. Franke, and Sebastiaan van Dijken. "Electric-field control of magnetic domain wall motion and local magnetization reversal". In: *Scientific Reports* 2.1 (Feb. 2012), p. 258. ISSN: 2045-2322. DOI: 10.1038/srep00258. URL: https://doi.org/10.1038/srep00258.

[35] Tuomas H. E. Lahtinen, Jussi O. Tuomi, and Sebastiaan van Dijken. "Pattern Transfer and Electric-Field-Induced Magnetic Domain Formation in Multiferroic Heterostructures". In: *Advanced Materials* 23.28 (2011), pp. 3187–3191. DOI: https://doi.org/10.1002/adma.201100426. eprint: https://onlinelibrary.wiley.com/doi/pdf/10.1002/adma.201100426. URL: https://onlinelibrary.wiley.com/doi/abs/10.1002/adma.201100426.

[36] D. Kuźma et al. "Spin wave propagation properties across configurational antiferro/ferro-magnetic transitions". In: *Journal of Applied Physics* 124.22 (Dec. 2018), p. 223902. ISSN: 0021-8979. DOI: 10.1063/1.5057419. eprint: https://pubs.aip.org/aip/jap/article-pdf/doi/10.1063/1.5057419/13708421/223902_1_online.pdf. URL: https://doi.org/10.1063/1.5057419.

6

MAGNONIC METAL-TO-INSULATOR TRANSITION IN MULTIFERROIC HETEROSTRUCTURES

ABSTRACT

We demonstrate that adjusting the polarization of ferroelectric domains provides an effective means to control the magnon conductivity in the ferromagnetic layer of a multiferroic magnonic system. By tuning this parameter, the system can be driven from a metallic state - characterized by a vanishing frequency gap and a linear frequency–wavevector dispersion - to an insulating state, where a frequency gap of about 1 GHz and a parabolic dispersion emerge. The ferroelectric film is engineered as a periodic sequence of domains with alternating polarization directions. Through inverse magnetostriction, this periodic arrangement induces a spatially modulated magnetic anisotropy in the adjacent ferromagnetic layer, giving rise to a sinusoidal magnetization profile. The amplitude of this modulation can be precisely controlled by adjusting the induced anisotropy, enabling reversible and fine-tuned manipulation of both the dispersion curvature at the Brillouin zone boundary and the width of the frequency gap. We further extend Dirac's magnon framework to this configuration, revealing intriguing consequences for magnon mobility. These results broaden the potential applications of voltage-controlled-bandgap metamaterials, establish the criteria for realizing a magnonic metallic phase in ferromagnetic films, and illustrate how a single unpatterned film can be reversibly switched between magnonic metal and magnonic insulator states.

6.1 PRELIMINARY FRAMEWORK

A central pursuit in the field of Magnonics is to establish mechanisms by which magnon propagation can be not only guided and filtered, but also switched between qualitatively distinct *regimes of transport*. This challenge is closely reminiscent of condensed matter physics, where electronic systems may undergo metal-insulator transitions, thereby radically altering their charge transport properties. Translating this paradigm to magnons, one would seek an artificial medium in which collective spin excitations can be continuously tuned from *freely propagating*, nearly "metallic" modes, to *blocked*, "insulating" *regimes* characterized by the opening of a frequency gap. Such a transition, if controllable in real time and with low energy expenditure, would represent a milestone for the implementation of magnon-based logic and memory devices.

Our recent work has demonstrated that a ferroelectric/ferromagnetic bilayer provides precisely such a scenario [1]. Through the *inverse magnetostrictive effect*, the polarization of ferroelectric stripe domains imprints a *periodically varying uniaxial anisotropy* on the adjacent ferromagnetic film. Upon relaxation, the magnetization of the ferromagnet assumes a sinusoidal spatial distribution. Crucially, the *amplitude* of this sinusoidal modulation is directly controlled by the ferroelectric domain polarization, and thus by the externally applied electric field. This vertical coupling mechanism translates electric-field inputs into magnetization textures, establishing a pathway for voltage-controlled and reconfigurable magnonic crystals.

6.2 INTRODUCTION

The *voltage* (or *electric field*)*-driven control* of ferromagnetic systems is widely viewed as a key paradigm for future low-power, highly miniaturized devices [2, 3, 4]. Among the various strategies explored, an especially effective one couples a ferromagnetic film to a ferroelectric substrate hosting ferroelastic stripe domains. In such a heterostructure, applying a voltage or electric field to the substrate allows one to tune the magnetic response of the ferromagnetic layer [5, 6, 7, 8]. The underlying mechanism combines strain transfer with *inverse magnetostriction*: the periodic ferroelastic domains of the substrate impart a spatially modulated strain to the ferromagnet, which in turn imprints a corresponding pattern of magnetic stripe domains. The coupling strength scales with the ferroelectric domain polarization, a quantity that can be efficiently adjusted by an external electric field. A prototypical realization of this mechanism is found in $Fe/BaTiO_3$ heterostructures, which have been extensively investigated as model systems of strain-mediated magnetoelectric coupling [9, 10, 11, 12].

Beyond this specific platform, controlling magnons at the nanoscale via vertical interlayer coupling in multilayers has emerged as a particularly promising direction within the broader field of 3D Magnonics [13, 14, 15, 16]. In parallel, extensive work has focused on magnonic band structures, especially on the formation of frequency bandgaps in magnonic metamaterials. These gaps enable functionalities such

as spin-wave filters and magnonic mirrors, which are central to wave-based information processing [17, 18, 19, 20].

The appearance of a magnonic bandgap indicates that spin-wave propagation is suppressed in a certain frequency interval and along specific crystallographic directions. When the gap becomes independent of propagation direction, the system effectively acts as an omnidirectional magnonic filter. In a composite, magnons traveling along a waveguide can be entirely reflected at the interface with a material hosting a frequency bandgap [21, 22, 23].

By analogy with electrons in solids, a magnonic metamaterial can be classified as *conducting* or *insulating* for magnon transport depending on whether a *magnonic bandgap* is absent or present along the propagation direction. Note that even a uniformly magnetized film functions as a magnon conductor; however, without any periodic modulation, it does not develop a true band structure. To emphasize the distinction, an artificial crystal with a periodic modulation - either geometric or magnetic - can be termed a "magnonic metal", in direct analogy with electronic conductors built from atoms arranged in a crystal lattice.

In ferroelectric/ferromagnetic bilayers, the interlayer coupling is governed entirely by inverse magnetostriction. The interaction strength can be continuously tuned by adjusting the ferroelectric polarization state, itself controlled by an external electric field. This makes ferroelectric/ferromagnetic heterostructures compelling platforms for voltage-controlled magnonic devices [24, 25, 26].

In this work, inverse magnetostriction is modeled by imposing a *periodically modulated uniaxial anisotropy*, K_u, in a ferromagnetic film. The periodic modulation is set by the orientation of the ferroelectric domain polarization, which induces a corresponding periodic variation of magnetic anisotropy in the ferromagnetic layer. Our simulations show that when K_u remains moderate (specifically below 10^5 J/m^3) the relaxed state in the ferromagnetic film exhibits a continuous sinusoidal magnetization profile, see Fig. 6.1(a). The spatial amplitude of the undulation, denoted Y_0, grows with K_u. Y_0 relates to the magnetization components at the origin (Fig. 6.1(b)) through the relation introduced in Chapter 4:

$$Y_0 = \frac{m_y^0}{m_x^0}\left(\frac{a}{2\pi}\right). \tag{6.1}$$

For instance, taking $m_y^0/m_x^0 = 1.0$ and $a = 256$ nm yields an undulation amplitude of 40.8 nm. This estimate is not merely academic; it can guide both the structural design and the experimental readout via magnetic force microscopy or space-resolved magneto-optic Kerr effect. The ultimate idea is to exploit the magnetization undulation to realize an artificial magnonic crystal. Remarkably, the system can be reversibly toggled between a "metallic" and an "insulating" magnonic state simply by controlling a single parameter. Physically, a multiferroic bilayer is prepared with a periodic alternation of ferroelectric domain polarizations; inverse magnetostriction then induces a sinusoidal magnetization texture in the ferromagnetic layer that strongly alters magnon dynamics. The undulation amplitude Y_0 can be tuned continuously by varying K_u, which is in turn controlled by the electric field acting on the ferroelectric polarization. Thus, the electric field

becomes the central control knob. In contrast with artificial spin-ice/straight-film hybrids - where spin-wave dispersions often exhibit weakly dispersive branches and only modestly tunable gaps [15, 27, 28] - the present strategy offers a far stronger handle, producing highly dispersive bands with sizable, adjustable bandgaps.

Even more intriguingly, we show that the system can be tuned to close the frequency gap entirely while maintaining periodicity. In this regime, the dispersion near the Brillouin zone (BZ) edge changes character from parabolic to linear (and vice versa), creating the characteristic "X"-shaped crossing reminiscent of graphene's Dirac cones at the K point. The simultaneous presence of a zero gap and linear dispersion, typical of free carriers in electronic metals, stands in sharp contrast with finite gaps and parabolic dispersions associated with insulating behavior. In this sense, the system undergoes a reversible magnonic *metal-to-insulator transition*.

We further interpret the simulations within the *framework of Dirac magnons* [29], extending it to one-dimensional lattices and continuous media. This analysis yields fresh insight into controlling magnon propagation. Notably, we find that the slope of the dispersion, i.e., the group velocity v_g, can be finely adjusted via K_u and, for sufficiently large K_u, can even be driven to zero. This unique functionality enables the same physical system to act either as a magnonic waveguide ($v_g \neq 0$) or as a dynamic memory ($v_g = 0$), with the possibility of switching on the fly during propagation. Such capabilities place the system within the class of dynamic or reconfigurable magnonic crystals [30], where periodicity and spin-wave properties are governed by external stimuli such as magnetic fields [31, 32, 33], spin-polarized currents [34], laser heating [35] or strain waves generated by surface acoustic waves [36, 37]. A related concept, i.e., dynamic electromagnonic crystals, has been proposed in multiferroics [6, 38, 39, 40]. Those systems, however, specifically probe hybridization between spin and electromagnetic waves (electromagnons), typically emphasizing wavevector regions where hybridization occurs ($\sim 10^3$ rad/m) [41, 42], about four orders of magnitude smaller than the wavevectors relevant here ($\sim 10^7$ rad/m). Moreover, in electromagnonic systems the term "gap" often refers to anticrossing features in the coupling region rather than to Bragg gaps at the BZ edge [38], and the resulting gaps are generally small (MHz) compared with the GHz-scale bandgaps found in our simulations. Consequently, electromagnonic crystals usually rely on large periodicities in the 10–800 μm range [6, 39], whereas our model targets the nanometric scale (~ 1 μm). While conceptual analogies exist, electromagnonic crystals and the undulated ferromagnetic systems explored here address fundamentally different regimes and applications.

To our knowledge, a direct investigation of magnetization undulation and its tunability (specifically, the possibility to reversibly and continuously sweep the frequency gap from zero to several GHz in a uniform, unpatterned system) and its correlation with the curvature of the magnon dispersion (effective magnon mass) has not been reported before, particularly in the context of voltage-controlled magnon transport. For these reasons, the voltage-induced magnetization undulation proposed here represents a meaningful step forward. We

demonstrate controlled, reversible manipulation of the magnon dispersion curvature and gap magnitude - capabilities that are essential for versatile spin-wave devices such as filters, mirrors, reconfigurable waveguides, and magnonic memories. Overall, this approach enriches the landscape of dynamic magnonic crystals by introducing a new, voltage-driven degree of freedom.

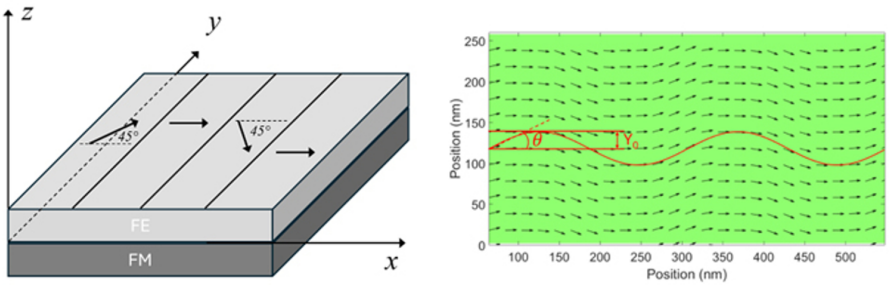

Figure 6.1: Schematic of the ferroelectric/ferromagnetic bilayer, restricted to the primitive unit cell, showing the ferroelectric domain polarization orientation. (b) Magnetization map (two primitive cells shown) after relaxation for $K_u = 5 \times 10^4$ J/m^3. The sinusoidal pattern has amplitude Y_0; at the origin, the angle between magnetization vectors is $\theta = \arctan\left(\frac{m_y^0}{m_x^0}\right)$, with m_x^0 and m_y^0 the magnetization components at the origin.

6.3 METHODS AND RESULTS

We perform micromagnetic simulations using the GPU-accelerated MuMax3 package [43]. The system is the one described in Chapters 4 and 5: an effectively infinite ferromagnetic film, thickness 5 nm, represented by a square primitive cell with lattice constant $a = 256$ nm and replicated 800 times in-plane (quasi-periodic boundary conditions). The film is discretized into $4 \times 4 \times 5$ nm^3 cells. The magnetic material is permalloy with saturation magnetization $M_S = 800$ kA/m, exchange stiffness $A_{ex} = 1.0 \times 10^{-11}$ J/m, and gyromagnetic ratio $\gamma = 185$ rad GHz/T. To accelerate relaxation, we use a fictitiously large damping $\alpha_G = 0.9$; the subsequent excitation stage is simulated with $\alpha_G = 0$ to allow long-lived precession and clean Fourier spectra. The primitive cell is divided into four equal stripes, each with the same uniaxial anisotropy magnitude K_u but with alternating easy-axis directions ordered as $+45°$, $0°$, $-45°$, $0°$ (Fig. 6.1(a)). To access ~ 10 GHz frequencies, we apply a uniform bias field $B_0 = 0.1$ T along x, as in Chapters 4 and 5. From an initially saturated state, the film relaxes under the combined bias field and periodic anisotropy into a sinusoidal magnetization equilibrium, maintained as long as $K_u \lesssim 10^5$ J/m^3. Above this threshold, the magnetization no longer follows a smooth sine profile but breaks into domains nearly aligned with local easy axes, separated by sharp walls inside the primitive cell. Therefore, we restrict to $K_u \leq 5 \times 10^4$ J/m^3, corresponding to an effective anisotropy field $B_{\text{anis}} \approx 62.5$ mT. It is worth noting that in the literature the anisotropy is often expressed directly in terms of its associated magnetic field, which is typically even smaller than this value [44, 45]. In this context, our choice of the low-anisotropy

regime is not only computationally convenient but also physically motivated. Indeed, in $Fe/BaTiO_3$ heterostructures, the strong anisotropy imprinted by ferroelastic ferroelectric stripes leads to 90°-rotated easy axes and the formation of magnetic domains with sharp magnetization discontinuities. By contrast, here we intentionally operate in a weaker-coupling regime - effectively reducing the ferroelectric/ferromagnetic coupling (e.g., via electric-field control of the ferroelectric polarization) - so that the ferromagnet relaxes into a continuous sinusoidal magnetization distribution suitable for magnonic band engineering.

To compute magnonic dispersions, we employ a supercell of 200 primitive cells along the undulation direction (x), providing a wavevector resolution $\delta k_x \simeq 0.012 \times 10^7$ rad/m. We excite the system with a space–time sinc magnetic field of amplitude 1 mT, cutoff frequency 40 GHz, and maximum wavevector $k_x = 0.0490$ rad/nm. Magnetization snapshots are sampled with $\delta t = 25$ ps and Fourier transformed in space and time. The resulting spectra yield dispersion relations with Nyquist frequency $f_N = 20$ GHz and frequency resolution $\delta f = 0.01$ GHz. In addition, spatially resolved Fourier coefficients are used to extract mode profiles: by fixing a frequency corresponding to a point on the dispersion, we plot the real part of the z-component [46] of the dynamic magnetization to visualize the mode.

As discussed in Chapter 4, in periodic systems spin waves are Bloch waves with magnetization fluctuations:

$$\delta m_k(\boldsymbol{r}) = \delta \tilde{m}_k(\boldsymbol{r}) e^{i\boldsymbol{k}\cdot\boldsymbol{r}}, \tag{6.2}$$

where $\tilde{m}_k(\boldsymbol{r})$ is a cell function with lattice periodicity, $\boldsymbol{k}$ is the wavevector, and $\boldsymbol{r}$ the position [47]. For sinusoidal magnetization and small Y_0, the dynamics is relatively straightforward and consists of Bloch waves whose cell functions carry nodal structures. These modes are conventionally classified as backward volume spin waves (m-BV), with nodal lines perpendicular to x, or Damon–Eshbach (n-DE) modes, with nodal lines parallel to x [48, 49, 50, 51]. Mixed (m, n) modes can also appear. In the reduced-zone scheme, the number of nodal lines defines the band index at a given wavevector, directly connecting microstructure to dispersion [20]. Since the magnetization flux oscillates along x, we restrict our analysis to this direction, i.e., to backward waves.

We compute dispersions for K_u values spanning over four decades, from 1×10^1 to 5×10^4 J/m^3, a range consistent with experimentally reported inverse-magnetostriction-induced anisotropies [10, 52, 53, 54, 55, 11]. An important symmetry emerges: the spin dynamics is invariant under mirror reflection of the magnetization map with respect to the x axis (the σ_h operation in Ref. [56]). Consequently, although the geometric primitive cell has side $a = 256$ nm, the physical periodicity of the dynamic problem is halved ($d = 128$ nm). Thus, the physical BZ boundary shifts to $2\pi/d \approx 2.45 \times 10^7$ rad/m, i.e., twice the value associated with the geometric cell. Our numerics fully confirm this prediction (dashed vertical lines in Fig. 6.2).

Figure 6.2 shows six representative dispersion sets illustrating the evolution from metallic to insulating magnonic behavior as K_u increases. For $K_u \lesssim 0.04$ kJ/m^3 (not shown), the magnetization remains essentially uniform and no folding into the reduced zone appears.

In that limit, the system is indistinguishable from a uniform film ($K_u = 0$), with no periodic signature or band features. This highlights a threshold: below $K_u \approx 0.04$ kJ/m^3, anisotropy is too weak to perturb uniform magnetization against exchange and dipolar interactions. Experimentally, this implies that to observe a genuine periodic response in permalloy (metallic or insulating in the magnonic sense), the ferroelectric overlayer must induce anisotropy beyond this critical value; otherwise the film behaves as uniform, lacking band structures and the frequency-wavevector trade-offs characteristic of true magnonic crystals.

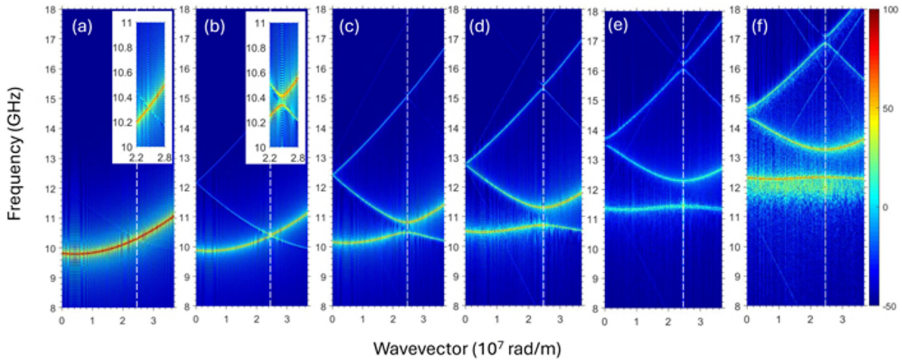

Figure 6.2: Dispersion curves along x for (a) $K_u = 1.0 \times 10^2$, J/m^3 (metal-like), (b) $K_u = 1 \times 10^3$, J/m^3 (insulator-like), (c) $K_u = 5 \times 10^3$, J/m^3, (d) $K_u = 1 \times 10^4$, J/m^3, (e) $K_u = 2 \times 10^4$, J/m^3, and (f) $K_u = 3 \times 10^4$, J/m^3. Insets in (a) and (b) magnify the BZ-edge region using a different aspect ratio. The blurring in (f) is a simulation artifact. The BZ boundary at $k = 2.45 \times 10^7$, rad/m demonstrates that the physical lattice constant is $d = 128$ nm, i.e., half the geometric one a.

6.3.1 *Magnon metal*

Within $0.04 \leq K_u \leq 0.4$ kJ/m^3, the dispersion closely follows that of a uniformly magnetized film, but now folds into the reduced BZ (see Fig. 6.2(a)). In this regime, the gap is essentially negligible ($<$ 0.01 GHz), and the curves meet at the zone boundary in an "X"-shaped crossing with locally linear behavior. Under these conditions, magnons effectively behave as "free" excitations: frequency and wavevector can be tuned continuously by arbitrarily small perturbations, e.g., from a microwave antenna. This echoes the "free electron" picture in metals, where infinitesimal voltages set carriers in motion.

A striking aspect is that varying K_u within this metallic window hardly alters the dispersion beyond the folding itself. In other words, the group velocity, and thus the magnon mobility, remains quite robust against anisotropy changes. The situation recalls graphene, in which the physics near the Dirac point is largely insensitive to small perturbations. It is thus natural to reinterpret the dispersion by recentering the reference frame at the BZ edge (the Dirac point), where the main branch intersects its folded replica. Around this crossing, the standard effective-mass definition [47] based on a parabolic dispersion no longer applies. A perfectly linear dispersion would imply zero

curvature and hence an infinite mass, clearly at odds with the observed high mobility.

To resolve this, we adopt an alternative *effective mass* definition tailored to the linear regime. Let p be the magnon momentum and $\hbar$ the reduced Planck constant. We write [57]:

$$m^* = \frac{p}{v_g} = \frac{\hbar\kappa}{v_g} = \frac{\hbar\kappa}{\partial\omega/\partial\kappa}, \tag{6.3}$$

where $\kappa = k - \pi/d$, with d the physical lattice constant. At the Dirac point ($\kappa \to 0$), the effective mass vanishes ($m^* \to 0$), indicating maximal mobility. This supports the interpretation of "free magnons," highly responsive in both frequency and wavevector. Equation (6.3) applies to non-dispersive magnons, i.e., when v_g depends linearly on k near the BZ edge.

In a narrow neighborhood of the BZ boundary, the two branches forming the "X" have identical slopes due to spatial inversion symmetry of the sinusoidal magnetization along x. Although the system is strictly one-dimensional, the analogy with graphene suggests that the magnon dispersion near the crossing is captured by a Dirac form [29, 58, 59]:

$$\omega_\pm(\kappa) = \omega(\pi/d) \pm v_g|\kappa|, \tag{6.4}$$

where $\omega = 2\pi\nu$ is the angular frequency, $\frac{\epsilon}{\hbar} \equiv 2\pi\nu(\frac{\pi}{d})$, and v_g plays the role of a Dirac velocity. The $\pm$ encodes the symmetry of the two crossing branches. The straight line through $\nu(\frac{\pi}{d})$ locally approximating the dispersion at the zone edge can be written explicitly as:

$$\nu(k) = \nu_0 + \left(\frac{d}{\pi}\right)[\nu(\tfrac{\pi}{d}) - \nu_0], \tag{6.5}$$

where d is the physical lattice constant and $\nu_0 \equiv \nu(0)$ is not necessarily an actual point on the global dispersion. This straight-line form underlies Eq. (6.4). In a linear lattice like the present one, the group velocity relates to the *hopping rate* ν_t via:

$$v_g = 2\pi\frac{\partial\nu}{\partial k} = 2\pi\frac{d}{\pi}[\nu(\tfrac{\pi}{d}) - \nu_0] = 2d\nu_t. \tag{6.6}$$

Hence the hopping frequency $\nu_t = \nu(\pi/d) - \nu_0$ is directly proportional to v_g. Physically, ν_t measures how fast magnons hop across half a primitive cell ($d/2$), corresponding to a phase shift of $\pi/2$. As the dispersion flattens, $\nu_t \to 0$ and propagation is quenched.

Referring to the zone boundary (Dirac point), one can view Dirac magnons as *non-dispersive wave packets*. Indeed, at $k = \frac{\pi}{d}$ (i.e., $\kappa \to 0$), for the phase velocity v_p we have:

$$\frac{\partial v_p}{\partial\kappa} = \frac{\partial}{\partial\kappa}\frac{\omega(\kappa)}{\kappa} = \frac{1}{\kappa}\frac{\partial\omega(\kappa)}{\partial\kappa} - \frac{\omega(\kappa)}{\kappa^2} = \frac{1}{\kappa}(v_g - v_p). \tag{6.7}$$

This perspective emphasizes how a sinusoidal magnetization effectively turns the film into a Dirac material, characterized by $v_g = v_p$ across a broad wavevector interval at the BZ edge. Under such conditions, magnon wave packets become non-dispersive and travel ballistically over long distances, preserving momentum. This is appealing for magnonics, where information is carried by spin waves. The hopping rate ν_t can be treated as an information-transfer metric, with its value

determined by the underlying interactions. Exchange dominates in this regard: in ultrathin films (here 5 nm), exchange makes the magnetization stiffer and promotes coherent precession, boosting magnon frequencies and supporting propagation. By contrast, dipolar interactions favor decoherence over distance [49], while anisotropy tends to suppress v_g. Engineering the balance among these mechanisms is crucial for desired transport properties.

To illustrate the tunability of ν_t, we compare analytical dipole–exchange backward-wave dispersions [60] for three systems (Fig. 6.3) designed to share the same BZ-edge frequency (10.32 GHz) but to exhibit very different v_g. The black curve reproduces, analytically and without reduced-zone folding, the dispersion in Fig. 6.2(a). From a linear fit, we obtain $v_g \approx 314$ m/s, $\nu_0 = 9.095$ GHz, and $\nu(\pi/d) \equiv \nu(\kappa = 0) = 10.32$ GHz, giving a hopping rate $\nu_t = 1.225$ GHz. The red curve is designed so that $\nu_t = \nu(\pi/d)$ and refers to a 100 nm thick fictitious film with $M_S = 900$ kA/m, $A_{ex} = 14.0 \times 10^{-11}$ J/m, and $B_0 = 10$ mT. Its linear approximation (tangent) at the BZ edge (dashed red) gives $\nu_t \simeq 10.32$ GHz, i.e., $v_g \simeq 2.64$ km/s. The blue curve corresponds to another fictitious material designed so that $\nu_t \sim \nu(\pi/d)$. To keep the same edge frequency (10.32 GHz), we use: thickness 1.5, μm, $M_s = 1500$ kA/m, $A_{ex} = 50 \times 10^{-11}$ J/m, $\gamma = 150$ rad GHz/T, and $B_0 = 10$ mT. Its tangent at the BZ edge (dashed blue) yields $\nu_t \approx \nu(\pi/d) \approx \nu_0 = 19.6$ GHz ($\nu_0 \simeq 9.3$ GHz), corresponding to $v_g \simeq 5.02$ km/s.

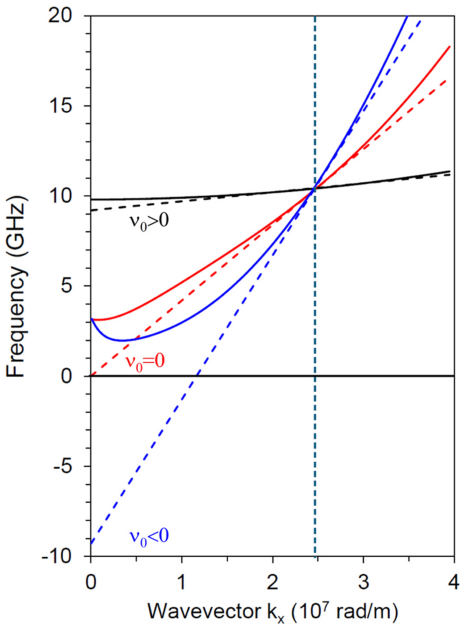

Figure 6.3: Dispersion $\nu(k)$ for three systems with different geometric and magnetic parameters, with increasing exchange stiffness and thus increasing hopping rate. Curves follow the analytical backward-wave relation of Ref. [60], plotted without folding to the first BZ. Dashed straight lines are tangents at the BZ edge (vertical dashed line): black shows a case with $\nu_0 > 0$ and small ν_t; red has larger exchange and is designed for $\nu_0 = 0$; blue has $\nu_0 < 0$ and thus very large exchange and ν_t.

Extending Dirac's magnon picture to our voltage-tunable sinusoidal magnetization shows how to realize a metallic magnonic state (periodic bands with linear crossings and vanishing gap at the BZ

edge): anisotropy is necessary, and our study identifies a threshold $K_u \approx 0.04$ kJ/m^3. In this regime, magnons behave as massless packets, with mobility tunable by magnetic and geometric design (Fig. 6.3). The fact that magnons - like electrons in solids (and in graphene) - can be described as localized wave packets [61] underpins extending Dirac's framework to our case of a linear lattice embedded in a continuum. As wave packets, magnons carry a phase velocity (set by ω) and a distinct group velocity (governing transport), each determined by the underlying interactions. Consequently, a ferromagnetic film with a suitably engineered periodic anisotropy can indeed be regarded as the magnonic analog of a metallic material.

6.3.2 *Magnon insulator*

While a finite anisotropy is required to establish magnonic metallic behavior, too large an anisotropy drives the system into a magnonic insulator. For $K_u \gtrsim 0.4 \times 10^3$ J/m^3 (Fig. 6.2(b)–(f)), a frequency gap opens due to symmetry breaking in the vertical (anisotropy) coupling experienced by spin-wave modes. The lifted degeneracy goes hand in hand with increased curvature, which evolves toward a parabolic form. In this regime, magnons acquire an effective mass defined as [47]:

$$m^* = \hbar^2 \left(\frac{\partial^2 E}{\partial k^2} \right)^{-1} = \hbar \left(\frac{\partial^2 \omega}{\partial k^2} \right)^{-1}, \tag{6.8}$$

valid for dispersive magnons. As in electronic systems, magnons thus develop an *inertia*, reducing their responsiveness to external driving. Practically, if an antenna excites magnons at a given frequency, a larger m^* demands a larger k due to the reduced curvature. Similarly, for fixed kinetic energy, a larger mass implies a larger k, since:

$$v_g = \hbar k / m^*. \tag{6.9}$$

Finally, for a given frequency shift $\delta\nu$, the wave-packet spread δk must grow with m^*. Intuitively, to "hop" across half a cell (Fig. 6.4, from (a) to (b)), magnons require extra energy that equals the bandgap. At the BZ edge, this requirement blocks continuous propagation, leaving only stationary resonances. The extra cost increases with K_u (Fig. 6.2(c)–(f)) and is directly tied to the periodic anisotropy that models inverse magnetoelastic coupling in the multiferroic bilayer.

For example, at $K_u = 5 \times 10^3$ J/m^3, a parabolic fit of the upper branch near the BZ edge (Fig. 6.2(c)) gives $m^* \approx 5.59 \times 10^{-27}$ kg ($\sim$ 6138 electron masses). Increasing anisotropy fourfold to $K_u = 2 \times 10^4$ J/m^3 (Fig. 6.2(e)) raises the mass to 1.198×10^{-26} kg ($\sim$ 13,153 electron masses). Thus, as the parabola broadens (smaller curvature), the effective mass increases, and so does magnon inertia. In parallel, the gap grows from about 0.380 GHz at $K_u = 5 \times 10^3$ J/m^3 to roughly 0.800 GHz at $K_u = 2 \times 10^4$ J/m^3.

The bandgap originates from the interaction of backward volume modes (m-BV, $m = 0, 1, 2, \ldots$) with the periodic anisotropy. Since we only consider propagation along x (parallel to the mean magnetization), the relevant waves are backward modes. At the BZ edge ($k = \pi/d$), two consecutive modes, m-BV and $(m+1)$-BV, are out of phase by $\pi/2$ (shifted by one-quarter wavelength). Consequently, they

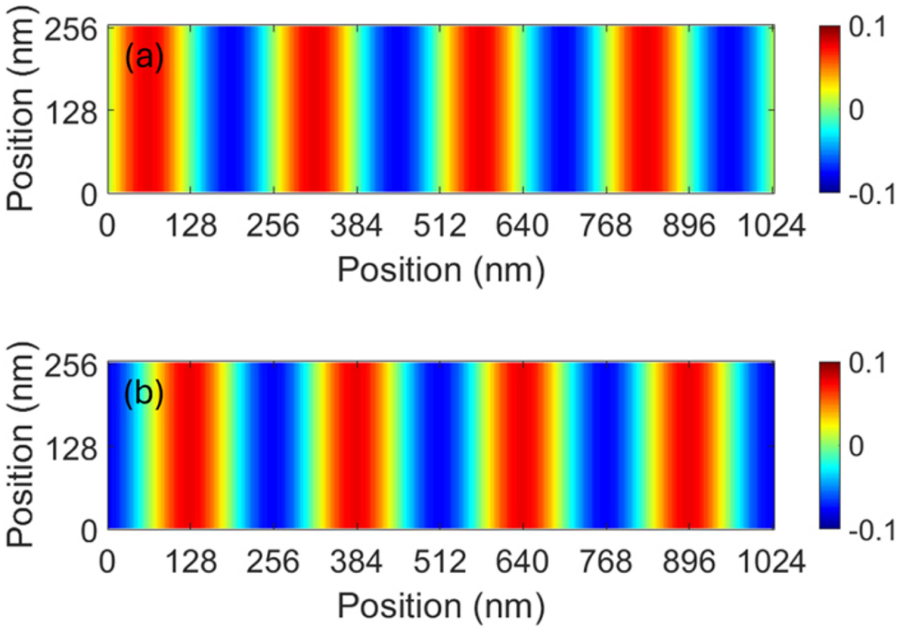

Figure 6.4: Mode profiles at the BZ edge for the magnon metal case $K_u = 1 \times 10^2$ J/m^3: (a) F mode (o-BV) and (b) 1-BV. They become indistinguishable upon translation by $d/2$, both occurring at $\sim$ 10.3 GHz. Four geometric BZs are shown ($a = 256$ nm), corresponding to eight physical BZs along x ($d = 128$ nm). The color scale indicates mode amplitude (arb. units).

couple differently to the anisotropy field (e.g., the fundamental o-BV has nodes at the 0° easy axis, while the 1-BV samples the +45° axis; see Fig. 6.4). This symmetry breaking lifts their degeneracy and opens a frequency gap. Notably, the gap forms only beyond the critical threshold $K_u \gtrsim 0.4 \times 10^3$ J/m^3.

Our simulations show that the gap increases monotonically with K_u and tends toward a saturation value of about 0.9 GHz (Fig. 6.5). Although a detailed engineering study is beyond our scope, both the slope and the saturation level can, in principle, be tailored through material choice, adding flexibility for device design.

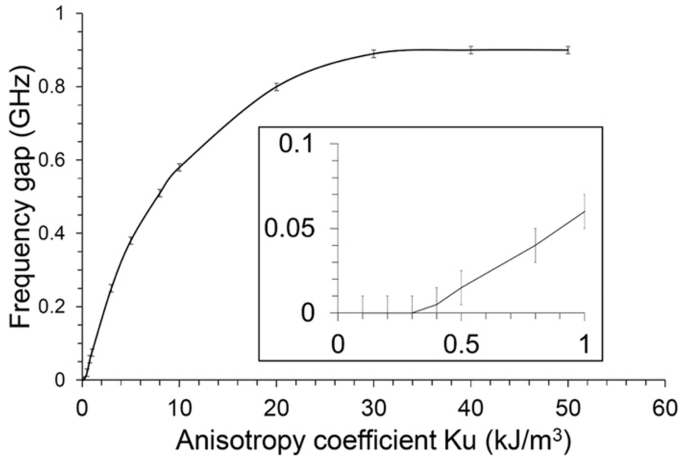

Figure 6.5: Frequency gap from simulations as a function of the anisotropy coefficient K_u. The uniform error bar corresponds to 0.01 GHz (simulation resolution). The inset shows that a nonzero gap appears only beyond the threshold $K_u = 0.4 \times 10^3$ J/m^3.

A further notable effect emerges at very large anisotropy (e.g., $K_u \approx 2 \times 10^4$ J/m^3): the lowest-frequency branch becomes nearly flat, while the upper branch remains parabolic. In that case, magnons in the lower band behave as stationary resonances, whereas those in the upper band remain propagating, as seen in Figs. 6.2(e)-(f). This closely resembles semiconductors, where valence-band states are localized while conduction-band states are delocalized. The coexistence of propagating and stationary modes in the same system (with a tunable gap) is particularly attractive for magnonic applications in filtering and information processingn [62, 63].

6.4 CONCLUSIONS

We have demonstrated a multiferroic magnonic crystal that can be continuously and reversibly tuned from a metallic (zero gap, linear dispersion) to an insulating (finite gap, parabolic dispersion) state for magnon propagation, in real time and controlled by a single external parameter. The ultimate knob is the voltage applied to the ferroelectric overlayer. Via inverse magnetoelastic coupling, the ferroelectric domain configuration is vertically transferred to the ferromagnetic film, which we model as a periodically varying anisotropy axis. The result is a sinusoidal magnetization landscape functioning as a tunable magnonic crystal.

The key transport quantities - frequency gap, group velocity, and effective mass - can be continuously tuned by the uniform anisotropy coefficient across a broad range ($0 \leq K_u \leq 5 \times 10^4$ J/m^3). We extended the Dirac-magnon formalism to a linear lattice in a continuous medium, showing that in the gapless window ($0.04 \leq K_u \leq 0.4$ kJ/m^3) the system supports massless magnons with linear dispersion and high mobility. Within this framework, we identify the hopping rate as the central parameter governing magnonic conductivity, directly linked to the balance of exchange, dipolar, and anisotropy interactions.

In the insulating regime ($K_u \gtrsim 0.4$ kJ/m^3), the frequency gap grows monotonically with K_u, initially approximately linearly and then approaching saturation. Simultaneously, the parabolic curvature correlates with the effective magnon mass, which increases with anisotropy. At high K_u, the lower band flattens, yielding stationary (non-propagating) modes, while the upper band remains dispersive. Hence, sinusoidally magnetized films at large K_u feature both stationary and propagating magnons separated by a ~ 1 GHz window. This duality opens the door to selectively exciting either propagating information carriers or dynamically stored states within the same physical device.

These results outline a pathway to low-dissipation, miniaturized magnonic technologies in which spin waves convey information. In particular, voltage-controlled magnetic anisotropy and angular-momentum transfer could enable operation with negligible or greatly reduced electric current. As a result, such devices are not only scalable to smaller footprints but can also achieve higher clock rates, free from the constraints imposed by Joule heating.

BIBLIOGRAPHY

[1] Pietro Micaletti et al. "Magnonic analog of a metal-to-insulator transition in a multiferroic heterostructure". In: *Journal of Applied Physics* 137 (2025), p. 153906. DOI: 10.1063/5.0250690. URL: https://doi.org/10.1063/5.0250690.

[2] B. Rana and Y. Otani. "Towards magnonic devices based on voltage-controlled magnetic anisotropy". In: *Communications Physics* 2.1 (2019), p. 90. DOI: 10.1038/s42005-019-0189-6. URL: https://doi.org/10.1038/s42005-019-0189-6.

[3] L. Lannelongue et al. "Greener principles for environmentally sustainable computational science". In: *Nature Computational Science* 3.6 (2023), pp. 514–521. DOI: 10.1038/s43588-023-00461-y. URL: https://doi.org/10.1038/s43588-023-00461-y.

[4] M. Mitchell Waldrop. "More than Moore". In: *Nature* 530 (2016), pp. 144–147. DOI: 10.1038/530144a. URL: https://doi.org/10.1038/530144a.

[5] Maxim Mostovoy. "Multiferroics: different routes to magnetoelectric coupling". In: *npj Spintronics* 2.1 (June 2024), p. 18. ISSN: 2948-2119. DOI: 10.1038/s44306-024-00021-8. URL: https://doi.org/10.1038/s44306-024-00021-8.

[6] A. B. Ustinov et al. "Dynamic electromagnonic crystal based on artificial multiferroic heterostructure". In: *Communications Physics* 2.1 (2019), p. 137. DOI: 10.1038/s42005-019-0240-7. URL: https://doi.org/10.1038/s42005-019-0240-7.

[7] H. Qin et al. "Electric-field control of propagating spin waves by ferroelectric domain-wall motion in a multiferroic heterostructure". In: *Advanced Materials* 33.27 (2021), p. 2100646. DOI: 10.1002/adma.202100646. URL: https://doi.org/10.1002/adma.202100646.

[8] B. Van de Wiele et al. "Tunable short-wavelength spin wave excitation from pinned magnetic domain walls". In: *Scientific Reports* 6.1 (2016), p. 21330. DOI: 10.1038/srep21330. URL: https://doi.org/10.1038/srep21330.

[9] M. E. Jamer et al. "Long-range electric field control of permalloy layers in strain-coupled composite multiferroics". In: *Physical Review Applied* 10 (2018), p. 044045. DOI: 10.1103/PhysRevApplied.10.044045. URL: https://doi.org/10.1103/PhysRevApplied.10.044045.

[10] T. H. E. Lahtinen, J. O. Tuomi, and S. van Dijken. "Pattern transfer and electric-field-induced magnetic domain formation in multiferroic heterostructures". In: *Advanced Materials* 23.28 (2011), pp. 3187–3191. DOI: 10.1002/adma.201100426. URL: https://doi.org/10.1002/adma.201100426.

[11] T. H. E. Lahtinen et al. "Alternating domains with uniaxial and biaxial magnetic anisotropy in epitaxial Fe films on $BaTiO_3$". In: *Applied Physics Letters* 101.26 (2012), p. 262405. DOI: 10.1063/1.4773482. URL: https://doi.org/10.1063/1.4773482.

[12] S. Hämäläinen et al. "Tunable short-wavelength spin-wave emission and confinement in anisotropy-modulated multiferroic heterostructures". In: *Physical Review Applied* 8 (2017), p. 014020. DOI: 10.1103/PhysRevApplied.8.014020. URL: https://link.aps.org/doi/10.1103/PhysRevApplied.8.014020.

[13] A. Barman et al. "The 2021 magnonics roadmap". In: *Journal of Physics: Condensed Matter* 33.41 (2021), p. 413001. DOI: 10.1088/1361-648X/abec1a. URL: https://doi.org/10.1088/1361-648X/abec1a.

[14] T. Dion et al. "Ultrastrong magnon-magnon coupling and chiral spin-texture control in a dipolar 3D multilayered artificial spin-vortex ice". In: *Nature Communications* 15.1 (2024), p. 4077. DOI: 10.1038/s41467-024-48080-z. URL: https://doi.org/10.1038/s41467-024-48080-z.

[15] R. Negrello et al. "Dynamic coupling and spin-wave dispersions in a magnetic hybrid system made of an artificial spin-ice structure and an extended NiFe underlayer". In: *APL Materials* 10 (2022), p. 091115. DOI: 10.1063/5.0102571. URL: https://doi.org/10.1063/5.0102571.

[16] F. Montoncello et al. "A Brillouin light scattering study of the spin-wave magnetic field dependence in a magnetic hybrid system made of an artificial spin-ice structure and a film underlayer". In: *Journal of Applied Physics* 133 (2023), p. 083901. DOI: 10.1063/5.0140866. URL: https://doi.org/10.1063/5.0140866.

[17] X. R. Wang, X. Gong, and K. Y. Jing. "Supermirrors and spin wave amplifications". In: *Applied Physics Letters* 124.8 (2024), p. 082403. DOI: 10.1063/5.0195063. URL: https://doi.org/10.1063/5.0195063.

[18] L. C. Parsons. "Influence of spin wave attenuation on a ferromagnetic nanowire-based magnonic Bragg mirror". In: *Journal of Magnetism and Magnetic Materials* 426 (2017), pp. 794–799. DOI: 10.1016/j.jmmm.2016.10.080. URL: https://doi.org/10.1016/j.jmmm.2016.10.080.

[19] R. Huber, T. Schwarze, and D. Grundler. "Nanostripe of subwavelength width as a switchable semitransparent mirror for spin waves in a magnonic crystal". In: *Physical Review B* 88 (2013), p. 100405. DOI: 10.1103/PhysRevB.88.100405. URL: https://doi.org/10.1103/PhysRevB.88.100405.

[20] J. D. Joannopoulos et al. *Photonic Crystals: Molding the Flow of Light*. 2nd. Princeton University Press, 2008. ISBN: 9780691124568.

[21] P. Bhattacharjee and S. Barman. "Control of band gap of spin waves in width-modulated nanostrip using voltage-controlled magnetic anisotropy: Spin wave filter". In: *2023 Second International Conference on Electrical, Electronics, Information and Communication Technologies (ICEEICT)*. IEEE, 2023, pp. 1–4. DOI: 10.1109/ICEEICT57430.2023.10090057.

[22] P. Frey et al. "Reflection-less width-modulated magnonic crystal". In: *Communications Physics* 3.1 (2020), p. 17. DOI: 10.1038/s42005-020-0281-y. URL: https://doi.org/10.1038/s42005-020-0281-y.

[23] Q. Wang et al. "Voltage-controlled nanoscale reconfigurable magnonic crystal". In: *Physical Review B* 95 (2017), p. 134433. DOI: 10.1103/PhysRevB.95.134433. URL: https://doi.org/10.1103/PhysRevB.95.134433.

[24] C.-G. Duan et al. "Surface magnetoelectric effect in ferromagnetic metal films". In: *Physical Review Letters* 101 (2008), p. 137201. DOI: 10.1103/PhysRevLett.101.137201. URL: https://doi.org/10.1103/PhysRevLett.101.137201.

[25] M. Staruch et al. "Reversible strain control of magnetic anisotropy in magnetoelectric heterostructures at room temperature". In: *Scientific Reports* 6.1 (2016), p. 37429. DOI: 10.1038/srep37429. URL: https://doi.org/10.1038/srep37429.

[26] M. Balinskiy et al. "Magnetoelectric spin wave modulator based on synthetic multiferroic structure". In: *Scientific Reports* 8.1 (2018), p. 10867. DOI: 10.1038/s41598-018-28878-w. URL: https://doi.org/10.1038/s41598-018-28878-w.

[27] S. Mamica et al. "Spin-wave dynamics in artificial anti-spin-ice systems: Experimental and theoretical investigations". In: *Physical Review B* 98 (2018), p. 054405. DOI: 10.1103/PhysRevB.98.054405. URL: https://doi.org/10.1103/PhysRevB.98.054405.

[28] E. Iacocca et al. "Reconfigurable wave band structure of an artificial square ice". In: *Physical Review B* 93 (2016), p. 134420. DOI: 10.1103/PhysRevB.93.134420. URL: https://doi.org/10.1103/PhysRevB.93.134420.

[29] S. S. Pershoguba et al. "Dirac magnons in honeycomb ferromagnets". In: *Physical Review X* 8 (2018), p. 011010. DOI: 10.1103/PhysRevX.8.011010. URL: https://doi.org/10.1103/PhysRevX.8.011010.

[30] A. V. Chumak, A. A. Serga, and B. Hillebrands. "Magnonic crystals for data processing". In: *Journal of Physics D: Applied Physics* 50.24 (2017), p. 244001. DOI: 10.1088/1361-6463/aa6a65. URL: https://doi.org/10.1088/1361-6463/aa6a65.

[31] A. K. Dhiman et al. "Reconfigurable magnonic crystals: Spin wave propagation in Pt/Co multilayer in saturated and stripe domain phase". In: *APL Materials* 12.11 (2024), p. 111106. DOI: 10.1063/5.0227380. URL: https://doi.org/10.1063/5.0227380.

[32] F. Ma et al. "Skyrmion-based dynamic magnonic crystal". In: *Nano Letters* 15.6 (2015), pp. 4029–4036. DOI: 10.1021/acs.nanolett.5b00996. URL: https://doi.org/10.1021/acs.nanolett.5b00996.

[33] P. Micaletti et al. "A sinusoidal magnetization distribution as an original way to generate a versatile magnonic crystal for magnon propagation". In: *Journal of Magnetism and Magnetic Materials* 622 (2025), p. 172959. DOI: 10.1016/j.jmmm.2025.172959. URL: https://doi.org/10.1016/j.jmmm.2025.172959.

[34] A. V. Chumak et al. "A current-controlled, dynamic magnonic crystal". In: *Journal of Physics D: Applied Physics* 42.20 (2009), p. 205005. DOI: 10.1088/0022-3727/42/20/205005. URL: https://doi.org/10.1088/0022-3727/42/20/205005.

[35] M. Vogel et al. "Optically reconfigurable magnetic materials". In: *Nature Physics* 11 (2015), pp. 487–491. DOI: 10.1038/nphys3325. URL: https://doi.org/10.1038/nphys3325.

[36] R. G. Kryshtal and A. V. Medved. "Surface acoustic wave in yttrium iron garnet as tunable magnonic crystals for sensors and signal processing applications". In: *Applied Physics Letters* 100.19 (2012), p. 192410. DOI: 10.1063/1.4714507. URL: https://doi.org/10.1063/1.4714507.

[37] R. G. Kryshtal and A. V. Medved. "Surface acoustic waves in dynamic magnonic crystals for microwave signals processing". In: *Ultrasonics* 94 (2019), pp. 60–64. DOI: 10.1016/j.ultras.2018.12.003. URL: https://doi.org/10.1016/j.ultras.2018.12.003.

[38] I. A. Ustinova, A. A. Nikitin, and A. B. Ustinov. "Dynamic magnonic crystal based on a layered ferrite–ferroelectric structure". In: *Technical Physics* 61.3 (2016), pp. 473–476. DOI: 10.1134/S1063784216030233. URL: https://doi.org/10.1134/S1063784216030233.

[39] A. A. Nikitin et al. "Dynamic electromagnonic crystals based on ferrite-ferroelectric thin film multilayers". In: *Physical Review B* 109 (2024), p. 024440. DOI: 10.1103/PhysRevB.109.024440. URL: https://doi.org/10.1103/PhysRevB.109.024440.

[40] A. A. Nikitin et al. "Dynamic magnonic crystals based on vanadium dioxide gratings". In: *Physical Review Applied* 20 (2023), p. 044026. DOI: 10.1103/PhysRevApplied.20.044026. URL: https://doi.org/10.1103/PhysRevApplied.20.044026.

[41] V. E. Demidov, B. A. Kalinikos, and P. Edenhofer. "Dipole-exchange theory of hybrid electromagnetic-spin waves in layered film structures". In: *Journal of Applied Physics* 91.12 (2002), pp. 10007–10016. DOI: 10.1063/1.1475373. URL: https://doi.org/10.1063/1.1475373.

[42] A. A. Nikitin et al. "Dispersion characteristics of spin-electromagnetic waves in planar multiferroic structures". In: *Journal of Applied Physics* 118.18 (2015), p. 183901. DOI: 10.1063/1.4935266. URL: https://doi.org/10.1063/1.4935266.

[43] A. Vansteenkiste et al. "The design and verification of MuMax3". In: *AIP Advances* 4.10 (2014), p. 107133. DOI: 10.1063/1.4899186. URL: https://doi.org/10.1063/1.4899186.

[44] R. O. Serha et al. "Magnetic anisotropy and GGG substrate stray field in YIG films down to millikelvin temperatures". In: *npj Spintronics* 2.1 (2024), p. 29. DOI: 10.1038/s44306-024-00030-7. URL: https://doi.org/10.1038/s44306-024-00030-7.

[45] D. Lebeugle et al. "Electric field switching of the magnetic anisotropy of a ferromagnetic layer exchange coupled to the multiferroic compound". In: *Physical Review Letters* 103 (2009), p. 257601. DOI: 10.1103/PhysRevLett.103.257601. URL: https://doi.org/10.1103/PhysRevLett.103.257601.

[46] The z-component is usually relevant in the experiments, either ferromagnetic resonance or Brillouin light scattering.

[47] C. Kittel, P. McEuen, and John Wiley & Sons. *Introduction to Solid State Physics*. John Wiley & Sons, 2015. ISBN: 9788126535187. URL: https://books.google.it/books?id=rAMujwEACAAJ.

[48] F. Montoncello and G. Gubbiotti. "Controlling the three dimensional propagation of spin waves in continuous ferromagnetic films with an increasing out of plane undulation". In: *Scientific Reports* 11 (2021), p. 21344. DOI: 10.1038/s41598-021-00479-0. URL: https://doi.org/10.1038/s41598-021-00479-0.

[49] B. A. Kalinikos and A. N. Slavin. "Theory of dipole-exchange spin wave spectrum for ferromagnetic films with mixed exchange boundary conditions". In: *Journal of Physics C: Solid State Physics* 19.35 (1986), p. 7013. DOI: 10.1088/0022-3719/19/35/014. URL: https://doi.org/10.1088/0022-3719/19/35/014.

[50] R. W. Damon and J. R. Eshbach. "Magnetostatic modes of a ferromagnet slab". In: *Journal of Physics and Chemistry of Solids* 19.3 (1961), pp. 308–320. DOI: 10.1016/0022-3697(61)90041-5. URL: https://doi.org/10.1016/0022-3697(61)90041-5.

[51] G. Gubbiotti et al. "Spin wave dispersion and intensity correlation in width-modulated nanowire arrays: A Brillouin light scattering study". In: *Journal of Applied Physics* 124 (2018), p. 083903. DOI: 10.1063/1.5047393. URL: https://doi.org/10.1063/1.5047393.

[52] Tuomas H. E. Lahtinen, Kévin J. A. Franke, and Sebastiaan van Dijken. "Electric-field control of magnetic domain wall motion and local magnetization reversal". In: *Scientific Reports* 2.1 (Feb. 2012), p. 258. ISSN: 2045-2322. DOI: 10.1038/srep00258. URL: https://doi.org/10.1038/srep00258.

[53] K. J. A. Franke et al. "Reversible electric-field-driven magnetic domain-wall motion". In: *Physical Review X* 5 (2015), p. 011010. DOI: 10.1103/PhysRevX.5.011010. URL: https://doi.org/10.1103/PhysRevX.5.011010.

[54] Z. Zhou et al. "Interfacial charge-mediated non-volatile magnetoelectric coupling in multiferroic heterostructures". In: *Scientific Reports* 5.1 (2015), p. 7740. DOI: 10.1038/srep07740. URL: https://doi.org/10.1038/srep07740.

[55] S. Homkar et al. "Ultrathin regime growth of atomically flat multiferroic gallium ferrite films with perpendicular magnetic anisotropy". In: *Physical Review Materials* 3 (2019), p. 124416. DOI: 10.1103/PhysRevMaterials.3.124416. URL: https://doi.org/10.1103/PhysRevMaterials.3.124416.

[56] M. Tinkham. *Group Theory and Quantum Mechanics*. Dover Publications, 2003. ISBN: 9780486435032.

[57] V. Ariel and A. Natan. "Electron effective mass in graphene". In: *2013 International Conference on Electromagnetics in Advanced Applications (ICEAA)*. IEEE, 2013, pp. 696–698. DOI: 10.1109/ICEAA.2013.6632357.

[58] J. Fransson, A. M. Black-Schaffer, and A. V. Balatsky. "Magnon Dirac materials". In: *Physical Review B* 94 (2016), p. 075401. DOI: 10.1103/PhysRevB.94.075401. URL: https://doi.org/10.1103/PhysRevB.94.075401.

[59] L. Giovannini. "Dirac magnons in honeycomb nanostructures". In: *Physical Review B* 107 (2023), p. 104418. DOI: 10.1103/PhysRevB.107.104418. URL: https://doi.org/10.1103/PhysRevB.107.104418.

[60] G. Venkat et al. "Proposal for a standard micromagnetic problem: Spin wave dispersion in a magnonic waveguide". In: *IEEE Transactions on Magnetics* 49 (2013), p. 524. DOI: 10.1109/TMAG.2012.2206820. URL: https://doi.org/10.1109/TMAG.2012.2206820.

[61] M. El-Batanouny. *Advanced Quantum Condensed Matter Physics: One-Body, Many-Body, and Topological Perspectives*. Cambridge University Press, 2020. ISBN: 9781108475167. DOI: 10.1017/9781108562010. URL: https://doi.org/10.1017/9781108562010.

[62] A. Frotanpour et al. "Magnetization dynamics of a Fibonacci-distorted Kagome artificial spin ice". In: *Physical Review B* 102 (2020), p. 224435. DOI: 10.1103/PhysRevB.102.224435. URL: https://doi.org/10.1103/PhysRevB.102.224435.

[63] A. Mahmoud et al. "Introduction to spin wave computing". In: *Journal of Applied Physics* 128 (2020), p. 161101. DOI: 10.1063/5.0019328. URL: https://doi.org/10.1063/5.0019328.

7

ANISOTROPY-DRIVEN POPULATION TRANSFER IN MAGNONIC DIRECTIONAL NANOCOUPLERS

ABSTRACT

In this Chapter, by means of micromagnetic simulations and analytical models, we investigate spin waves in a directional nanocoupler made of YIG. This device, widely used in ordinary electronics and integrated circuits, is a suitable platform for magnon propagation under metal or insulator conditions, and represents a versatile testbed for the implementation of a sinusoidal magnetization. We are interested in the population transfer *pt* between the two waveguides of this device when only one is excited with a specific frequency. It is known that *pt* can be tuned in different ways; here, we suggest an approach based on the introduction, in the region where the conduits are close, of a uniaxial magnetic anisotropy K_u (within a specific range) with a periodic orientation of the easy axis. This condition, which induces the local magnetization to relax to an undulated distribution, is technically fulfilled with the superposition of a chain of ferroelectric domains with periodic polarization directions. We find out how this method is versatile since it allows an extremely accurate control of *pt* levels just by varying K_u. This behavior is also properly described by our simple model which reproduces the data in the weak K_u regime $[0, 1000$ $\mathrm{J/m^3}]$, regardless of the anisotropy modulation period Λ considered. By means of the aforementioned arrangements and within this K_u window, the directional nanocoupler can function as a large number of devices with low dissipation properties. For higher K_u values, accessible for short Λ, we assist at a substantial stabilization of *pt* towards intermediate levels which is described by our phenomenological approach. In conclusion, K_u represents a new degree of freedom to easily manipulate *pt*. We also provide an outlook on future investigations regarding the directional coupler, with particular emphasis on the realization of power transfer schemes based on the Stimulated Raman Adiabatic Passage (STIRAP) protocol.

7.1 INTRODUCTION

The field of Magnonics investigates the use of spin waves and their quanta, known as magnons, as carriers of information in nanoscale circuits [1], aiming to reduce energy dissipation and achieve wavelengths well below those of electromagnetic waves at the same frequency. In this regard, a crucial component for integrated circuits is the *directional coupler*, a device originally introduced in optics [2, 3, 4] and more recently exploited in microelectronics [5], plasmonics [6] and photonics [7, 8]. Lately, the directional coupler has also been investigated in the field of magnonics [9, 10]. In this context, a key feature under study, since it determines the efficiency and functionality of magnonic logic elements, is the *controllable transfer* of spin-wave power, i.e., the *population transfer pt*, between two spatially separated channels.

Traditional directional couplers rely on two parallel waveguides placed in close proximity over a sufficiently wide coupling region [11]; lately though there has been a focus on more complex geometries [12] to overcome physical limitations, e.g., phase mismatch, narrow bandwidth, while meeting practical requirements for compactness and manufacturing tolerance. By controlling *pt*, the directional coupler can be reconfigured to work as a connector of magnonic conduits, a tunable power divider, a frequency separator, or even a multiplexer. This result has been achieved in different ways by the scientific community: first of all, as studied in [9], the application of certain excitation frequencies. Secondly, also variations in the pulse amplitude can contribute to changes in the levels of *pt* [10]. In this theoretical and numerical investigation, in which we employ a bent geometry that brings two waveguides into proximity for coupling and then separates them, facilitating in this way blueprint and minimal backscattering, we suggest the introduction, in the proximity region of the waveguides, of a *uniaxial magnetic anisotropy* K_u with a *periodic orientation* of the easy axis that simulates a prearranged sequence of ferroelectric domains with periodic polarization directions. The use of K_u has been extensively investigated in Chapter 6. The resulting relaxed magnetization assumes a sinusoidal distribution, whose properties have been examined in Chapter 4, with an amplitude varying with K_u, which is a full-fledged degree of freedom. The control of *pt* is ultimately achieved through the voltage applied to the ferroelectric layer, which in turn favors low-dissipation operation of the device. Within this overall picture, we draw an analogy with the excitation scheme at the *atomic level*, which provides an intuitive framework to describe the energy transfer mechanism in the directional coupler. In an atom, excitation occurs when an electron absorbs sufficient energy from an external field, typically a RF stimulus, and transitions from a lower to a higher energy state; the subsequent relaxation to the ground state leads to the emission of energy, either spontaneously or through stimulated processes [13]. In the present system, the excited and final states correspond respectively to the first and second waveguides of the directional coupler, where a certain amount of power is progressively transferred. The parameter K_u plays a role analogous to that of the external stimulating field in atomic physics, as it governs the probability of energy transfer between the two waveguides, effectively

controlling the coupling dynamics. In this sense, tuning K_u enables direct control over the excitation and relaxation pathways of the system, favoring low-dissipation operation and providing a clear physical interpretation of the observed behavior.

It has been shown in [9, 14] that the *dipolar coupling* of the two waveguides splits the fundamental spin-wave mode into symmetric and antisymmetric collective modes. Their interference causes a periodic exchange of energy between the waveguides, characterized by a *coupling length* L_c that depends on the device geometry, spin-wave wave number and the static magnetization configuration. Here, we demonstrate that varying K_u determines a corresponding variation of L_c and consequently a change of the levels of the population transfer. We also develop a simple model reproducing the results obtained with the simulations in the weak K_u regime (0–1000 J/m^3) regardless of the *anisotropy modulation period* Λ considered as well as, for short Λ only - for the reasons that will be explained in the following - a phenomenological description for a stronger K_u regime ($>$ 1000 J/m^3). Since no external magnetic field is applied thoroughout the investigation, the reduction of both electromagnetic interference and thermal effects are ensured for future technical implementations.

7.2 SYSTEM

Inspired by the geometrical characteristics of the device studied in [9], our directional coupler consists of two parallel yttrium iron garnet (YIG) nanowires - each 30μm long, 100 nm wide, 50 nm thick - separated by a gap δ of 30 nm in the proximity region. The angle between the sections is $\theta = 20°$. Since the corners of the coupler can act as secondary SW sources, it is convenient to introduce a translational shift $s = 100$ nm between the two waveguides in order to preserve the primary function of the device. The length of the coupled waveguides L_W, i.e., the aforementioned proximity region, is set equal to 4900 nm. We perform micromagnetic simulations by means of the GPU-accelerated software MuMax3 [15]. The material parameters are the standard ones for YIG: Gilbert damping constant $\alpha_G = 2 \cdot 10^{-4}$ saturation magnetization $M_S = 1.4 \times 10^5$ A/m, exchange stiffness $A_{ex} = 3.5$ pJ/m and gyromagnetic ratio $\gamma = 176$ rad GHz/T (standard values). The system is discretized into micromagnetic cells with dimension $5 \times 5 \times 10$ nm^3. The uniaxial magnetic anisotropy is set with the same magnitude K_u, but with different orientation of the easy axis according to the following (periodic) order, the same discussed in Chapter 6: 45°, 0°, -45°, 0°. This pattern, repeated along $L = L_W + 2s$, ensures in this region a sinusoidal arrangement of the magnetic moments after the relaxation process as already discussed (no external magnetic field is involved). Several anisotropy modulation periods Λ have been considered, from 40 nm to 1000 nm. For ground-state preparation, the system is relaxed to equilibrium prior to dynamical excitation and after the application of K_u. As can be observed in Fig. 7.1, which illustrates a sketch of the device, spin waves are excited by applying a localized, non-uniform sine-shaped magnetic field pulse on the out-of-plane component (z direction) over a 20 nm region located near the corner of one of the waveguide; in this way, only the driven guide

is excited and the coupling section remains field-free, establishing a well-defined single-mode input and preventing any bias-field or spectral contamination where the symmetric and antisymmetric modes form. The excitation frequency f_0 is set equal to 2.88 GHz because, at this value, in addition to minimal damping and instrumental compatibility, the dipolar splitting Δf gives a coupling length such that, being $L_W = 3L_c$, the wave undergoes a complete π-phase exchange precisely at the device exit, yielding near-unity power transfer [9], at least for zero K_u. We will see that the introduction of K_u, modifying this relation, will result in a different pt (at the same f_0).

The pulse amplitude b_0 is set equal to 1 mT, while the cutoff frequency is $f_c = 20$ GHz. The determination of pt levels requires the analysis of the power output outside L. More precisely, time-resolved magnetization data $m(x, y, z; t)$ are recorded for a total time $T = 25$ ns (to ensure propagation of the spin waves along L and for a sufficient trait of the regions at the exit) with time steps $\Delta t = 50$ ps. The measurement of pt first involves calculating the two integrals I_1 (excited guide) and I_2 (not excited guide) of the square modulus of the out-of-plane component of magnetization over two extended regions (500 nm along x) at the exit of the conduits; finally, the ratio $I_2/(I_1 + I_2)$ is calculated. As for dispersion relations, a two-dimensional fast Fourier transform is performed in space and time. In this case, T is set equal to 60 ns, yielding a frequency resolution $\delta f = 0.02$ GHz up to the highest resolvable frequency $f_{max} = 10$ GHz.

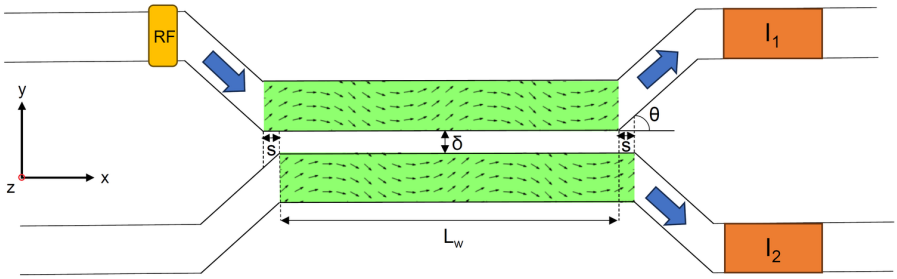

Figure 7.1: Sketch of the directional nanocoupler simulated throughout the investigation. The proximity region is characterized by the presence of an undulated alignment of the spin which is the consequence of the local relaxation of the system after the anisotropy is applied. RF corresponds to the excitation zone, I_1 and I_2 represent the physical regions of the system in which pt levels are measured. L_w is the length of the coupled waveguides (4900 nm), s the translational shift of 100 nm, $\delta = 30$ nm is the gap between the waveguides along L_w and $\theta = 20°$ the angle between the two different regions of the device.

It is known [9, 16] that in a directional coupler the dipolar interaction lifts the degeneracy of the lowest width mode, producing *two collective modes* - one *symmetric* (wave number k_s) and one *antisymmetric* (wave number k_{as}) - for the same excitation frequency. In this regard, for $f_0 = 2.88$ GHz, we are in a single-mode regime (higher modes are separated by several GHz at nanometric dimensions), so the coupling involves only the two symmetric/anti-symmetric branches of the fundamental mode. When only one waveguide is excited, these two modes interfere during propagation, periodically transferring energy back and forth between the guides. The coupling length L_c is

defined as the distance over which a *complete* energy transfer occurs (i.e., the position of the first maximum of energy in the not excited guide starting from the first maximum in the excited guide). Equivalently, it can be written as: $L_c = \frac{\pi}{|k_s - k_{as}|}$, which yields: $L_c = \frac{v_g}{2\Delta f_0}$, where $\Delta f_0 = |f_{as} - f_s|$ is the *frequency splitting* between these two modes and $v_g = \frac{\partial \omega(k)}{\partial k}$ is the *group velocity* of the fundamental mode of the isolated waveguide. In absence of K_u, the population transfer pt for a directional coupler in which a spin wave is originally excited in only one waveguide can be expressed in terms of the normalized output power. In fact, we have $p_1 = cos^2(\pi L_W/(2L_c))$ for the excited waveguide and $p_2 = sin^2(\pi L_W/(2L_c))$ for the non-excited waveguide, from which we get: $pt = p_2/(p_1 + p_2) = p_2$ [17]. For completeness, the step-by-step derivation of these relations - starting from the decomposition into symmetric and antisymmetric supermodes, their propagation with different wave numbers, and their interference at the output - is provided in Appendix 7.6. When K_u is introduced, the above relations must be reworked taking into consideration their dependence on K_u. This represents the theoretical contribution of the present investigation. In our simulations, as already anticipated, we introduce along L a uniaxial magnetic anisotropy K_u with a periodic arrangement. This structure mimics, from a physical point of view, a prearranged sequence of ferroelectric domains with alternating polarization directions. We consider several anisotropy values, ranging from 0 to 2000 J/m^3 with steps of 100 J/m^3, with a distinction: the interval $[0, 1000$ J/m$^3]$ is regarded as the *weak* K_u regime, while values from 1100 to 2000 J/m^3 belong to the *strong* K_u regime.

7.3 RESULTS

Here we provide a comprehensive analysis of pt as a function of K_u, examining how the coupling dynamics evolve from weak to strong K_u regimes. We first discuss the weak anisotropy window, where the system remains only mildly perturbed and the dependence of pt on K_u can be captured through a simplified phenomenological model built upon the behavior of v_g and Δf_0. We then move to the strong anisotropy regime, where the magnetization becomes highly modulated and additional mechanisms, such as magnetostatic self-cancellation, enhanced scattering, and background transfer channels, play a decisive role in shaping the measurable pt. Finally, we analyze the evolution of the coupling length L_c and its connection to the dispersion curves over an extended K_u range, showing how the increasing anisotropy progressively reduces the effective propagation channel, eventually preventing a well defined coupling process and marking the transition beyond the operational window of the device. Together, these results outline the full anisotropy-dependent landscape of the directional coupler.

7.3.1 *Weak anisotropy regime*

Here we present the main outcomes of our investigation regarding the weak K_u regime. First of all, it can be noted in Fig. 7.2 that pt

is mostly independent on the specific anisotropy modulation period Λ: in fact, the functional trend is the same for all the configurations studied.

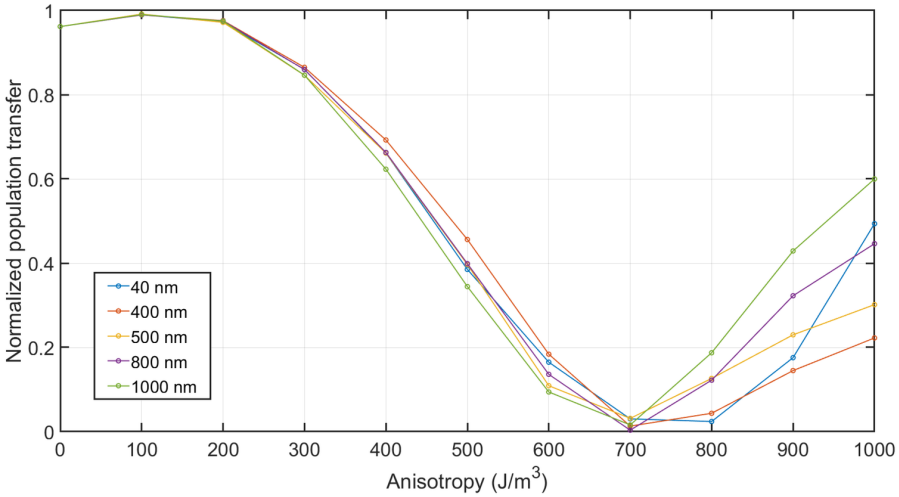

Figure 7.2: Population transfer as a function of the applied K_u for different anisotropy modulation periods Λ in the weak regime. An universal behavior of pt regardless of the period of anisotropy is observed. We choose $\Lambda = 1000$ nm (green line) because of the fabrication feasibility of the micron-scale.

This implies that it is possible to choose one value of Λ without loss of generality. We select $\Lambda = 1000$ nm because the micron-scale is technologically practical: consisting of only a few ~ 250 nm segments with well-defined easy-axis orientations ($0°, \pm 45°$), it spans the entire coupling region between the two waveguides. This makes the effective coupling profile reproducible from device to device using standard nanofabrication, whereas a deeply sub-100-nm pattern would require tens to hundreds of nominally identical unit cells and would map any small lithographic deviation directly into large variations of the measured pt. Therefore, the following quantitative discussion will refer specifically to the $\Lambda = 1000$ nm case, although the same considerations apply more generally, since the overall trend remains essentially unchanged apart from minor numerical differences.

Fig. 7.3 shows the behavior of pt levels (blue dots) as a function of the applied K_u for $\Lambda = 1000$ nm (green line of Fig. 7.2): an almost full pt is observed in the total absence of K_u or for extremely low values (up to 200 J/m^3). Then, for higher values and up to 800 J/m^3, energy transfer is progressively inhibited until it vanishes completely (after that, we assist at a rapid pt increase of up to 50% for 1000 J/m^3). Ultimately, we realize an extremely versatile device which, at the fixed excitation frequency of 2.88 GHz, allows to explore as many pt levels as desired in the weak K_u regime, moving from a complete, passing through an intermediate and concluding with a vanishing pt between the waveguides by means of variations in K_u and, therefore, referring to the ferroelectric overlayer, in a polarization current. The tunability of such a directional nanocoupler makes it suitable for real-world applications where high accuracy is required.

In order to describe the evolution of pt in the weak K_u regime with a simple model, preliminary considerations on the behavior of v_g and Δf_0 are necessary because, as mentioned above, they are

the building blocks of the coupling length L_c and, ultimately, of pt itself. As for v_g, the starting group velocity without any applied anisotropy is estimated to be around 460 m/s, a value in accordance with previous studies [18, 19]. When K_u is introduced, we initially assist at a slight progressive v_g decrease until the threshold of 1000 J/m^3 is reached. We find $v_g(K_u = 1000\ \mathrm{J/m^3}) \simeq 0.9 v_g(K_u = 0\ \mathrm{J/m^3})$ in this specific case, so we can reasonably assume v_g to be constant in this range. This choice is dictated by two physical reasons: first of all, in a YIG spin wave conduit the additional field produced by the uniaxial anisotropy is equal to $\mu_0 H_\alpha = 2K_u/M_s$ (with H_α anisotropy field introduced in Chapter 1), so that for $K_u \leq 1000\ \mathrm{J/m^3}$ one gets $\mu_0 H_\alpha \lesssim 8\% \cdot \mu_0 M_s$, with $\mu_0 M_s \approx 176$ mT. This means that the effects of introducing a weak anisotropy on the effective magnetic field governing the dynamics of the system are minimal. Furthermore, in Chapter 6, focusing on the effects of anisotropy on the magnonic band structures, we found that, for a similar system and within this weak anisotropy window, the dispersion curve is almost indistinguishable from the one in absence of anisotropy. As a consequence, in this range the group velocity v_g can be safely assumed to be constant in our model regardless of the applied K_u.

The same considerations do not apply to the frequency splitting Δf_0 which is directly proportional to H_α, therefore even modest values of K_u increase Δf_0 almost linearly. Hence, in the range $[0, 1000\ \mathrm{J/m^3}]$ it is reasonable to expand at first order the frequency splitting as: $\Delta f_W(K_u) = \Delta f_0 + \beta K_u$, with β constant and the subscript $_W$ a reference for the weak K_u regime. We find that, starting from 0.14 GHz for no applied K_u and reaching 0.19 GHz for $K_u = 1000\ \mathrm{J/m^3}$, $\Delta f_W(K_u)$ increases with a linear trend with slope $\beta = 5.7 \cdot 10^4$ GHz·m^3/J and intercept $\Delta f_0 = 0.13$ GHz. The high coefficient of determination $R^2 \simeq 0.95$ indicates that the model explains a substantial proportion of the variance, confirming its strong fit to the data.

To summarize, the coupling length L_c is now dependent on K_u, and this leads to the following population transfer:

$$pt(K_u) = sin^2\left(\frac{\pi L_W}{v_g}\left[\Delta f_0 + \beta K_u\right]\right). \tag{7.1}$$

This functional form is used to perform the optimal fit of the corresponding simulation data (red line of Fig. 7.3): we can notice a substantial agreement between simulations and theoretical predictions, further supported by the value of the parameters of the optimal fit which are very close with our starting guess (expected $L_w \Delta f_0 / v_g = 1.46$ vs. optimal fit value $= 1.37$ and expected $\beta/\Delta f_0 = 4 \cdot 10^{-4}$ m^3/J vs. optimal fit value $= 6 \cdot 10^{-4}$ m^3/J).

7.3.2 *Strong anisotropy regime*

Let us now consider the strong K_u regime, i.e., $K_u \gtrsim 1000\ \mathrm{J/m^3}$. In this case, the anisotropy modulation period Λ plays a crucial role with respect to pt. In fact, at fixed K_u, we consistently find that larger Λ yield output intensities too low to reliably extract pt, whereas smaller Λ maintain sufficient signal for a robust quantification. In practice, this means that, under identical operating conditions, pt becomes

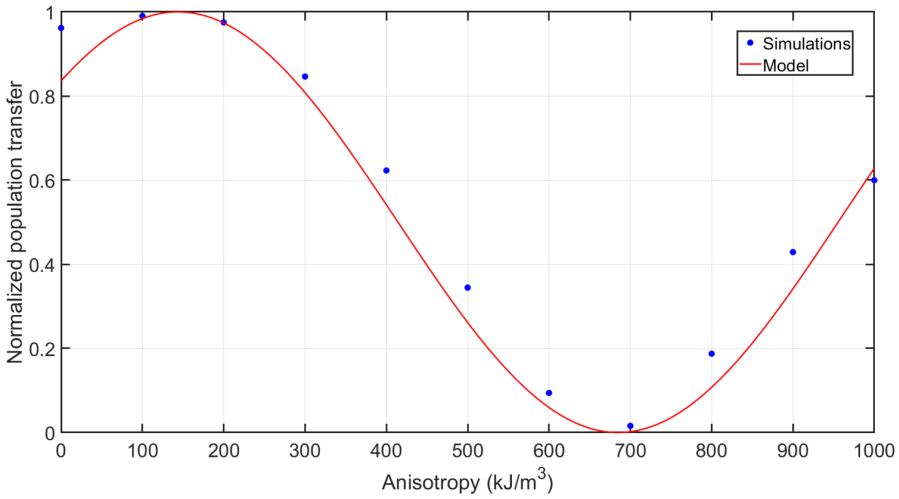

Figure 7.3: Population transfer (blue dots) as a function of the applied K_u in the weak regime for $\Lambda = 1000$ nm and theoretical model (red line), which properly describes its behavior. It can be noted that almost every pt percentage can be realized within this K_u range making it suitable for real-world applications.

effectively unmeasurable as Λ increases, while it remains observable for shorter Λ. From our simulations we consistently observe that, at fixed K_u, larger Λ (e.g., $\Lambda \sim 1$ μm) produce a more pronounced spatial undulation of the magnetization than short Λ (e.g., $\Lambda \sim 40$ nm); the modulation amplitude increases and the interfaces sharpen as K_u is raised. Building on this observation, we interpret the improved measurability at short Λ as a dipolar effect: the many closely spaced interfaces generate alternating magnetostatic charges whose stray fields largely close locally, distributing the magnetostatic constraint and effectively clamping the growth of the magnetization modulation as K_u increases. As a result, the forward signal does not collapse along the interaction region and the population transfer remains quantifiable at comparatively high K_u. While the dipolar self-cancellation provides a consistent primary explanation, we speculate that secondary factors may contribute in a complementary manner: for instance, reduced interfacial mismatch for finely segmented patterns can lower reflections at block boundaries; furthermore, measurement-related issues (e.g., normalization and signal-to-noise at very low output power) can accentuate the apparent loss of observability for longer Λ. These effects, although likely subdominant, could reinforce the observed robustness of short Λ at high K_u.

We now focus on the short-period modulation anisotropy pattern with $\Lambda = 40$ nm, which probes the regime where interfacial magnetostatic charges are densely interleaved and largely self-cancel, keeping the forward signal within the measurable dynamic range even at comparatively high K_u. This Λ limit is also physically informative since it provides a clean benchmark to compare against longer Λ that tend to accumulate uncompensated magnetostatic charges and lose observability.

In Fig. 7.4, for $\Lambda = 40$ nm we can notice a maximum of pt in correspondence of 1200 J/m^3 and an overall stabilization towards intermediate pt levels as K_u is increased, even if the spread if more limited, ranging from 40 to 90%, hence not realizing a complete or

vanishing pt (blue dots). As a result, we can conclude that this regime, despite certainly worthy of investigation by means of micromagnetic simulations and phenomenological insight into the constituent physical quantities, has less practical fallouts than the weak one, unless: 1) K_u cannot be tuned with accuracy for very high K_u values; 2) there is exclusive interest in power divider applications.

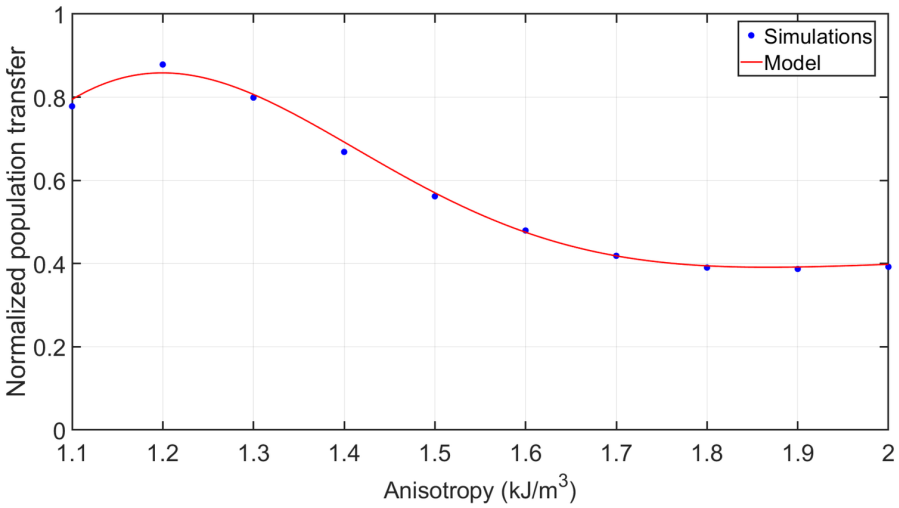

Figure 7.4: Population transfer (blue dots) as a function of the applied K_u in the strong regime ($\Lambda = 40$ nm). We notice a limited range of pt levels which results in an almost asymptotic intermediate splitting of the spin waves for very high K_u. Red line: phenomenological model.

When $K_u \gtrsim 1000\,\mathrm{J/m^3}$ the anisotropy field becomes larger and more comparable to the dipolar or bias fields and the magnetization significantly tilts: as a consequence, v_g, being affected by the change in the dynamics, must now be modeled as an explicit function of K_u. More precisely, $v_g(K_u)$ decreases due to the non negligible undulation of the magnetization and approaches a plateau $v_{gr,\infty}$ beyond which it makes no physical sense to investigate spin wave propagation. Furthermore, the symmetric and antisymmetric modes increase their distance until they reach, for $K_u \to \infty$, a maximum frequency splitting $\Delta f_{\max}$. According to previous studies [20, 21], the condition that must be fulfilled in order to retain the validity of coupled-mode theory in perturbative regime is $\Delta f_{\max}/f_0 \ll 1$, therefore we set $\Delta f_{\max} \simeq 0.40$ GHz. Hence, being Δf and v_g limited, also the coupling length L is bounded from below, tending to the finite limit $L_{\min} = v_{gr,\infty}/(2\Delta f_{\max})$ - beyond the purpose of this investigation - for physical reasons. A simple phenomenological model that in the strong K_u regime reproduces the behavior of v_g and Δf is therefore the following ansatz:

$$v_g(K_u) = v_g e^{-\delta K_u} + v_{g,\infty}, \tag{7.2}$$

$$\Delta f(K_u) = \Delta f_w^* + (\Delta f_{max} - \Delta f_w^*)\left[1 - e^{-\gamma K_u}\right], \tag{7.3}$$

where γ and δ are exponential constants to be determined through data and $\Delta f_W^* = \Delta f_W(K_u = 1000\,\mathrm{J/m^3})$. It can be noted that Eqs. (7.2) and (7.3) have general validity regardless of the applied K_u. As for Eq. (7.2), we have introduced a simplified model for the weak K_u regime,

which has fewer parameters, makes the proportionality between K_u and $pt(K_u)$ more immediate and introduces an error smaller than typical experimental uncertainties. Eq. (7.3) instead reduces to the correspondent equation in the weak K_u regime upon the identifications $\Delta f_W^* = \Delta f_W(K_u)$ and $(\Delta f_{\max} - \Delta f_W^*)\gamma = \beta$ between the weak and the strong K_u regimes.

In this case, for v_g we consider an exponential fit which, applied to the data at our disposal, yields $v_g \simeq 440$ m/s, $\delta \sim 3 \cdot 10^{-4}$ and $v_{g,\infty} \simeq 80$ m/s, values definitely coherent with the physical system under investigation ($R^2 \simeq 0.9$ and maximum relative error of 4 percentage points): in fact, we recover the group velocity in the weak K_u regime and find that its plateau $v_{g,\infty}$, below which all features of the directional coupler are suppressed, is in agreement with the literature that will be discussed in Sec. 7.3.3, devoted to higher K_u regimes.

As for Δf, we introduce an exponential saturating fit which results in $\gamma \sim 6 \cdot 10^{-4}$, with an $R^2 \simeq 0.82$ and maximum relative error - the very last value - around 10 percentage points.

Moving to pt in the strong K_u regime - which implies, as already observed, a very undulated magnetization - we believe that there are two additional mechanisms that should be taken into consideration.

1. Above a certain threshold, which is 1000 J/m^3 for the reasons related to the influence of H_α discussed previously, K_u introduces a non-negligible additional distance-dependent scattering loss. In fact, a spatially periodic increase of K_u deepens the effective field and reduces, as observed, the spin-wave v_g, thereby increasing the dwell time within L. This process (along with the Gilbert damping, which is, however, always present) acts on the field amplitude, so the transferred power pt contains an exponential damping factor which be seen as the consequence of a symmetry breaking that leads to the non conservation of pt at high K_u. Omitting this exponential term would overestimate the oscillation depth and lead to an unrealistically perfect population transfer.

2. Dipolar fringe fields, also considering the close gap $\delta = 30$ nm between the two waveguides, create an incoherent pathway that transports an L_c-independent fraction of pt to the non-excited guide. This appears as a flat "background floor" that is always present in this range, regardless of the applied K_u.

In light of the above considerations, we can assume that in the strong K_u regime the behavior of pt is adequately described as follows:

$$pt(K_u) = sin^2\left[\frac{\pi L_w \, \Delta f(K_u)}{v_{\mathrm{gr}}(K_u)}\right] e^{-\eta K_u} + C_{bg}, \tag{7.4}$$

where the extended forms of $v_g(K_u)$ and $\Delta f(K_u)$ are those of Eqs. (7.2) and (7.3), η is an exponential constant to be determined through data and C_{bg} is a constant, i.e. the aforementioned "background floor". With this functional form, we perform the optimal fit of the corresponding simulation data (red line of Fig. 7.4), including all physical parameters in order to verify the general validity of our assumption: there is a good agreement between simulations and phenomenological model,

further supported by the value of the parameters of the optimal fit which are quite similar to our starting guess, as can be seen in Tab. 7.1.

Parameters	v_g (m/s)	δ (m^3/J)	$v_{g,\infty}$ (m/s)	Δf_{max} (GHz)	γ (m^3/J)	η (m^3/J)	C_{bg}
Expected	440	$3 \cdot 10^{-4}$	80	0.4	$6 \cdot 10^{-4}$	$3.0 \cdot 10^{-3}$	0.40
Optimal	394	$2 \cdot 10^{-4}$	95	0.3	$7 \cdot 10^{-4}$	$2.9 \cdot 10^{-3}$	0.39

Table 7.1: Comparison of parameters: nominal values vs. optimal fit. The agreement is remarkable, suggesting the validity of the phenomenological model in the strong K_u regime ($\Lambda = 40$ nm).

7.3.3 *Coupling length, higher anisotropy regimes and dispersion curves*

We show the evolution of the coupling length L_c - determined, accordingly to the discussion in Sec. 7.2, as the distance over which a complete energy transfer occurs - as a function of K_u in both regimes investigated in the $\Lambda = 40$ nm case (see Fig. 7.5). It can be noted, net of the erratic behavior due to the difficult data acquisition, an evident linear decreasing trend of L_c as K_u increases. This effect can be understood at the mathematical level by considering, regime by regime, the proposed functional forms for Δf and v_g and their behavior as K_u is applied. The $\Lambda = 40$ nm case has been selected as representative since it offers the possibility to investigate a wider range of K_u, but the overall linear decreasing trend remains consistent for all other cases considered.

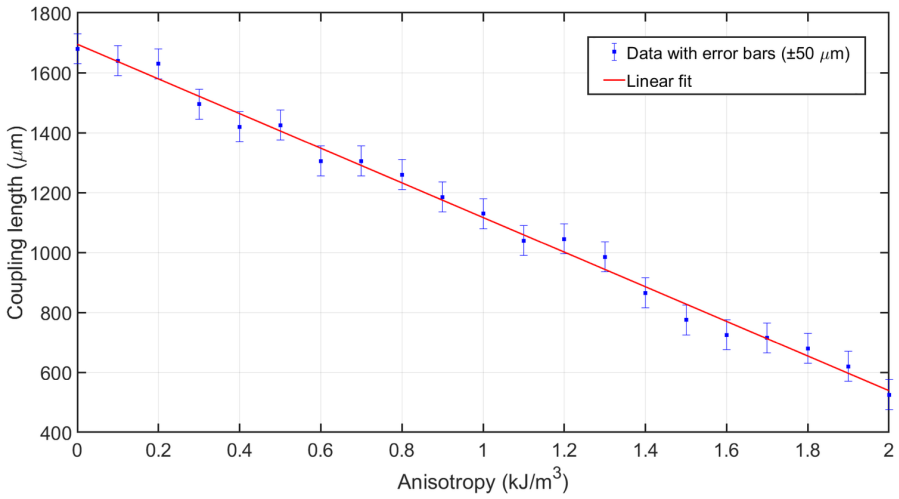

Figure 7.5: Evolution of the coupling length L_c as a function of the anisotropy K_u. The data are plotted with an error bar because of the limited precision of the method related to the data acquisition. However, the linear decreasing fit (in red) intercepts all points net of the uncertainties. Parameters of the fit: m $= -5.78 \cdot 10^{-1}$m/J, q $= 1695 \cdot 10^{-6}$ m.

As already remarked, above a critical K_u, the relaxed sinusoidal magnetization, now very undulated, breaks the uniform spin-wave channel into alternating propagating and evanescent (or highly reflective) segments, so that no continuous pathway remains and stationary waves formation along L occurs before the definitive suppression.

For the system under investigation, K_u values higher than 2000 J/m^3 forbid a clean population transfer.

Higher K_u values than those considered lead first to the *suppression* of *pt* because the pronounced undulated arrangement of the spins along L_c results in an effective field which behaves like a potential well: the spin waves are confined within it and become almost stationary, causing their intensity in the colormap to drop sharply and making the output signal - based on their propagation along the device - particularly difficult to measure. Even higher K_u values lead to the *evanescence* of spin waves since the strong perturbation definitely breaks the unambiguous correspondence between frequency and wave number and opens a band-gap range where the equation of motion admits only solutions at complex wavevector, so that the concept of v_g is physically meaningless [22]. Under these two peculiar conditions, the device no longer acts as a directional coupler: the almost stationary and eventually evanescent spin waves enable other practical functions that have already been demonstrated experimentally - ranging from an ultracompact reject-band filter [23], to a low-phase-noise delay line [24], and even slow-wave resonators that hybridize magnons and photons [25], which, however, are beyond the scope of this investigation. To sum up, once the magnetization is locked to the easy axis introduced with the periodic patterning, which means very high K_u values, additional K_u no longer alters the coupling dynamics and makes *pt* ineffective and not detectable.

Among the different Λ configurations, the case with $\Lambda = 40$ nm represents the most comprehensive scenario, also with regard to the dispersion relations, as it allows for a thorough analysis of spin-wave propagation in a directional coupler reconfigured through the application of a magnetic anisotropy. Figure 7.6 shows the magnonic band diagrams as a function of K_u. The flat band at 2.88 GHz corresponds to the excitation frequency f_0; its intersection with the curves associated with the antisymmetric (upper) and symmetric (lower) modes defines the wavevector difference $|k_s - k_{as}|$, which enters the expression of the coupling length L_c introduced in Sec. 7.2 [9]. As K_u increases, a clear shift of the dispersion curves toward higher frequencies is observed, resulting from the enhancement of the anisotropy field H_α and, consequently, of the effective field experienced by the magnons. It can also be noted that, with increasing K_u, the wavevector difference $|k_s - k_{as}|$ progressively increases, leading to a decrease of L_c, in excellent agreement with the trend reported in Fig. 7.5. Furthermore, the magnonic band diagrams provide a crucial validation of the operating range of the directional coupler. In particular, panel (d) of Fig. 7.6 shows that for K_u values exceeding the operational range (e.g., $K_u = 3500$ J/m^3 for visual clarity, although this effect becomes evident already for K_u slightly above 2000 J/m^3), the intersection between the antisymmetric-mode curve and the flat band corresponding to f_0 no longer occurs. In this condition, a proper coupling length L_c cannot be defined, with all the consequent implications on the device operability previously discussed.

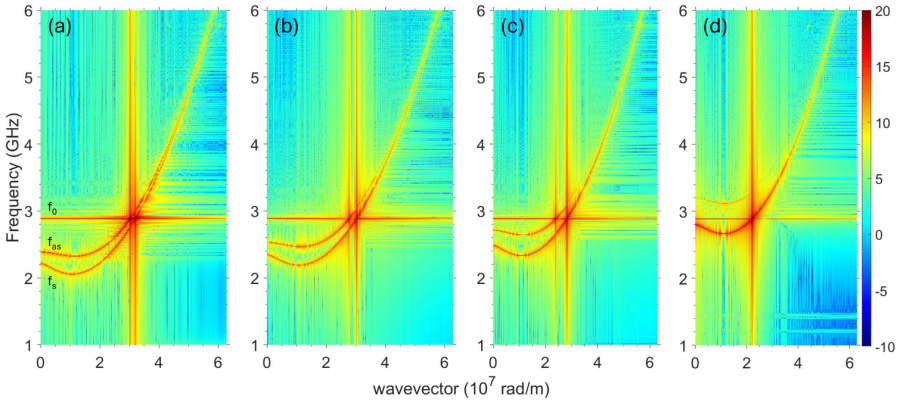

Figure 7.6: Magnonic band diagrams as a function of the applied K_u (Λ = 40 nm). (a): 0 J/m^3, (b): 700 J/m^3, (c): 1500 J/m^3, (d): 3500 J/m^3.

7.4 STIRAP PROTOCOL APPLIED TO THE DIRECTIONAL COUPLER

In this section, we first review the *Stimulated Raman Adiabatic Passage* (STIRAP) protocol and then apply it to the directional coupler, implementing a *dark-state scheme* for a versatile *pt*. STIRAP is a method to transfer population between two long-lived states of a three-level atom while keeping the lossy intermediate state essentially unoccupied [26, 27]. To understand how such transfer can occur without populating the middle level, it is convenient to recall the generic three-level Λ configuration, in which the atom possesses two ground or metastable states, $|1\rangle$ and $|2\rangle$, both optically coupled to a short-lived excited state $|3\rangle$. One laser field (the pump) addresses the $|1\rangle \leftrightarrow |3\rangle$ transition. A second field (the Stokes) addresses $|3\rangle \leftrightarrow |2\rangle$. In conventional excitation schemes one would raise population from $|1\rangle$ to $|3\rangle$ and then stimulate it down to $|2\rangle$, unavoidably exposing the atom to spontaneous emission from $|3\rangle$. STIRAP takes a different route: by shaping and ordering the two light fields appropriately, the atomic state follows a coherent superposition of $|1\rangle$ and $|2\rangle$ that contains virtually no $|3\rangle$ component. In other words, the atom is guided around the lossy level rather than through it. The key feature of the STIRAP protocol is the counterintuitive pulse sequence. The Stokes field, which couples the intermediate and the final state, is switched on first and reaches its maximum before the pump field rises; the two pulses then overlap in time, and finally the Stokes field decays after the pump. At the beginning of the sequence the atom, prepared in $|1\rangle$, "sees" a strong optical coupling between $|3\rangle$ and $|2\rangle$ and only a weak coupling from $|1\rangle$ to $|3\rangle$. Under these conditions, the dressed atomic eigenstates include a particular superposition of $|1\rangle$ and $|2\rangle$ that is decoupled from $|3\rangle$, often called the *dark state* (Fig. 7.7(a)). As the temporal envelopes evolve, this superposition continuously rotates from being almost entirely $|1\rangle$ to being almost entirely $|2\rangle$. If the change is slow enough and the two-photon resonance between $|1\rangle$ and $|2\rangle$ is maintained, the atomic state adiabatically follows this superposition from start to finish, achieving nearly unit population transfer while the intermediate state remains unpopulated at all times.

From a device perspective, the three-level viewpoint highlights why STIRAP is a preferred primitive for state preparation and quantum control. Because the intermediate state remains dark, the method is

inherently low-dissipation and preserves coherence during transfer, which is invaluable when the target state will be used for precision metrology, quantum logic, or storage. Because the process is adiabatic and geometric in nature, it is resistant to moderate fluctuations of intensity and pulse duration, and its outcome can be tuned by controlling the relative phase of the two fields to set the final quantum phase of $|2\rangle$. And because the underlying requirement is simply the existence of two long-lived levels connected through a common, optically accessible partner, the same three-level blueprint extends across platforms: from neutral atoms and trapped ions to molecules, color centers and semiconductor quantum wells.

The three-level viewpoint of STIRAP can be carried over to a magnonic directional coupler [28] by mapping the two parallel spin-wave guides to the long-lived endpoints and introducing a deliberately lossy *intermediate* waveguide that must remain unpopulated, i.e., dark. To make this identification explicit, we now label:

- the initially excited waveguide as $|1\rangle$ (initial state);
- the target waveguide as $|2\rangle$ (final state);
- the thin, high-damping intermediate guide as $|3\rangle$ (the dark state).

As in atomic STIRAP, the goal is to transfer energy and phase from $|1\rangle$ to $|2\rangle$ while keeping $|3\rangle$ essentially unoccupied, so that dissipation in the lossy channel is avoided, even though its presence is essential to enable the transfer. In fact, our preliminary simulations indicate that, when the gap δ between the two waveguides exceeds 140 nm, population transfer to the unexcited waveguide is effectively suppressed, as can be seen in Fig. 7.7(b). This behaviour can be ascribed to the progressive weakening of the dipolar coupling between the two channels as their separation increases, which ultimately prevents efficient energy exchange across the structure.

In contrast, when an intermediate waveguide made of a material with higher magnetic damping than YIG, such as permalloy, is introduced between the two low-loss channels, the coupling behaviour changes significantly. The intermediate layer effectively assumes the role of a dark state, mediating an indirect but coherent coupling between the two waveguides. Under these conditions, and for the same δ, a clear pt ($\sim$ 30%) is recovered. The physical picture is that the presence of the dissipative conduit enables an adiabatic pathway in which energy is coherently transferred between the two YIG guides while the strongly damped intermediate region remains only virtually excited (Fig. 7.7 (c)). Furthermore, for the same geometry, pt can be enhanced an varied at will by applying in the coupling region a uniaxial magnetic anisotropy with amplitude K_u with periodic polarization directions. In Fig. 7.8, pt is shown as a function of the uniaxial anisotropy constant K_u for a directional coupler operating under the STIRAP protocol, with an anisotropy modulation period of $\Lambda = 40$ nm (however, the overall trend is qualitatively similar for all values of Λ examined throughout this study).

It follows that, even when the STIRAP protocol is applied to the directional coupler, both v_g and Δf remain governed by the same control parameter, namely, the voltage applied to the ferroelectric

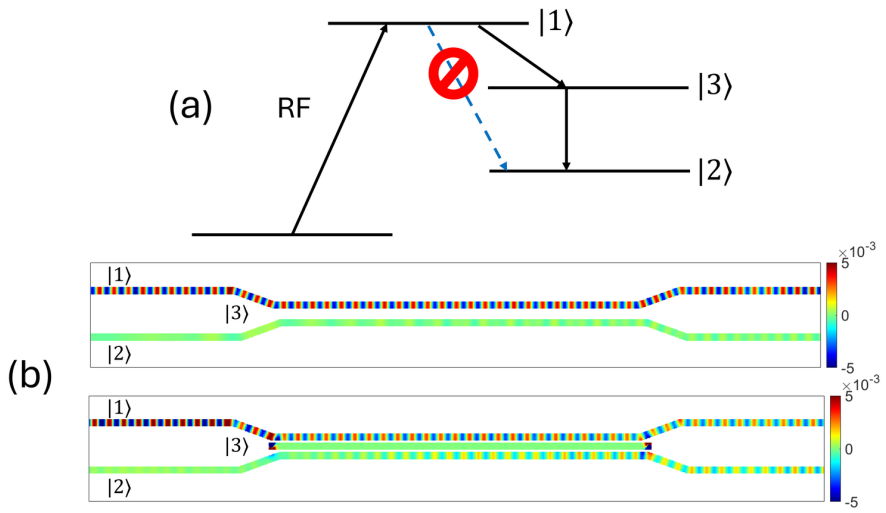

Figure 7.7: (a): schematic of the STIRAP protocol: population is transferred from $|1\rangle$ to $|2\rangle$ while the lossy intermediate level $|3\rangle$ remains unoccupied owing to destructive interference (dark state). Direct transition from $|1\rangle$ to $|2\rangle$ is forbidden. (b): simulated spin-wave propagation in a directional coupler with direct dipolar coupling between the excited ($|1\rangle$) and the not-excited waveguide ($|2\rangle$). For $\delta \geq 140$ nm, population transfer is negligible (here, $\delta = 140$ nm). (c): same geometry with a high-damping intermediate guide ($|3\rangle$) made of permalloy (width 100 nm) inserted between the two YIG channels, acting as a dark conduit that enables adiabatic energy transfer from $|1\rangle$ to $|2\rangle$, in analogy with STIRAP.

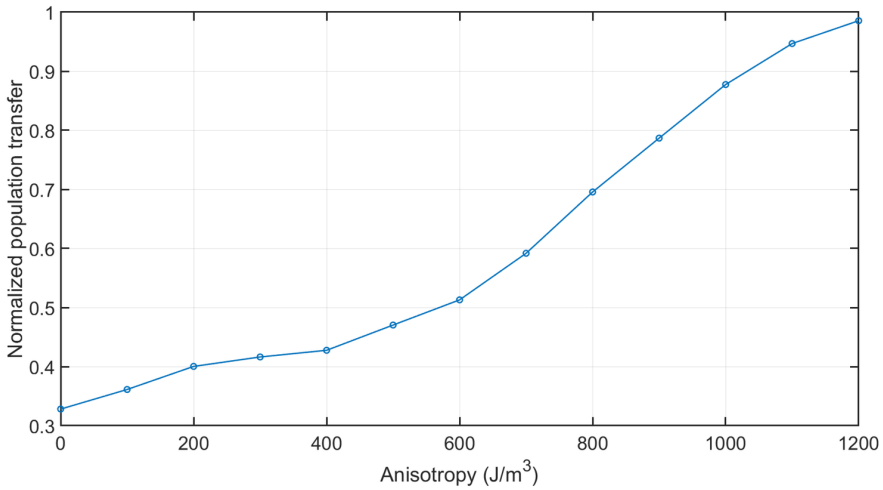

Figure 7.8: Population transfer efficiency (blue dots) as a function of the uniaxial anisotropy constant K_u in a STIRAP-based directional coupler with modulation period $\Lambda = 40$ nm. The blue line is a guide for the eye.

overlayer, which induces a sinusoidal magnetization in the underlying ferromagnetic structure.

By mapping STIRAP onto a magnonic directional coupler, we have identified a coherent pathway to shuttle spin-wave energy and phase between spatially separated YIG guides while keeping a deliberately lossy intermediate channel effectively dark. Even when direct dipolar exchange is suppressed at larger separations, the insertion of a high-damping conduit and the use of spatially patterned uniaxial anisotropy K_u recover and tune the transfer, suggesting near-term applications

in reconfigurable, low-dissipation interconnects, robust signal routing and phase-preserving magnonic logic. At the same time, the features that enable this behavior also set the limits of the present study, which should be regarded as embryonic: the analysis is based on simplified geometries and preliminary simulations. Addressing these aspects through targeted experiments, systematic optimization of K_u and geometry, dispersion engineering and extensions to multi-port networks or time-modulated couplings will determine the practical reach of the approach. Thus, the present results represent both a preliminary validation and a starting point for further development, indicating that adiabatic control concepts can be fruitfully transplanted into magnonics, opening a promising, if still early, route to scalable coherent spin-wave circuitry.

7.5 CONCLUSIONS

In this study, we investigated the magnonic directional nanocoupler and the possibility to finely control the levels of the population transfer between the waveguides in order to reconfigure its functionality and make it work as a variety of devices in real-world applications, namely in integrated circuits. This result can be achieved in many ways, depending on the available equipment and the desired accuracy: here, we suggest the use, as an effective degree of freedom, of a uniaxial magnetic anisotropy with different orientation of the easy axis in the proximity region realizing a periodic undulated pattern. With a proper prearranged sequence of ferroelectric domains with periodic polarization it is possible to obtain such a configuration. As a consequence, the local magnetization relaxes to a sinusoidal distribution of the magnetic moments whose oscillation amplitude is proportional to the magnitude of the applied anisotropy. This has been shown to lead, after the excitation of the system to a specific frequency and a bare temporal evolution, to a change in the propagation of the spin waves, more precisely in the group velocity, and in the frequency splitting of the symmetric and antisymmetric mode; their ratio (up to a constant) is found to be approximately linear decreasing for increasing anisotropy. The variations of the group velocity and the frequency splitting imply a modification of the intensity of the population transfer which covers, within a limited window of anisotropy values, a complete variety of possible levels. We observe an almost complete rise in pt when K_u is absent or at very low values, followed by a progressive inhibition of energy transfer until it vanishes entirely between 200 and 800 $\mathrm{J/m^3}$, and then a rapid increase of pt of up to 50 % at 1000 $\mathrm{J/m^3}$. In this way, a broad spectrum of device functionality is ensured, regardless of the anisotropy modulation period Λ considered. In this regime, we develop a simple theoretical model with the reasonable assumption of constant group velocity which accurately reproduces the data obtained by means of micromagnetic simulations. Higher K_u values, limited to short Λ, up to 2000 $\mathrm{J/m^3}$ for $\Lambda = 40$ nm (above this threshold the device losts its functionality because of initial stationarity and then evanescence of spin waves) result, after an almost complete population transfer, in a stabilization towards an intermediate passage of magnonic energy in the not excited conduit.

In this case, a phenomenological model based on a decreasing exponential form for the group velocity and an increasing saturating one for the frequency splitting, allows to reproduce the data obtained with simulations. The analysis of the dispersion curves as a function of K_u provides further evidence supporting the previously discussed trends and validating the operating mechanism of the device. We have also shown, through preliminary simulations, that a YIG directional coupler can implement a STIRAP-like transfer when it is augmented by an intermediate high-damping permalloy waveguide acting as the dark channel. For large inter-guide separations where direct dipolar exchange yields negligible pt (e.g., $\delta \gtrsim 140$ nm), the permalloy conduit, together with spatially patterned uniaxial anisotropy K_u, restores and electrically tunes pt. These results point to a reconfigurable, low-dissipation building block for coherent magnonic routing. In this regard, further analyses are ongoing.

7.6 APPENDIX

Derivation of the expression for the population transfer

In this Appendix we show the calculations that lead to the expression of the populaton transfer. Two identical waveguides, coupled by dipolar interactions, support two eigenmodes: a symmetric mode with wave number k_s and an antisymmetric mode with wave number k_{as}. The wave number mismatch is defined as $\Delta k = |k_s - k_{as}|$. The field in the excited waveguide can be expressed as the superposition of the two eigenmodes:

$$\Psi(x=0) = \frac{1}{\sqrt{2}}\left(\psi_s + \psi_{as}\right).$$

Thus, the general expression for the field is:

$$\Psi(x) = \frac{1}{\sqrt{2}}\left(\psi_s e^{ik_s x} + \psi_{as} e^{ik_{as} x}\right).$$

For the two waveguides we obtain:

$$\Psi_1 = \frac{1}{\sqrt{2}}\left(\psi_s + \psi_{as}\right),$$

$$\Psi_2 = \frac{1}{\sqrt{2}}\left(\psi_s - \psi_{as}\right).$$

The projection of $\Psi(x)$ on Ψ_1 and Ψ_2 gives the field amplitudes in the two guides:

$$\Psi_1(x) = \frac{1}{2}\left(e^{ik_s x} + e^{ik_{as} x}\right) = e^{i\frac{(k_s+k_{as})x}{2}} \cos\left(\frac{\Delta k}{2} x\right),$$

$$\Psi_2(x) = \frac{1}{2}\left(e^{ik_s x} - e^{ik_{as} x}\right) = i\, e^{i\frac{(k_s+k_{as})x}{2}} \sin\left(\frac{\Delta k}{2} x\right).$$

The optical power is given by the squared modulus of the fields:

$$P_1(x) \propto |\Psi_1(x)|^2 = \cos^2\left(\frac{\Delta k}{2} x\right),$$

$$P_2(x) \propto |\Psi_2(x)|^2 = \sin^2\left(\frac{\Delta k}{2} x\right).$$

Now let L_W denote the length of the coupling region. The normalized output power in each guide is then:

$$P_{1,\text{out}} = P_{\text{in}} \cos^2\left(\frac{\Delta k\, L_W}{2}\right),$$

$$P_{2,\text{out}} = P_{\text{in}} \sin^2\left(\frac{\Delta k\, L_W}{2}\right).$$

We define the coupling length as:

$$L_c \equiv \frac{\pi}{\Delta k} \quad \text{(for complete transfer)}.$$

The distance at which the two modes have accumulated a relative phase difference $\Delta\phi = \Delta k\, L_c = \pi$ is thus L_c. The population transfer

coefficient is defined as the ratio of the output power in the non-excited waveguide to the input power:

$$pt = \frac{P_{2,\text{out}}}{P_{\text{in}}} = \sin^2\left(\frac{\pi L_W}{2L_c}\right). \tag{7.A1}$$

Eq. (7.A1) quantifies the fraction of power transferred from one waveguide to the other within the coupling region.

BIBLIOGRAPHY

[1] Krzysztof Szulc et al. "Reconfigurable Magnonic Crystals Based on Imprinted Magnetization Textures in Hard and Soft Dipolar-Coupled Bilayers". In: *ACS Nano* 16.9 (2022). PMID: 36043881, pp. 14168–14177. DOI: 10.1021/acsnano.2c04256. eprint: https://doi.org/10.1021/acsnano.2c04256. URL: https://doi.org/10.1021/acsnano.2c04256.

[2] Enrique A. J. Marcatili. "Dielectric rectangular waveguide and directional coupler for integrated optics". In: *The Bell System Technical Journal* 48.7 (1969), pp. 2071–2102.

[3] David Marcuse. "The coupling of degenerate modes in two parallel dielectric waveguides". In: *The Bell System Technical Journal* 50.6 (1971), pp. 1791–1816.

[4] Weng W. Huang. "Coupled-mode theory for optical waveguides". In: *Journal of the Optical Society of America A* 11.3 (1994), pp. 963–969.

[5] David M. Pozar. *Microwave Engineering*. 4th ed. Hoboken, NJ: Wiley, 2012. ISBN: 978-0470631553.

[6] Alessandro Tuniz et al. "Directional Coupling to a $\lambda/5000$ Nanowaveguide". In: *ACS Nano* 18.44 (2024). PMID: 39433463, pp. 30626–30637. DOI: 10.1021/acsnano.4c09434. eprint: https://doi.org/10.1021/acsnano.4c09434. URL: https://doi.org/10.1021/acsnano.4c09434.

[7] Chih-Zong Deng et al. "Near-Zero-Index Slabs on Bloch Surface Wave Platform for Long-Range Directional Couplers and Optical Logic Gates". In: *ACS Nano* 16.2 (2022). PMID: 35119823, pp. 2224–2232. DOI: 10.1021/acsnano.1c08318. eprint: https://doi.org/10.1021/acsnano.1c08318. URL: https://doi.org/10.1021/acsnano.1c08318.

[8] Dries Vercruysse et al. "Single Asymmetric Plasmonic Antenna as a Directional Coupler to a Dielectric Waveguide". In: *ACS Photonics* 4.6 (2017), pp. 1398–1402. DOI: 10.1021/acsphotonics.7b00038. eprint: https://doi.org/10.1021/acsphotonics.7b00038. URL: https://doi.org/10.1021/acsphotonics.7b00038.

[9] Qi Wang et al. "Reconfigurable nanoscale spin-wave directional coupler". In: *Science Advances* 4.1 (2018), e1701517. DOI: 10.1126/sciadv.1701517. eprint: https://www.science.org/doi/pdf/10.1126/sciadv.1701517. URL: https://www.science.org/doi/abs/10.1126/sciadv.1701517.

[10] Xu Ge et al. *Deeply Nonlinear Magnonic Directional Coupler*. 2025. arXiv: 2505.13829 [cond-mat.mes-hall]. URL: https://arxiv.org/abs/2505.13829.

[11] Sasson Somekh. "Optical Directional Couplers". In: *Introduction to Integrated Optics*. Ed. by Michael K. Barnoski. Boston, MA: Springer US, 1974, pp. 265–314. ISBN: 978-1-4684-2082-1. DOI: 10.1007/978-1-4684-2082-1_11. URL: https://doi.org/10.1007/978-1-4684-2082-1_11.

[12] George F. R. Chen et al. “Broadband Silicon-On-Insulator directional couplers using a combination of straight and curved waveguide sections”. In: *Scientific Reports* 7.1 (2017), p. 7246. DOI: 10.1038/s41598-017-07618-6. URL: https://doi.org/10.1038/s41598-017-07618-6.

[13] B.W. Shore. *The Theory of Coherent Atomic Excitation: Simple atoms and fields*. The Theory of Coherent Atomic Excitation. Wiley, 1990. ISBN: 9780471524175. URL: https://books.google.it/books?id=pyBRAAAAMAAJ.

[14] Abdulqader Mahmoud et al. “Introduction to spin wave computing”. In: *Journal of Applied Physics* 128 (Oct. 2020), p. 161101. DOI: doi.org/10.1063/5.0019328. URL: http://doi.org/10.1063/5.0019328.

[15] Arne Vansteenkiste et al. “The design and verification of MuMax3”. In: *AIP Advances* 4.10 (2014), p. 107133. DOI: 10.1063/1.4899186.

[16] S.A. Odintsov et al. “Bilayer magnonic crystal directional coupler: Interlayer spin-wave coupling and formation of localized beams within a three-dimensional magnonic architecture”. In: *Phys. Rev. Appl.* 23 (3 Mar. 2025), p. 034043. DOI: 10.1103/PhysRevApplied.23.034043. URL: https://link.aps.org/doi/10.1103/PhysRevApplied.23.034043.

[17] Hiroshi Sasaki and Nobuo Mikoshiba. “Directional coupling of magnetostatic surface waves in a layered structure of YIG films”. In: *Journal of Applied Physics* 52.5 (May 1981), pp. 3546–3552. ISSN: 0021-8979. DOI: 10.1063/1.329134. eprint: https://pubs.aip.org/aip/jap/article-pdf/52/5/3546/18392919/3546_1_online.pdf. URL: https://doi.org/10.1063/1.329134.

[18] Stefan Maendl and Dirk Grundler. “Multi-directional emission and detection of spin waves propagating in yttrium iron garnet with wavelengths down to about 100 nm”. In: *Applied Physics Letters* 112.19 (May 2018), p. 192410. ISSN: 0003-6951. DOI: 10.1063/1.5026060. eprint: https://pubs.aip.org/aip/apl/article-pdf/doi/10.1063/1.5026060/14141599/192410_1_online.pdf. URL: https://doi.org/10.1063/1.5026060.

[19] Huajun Qin et al. “Propagating spin waves in nanometer-thick yttrium iron garnet films: Dependence on wave vector, magnetic field strength, and angle”. In: *Phys. Rev. B* 98 (22 Dec. 2018), p. 224422. DOI: 10.1103/PhysRevB.98.224422. URL: https://link.aps.org/doi/10.1103/PhysRevB.98.224422.

[20] A. Yariv. “Coupled-mode theory for guided-wave optics”. In: *IEEE Journal of Quantum Electronics* 9.9 (1973), pp. 919–933. DOI: 10.1109/JQE.1973.1077767.

[21] H. A. Haus, W. P. Huang, and A. W. Snyder. “Coupled-mode formulations”. In: *Opt. Lett.* 14.21 (Nov. 1989), pp. 1222–1224. DOI: 10.1364/OL.14.001222. URL: https://opg.optica.org/ol/abstract.cfm?URI=ol-14-21-1222.

[22] Pascal Frey et al. “Reflection-less width-modulated magnonic crystal”. In: *Communications Physics* 3 (Jan. 2020), p. 17. DOI: 10.1038/s42005-020-0281-y.

[23] Aleksei A. Nikitin and Erkki Lähderanta. "Spin-wave signal rejection in magnonic waveguides induced by conducting films with a single groove". In: *Phys. Rev. Appl.* 22 (6 Dec. 2024), p. 064049. DOI: 10.1103/PhysRevApplied.22.064049. URL: https://link.aps.org/doi/10.1103/PhysRevApplied.22.064049.

[24] Elena Bankowski et al. "Magnonic crystal as a delay line for low-noise auto-oscillators". In: *Applied Physics Letters* 107.12 (Sept. 2015), p. 122409. ISSN: 0003-6951. DOI: 10.1063/1.4931758. eprint: https://pubs.aip.org/aip/apl/article-pdf/doi/10.1063/1.4931758/13146198/122409_1_online.pdf. URL: https://doi.org/10.1063/1.4931758.

[25] Jing Xu et al. "Slow-Wave Hybrid Magnonics". In: *Phys. Rev. Lett.* 132 (11 Mar. 2024), p. 116701. DOI: 10.1103/PhysRevLett.132.116701. URL: https://link.aps.org/doi/10.1103/PhysRevLett.132.116701.

[26] K. Bergmann, H. Theuer, and B. W. Shore. "Coherent population transfer among quantum states of atoms and molecules". In: *Rev. Mod. Phys.* 70 (3 July 1998), pp. 1003–1025. DOI: 10.1103/RevModPhys.70.1003. URL: https://link.aps.org/doi/10.1103/RevModPhys.70.1003.

[27] Nikolay V. Vitanov et al. "Stimulated Raman adiabatic passage in physics, chemistry, and beyond". In: *Rev. Mod. Phys.* 89 (1 Mar. 2017), p. 015006. DOI: 10.1103/RevModPhys.89.015006. URL: https://link.aps.org/doi/10.1103/RevModPhys.89.015006.

[28] Q. Wang et al. "Stimulated-Raman-adiabatic-passage mechanism in a magnonic environment". In: *Applied Physics Letters* 118.18 (May 2021), p. 182404. ISSN: 0003-6951. DOI: 10.1063/5.0046046. eprint: https://pubs.aip.org/aip/apl/article-pdf/doi/10.1063/5.0046046/13008471/182404_1_online.pdf. URL: https://doi.org/10.1063/5.0046046.

8

CONCLUDING REMARKS

ABSTRACT

In this final Chapter, we discuss the main conclusions that were drawn from the research in this thesis. The purpose is to synthesize the key findings obtained throughout the different stages of the work, highlighting their physical implications and their contribution to the advancement of the field of programmable Magnonics.

8.1 CONCLUSIONS

In this thesis work we developed and validated a versatile route to program magnon transport in uniform ferromagnetic films by imprinting a controlled, nanoscale undulation of the equilibrium magnetization. The central message is that the *amplitude* of the undulation of a *sinusoidal magnetization* texture constitutes actionable, low-dissipation control knob for magnonic spectra and transport. This is achieved by means of textures realized via tailored *bias fields*, *patterned anisotropies* and especially *multiferroic coupling*. We based our analysis on a combined methodology: GPU-accelerated micromagnetic simulations solving the Landau–Lifshitz–Gilbert equation [1, 2], spatiotemporal Fourier analysis of space–time magnetization maps [3] and compact analytical models that rationalize the numerical trends.

The first line of results concerns the controlled introduction of periodicity in a thin ferromagnetic film by superimposing a spatially sinusoidal bias field B_S on top of a uniform field B_0 [4]. This operation turns a uniform film into a *magnonic crystal*: *Bragg scattering* at the Brillouin-zone boundary *lifts the degeneracy* between counter-propagating modes, *opens frequency gaps* and *reshapes modal symmetries*. A subtle but consequential point is that the *physical* primitive cell of the dynamics is half of the geometric period of the imposed texture. Because the dynamics is insensitive to the sign of the local magnetization crest, only the absolute value of the undulation matters; this halves the operative periodicity experienced by spin waves and clarifies the connection between the imposed Zeeman term and the observed band-structure features. When the periodic field is made *chiral* (B_C), the mirror symmetry of the primitive cell is explicitly broken. The two halves of the cell become inequivalent: in one, magnetization and chiral field are predominantly aligned; in the other, they are largely antiparallel, enhancing the local divergence the magnetization and deepening the effective field well set by the demagnetizing interaction. This asymmetric landscape supports a uniform yet spatially *localized* solution with essentially flat dispersion. The mode is stationary, coexists with propagating modes of similar symmetry and exhibits an *effective gyromagnetic ratio* larger than the FMR value in Permalloy, pointing to opportunities for compact magnetic sensing [5] and for on-demand dynamic storage within the same conduit. Notably, such a localized flat mode does not arise in a uniformly magnetized film and is not induced by a purely sinusoidal field without chirality. The fact that it emerges at low bias and remains dispersionless as B_C is tuned makes it an appealing primitive for memory-in-waveguide architectures.

A second strand explores a particularly efficient actuation scheme in which the magnitude of B_S is kept fixed - and can therefore be chosen very small to mitigate Joule heating - while only its *fan angle* Θ_F (i.e., the angular spread of the field) is varied [6]. In the regime $B_0 > B_S$, this single geometric parameter provides an effective means of tuning the magnonic response: the Brillouin-zone gap increases almost *quadratically* with Θ_F, whereas its center shifts to lower frequencies. When $B_0 < B_S$, the same trends persist below a *critical* fan angle Θ_F^{crit}. The scaling of the band gap originates from the periodic Zeeman term,

whereas the downward shift of the band center reflects the modulation of the internal dipolar field. The practical implication is that magnonic pass/stop channels can be toggled in real time by a knob that does not rely on large currents. Frequency-selective routing and demultiplexing follow naturally by steering the spectral position and width of the gap, thus enabling reconfigurable filtering and path selection without altering the physical layout of the conduit.

The third achievement concerns a multiferroic bilayer in which a ferroelectric overlayer with periodically varying polarization transfers, via *inverse magnetoelastic effect*, a *spatially periodic uniaxial anisotropy* to the underlying ferromagnet [7]. In the simulations, this vertical coupling is modeled by a periodically modulated easy axis with uniform anisotropy strength K_u, which drives the ferromagnet into a continuous sinusoidal ground state. By tuning K_u electrically, the system is reversibly driven from a *magnonic metallic state*, characterized by a gapless, linear (Dirac-like) dispersion and high mobility, to a *magnonic insulating state* in which a finite frequency gap opens, grows nearly linearly at first, and then approaches saturation. In the insulating regime the curvature of the lower band increases, the effective magnon mass rises and the band progressively flattens until stationary, non-propagating modes dominate within a frequency interval on the order of ~ 1 GHz. The upper branch remains dispersive, so that localized storage and long-range transport can coexist in the same physical structure and be selected by frequency. Extending *Dirac's magnon picture* from discrete lattices to this continuous periodic medium clarifies that the effective "hopping rate" - and with it the magnon conductivity - emerges from the balance among exchange, dipolar, and anisotropy interactions [8, 9]. The voltage control of K_u thus becomes the ultimate actuator for a real-time, reversible magnonic metal–insulator transition, a key capability for low-dissipation magnonic logic and memory [10].

Finally, these ideas are translated to the device level by studying a *directional nanocoupler* formed by two parallel magnonic waveguides made of YIG. In the coupling region the easy axis is periodically rotated to imprint a sinusoidal modulation of the equilibrium magnetization. The dipolar interaction between the conduits splits the fundamental mode into *symmetric* and *antisymmetric* combinations, and the periodic undulation modulates both the *group velocity* v_g and the *frequency splitting* Δf between these modes [11]. As K_u is increased from zero, the *population transfer pt* initially rises toward completeness, then is progressively suppressed and nearly vanishes within a window of a few hundred J/m^3, before resurging to a substantial fraction at around 1 kJ/m^3. In practice, the directional coupler can be reconfigured to act as a power divider, a connector, or a frequency-selective multiplexer by voltage-tuning the anisotropy landscape in its coupling region. This dependence is robust to the choice of the anisotropy modulation period Λ in the experimentally relevant range; at shorter Λ, the functional range can be extended to higher K_u values before stationary behavior and evanescence suppress the device functionality. Simple theoretical descriptions capture these regimes: a constant v_g approximation suffices at low K_u, while at larger K_u phenomenological laws for a decreasing v_g and a saturating mode splitting reproduce

the simulated transfer curves with good fidelity. We have also shown that a STIRAP-inspired *three-level protocol* implemented on the same directional coupler can be mapped onto a three-guide magnonic structure. In this picture, the two low-loss YIG channels play the role of long-lived endpoint states, while a thin, strongly damped permalloy guide acts as the *dark intermediate state* that enables nearly loss-free transfer even when direct dipolar coupling between the outer guides is too weak. Micromagnetic simulations confirm that, for separations where a conventional coupler fails, the presence of this lossy conduit and a suitable pattern of uniaxial anisotropy restore a sizable population transfer that can be tuned by the same voltage-controlled K_u used elsewhere in this work. This establishes STIRAP as a natural design principle for robust, phase-coherent spin-wave routing in realistic, dissipative magnonic networks. More broadly, it illustrates how adiabatic control concepts borrowed from quantum optics can complement static band-structure engineering, enriching the toolbox for programmable, low-dissipation magnonic circuitry.

Naturally, there are limitations that bound the quantitative extrapolation of these findings to experiment and product-relevant environments. For instance, finite damping will broaden spectral features and shorten the lifetime of flat-band modes; disorder, edge roughness and finite-size effects may scatter magnons and reduce bandgap contrast. The realized K_u and its spatial fidelity depend on the ferroelectric domain configuration and strain transfer. The practical realization of a chiral bias field may rely on interfacial Dzyaloshinskii–Moriya interaction, chiral multiferroics or patterned current paths, each presenting specific implementation constraints. However, these caveats do not undermine the mechanisms uncovered here (e.g., Bragg scattering from a programmable periodic potential, symmetry breaking, anisotropy-driven mass renormalization) but they do emphasize the need for careful co-design of materials, patterning and measurement.

The outlook that follows from this work is both concrete and, in several respects, immediately actionable. On the experimental front, Brillouin light scattering, time-resolved magneto-optical Kerr microscopy and scanning-probe magnetometry can validate the predicted gap opening and tuning by Θ_F and K_u, map the emergence of further modes and quantify group-velocity and effective-mass renormalization. On the materials side, advances in multiferroic interfacing and nanoscale domain engineering should make it possible to transfer anisotropy patterns with the spatial fidelity assumed in the simulations and to actuate them by voltage with low leakage and high endurance. On the device level, time-multiplexed voltage gating could dynamically switch, on nanosecond timescales, between propagating and stationary regimes, thus enabling hybrid logic–memory operations. Finally, inverse-design strategies that combine compact models with global optimization or machine learning approaches could map desired transfer functions (e.g., filters, delay lines, demultiplexers, or directional couplers) onto realizable texture parameter sets, accounting for fabrication constraints.

BIBLIOGRAPHY

[1] Daniel D. Stancil and Anil Prabhakar. *Spin Waves: Theory and Applications*. Springer, 2009.

[2] A. Vansteenkiste et al. "The design and verification of MuMax3". In: *AIP Advances* 4.10 (2014), p. 107133. DOI: 10.1063/1.4899186. URL: https://doi.org/10.1063/1.4899186.

[3] B. Van de Wiele and F. Montoncello. "A continuous excitation approach to determine time-dependent dispersion diagrams in 2D magnonic crystals". In: *J. Phys. D: Appl. Phys.* 47 (2014). 10.1088/0022-3727/47/31/315002, p. 315002.

[4] P. Micaletti et al. "A sinusoidal magnetization distribution as an original way to generate a versatile magnonic crystal for magnon propagation". In: *Journal of Magnetism and Magnetic Materials* 622 (2025), p. 172959. ISSN: 0304-8853. DOI: https://doi.org/10.1016/j.jmmm.2025.172959. URL: https://www.sciencedirect.com/science/article/pii/S0304885325001908.

[5] Md Shamim Sarker et al. "Sensitivity enhancement in magnetic sensor using CoFeB/Y3Fe5O12 resonator". In: *Scientific Reports* 12.1 (June 2022), p. 11105. ISSN: 2045-2322. DOI: 10.1038/s41598-022-15317-0. URL: https://doi.org/10.1038/s41598-022-15317-0.

[6] Hyeon Woo Park et al. *Magnon thermal conductivity in multiferroics with spin cycloids*. 2025. arXiv: 2503.11135 [cond-mat.mtrl-sci]. URL: https://arxiv.org/abs/2503.11135.

[7] Pietro Micaletti et al. "Magnonic analog of a metal-to-insulator transition in a multiferroic heterostructure". In: *Journal of Applied Physics* 137 (2025), p. 153906. DOI: 10.1063/5.0250690. URL: https://doi.org/10.1063/5.0250690.

[8] J. Fransson, A. M. Black-Schaffer, and A. V. Balatsky. "Magnon Dirac materials". In: *Physical Review B* 94 (2016), p. 075401. DOI: 10.1103/PhysRevB.94.075401. URL: https://doi.org/10.1103/PhysRevB.94.075401.

[9] Sergey S. Pershoguba et al. "Dirac Magnons in Honeycomb Ferromagnets". In: *Phys. Rev. X* 8 (1 Jan. 2018), p. 011010. DOI: 10.1103/PhysRevX.8.011010. URL: https://link.aps.org/doi/10.1103/PhysRevX.8.011010.

[10] V. Ariel and A. Natan. "Electron effective mass in graphene". In: *2013 International Conference on Electromagnetics in Advanced Applications (ICEAA)*. IEEE, 2013, pp. 696–698. DOI: 10.1109/ICEAA.2013.6632357.

[11] Qi Wang et al. "Reconfigurable nanoscale spin-wave directional coupler". In: *Science Advances* 4.1 (2018), e1701517. DOI: 10.1126/sciadv.1701517. eprint: https://www.science.org/doi/pdf/10.1126/sciadv.1701517. URL: https://www.science.org/doi/abs/10.1126/sciadv.1701517.

RINGRAZIAMENTI

Al termine di ogni percorso, è bene soffermarsi un attimo su ciò che è stato e, poiché detesto essere a qualsiasi titolo un debitore, intendo manifestare, a mo' di quella che ritengo una minima forma di compensazione e risarcimento, la mia riconoscenza a chi ha reso innanzitutto possibile e poi affrontabile questo triennio, da cui auspico di trarre vantaggi tangibili in futuro, fermo restando che le basi immateriali sono state gettate.

Desidero quindi ringraziare il Prof. Federico Montoncello, mio ottimo supervisore, per il suo energico coinvolgimento nelle mie vicende - o forse, più onestamente, dovrei dire vicissitudini - e la sua straordinaria disponibilità in qualunque ambito. Per parafrasare alcune sue lancinanti massime, mi ha insegnato, con le parole e con l'esempio, una cruciale lezione di vita, ossia che "la perfezione va sempre rasentata" anche quando "non ci sono nemmeno i mezzi per potersi comprare fazzoletti con cui asciugarsi le lacrime dovute alla mancanza dei mezzi stessi".

Esprimo la mia gratitudine al Prof. Ezio Iacocca per il suo supporto prima, durante e dopo il mio soggiorno presso l'Università del Colorado | Colorado Springs e per avermi mostrato quanto a volte sia salutare vedere le cose in una prospettiva diversa.

Colgo l'occasione per porgere i miei ringraziamenti al Prof. Federico Spizzo per la sua umanità e la sua vicinanza in un frangente per me non particolarmente roseo. A questo proposito, sono riconoscente ai medici dell'Ospedale Infermi di Rimini e al personale sanitario per la gestione, per ora esemplare, dei miei problemi di salute.

Inoltre, la mia gratitudine va ai nuclei del Circolo Estense Circense e della Divisione Romagnola Guasconi in virtù dello svago e del senso di leggerezza che hanno saputo offrirmi nei periodi più foschi.

I miei genitori sono stati un imprescindibile punto di sostegno e riferimento durante questi anni, nonostante le difficoltà, e a loro va il mio più sentito grazie. Ho il raro privilegio di essere un figlio fortunato; grazie Silvia, grazie Paolo.

Infine, senza voler scadere nella megalomania che affligge troppi studenti durante la stesura dei ringraziamenti, vorrei riconoscere, per quanto mi è dato, i giusti meriti alla mia inerte ostinazione, immaginando - probabilmente a torto - di poterla disgiungere dalla mia persona.

ACKNOWLEDGEMENTS

At the end of each journey, it is good to pause for a moment and reflect on what has been, and since I hate being indebted in any way, I would like to express, as a form of what I consider to be minimal compensation and recompense, my gratitude to those who made it possible in the first place and then made it manageable this three-year period, from which I hope to derive tangible benefits in the future, given that the intangible foundations have been laid.

I would therefore like to thank Prof. Federico Montoncello, my excellent supervisor, for his energetic involvement in my affairs - or perhaps, more honestly, I should say vicissitudes - and his extraordinary availability in all areas. To paraphrase some of his poignant maxims, he taught me, through words and example, a crucial life lesson, namely that "perfection must always be striven for" even when "there are not even the means to buy tissues to dry the tears caused by the lack of those means."

I would like to express my gratitude to Prof. Ezio Iacocca for his support before, during, and after my stay at the University of Colorado | Colorado Springs, and for showing me how beneficial it can sometimes be to see things from a different perspective.

I would like to take this opportunity to thank Prof. Federico Spizzo for his humanity and closeness during a time that was not particularly rosy for me. In this regard, I am grateful to the doctors at the Infermi Hospital in Rimini and the healthcare staff for their exemplary management of my health problems.

Furthermore, I am grateful to the Circolo Estense Circense and Divisione Romagnola Guasconi groups for the entertainment and sense of lightheartedness they offered me during the darkest times.

My parents have been an indispensable source of support and guidance during these years, despite the difficulties, and I offer them my heartfelt thanks. I have the rare privilege of being a lucky son; thanks Silvia, thanks Paolo.

Finally, without wanting to fall into the megalomania that afflicts too many students when writing acknowledgments, I would like to give credit, as far as I can, to my inert obstinacy, imagining - probably wrongly - that I can separate it from my person.